Space Science Reviews (2025) 221:42
https://doi.org/10.1007/s11214-025-01161-x

The AstroPAH 10 Years of Science Review

Helgi Rafn Hrodmarsson[1] · Isabel Aleman[2] · Alessandra Candian[3] · Sandra Wiersma[4] · Julianna Palotás[5] · David Dubois[6] · Ameek Sidhu[7,8] · Donatella Loru[9] · Pavithraa Sundarajan[10] · Ella Sciamma-O'Brien[6] · Alexander G.G.M. Tielens[10]

Received: 20 June 2024 / Accepted: 19 March 2025

Abstract
We celebrate the first ten years of the AstroPAH Newsletter by giving an overview of the scientific advances in the field of polycyclic aromatic hydrocarbons (PAHs) in astronomical environments that have been disseminated through the AstroPAH newsletter. This overview comprises ten chapters – each of which comprising subsections focused on observations, experiments, theory, and modeling – dedicated to subjects such as infrared emission, ultraviolet processing, dust, H2 formation, galaxies, dark molecular clouds, Herbig Ae/Be stars and protoplanetary disks, solar system objects, the diffuse interstellar bands, and the anomalous microwave emission.

Keywords Polycyclic aromatic hydrocarbons · Astrochemistry · Molecular physics · Molecular spectroscopy · Infrared: general

1 Introduction

Since the 1970s, ground-based and airborne observations of the sky have revealed an overabundance of mid-IR emission features in H II regions, planetary nebulae (PNe), and reflection nebulae (RNe). Thanks to advances in instrumentation over the last decades, these emission features were found to be a ubiquitous and omnipresent indicator of the presence of polycyclic aromatic hydrocarbons (PAHs) and related species (Tielens 2008, 2021). With the advances in ground-based observatories, as well as airborne and space telescopes, not only has the observable spectral range increased, but also the sensitivity level and spatial resolution from which we can analyze a veritable zoo of astronomical objects and their diverse spectral features in great detail. Large carbon-bearing species, such as PAHs and other members of their molecular family, can produce features from the ultraviolet (UV) to the submillimeter wavelength ranges. To successfully disentangle these features, observations have often been carefully guided by laboratory and theoretical work, as well as dedicated models. To fully appreciate an astronomical spectrum, interdisciplinary approaches that allow us to paint a picture of the cosmic evolution of the different environments in space are critical.

Extended author information available on the last page of the article

Published online: 06 May 2025

"The Molecular Physics of Interstellar PAHs" workshop was held at the Lorentz Center in Leiden, the Netherlands, in July 2013.[1] One of the main goals of the interdisciplinary and international group of scientists reunited there was to discuss strategies to advance the understanding of astronomical PAHs and how to maximize the scientific output obtained from observations. During the workshop discussions, the creation of a monthly newsletter was suggested to keep the PAH community informed of the latest developments in astronomical PAH research and as a tool to promote constant communication between the different fields (astronomy, chemistry, physics, *etc.*) working with PAHs.

The key astronomical questions related to PAHs that the participants defined at the time were:

- How does the astronomical PAH spectrum vary across the universe and over cosmic time?
- What can we learn from the astronomical PAH spectra about the interaction of stars with their environment and the characteristics and evolution of galaxies?
- What is the molecular inventory of astronomical PAHs, where do they come from and what is their role in the origin of life?

Strategies to tackle these questions were also proposed:

- increase spectral bandwidth for a diversity of astronomical objects,
- enhance guidance and prediction from laboratory and calculated data,
- develop an astronomer friendly toolbox to analyze astronomical observations based on the molecular physics driving the emission,
- increase diversity and spatial decomposition of astronomical objects,
- encourage interdisciplinary collaboration

For anyone newly entering the research field of PAHs in space, it is abundantly clear that different researchers across the wide spectrum of disciplines appear to speak different languages. The necessity for a multidisciplinary approach in the field of PAH research (laboratory, theory, astronomical observations; physics, chemistry, astronomy, *etc.*) complicates the interaction of researchers and students with different backgrounds, as we speak in different modals of jargon, and publish in different academic journals.

AstroPAH[2] was created to bridge this gap in communication between scientists to help promote further development in the field. AstroPAH has been publishing abstracts of newly accepted papers, theses, and dissertations relevant to the world of interstellar PAHs, jobs and meetings announcements, opportunities for collaborations, and special articles ("In Focus") about any topic relevant to the PAH research, scientist interviews or presentations of facilities for over 10 years. During this time, the newsletter has been publishing contributions from the research community and has therefore been in a privileged position to observe the evolution of research on PAHs in space. It is therefore appropriate to commemorate the first ten years of AstroPAH by providing the community with an overview of what has been accomplished in the preceding decade through an organized compilation of the hundreds of research works that have been submitted to AstroPAH as abstracts.

It should be made clear that our compilation does not represent all of the PAH related research conducted during the past ten years, but rather the research contained in contributed papers presented in the AstroPAH newsletter.

Reviews related to interstellar PAHs were originally conducted by Puget and Leger (1989), Allamandola et al. (1989), and twenty years later by Tielens (2008). Here we present

[1] https://www.lorentzcenter.nl/the-molecular-physics-of-interstellar-pahs.html.

[2] https://astropah-news.strw.leidenuniv.nl/.

an overview of all the new research that has been disseminated through the AstroPAH newsletter over its first decade. The text has been organized into ten main themes:

(i) PAH emission from the infrared (IR) to the UV and its association with the unidentified IR bands (UIB) and the extended red emission (ERE),
(ii) photon-dominated or photodissociation regions (PDRs), PNe, and RNe with an emphasis on radiation-driven PAH formation, destruction, and their general excitation dynamics,
(iii) dust in space and the relation of PAHs to dust,
(iv) H_2 formation from PAHs and superhydrogenated PAHs,
(v) galaxies, active galactic nuclei (AGNs) with an emphasis on X-ray-driven destruction and dynamics,
(vi) cold molecular clouds with an emphasis on microwave (MW) spectroscopy,
(vii) star and planet formation, Herbig Ae/Be objects and protoplanetary disks,
(viii) our Solar System with an emphasis on Titan, meteorites, and comets,
(ix) the diffuse interstellar bands (DIBs) with emphasis on electronic spectroscopy, and
(x) the anomalous microwave emission (AME).

Each of these themes is discussed in a dedicated section, with each section divided into subsections to address observations, experiments, theory, and modeling. It is our hope that this review will serve as a reference tool to assist astronomers, experimentalists, theorists, and modelers in forging links across disciplines in order to address profound questions about our Universe, following the goal of AstroPAH.

2 PAH Emission from the Infrared to the Ultraviolet - the Association of PAHs with the Unidentified Infrared Bands, Extended Red Emission, and Blue Luminescence

2.1 Observations

2.1.1 PAHs and the Unidentified IR Bands

The mid-IR observations of a wide variety of sources ranging from objects in our Solar System and the local interstellar medium (ISM) to the ISM of galaxies, have unveiled broad emission features that dominate the spectra. These features include strong bands observed at 3.3, 6.2, 7.7, 8.6, 11.2, and 12.7 μm (Fig. 1; Tielens 2008; Li 2020; Peeters et al. 2021). The mystery behind the carriers of these features resulted in them being collectively labeled as the 'unidentified' IR emission (UIE) features (Kwok 2022), 'unidentified' IR bands (UIBs), and, more recently, aromatic infrared bands (AIBs). In this review, we will adhere to the acronym AIBs considering the widespread consensus that PAHs are the principal molecular carriers of these features. PAHs comprise an essential component of the ISM and other astronomical objects and play an important role in multiple astrophysical environments and processes (Li 2020). PAHs absorb UV photons and redistribute their absorbed energy over various vibrational modes. The vibrationally excited PAHs then de-excite via IR fluorescence, resulting in the broad bands we observe. Typically, these observed AIBs have been attributed to PAHs containing between 50 to 70 carbon atoms. Li and Draine (2001) found the mean number of carbon atoms in one PAH molecule equal to $N_C = 100$ by modeling the PAH emission from the diffuse ISM, but recent work suggests this number is smaller (see Sect. 2.4.2). In the context of astronomy, it is important to note that the term 'PAHs'

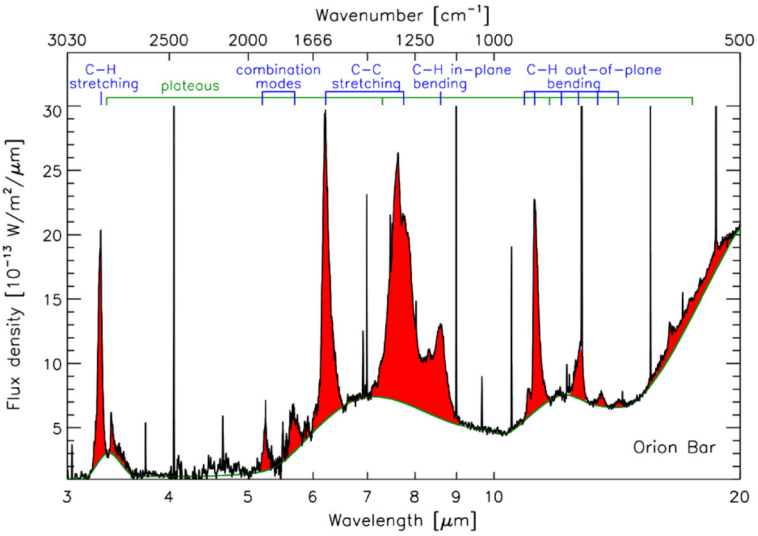

Fig. 1 The IR spectrum of the Orion Bar, a PDR in the Orion Nebula, observed by the Infrared Space Observatory (ISO). The AIBs are shown in red, superimposed on top of broad plateaus. The corresponding vibrational modes are labeled at the top. Adapted with permission from Peeters et al. (2021). Copyright 2021 American Chemical Society

encompasses a wide range of molecules, including conventional PAHs and closely related variants such as PAHs with side groups, heterosubstituted PAHs, fully or partially (de)hydrogenated PAHs, and PAH clusters. Although fullerenes are also carbon-based and include hexagons, their aromaticity is different from that of PAHs. Ultimately, fullerenes can be aromatic if they follow Hirsch's law for symmetrical aromaticity, i.e., the number of valence π-electrons follows $2(n+1)^2$ (Hirsch et al. 2000). A similar law exists for open shell fullerenes, namely $2n^2+2n+1$ (Poater and Sola 2011).

Currently, there are two prevailing hypotheses regarding the astronomical PAH family: the "grandPAH" and the "multi-PAH" hypotheses. Andrews et al. (2015) discovered that the mid-IR spectra from bright regions in a few well-studied PDRs like NGC 7023, NGC 2023, and NGC 1333 exhibit similar PAH emissions and that a mixture of the most stable PAHs, the "grandPAHs", can account for the features in all those regions. Alternatively, Rosenberg et al. (2014) demonstrated that a random combination of at least 30 different PAHs can replicate the observed astronomical PAH emissions, thus proposing the "multi-PAH" hypothesis. The confirmation of the correct alternative awaits the identification of the individual PAH components responsible for the AIBs.

Carefully studying band intensity ratios provides important insights into the carriers of the AIBs. For example, the intensity ratio of the 3.3 μm aromatic C–H stretching emission features to the 3.4 μm aliphatic C–H emission feature can provide constraints on the chemical structures of the carriers, i.e., whether they are mainly aromatic or largely aliphatic or with a mixed aromatic/aliphatic structure (Fig. 2; Yang et al. 2017a). Previously, Yang et al. (2013) found that by assuming that the 3.4 μm emission from 35 sources is purely aliphatic and ignoring any contributions due to anharmonicity or superhydrogenated PAHs, then the total aliphatic content contributing to the AIBs is approximately 2%.

The cosmic PAH emission is remarkably similar across the Universe. However, upon closer inspection diversity is observed in both relative band strengths and band profiles for

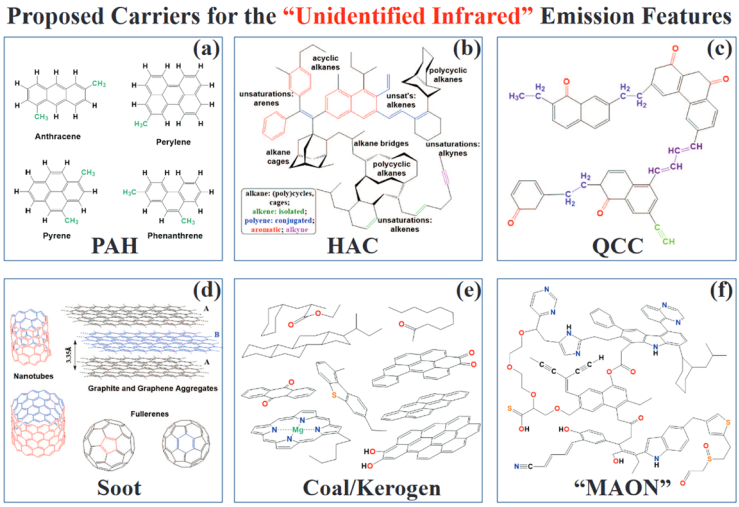

Fig. 2 Schematic structures for possible AIB carriers: (a) free-flying PAHs, (b) bulk hydrogenated amorphous carbon (HAC), (c) bulk quenched carbonaceous composites (QCC), (d) bulk soot, (e) bulk coal or kerogen, and (f) mixed aromatic/aliphatic organic nanoparticles (MAONs). Adapted with permission from Yang et al. (2017a). Copyright 2017 AAS

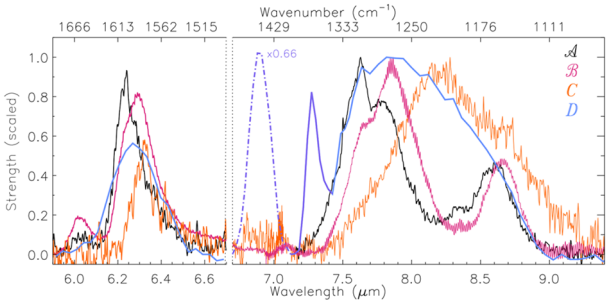

Fig. 3 Examples of different profile classes in the 6–9 μm PAH emission. Profiles are normalized to the peak intensity (Jy) in the 8 μm region. Strong aliphatic emission at 6.9 and 7.25 μm, (purple curve) is seen in class D. Class A is represented by IRAS 23133+6050, class B by HD 44179, class C by IRAS 13416-6243, and class D by IRAS f05110-6616. Adapted with permission from Peeters et al. (2021). Copyright 2021 American Chemical Society

collections of independent objects and spatially within extended structures (Peeters et al. 2021). The spectral profiles of the main PAH bands can be grouped into four different classes, A, B, C, and D, based mostly on the band peak position. The most prominent variations present in the 7.7 μm (1299 cm^{-1}) complex. The principal differences between these classes are exemplified in Fig. 3 and can be summarized as shown in Fig. 4. In general, interstellar material exhibits class A profiles (e.g., H II regions, RNe, and diffuse ISM clouds). On the other hand, circumstellar material displays profiles of classes B, C, and D. Post-Asymptotic Giant Branch (AGB) stars (stars at the end of their lifetimes) and Herbig Ae/Be stars (stars at the beginning of their lifetimes) exhibit those of classes B or C, but not D (Peeters et al. 2021).

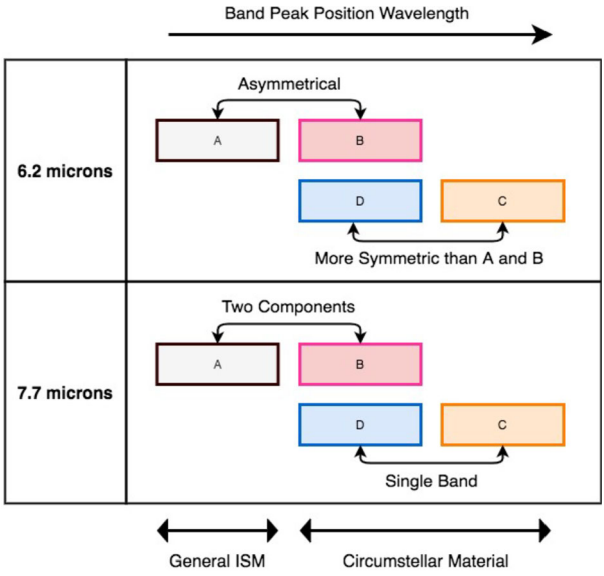

Fig. 4 General behavior and characteristics of the PAH bands spectral profile classes

Additionally, for the 6.2 μm band, the class A profile exhibits a peak at 6.2 μm and an asymmetric profile, whereas class B and C exhibit peaks at slightly longer wavelengths and have more symmetric profiles.

Class D profiles, although symmetric, have a peak position long-ward of class A but short-ward of classes B and C. The class A and B profiles feature traditional PAH bands at 7.7 and 8.6 μm but the distinction between them lies in the peak positions of two sub-components of the 7.7 μm band and the 8.6 μm band, with class B profiles peaking at longer wavelengths than class A profiles. On the other hand, class C and class D profiles display a single band in the 7–9 μm region. Class C profiles peak at 8.2 μm, while class D profiles peak at 7.7 μm. These profile variations are closely associated with the type of environment in which they are observed.

The detailed study of the 7.7 μm emission complex by (Shannon and Boersma 2019) showed that differences in PAH sizes can explain the largest shift observed in this PAH band (up to around 0.4 μm). Relatively small PAHs are consistent with class A spectra ($N_C \leq 60$), while larger PAHs are consistent with the red/very red class B spectra. According to this work, the transition from class B to class A is best explained by the variation in the PAH size distribution, with a small contribution of the aliphatic content and different charge states. The Shannon and Boersma (2019) results indicate a photochemical evolution of PAHs moving from shielded class C/B environments into the more exposed ISM class A PAH distribution, whereas traversing from class A to class B would indicate the incorporation of interstellar PAHs into ices around nascent star systems.

With the launch of James Webb Space Telescope (JWST), new PAH features are becoming accessible to us. The PAH model predicts many weak features in the 1–5 μm spectral range which contains fundamental information about the PAH population that is inaccessible via the much stronger PAH bands in the 5–20 μm region (Allamandola et al. 2021). The spectroscopic capabilities of the JWST Near Infrared Spectrograph (NIRSpec; Jakobsen et al. 2022) instrument on board JWST makes it possible to measure and fully characterize

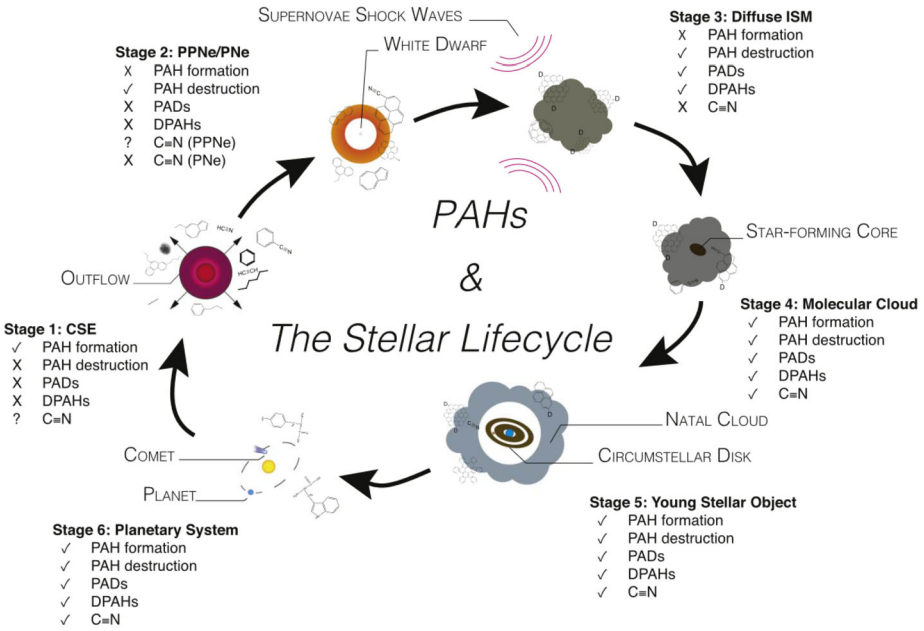

Fig. 5 The evolution of PAH populations in the lifetime of low-mass stars. Check and cross marks denote whether or not, respectively, the indicated formation, destruction, or emission takes place during that phase. C-rich stellar envelopes and preplanetary nebulae/planetary nebulae are denoted by acronyms CSE and PPNe/PNe, respectively. Adapted with permission from Allamandola et al. (2021). Copyright 2021 AAS

many of the PAH features expected in near IR range, which includes fundamental, overtone, and combination of C–D and C–N stretching bands of deuterated PAHs (also called PADs or DPAHs), cyano-PAHs, as well as overtones and combinations of the strong PAH bands that dominate the 5–20 μm range. Hence, we are a step closer to uncovering much greater nuances in the role PAHs play in the cosmic life cycle of matter (Fig. 5).

Now that the core concept of observing PAHs in interstellar environments has been introduced, what follows below is an overview of the research conducted from observations, which is then followed by IR spectroscopy, theory, and modeling relevant to PAH emission.

2.1.2 Physical Conditions and PAH Properties Derived from the PAH IR Band Characteristics

To first order, the observed PAH bands are very similar across various environments. However, a closer look reveals variations in their relative intensities, peak positions, and profile shapes. These variations reflect changes in the physical conditions of the environment where PAHs reside, which impact the PAH properties and, hence, the observed bands. Table 1 lists PAH band intensity ratios that reveal PAH physical properties.

The most prominent variations are observed in the relative intensity of the PAH bands at 6.6, 7.7, and 8.6 μm compared to the 3.3 and 11.2 μm bands. These variations indicate changes in the charge state of PAHs because the 6.2, 7.7, and 8.6 μm bands are more pronounced in the spectrum of cationic PAHs, while the 3.3 and 11.2 μm bands are stronger in the spectrum of neutral PAHs. The analysis of PAH observations across distinct environments and spatially across extended sources has shown that the charge state of PAHs is the

Table 1 PAH band ratios as diagnostics

PAH Band Ratio	Diagnostics[1]
3.3/11.2	PAH size
6.2/11.2	PAH charge
Sum of PAH bands /far IR flux[2]	PAH abundance

[1]See references in the text [2]See also Tielens (2021)

primary driver of variations observed in astronomical PAHs. A recent study involving Principal Component Analysis (PCA) of PAH emission in two RNe reaffirmed the significance of charge as the primary source of PAH variations (Sidhu et al. 2021). Furthermore, this study revealed an intricate aspect of ionic PAH bands, demonstrating that the 6.2 and 7.7 μm PAH bands exhibit systematic differences in behavior compared to the 8.6 and 11.0 μm PAH bands (see Sect. 2.4). Moreover, Peeters et al. (2017) showed that the cationic PAH bands exhibit different spatial morphologies, with 6.2 and 7.7 μm bands behaving as one group, while the 8.6 and 11.0 μm bands compose another.

Variations in the 3.3 and 11.2 μm PAH bands are indicative of changes in the size of PAH molecules (Knight et al. 2021a). Specifically, the 3.3 μm band arises from the C–H stretching mode of neutral PAHs, while the 11.2 μm band originates from the C–H out-of-plane bending mode of neutral PAHs. Smaller PAHs tend to become more vibrationally excited than larger PAHs. As a result, when they undergo de-excitation, smaller PAHs emit strongly at shorter wavelengths, whereas larger PAHs emit strongly at longer wavelengths. Given that the 3.3 and 11.2 μm bands are well-separated in terms of wavelengths and both emanate from neutral PAHs, the ratio between these bands remains independent of the charge state of the PAHs and serves as a reliable indicator of their size. Croiset et al. (2016) investigated variations in PAH size in the well-known reflection nebula NGC 7023 and found that the average size of PAHs decreases from approximately 70 carbon atoms in a cavity closer to the illuminating star to around 50 carbon atoms in a more distant PDR. Knight et al. (2021a) observed a similar decline in the average PAH size as one moves away from the illuminating source in another reflection nebula, NGC 2023. These works associate the variations in size to the increasing photoprocessing of PAHs subject to more intense radiation fields (photochemical evolution). A potential link between small and ionized PAHs in star-forming regions and larger PAHs in the gas surrounding evolved star was found in the study conducted by Anand et al. (2023).

It has been well-established that variations in the 10–15 μm spectral region provide insights into changes in the molecular edge structure of PAHs (Candian et al. 2012; Peeters et al. 2017). The bands in this region originate from the C–H out-of-plane bending modes, with the precise peak position of these bands depending on the number of adjacent peripheral C–H bonds. The detailed analysis of PAH emission bands and their sub-components has shown that the effects of molecular structure also extend to the intensity variations of other PAH bands. For example, in their analysis of the 3.3 μm PAH emission observed with UIST imager spectrometer at the United Kingdom Infrared Telescope (UKIRT) in the Red Rectangle nebula, Candian et al. (2012) interpreted the profile and distribution as the existence of two sub-components at 3.28 and 3.3 μm, attributed by the authors to the bay and non-bay hydrogen sites on small neutral PAHs, which exhibit distinct spatial distributions. Observations made by Tokunaga et al. (2022) (with the SpeX spectrograph at NASA Infrared Telescope Facility, IRTF), however, do not support this conclusion.

Recent studies have shown that in addition to the charge state, features in the 7–9 μm region are also sensitive to the molecular structure of PAHs, with compact PAHs featuring a strong 7.6 μm band, irregular PAHs featuring a strong 8.2 μm band, and large symmetric PAHs featuring a strong 8.6 μm band (Bauschlicher et al. 2008, 2009; Ricca et al. 2012; Peeters et al. 2017).

The chemical makeup of the PAH family also affects the relative intensity of PAH bands. For example, the observed intensity variations of the 3.3 μm and 3.4 μm bands reflect the aromatic to aliphatic composition of the carrier. The deuterated PAHs have also been observed in a handful of sources exhibiting two features in the 4.4–4.6 μm region, with one feature at 4.4 μm attributed to aromatic C–D stretching mode and the other at 4.65 μm to aliphatic C–D stretching mode (Peeters et al. 2004; Hudgins et al. 2004; Onaka et al. 2013; Doney et al. 2016).

Variations of the 3.3 μm feature have been studied with AKARI satellite data (Murakami et al. 2007). By decomposing the 3.3 μm feature profile into six components in a number of Galactic sources of different nature, Hammonds et al. (2015) found that one of the components centered at 3.28 μm was often the main contributor to the 3.3 μm emission feature. The 3.28 μm feature emitting regions seem to overlap with environments that show persistent aliphatic methylene emission. The authors suggested that this is due to the presence of interlinking methylene groups between aromatic hydrocarbons which suggests initial growth of carbonaceous dust particles.

Onaka et al. (2022) studied the NIR (2.5–5 μm) spectra, returned by the Infrared Camera on board the AKARI satellite, of a young stellar object (YSO) in the direction toward the Galactic center. Strong absorption features of H_2O and CO_2 ices along with the 3.3 μm PAH band were observed. A 4.4 μm emission feature was also observed and showed good correlation with the 3.3 μm PAH emission, which supports the hypothesis it comes from the aromatic C–D stretching vibration. This detection of aromatic C–D emission can inform us on the deuteration process of PAHs in the ISM and where the missing deuterium in the ISM could be stored. Onaka et al. (2022) noted that this detection "suggests that the dense envelope with UV radiation would be crucial to detect the 4.4 μm emission feature with a significant level which expedites deuteration of PAHs in cold, dense regions". This was also experimentally predicted by Wiersma et al. (2020) (see Sect. 2.2.1).

Massa et al. (2022) analyzed low-resolution Spitzer Space Telescope (hereafter just Spitzer) 5-14 μm spectra of the diffuse emission toward a sample of stars to study the connection between the extinction and emission properties of the dust grains in the lines of sight, and examine their response to different physical environments. This study resulted in a quantification of the PAH emission features and showed there is a strong correlation between the 2175 Å UV bump in the studied stars' extinction curves and the strengths of the major mid-IR PAH emission features for the same lines of sight.

Data from Spitzer and Infrared Space Observatory (ISO) were also used to investigate the 21 μm emission feature observed in the short-lived preplanetary nebula (PPN) phase of stellar evolution (Mishra et al. 2015). In particular, the relation between the 21 μm feature and the 30 μm feature, which always accompanies the 21 μm feature and is commonly observed in all stages of stellar evolution from the AGB phase to PPN to PNe, as well as the AIB observed in the PPN, was evaluated. This study showed that the 21 μm feature is not correlated with the 30 μm feature, which contradicts the hypothesis these two features could come from the same carrier. It also showed the 21 μm feature is not correlated with the AIBs, which goes against the hypothesis of large PAH clusters being the carriers of the 21 μm feature. Finally, it showed the 30 μm feature and the AIBs are also not

correlated, which does not support the hypothesis that PAHs may result from the decomposition or shattering of the 30 μm feature carriers (e.g. hydrogenated amorphous carbon, HAC).

The IR emission spectral energy distribution (SED) of 21 μm sources (AGB and post-AGB objects) were modeled using the 2-DUST radiative code for axisymmetric dusty systems (Mishra et al. 2016). The correlation between mass-loss rates and the unidentified 21 and 30 μm features seen in carbon-rich PPNe were investigated and it was found that the 21 μm feature correlated with the mass-loss rate in AGBs but not in stellar winds suggesting that its carrier could condense in the AGB phase but its excitation and/or generation requires UV photons which are available in PPNe but not in AGB stars. The 21 μm feature carrier could be destroyed by the more energetic photons available in PNe. Secondly, the 30 μm feature correlates with the AGB star mass loss rate and the stellar wind to a lesser extent suggesting that its carrier could condense both in the AGB and in the superwind[3] phases and can be excited by visible/near-IR photons.

Finally, the new data from the JWST are revolutionizing the field of AstroPAH. Among the different observational programs, the PDRs4ALL early release science program (Berné et al. 2022b) is currently studying the variation of the PAH feature across the Orion Bar PDR with unprecedented spatial and spectral resolution.

2.1.3 Extended Red Emission and Blue Luminescence

Another PAH-linked emission is the ERE. This is a broad emission band in the range from around 540 nm to 700 nm (sometimes extending beyond 800 nm). The ERE is a phenomenon that has been observed in many kinds of environments, circumstellar and interstellar, in our Milky Way and other galaxies. Although there are suggestions, the carriers of ERE are still unknown. This motivated Witt and Lai (2020) to review the observational constraints of this phenomenon to better define possible ERE carriers and their formation mechanism. They highlighted constraints such as, for example, those found in the study of (Lai et al. 2017). Their modeling of space (ISO and Spitzer) and ground-based observations (Rancho Del Sol Observatory) of the nebulae IC 59 and IC 63 suggested that isolated molecules or molecular ions capable of inverse internal conversion and recurrent fluorescence (RF) could explain the ERE observations. In addition, a comparison of the ERE intensities in these objects with those found in the diffuse ISM suggested that the lifetime of the ERE carriers in more intense UV radiation field environments (like in IC 59 and IC 63) are significantly reduced.

Another example is the study of ISO and Spitzer observations by comparison with laboratory measurements made by Sarre (2019). This study showed that those observations show strong similarities with graphene oxide nanoparticles, which are a significant component of interstellar dust.

Evidence of the existence of PAHs in space has also been observed in the UV range, in the form of a broad emission peaking around 378 nm, known as blue luminescence. As pointed out by Witt and Lai (2020), although the ERE and blue luminescence are often mentioned together, they do not appear to share the same carriers or the same excitation or emission process. The association of the blue luminescence with the fluorescence produced by small neutral PAHs is now a generally accepted idea (see Witt and Lai 2020, van Genderen et al. 2015, and references there in).

[3] A high-density stellar wind at the end of the AGB phase, which removes almost the entire hydrogen-rich star outer envelope (see Lagadec and Zijlstra 2008, and references therein).

2.2 Experiments

The process of obtaining IR spectra of PAHs is not a straightforward exercise (Oomens 2011). Traditional solid-state absorption, and Raman spectroscopy are relevant to meteorite and exoplanet research but gas-phase spectra, or rather the spectra of well-isolated PAHs are required to further understand the PAH AIB connection as well as connections to other carbon-based species. However, PAHs have low vapor pressures and therefore to measure their gas-phase spectra, ultra-high vacuum chambers are required on top of heating the PAHs to their sublimation temperatures. Although challenging, this technique has been used to acquire Fourier transform IR (FT-IR) spectra of PAH molecules.[4] Various other techniques have been developed to isolate PAHs and record their spectra at lower temperatures, such as solid-phase matrix isolation and different kinds of gas-phase action spectroscopy, including cavity ring down spectroscopy (CRDS). In the past decades, major advances have been made in free-electron laser (FEL) facilities around the world.

2.2.1 Infrared Multiple Photon Dissociation and Infrared Photodissociation Spectroscopy

The FELIX (Free Electron Laser for Infrared eXperiments) facility has been instrumental in the study the mid-IR spectra of PAHs from 5-15 μm, and more recently up to 100 μm, as only a few light sources in the world can access this range with the same intensity and tunability.

The study of IR spectra of gaseous PAH cations has been particularly prolific in the years that AstroPAH has been active. While the features in the 3–4 μm range show the C – H stretch, the combination of C – C stretching and C – H bending in the 5–15 μm range show "fingerprints" of the individual isomers of PAHs, which can aid in the identification of possible structure-specific features in the AIBs. Combined with density functional theory (DFT) calculations (see Sect. 2.3), PAH structures resulting from (de)hydrogenation or fragmentation can be identified, for example.

The technique most widely used at FELIX is infrared multiple photon dissociation (IRMPD). Gas-phase PAH ions are monitored with mass spectrometry as a "parent signal". When the laser hits a resonance frequency in the ion, it absorbs multiple photons in rapid progression until it fragments. This appears in the mass spectrum as a decline in the signal of the parent ion, which is scanned along the laser wavelength to construct the IR spectrum. The fragments themselves then carry information about the dissociation behavior of the studied PAH. Most often for PAHs, these species need to be "decorated" with an added proton or N atoms, so that the fragmentation energy is sufficiently low. Infrared photodissociation (IRPD) spectroscopy operates in a similar manner, only it is usually carried out at cryogenic temperatures where a noble gas atom or inert molecule can be attached via van der Waals interactions with the PAH ion. A single photon rather than many can dissociate the weakly bonded tag, and thus deplete the parent ion signal. IRPD typically offers enhanced resolution and less spectral shift compared to IRMPD at room temperature.

[4] Rather than shining a beam composed of only a single wavelength on a sample, in FT-IR a beam containing many frequencies of light is shined at once and measures how much of that beam is absorbed by the sample. Next, the beam is modified to contain a different combination of frequencies, giving a second data point. This process is rapidly repeated many times and a Fourier transform algorithm transforms these data into a spectrum.

Protonated tetralin (1,2,3,4-tetrahydronaphthalene) was studied with IRMPD over the 5.5–9.1 μm range to reveal on which C atom in the second ring the added proton would settle. The main ionic dissociation product was $C_7H_7^+$, for which the calculated breakdown paths predict a benzylium structure (Vala et al. 2017).

The isomeric structures of $C_7H_7^+$ had been a long-standing mystery themselves, until Jusko et al. (2018) used mid-IRPD and DFT predictions to study them. Toluene and benzyl chloride were used as precursors and using electron impact to fragment them resulted in the predominant production of tropylium and benzylium. With this study, it was successfully demonstrated that both isomers are the only long-lived isomers of $C_7H_7^+$.

The same technique was applied by Wenzel et al. (2022) to identify the H-loss fragments of methylated naphthalene, anthracene and pyrene as either containing a XCH_2^+ benzylium-like site, or a XC_7^+ tropylium-like site. Only spectral evidence for the benzylium-like isomers was found through strong absorptions in the 6.2 μm (1620 cm^{-1}) band. Depletion experiments led to the conclusion that a mixture of isomers is present for the methylated acenes, but only one isomer is present for methylated pyrene. Not all of the spectral complexity could be explained through calculations, possibly due to neon tagging effects that were unaccounted for. However, the 6.2 μm (1620 cm^{-1}) band has been detected in the AIBs and could hint at a significant methylated PAH presence in the ISM.

In addition, Wiersma et al. (2020) studied the deuteration of PAHs by investigating the IRMPD spectra of anthracene in its $[H-C_{14}H_{10}]^+$, $[D-C_{14}H_{10}]^+$ and $[H-C_{14}D_{10}]^+$ forms, and phenanthrene in its $[H-C_{14}D_{10}]^+$ form. These were compared to DFT predictions to determine the most likely placement of the additional H/D. It was shown that H−D scrambling is common in PAH cations under UV radiation where aliphatic D atoms migrate easily to a more strongly bound aromatic site, protecting it from elimination.

Panchagnula et al. (2020) also used IRPD and DFT prediction to study the IR spectra of doubly-dehydrogenated pyrene cations, revealing that double dehydrogenation on pyrene most likely takes place from the same ring at once, no matter which ring is subjected to dehydrogenation.

Considering that the majority of experimental IR spectroscopy experiments have been done on relatively small PAHs, the exploration toward PAHs within the suspected ISM size range of at least $N_C = 40$–50 is most pertinent. Large PAHs and fullerenes can be brought into the gas phase and protonated through atmospheric pressure chemical ionization (APCI) with a direct insertion probe (DIP) inlet. These protonated species then form a good candidate for IRMPD in the same way smaller species do. Palotás et al. (2021b) compared the gas-phase IRMPD spectra of room-temperature, protonated dicoronylene and hexa-perihexabenzocoronene (HBC) to DFT predictions, and showed that the protonation takes place at the periphery of the bay regions. Comparison to an emission spectrum from the Iris nebula (NGC 7023, see Sect. 3.1.1) showed some similarity in the aromatic features between 6 and 9 μm.

Using this APCI technique, the IRMPD spectrum of protonated C_{60} was also measured by Palotás et al. (2019). This spectrum was compared to the IR emission spectra of SMP SMC16 and SMP LMC56 (both PNe), showing a possible contribution from $C_{60}H^+$ in the range from 6–25 μm. It was suggested that (an IRMPD spectrum of) $C_{70}H^+$ could improve this match, which was later confirmed by the same group (Palotás et al. 2021a). Five protonation sites are possible for $C_{70}H^+$, but using DFT calculated spectra, it was confirmed that only one isomer was formed. Considering the presence of C_{60} in O-rich PNe (see Sect. 3.1.2), Palotás et al. (2022) also studied IRMPD and DFT spectra of $C_{60}O^+$ and $C_{60}OH^+$. For this study, an Optical Parametric Oscillator (OPO) was used to perform IRMPD in the 3 μm range, as well as FELIX to study the 6–25 μm range. Comparison of

both IRMPD spectra to the IR emission spectrum of SMP SMC16 showed no conflicts, which suggested a possible solution to the astronomically observed broadening of the classical C_{60}^+ 17.3 and 18.9 μm features.

IRMPD of astronomically relevant species is also possible for undecorated cations if the laser power is high enough, such as in the "i-POP" setup (see Sect. 3.2.4) wherein a small cloud of PAH cations in a quadrupole ion trap can be irradiated with a tightly focused FELIX beam. Zhen et al. (2017) used this setup to record the IRMPD spectra of the undecorated cation and dication of HBC ($C_{42}H_{18}$). The spectra were so similar that no diagnostic features specific to the dication were found. Comparison of these spectra to the AIBs in NGC 6946 and NGC 4569 showed a coincidence for the bands at 6.5, 7.7, 8.4, and 13.1 μm. Zhen et al. (2018a) also measured the IRMPD spectra of diindenoperylene ($C_{32}H_{16}$) and dicoronylene ($C_{48}H_{20}$), which are less symmetric than HBC, and then compared them to the IR emissions from NGC 7023 together with HBC. In another i-POP study of four increasingly large PAHs with different symmetries — perylene ($C_{20}H_{12}$), peropyrene ($C_{26}H_{14}$), ovalene ($C_{32}H_{14}$) and isoviolanthrene ($C_{34}H_{18}$) — Bouwman et al. (2019) found a reduction of molecular symmetry, creating a large variety of vibrational modes in the 7–9 μm range, and leading to the appearance of a broad distribution rather than individual bands.

Bouwman et al. (2015b) also used IRMPD to study the spectra of Polycyclic Aromatic Nitrogen-containing Hydrocarbons (PANHs) and their dissociation characteristics (see Sect. 3.2.1). This study showed that dissociative ionization of isomers quinoline and isoquinoline (both C_9H_7N) exhibits clear HCN fragmentation, which is found to be a principal characteristic of PANHs that only include one N-atom. On the other hand, the formation of PANHs has been shown to be efficient at low-temperatures via exothermic pyridine cation ($C_5H_5N^+$) and acetylene ion-molecule reactions, forming cationic quinolizinium ($C_9H_8N^+$) (Rap et al. 2022b). The formation of PANHs is further explored in Sect. 3.2.2.

Explorations into the far-IR are a particular challenge due to the lack of appropriate light sources, and the lowered energy per photon limiting the forms of action spectroscopy that remain feasible. IRMPD spectra of cationic phenanthrene, pyrene, and perylene over the 100–1700 cm^{-1} (6–95 μm) spectral range were achieved by Wiersma et al. (2022) using the Fourier-Transform Ion Cyclotron Resonance (FT-ICR) mass spectrometer integrated in the Free-Electron Laser for Intra-Cavity Experiments (FELICE) at FELIX. This capability had previously been demonstrated by studying the phenylium cation ($C_6H_5^+$) and its deuterated form ($C_6D_5^+$) in terms of their spectra and dissociation behavior (Wiersma et al. 2021a). In this spectral region, the absence of spectral congestion and the drastic reduction in bandwidth with respect to the mid-IR make the far-IR PAH fingerprints viable candidates for theoretical benchmarking, which could aid in searching for individual large PAHs in the ISM.

The mid-IR spectra of three dibenzopyrene ($C_{24}H_{14}^+$) isomers, which all exhibit different levels of symmetry, were investigated as well by (Bouwman et al. 2021b). Because the number of IR active bands increases as the symmetry of the PAHs reduces the IRMPD spectra of these irregular PAHs were dense. The resulted spectra lack the sharp signatures typical of astronomical IR bands, and rather look like the broad plateau underlying them. The photodissociation behavior of one of these isomers, namely dibenzo[a,l]pyrene was investigated in more depth by Wiersma et al. (2021b) who noted that the richness of the C–C stretching range make irregular PAHs a possible contributor to class D interstellar spectra. The dibenzopyrenes have also been subject to various other fragmentation studies, both experimental (Zhen et al. 2016a; Hrodmarsson et al. 2022) (Sect. 3.2.4) and theoretical (Rodriguez Castillo et al. 2018) (Sect. 3.3.2).

Other charge states of PAHs besides monocations have also been studied. Experimental IR spectra of three different PAH dications, namely, napthalene, anthracene, and phenanthrene in the fingerprint region 500–1700 cm^{-1} were recorded by Banhatti et al. (2021). They observe double ionization to compete with fragmentation which also includes channels where neutral acetylene (C_2H_2) is formed along with a fragment dication.

The IR spectra of deprotonated (closed-shell) PAH anions such as naphthyl, anthracenyl, and pyrenyl were investigated using carboxylated PAHs as precursors (Gao et al. 2014). Here, the relative band intensities of the IR spectra are found to be significantly different from those of neutral and positively charged PAHs, as well as radical anion PAHs which would result from electron attachment to a neutral PAH rather than depronation.

2.2.2 IRPD Studies Using an Optical Parametric Oscillator

Multiple IRPD experiments have also been carried out outside of FELIX, using an OPO laser in the 3 μm range (C−H and O−H stretch). For instance, the group of Otto Dopfer in Berlin has investigated the IR and DFT spectra of many PAH cations clustered with water. Infrared spectra obtained through IRPD (3000–3800 cm^{-1}) were obtained for the naphthalene$^+$ – H_2O cation (Chatterjee and Dopfer 2017) which allowed structural motif differences from the benzene$^+$ – H_2O cation to be discussed. Later work in the same spectral regime investigated the naphthalene$^+$ – $(H_2O)_n$ cation clusters with up to five H_2O units attached (Chatterjee and Dopfer 2018b) and then also protonated naphthalene$^+$ – $(H_2O)_n$ clusters to study the protonation site and the structure of the hydration network (Chatterjee and Dopfer 2020b). These studies showed that for $n \geq 3$, the proton affinity of the water cluster substantially exceeds the one of naphthalene, leading to intracluster proton transfer.

Comparison of naphthalene- and benzene-water clusters gives indications of the structure of the hydration network and the critical threshold size required for intracluster proton transfer for both systems.

The same group measured the 3 μm IR spectrum of protonated cyanobenzene ($C_6H_5CNH^+$) (Chatterjee and Dopfer 2018a), which was pertinent considering the ISM detection of benzonitrile (see Sect. 7.1), which makes the presence of a protonated counterpart in the ISM very likely.

Later, Chatterjee and Dopfer (2020a) investigated the IR spectrum of protonated pyrimidine-water clusters as well as protonated pyrimidine-N_2 complexes. Their combined spectroscopic and computational approach unequivocally showed that protonation of pyrimidine (Pym) occurs at one of the two equivalent basic ring N atoms and that the ligands in H^+Pym–L (L = N_2 or H_2O) preferentially form linear H-bonds to the resulting acidic NH group. Comparison to neutral Pym–$(H_2O)_n$ clusters reveals the drastic effects of protonation on microhydration with respect to both structure and interaction strength.

Studies involving the microhydration of PAHs and related molecules are also addressed in sections dedicated to PAHs in ices (Sect. 4.2.4) and microwave spectroscopy (Sect. 7.2).

2.2.3 UV-IR Ion Dip at FELIX

For the study of neutral PAHs, the use of UV–IR ion dip spectroscopy has been conducted at FELIX to evaluate predicted frequencies and potential energy surfaces as well as to probe the structure of individual molecules. Jet-cooled, neutral PAHs can be efficiently ionized using resonance-enhanced multiphoton ionization (REMPI) at frequencies specific to each molecule, and detected with different mass-spectrometry techniques. Considering that these molecules are jet cooled, they are probed starting from their vibrational and electronic

ground states. The REMPI technique provides detailed insight into how ladder climbing and anharmonicity influence IR-UV spectroscopy and therefore the resulting IR signatures in the far-IR region where our understanding of the underlying mechanisms is far from complete (Lemmens et al. 2020).

Since its introduction, the technique has been used at FELIX to record high-resolution IR spectra of jet cooled PAHs (coronene, peropyrene, ovalene, HBC) in the 3–100 μm region (Lemmens et al. 2021a) and IR spectra of naphthalene and acenaphthene dimers to investigate the effects of non-covalent $\pi - \pi$ stacking and CH–π interactions (Lemmens et al. 2021b). It was also used to analyze benzene in an argon plasma discharge, from which larger PAHs, radicals and intermediates were formed that could serve as promising candidates for radio astronomical searches (Lemmens et al. 2022).

Preitschopf et al. (2022) subsequently used IR-UV ion dip to study the contribution of the 2-methylallyl radical (C_4H_7) to molecular growth in a high-temperature microreactor. Mass-selected IR-UV ion dip spectra allowed the detection of the radical, along with various jet-cooled reaction products such as fulvene ($(CH{=}CH)_2C{=}CH_2$), benzene, styrene ($C_6H_5CH{=}CH_2$), para-xylene (C_8H_{10}) as well as PAHs like naphthalene, and methylated naphthalene. This work is closely related to that of PAH formation, which is further explored in Sects. 3.2.2 and 3.3.3.

2.2.4 UV-IR Ion Dip Using an OPO

Similarly to the work done in IRPD, an equivalent of UV-IR ion dip spectroscopy is also possible in the 3 μm range using an OPO. Several studies have explored the high-resolution IR spectra in this C–H stretch range, and compared them to anharmonic theoretical calculations, which are described in Sect. 2.3.2.

First, the absorption spectra of linear PAHs like naphthalene, anthracene and tetracene were measured by Maltseva et al. (2015). The comparison of these experimental results with harmonic predictions revealed that the fraction of the intensity that is not associated with fundamental transitions may easily exceed 50% and therefore it must not be neglected in such analyses.

Later, Maltseva et al. (2016) explored high-resolution IR absorption spectra of isolated phenanthrene, pyrene, benz[a]anthracene, chrysene, triphenylene, and perylene to study how the peripheral structure of irregular PAHs affects the shape and position of their 3 μm absorption band. They showed that the 3 μm region is dominated by effects of anharmonicity, resulting in many more bands than would have been expected in a purely harmonic approximation. Maltseva et al. (2018) also studied the high-resolution spectra of several methylated and hydrogenated PAHs in the 3 μm region. They again demonstrated that anharmonicity plays an important if not a dominant role, affecting both aromatic, aliphatic, and alkyl C–H stretching vibrations. Observationally, the variation in these methylated and hydrogenated compositions could account for the observed variations in the 3 μm emission spectra of carbon-rich and star-forming regions and that heavily hydrogenated PAHs form a significant fraction of the carriers of IR emission in regions with an anomalously strong 3 μm plateau.

2.2.5 IR Spectroscopy on the AILES Beamline

Another major advancement in recording IR spectra was achieved at the AILES (Advanced Infrared Line Exploited for Spectroscopy) beamline at the Synchrotron SOLEIL facility.[5] It

[5] https://astropah-news.strw.leidenuniv.nl/AstroPAH_0043.pdf.

was developed for absorption spectroscopy and is applied to the study of gas-phase as well as condensed-phase systems and covers the mid-IR to far-IR or THz range (5–4000 cm^{-1}). In addition to the increased flux and brilliance of the synchrotron light beam, the beamline is designed for a high level of mechanical stability to minimize the noise level.

Using the AILES beamline, Goubet and Pirali (2014) recorded far-IR spectra of azulene ($C_{10}H_8$) and isoquinoline (C_9H_7N) in the 400–560 cm^{-1} spectral region in a long absorption path cell at room temperature. Their measurements were accompanied by high-level anharmonic DFT calculations. The experimental results validate the theoretical approach, which they also applied to fourteen other PAHs and PANHs to derive reliable rotational parameters in a reasonable computational timeframe.

Gruet et al. (2014) applied a similar methodology to study the mid- and far-IR spectra of two diazanaphthalenes (i.e., naphthalenes containing two N atoms) supported by the same electronic structure calculations. This study included the detailed rotational analysis of several bands in a range from 166–818 cm^{-1}. A rotational spectrum of one of the isomers was also recorded in the range 4–20 GHz (or 0.125–0.667 cm^{-1}) using a Fourier Transform Microwave (FT-MW) spectrometer based in the PhLAM laboratory[6] in Lille, France (microwave spectroscopy is described in more detail in Sect. 7.2).

Martin-Drumel et al. (2014) also used AILES to record far-IR spectra of six flexible aromatic molecules, including two non-fused benzene rings (biphenyl, 2-phenyltoluene), in the range from 50–650 cm^{-1}. They successfully determined most of the active low-frequency vibrational modes of this family of molecules and revealed a significant influence of the skeletal structure on the low-frequency vibrational modes.

To expand even further on the complementarity allowed in the combined study of the far-IR spectrum (50–300 cm^{-1}) and microwave (4–20 GHz) spectrum, Pirali et al. (2015) measured a millimeter wave spectrum (140–220 GHz) of quinoline to study its three lowest vibrational states. The higher vibrational modes displayed severe complications in their spectra due to perturbations. To fully unravel the experimental results, the dataset was fitted with Watson A–reduction Hamiltonian augmented with Coriolis and Fermi vibration-rotation coupling terms and hyperfine nuclear spin-quadrupole coupling parameters for the N nucleus.

More recently, Chawananon et al. (2022) presented jet-cooled rovibrational mid-IR spectra of naphthalene, [1,5]naphthyridine, and biphenyl in collaboration between the AILES beamline and the MONARIS laboratory[7] in Paris using a tunable mid-IR quantum cascade laser (QCL) spectrometer (6–10 μm) coupled to a pulsed supersonic jet. The experimental results provided significantly improved literature values for the spectroscopic parameters, and comparison with the aforementioned quantum chemical calculations confirmed the predictive powers of the corrected calculated rotational parameters.

2.2.6 Matrix Isolation Spectroscopy

Matrix isolation spectroscopy was the method of choice for the study of PAH IR spectra during the early days of the AIB hypothesis (Hudgins and Allamandola 1999a,b). Gas-phase PAH are deposited together with a relatively inert gas onto a cold surface, so that the molecule is immobilized in the matrix. An absolute absorption spectrum can be recorded over a broad frequency range through FT-IR, while the molecule is in the vibrational ground state and often a very low or ground rotational state. Interactions with the matrix can lead to

[6]Laboratoire de Physique des Lasers, Atomes et Molécules.

[7]Le laboratoire de la Molécule aux Nano-objets: Réactivité, Interactions et Spectroscopies.

small, but difficult-to-predict shifts in band position or intensity, in particular for the classically used Ar and Ne matrices.

Roser et al. (2014) used Ar matrices to record the IR spectra of anthracene clusters from 400–4000 cm^{-1}, followed by those of phenanthrene, chrysene, pyrene, perylene and benzo[ghi]perylene (Roser and Ricca 2015).

Strelnikov et al. (2015) studied laboratory IR absorption spectra of C_{60}^{+} and C_{60}^{2+} in a 5 K Ne and Ar gas matrices and reported some overlap of C_{60}^{2+} IR features in NGC 7023. The UV oscillator strengths of C_{60}^{+} were presented as well, which are of great interest for the ionization dynamics of C_{60} (Hrodmarsson et al. 2020) and its relation to the assignment of four of the DIBs to C_{60}^{+} (see Sect. 10).

In recent years, the use of a *para*-H_2 as a matrix has been employed in the group of Y.-P. Lee in Taiwan. This matrix has a smaller effect on the vibrational bands in comparison to the aforementioned noble gases, and also allows for the relatively easy production of hydrogenated PAHs and their distinction from the parent (Tsuge et al. 2018).

Tsuge et al. (2016b) used a *para*-H_2[8] matrix to record the mid-IR spectrum of protonated ovalene. The close resemblance of the observed spectral patterns to that of the AIBs allowed Tsuge et al. (2016b) to suggest that protonated ovalene may contribute to the emission features of objects that emit class A spectra, such as the IRIS reflection nebula NGC 7023. Tsuge et al. (2016a) also recorded the IR spectra of neutral and hydrogenated ovalene. Their results implied that hydrogenation of PAHs can occur at temperatures as low as 3.2 K. The effects of hydrogenation and super-hydrogenation are further explored in Sect. 5 on H_2 formation.

These studies were then extended from planar PAHs to non-planar with the recording of the IR spectrum of protonated corannulene ($C_{20}H_{10}H^{+}$; Sundararajan et al. 2018) and monohydrogenated corannulene (Sundararajan et al. 2019). In studying the hydrogenation of corannulene, correspondences between the 3.3 and 3.4 μm bands of *rim*-$HC_{20}H_{10}$ and astronomically observed PAH emission features were found. The IR spectrum of *hub*-$C_{20}H_{10}H^{+}$ closely resembled the astronomical AIBs insisting the contribution of a non-planar PAH to the AIBs cannot be ignored. The same group also studied the IR spectra of protonated PANH quinoline and its radical form, 1-quinolinium, and quinolinyl, respectively (Tseng et al. 2022).

2.2.7 IR and Raman Spectroscopy of Solid, Crystalline PAHs

The near-IR is a spectral range that is used extensively in remote sensing, but is little studied in terms of PAH spectroscopy. Izawa et al. (2014) measured the near-IR reflectance spectra of powders of 47 PAHs from 350–2500 nm (0.35–2.5 μm). All spectra revealed three strong overtone bands around 880, 1145, and 1687 nm. Decorated PAHs with various inclusions such as aliphatic groups, alcohol groups or NH_2 groups showed their own diagnostic overtones, which could have important applications in the detection of PAH-bearing dust in a variety of planetary settings.

The same group also measured the Raman spectra of 48 different PAHs to determine the degree to which Raman spectra could be used to uniquely identify different PAH species, considering that the Mars rover Perseverance would be equipped with two Raman spectrometers (Cloutis et al. 2016). It was found that the arrangement and composition of phenyl rings and the type and position of functional groups can greatly affect fluorescence, positions, and

[8] In *para*-H_2 both the H nuclei have the same nuclear spin whereas in *ortho*-H_2 the H nuclei have opposite spins.

intensities of Raman peaks associated with the PAH backbone, and the introduction of new Raman peaks.

Gavilan et al. (2022) also used Raman spectroscopy to characterize pyrene in microcrystals and in pyrene-derived nanograins. While the microcrystalline material showed narrow bands that match well with previously derived spectra for powdered pyrene, the nanograins showed a broad graphitic band and several disordered bands that match the insoluble organic matter (IOM) found in the carbonaceous chondrules in the Allende meteorite.

2.2.8 Absorption Spectroscopy

Traditional absorption spectroscopic methods employing absorption cells and utilizing the Beer-Lambert law are still being used to deliver high-quality spectroscopic data to extract further information about PAHs and fullerenes relevant to various astronomical environments.

Brieva et al. (2016) presented a detailed mid-IR study of the T_{1u} bands of C_{60}. They found that the observed C_{60} emission in space is inconsistent with thermal and fluorescent mechanisms suggesting that unknown contributions might be present, either from contamination or from other mechanisms, and that it might not be possible to derive physical conditions from observational data. In cases where the contamination of the C_{60} emission lines can be removed or neglected, the accuracy in the estimation of the physical conditions of the astrophysical source could be improved.

Chakraborty et al. (2020) recorded absorption spectra of solid C_{60} from 1.65–2.78 μm (3596–6052 cm^{-1}) over the 11–300 K temperature range in an effort to derive anharmonicity factors which are descriptive of the typically linear shift of IR features with increasing temperature. They also measured IR spectra of pyrene microcrystals in KBr pellets from 14 K up to 723 K (Chakraborty et al. 2019).

2.2.9 Cavity Ring down Spectroscopy

CRDS is an ultra-sensitive, non-intrusive direct absorption technique, based on the measurement of the lifetime of probe photons trapped inside an optical cavity filled with a gas absorbent. It is a direct absorption experiment but unlike absorption cells where the path length (or the distance the light travels through the sample) is equal to the length of the cell, in CRDS, the light is trapped within two mirrors forming a cavity which greatly increases the path length. This allows much higher sensitivity when measuring very weak molecular spectra.

CRDS was used to record the first IR spectrum of c-$C_3H_3^+$, the smallest aromatic molecule, which is needed to so it can be included in astronomical IR surveys (Zhao et al. 2014). CRDS techniques have also been used to investigate UV/Vis spectra (see Sect. 3.2.6) and optical spectra relevant to the DIBs (see Sect. 10.2.1).

2.2.10 Emission Spectroscopy

Recently, a new experimental setup, FIREFLY (Fluorescence in the InfraRed from Excited FLYing molecules), has been designed to measure the IR emission spectra of gas-phase molecules following UV-laser excitation. This technique was recently applied to measure anharmonic IR emission spectra between 2.5 and 4.5 μm of phenylacetylene (C_6H_5CCH) and its isotopologue (C_6H_5CCD) in the gas phase (Lacinbala et al. 2022b). This work demonstrates the potential of time-resolved IR emission spectroscopy to explore anharmonicity offers an exciting new avenue in PAH research to measure IR emission spectra following the absorption of UV photons.

2.3 Theory

Computational chemistry, in particularly based on Density Function Theory (DFT) has been extensively used to explore the vibrational spectroscopy of PAHs and PAH-related species considering several parameters such as shape, hydrogenation, dehydrogenation, heteroatoms substitution, functional group addition, *etc.* The photophysics and photochemistry of PAHs in space is strongly influenced by anharmonicity which was seldom considered in astrophysical modeling in the past either because of the lack of available data or because the calculations were too computationally demanding (Candian and Mackie 2017). Experimental advances in procuring anharmonic vibrational spectra of PAHs have been described in great detail above and here we provide an overview of the theoretical advances that have been achieved during the past decade.

2.3.1 Computational Simulation of PAH Structure and Emission

Using DFT calculations in combination with a detailed emission model showed that the 11.2 μm feature can be fitted by a mass distribution of a few large neutral PAHs containing solo hydrogens (Candian and Sarre 2015). Sadjadi et al. (2015a) obtained a reasonable fitting of the 11.3 μm feature using a significant amount of oxygen-containing and/or magnesium-containing PAH molecules.

The evolution of PAHs in the ISM can give rise to PAHs with different side groups. Sadjadi et al. (2015b), based on a DFT study on the vibrational spectroscopy of large PAHs with aliphatic side groups, suggested that many of the unidentified IR emissions might not be purely aromatic vibrational modes but may represent coupled vibrational modes that include aliphatics, in particular in the 8 μm plateau.

Maurya and Rastogi (2015) calculated mid-IR spectra of eight vinyl-substituted PAHs. All of the obtained geometrical structures gave non-planar geometries apart from vinyl substitutions in the '2'-position in acenes. Maurya and Rastogi (2015) computed IR spectra of neutrals and monocations and identified new features at 6.64, 6.92, 7.27, 8.77, and 10.35 μm that fall close to some sub features in spectra of cool objects. More recently, theoretical studies on PAHs with phenyl groups have showed that these species exhibit bands near 695 and 741 cm^{-1} (14.4 and 13.5 μm), due to contribution from quintet C – H wag, that compare well with minor features at 14.2 μm and observed in several astrophysical objects (Maurya et al. 2023). Recent work by Bowey and Hofmeister (2022) suggests that the 6.9 μm feature could also be due to fine-grained carbonates.

Yang et al. (2016a) investigated the vibrational spectra of methylated PAHs and their cations by comparing the intensities of the 6.85 and 6.2 μm astronomical bands with the theoretical vibration of methylated PAHs and their cations. They found that the fraction of C atoms in methylene aliphatics is at most 10% in some astronomical spectra. Yang et al. (2016b) also utilized DFT to compute the IR spectra of PAHs with a wide range of sidegroups such as ethyl, propyl, butyl and several unsaturated alkyl chains as well as all the isomers of dimethyl-substituted pyrene. They found that the corresponding ratio between the 3.4 and 3.3 μm integrated areas are close to mono-methyl PAHs. This result is consistent with the predominantly aromatic nature of the unidentified IR emission carriers previously inferred from the 3.4/3.3 ratio[9] derived from mono-methyl PAHs.

Ricca et al. (2018) conducted a detailed DFT study of large PAHs with straight edges and showed that they are viable candidates for the emission in PDRs. Indeed, the 8.6/6.2

[9]Throughout this text the band intensity ratios will be represented by the ratios of the bands' central wavelengths in μm, a common type of simplification across fields.

and 7.6/6.2 intensity ratios computed in emission after the absorption of a 8 eV photon match the observed ratios obtained for the RNe NGC 1333, NGC 7023, and NGC 2023.

In a follow-up paper, Ricca et al. (2019) investigated PAHs with armchair edges that maximize the aromaticity (or Clars for short), showing that their spectra are more consistent with class B than class A sources. Few small Clar PAHs contribute to the fit of the class A source IRAS 23133+6050 while large Clar PAHs contribute to the fit of the class B sources IRAS 17347-3139, and NGC 7027. Overall, large Clar PAHs are potential emitters in class B sources. An early study of PAHs with armchair edges showed that sizes larger than 62 carbon atoms could be responsible for the 12.7 μm feature in H II regions (Candian et al. 2014).

Devi et al. (2020) used DFT to study five-member-ringed PAHs in terms of the effects of ionization and protonation on their characteristics in search for correlations with the AIBs. They suggested that the inclusion of a pentagonal ring could lead to an increase in the intensity of the 6–10 μm PAH emission features.

To study the effects of hydrogenation on a single, large PAH, Bauschlicher and Ricca (2014) used DFT to calculate the IR spectra of $C_{96}H_{26}$, corresponding to one H atom added to highly symmetrical circumcircumcircumcoronene ($C_{96}H_{24}$). The effects on the spectrum were observed to be minimal and independent of the charge. Later, Yang et al. (2020b) concluded from studying superhydrogenated PAHs, that astrophysical species are primarily aromatic and only marginally superhydrogenated.

Dehydrogenation was also the focus of several studies. Mackie et al. (2015) found that upon dehydrogenation, 71% of the PAHs develop pentagons in their carbon skeleton. Because of that, dehydrogenated PAHs exhibit some characteristic features, in particular around 10.68 μm, in addition to a forest of weaker features which were searched for in NGC 7023 where a weak feature was detected at 10.68 μm in 5 out of 6 positions. The presence of this feature at 10.68 μm in NGC 7023 was interpreted as tentative evidence for dehydrogenated PAHs in these environments which then disappear closest to the illuminating star where C_{60} is detected. On the other hand, dehydrogenated PAH anions could be significantly contributing to the 3.3 μm region (Buragohain et al. 2018).

Kerkeni et al. (2022) evaluated the efficiency of several computational chemistry methodologies to extend the prediction network of vibrational spectra to large sized PAHs comprising up to 1500 carbon atoms. Employing classical mechanics methods with improved atomic point charges, semi-empirical PM3 and Density Functional Tight Binding (DFTB), and DFT (B3LYP), they conduct global optimizations and frequency calculations in order to investigate the impact of PAH size on the vibrational band positions. To this end, a general frequency scaling function was developed to shift the 3.3, 6.2, 7.7, 8.6, 11.3, 12.7, and 17.0 μm bands, and provide a systematic comparison versus the three methods for each PAH.

The IR spectra of PAH clusters were also investigated. For example, Ricca et al. (2013) and Dontot et al. (2019, 2020) investigated the IR spectra of homogeneous pyrene clusters, in both cationic and neutral forms. PAH clusters relate closely to dust, which is explored in Sect. 4.

DFT calculations of IR spectra of deuteronated PAHs ($DPAH^+$) and deuterium-containing PAH variants suggested that these species could be potential carriers of the bands at 4.4 and 4.65 μm, due to C−D stretches, observed toward the Orion Bar and M17 (Buragohain et al. 2015, 2016, 2020). To explore the hypothesis that PAHs could be a possible reservoir of interstellar deuterium, Yang et al. (2020a) investigated the vibrational spectra of monodeuterated PAHs. Their comparison of the computationally-derived mean band-strength ratios for neutral PAHs with the mean ratio of observed intensities showed that the degree of deuteration is around 2.4% corresponding to a D enrichment of a factor of 1200 with respect to the interstellar D/H abundance.

PAHs with straight edges having solo–duo and solo–duo–trio C–H modes along with PAHs with irregular edges were studied theoretically to understand the effect of molecular geometry on the interstellar C–H stretch vibrations at 3.3 μm (Vats et al. 2023a). 125 PAHs from the NASA Ames PAH IR Spectroscopic Database (see Sect. 3.1.1) of varying geometries, sizes, charge states, and symmetries were studied and the authors showed that the individual solo, duo, and trio C–H stretches follow an order in the peak wavelength and intensity. Hence, the presence of solo, duo, and trio modes in the C–H stretching band must be considered when interpreting accurate data from JWST to further explain the variations in the 3.3 μm band.

PAHs can include atoms other than carbon, for example nitrogen or phosphorus. Comparing DFT computed IR spectra of PANHs with Spitzer spectra of the NGC 7023 PDR, Ricca et al. (2021) found that pure PAH cations can account for the class A 6.2 μm PAH emission, with the 6.2 μm band position being dependent on molecular geometry. PANHs are required to reproduce the most blue-shifted 6.2 μm bands observed in class A sources, albeit PANH cations come with strong 11.0 μm emission. By assuming that all of the 11.0 μm feature is due to PANHs, an upper limit of 12% for the PANHs cation contribution to the 6.2 μm emission band is obtained. In addition, the fits show that shielded environments, such as the more benign regions of NGC 7023, could sustain protonated PANHs.

The following year, DFT was used to calculate the IR spectra of various PANHs where N, NH, and NH_2 had been incorporated into the PAH structure (Vats and Pathak 2022). The results implied that the bands at 6.2 and 11.2 μm can arise from the same charge state of some PANHs arguing that there might be some N-abundant astronomical regions where this ratio is not a direct indicator of the PAHs' ionization state.

Phosphorus-containing PAHs (PAPHs) were also studied computationally in terms of their mid-IR spectra, showing that P−H stretching appears between 2300 and 2700 cm^{-1} (3.7 and 4.3 μm; Oliveira et al. 2020).

2.3.2 Anharmonicity

The large majority of studies reported so far calculated the vibrational spectra of PAHs and related molecules in the harmonic approximation, but some effort has been put into investigating the anhamonicity of PAHs.

In a series of papers, Mackie et al. (2015, 2016, 2018a) calculated the anharmonic vibrational spectrum of a sample of 16 PAHs and compared the results with available experimental spectra obtained with different techniques.

The comparisons show that considering anharmonicity significantly improves the match between calculations and experimental spectra, eliminating the usual need for an empirical scaling factor to bring harmonic calculations in line with experiment.

The importance of anharmonicity prompted other calculations and improvements to the simulations above. Mackie et al. (2018b) described how to obtain a fully theoretical IR cascade spectra of PAHs including an anharmonic second order vibrational perturbation theory treatment, the inclusion of Fermi resonances through polyads and the calculation of anharmonic temperature band shifts and broadenings. Mulas et al. (2018) developed a new code to calculate anharmonic vibrational spectra of PAHs considering all modes and describing all IR transitions, including bands that become active due to resonances, as well as overtone, combination, and difference bands. Benchmarking calculations were performed on coronene and pyrene. The theoretical band positions were found to be significantly improved compared to harmonic DFT calculations. The band intensities agree reasonably with the experiments, with the accuracy of the underlying calculations of the quartic force field

resulting in most of the discrepancies. The same group calculated the IR spectra of pyrene with DFTB at different temperatures to obtain anharmonicity parameters (Chakraborty et al. 2021).

2.3.3 Fullerenes and Carbon Clusters

The discovery of buckminsterfullerene (C_{60}) in space has been a great incentive to investigating the vibrational spectra and the structures of carbon cages and clusters and the steps in the photochemical evolution of PAHs leading to fullerenes.

In this respect, Álvaro Galué (2014) calculated the IR signatures of pyramidal carbons as intermediates in ongoing fullerenization of carbon-based interstellar materials using large planar PAHs as starting points, and connecting their vibrations to the AIBs . Following this work, Álvaro Galué and Díaz Leines (2017) showed how including non-planar structural defects in an aromatic core modulates the electronic-vibration coupling that activates the delocalized π-electron contribution to aromatic vibrational modes. The modulation naturally disperses C=C stretching modes in band patterns that readily resemble the AIBs in the elusive 6–9 μm range. The electron-vibration interaction mechanics governing the defect-induced band patterns underscores the importance of π delocalization in the emergence of AIBs .

Adjizian et al. (2016) studied with DFT the neutral and charged small fullerenes C_{20}, C_{24}, C_{26}, C_{28}, C_{30}, and C_{60}, finding that negatively charged fullerenes have significantly stronger absorption intensities than neutral species and suggesting that small cage fullerenes and metallic endofullerenes may be responsible for many of the unassigned interstellar IR spectral lines. Candian et al. (2019) expanded the study to fullerene cages between 44 and 70 carbon atoms and showed that smaller cages (i.e., 44, 50, and 56 atom) can possibly be present in several PNe, as, for example, Tc 1, SMP SMC 16, and SMP LMC 56. Zhang et al. (2017a) investigated fulleranes ($C_{60}H_m$, $m = 1$–60) and proposed that the observed IR bands assigned to C_{60} could be due to a mixture of fullerenes and fulleranes which provides an explanation for the observed scatter of the C_{60} band ratios. Recently, IR spectra of $C_{60}H^+$, $C_{60}D^+$, $C_{60}H_{18}{}^+$, and $C_{60}D_{18}{}^+$ have also been computed using DFT by Vats and Pathak (2023) who further supported the notion that because of spectral overlap, that IR bands ascribed to C_{60} are a mixture of pure and slightly protonated and deuteronated fullerenes, hence explaining the observed scattering of the observed C_{60} band ratios.

Zhang et al. (2017a) also suggested that a feature around 15 μm due to the breathing mode of heavily hydrogenated C_{60} may be detectable astronomically. Analysis of the structural differences of isomers for specific cluster sizes (e.g. 24, 60) also provided insight on their vibrational similarities and stability (Dubosq et al. 2019; Calvo et al. 2021; Karri et al. 2022).

The mechanism of RF was investigated as well for isolated carbon clusters containing 24–60 C atoms as a function of internal energy (Lacinbala et al. 2022a). They found RF to be highly competitive with vibrational emission and the behaviors predicted for clusters of various sizes and archetypal structures indicate that the IR emission spectra are strongly influenced by RF. They furthermore obtained an energy gap law for the evolution of the RF rate constant depending on the electronic excitation state.

RF – as originating from stellar photon absorption by C_n ($n = 24, 42, 60$) carbon clusters – has also been shown capable of accounting for the IR emission detected in various interstellar environments (Lacinbala et al. 2023a). The collective emission signature of carbon cluster samples induced irradiation from a 20,000 K blackbody source was modeled with a kinetic Monte Carlo stochastic approach based on harmonic vibrational densities of states from cages, flakes, pretzels, and branched isomers. It was found that RF from C_{60} cages and

flakes (with little or no *sp* carbon atoms) and C_{42} cages are able of explain the near-IR continuum emission observed in several RNe and PNe. Assuming that the continuum emission observed toward NGC 7023 is due to RF induced by UV or visible photon absorption in neutral cage carbon clusters containing 30–60 atoms, the carriers contain about 0.1–1.5% of the interstellar carbon abundance.

Some of the same authors also followed up a theoretical/modeling investigation of $C_{24}H_n$ ($n = 0$, 6, 12, 18, 24) isomers (Dubosq et al. 2023) (see also work by Pla et al. (2021) described in Sect. 3.3.2). They wanted to investigate the influence of the hydrogenation rate on the mid-IR spectra of populations of carbon clusters in order to constrain the n_H/n_C ratios in regions of the ISM where carbon is an important component. The shapes and the relative intensities of the bands centered at 3.25 and 3.40 μm that are assigned to the C–H stretch of sp^2 and sp^3 carbon atoms, respectively, present a clear dependence on the n_H/n_C ratio. A comparison with the spectrum from the Orion bar H2S1, the most interesting candidate appears to be the flake population which is the most energetically favorable family of clusters, possessing a high content of five and six membered carbon rings, being mostly planar, with no *sp* carbon atoms, and with a n_H/n_C ratio of lower than 0.5. The results bring some constraints to the structural features and on the n_H/n_C ratio of the hydrogenated carbon populations emitting in the mid-IR domain in objects such as PPNe and RNe.

Their next paper focused on a computational model of the emission spectrum of isolated carbon clusters, assuming a broad distribution of isomers that are likely populated under the experimental conditions (Lacinbala et al. 2023b). The contributions of individual structures to the global spectrum correspond to the relaxation via RF and vibrational emission, electronic and vibrational structures being described by a simple but efficient DFTB scheme. Their model predicts a blackbody-like emission spectrum that is naturally broad and correctly accounts for the experimental measurements, except for a maximum that is quantitatively shifted with respect to Wien's displacement law.

The extent of the potential sizes of fullerenes have also been investigated theoretically (Gatchell et al. 2023). The largest stable single shell fullerene is found to include 10,000 carbon atoms. As the structures grow, the energy per atom begins to approach that of graphite. Onion structures and graphite are very similar in ground state energy, leading to the hypothesis that in certain temperature ranges, fullerene onions could be the lowest free energy states for large carbon particles.

2.3.4 Small Aromatic Molecules

The relatively high abundance of c-C_3H_2 (or cyclopropenylidene) in the ISM inspired a lot of theoretical work by the Fortenberry group. c-C_3H_2 constitutes one of the smallest known aromatic molecules and might be an important intermediate in the formation of PAHs in space, particularly since it is so abundant that both its deuterated forms and C-13 isotoplogues are observed as well.

c-C_3H_2 also presents some significant challenges as it exhibits the so-called out-of-plane bending (OPB) motions which are challenging to tackle theoretically (Fortenberry et al. 2018; Lee and Fortenberry 2021). Additionally, related species like the c-C_3H^- anion and its neutral counterpart, c-C_3H, possess strong Jahn-Teller effects which makes them quite floppy molecules due to the symmetry breaking frequencies (Bassett and Fortenberry 2017).

High-level theoretical methods have been benchmarked to calculate anharmonic frequencies of these small tricyclic aromatics (Agbaglo and Fortenberry 2019) which have subsequently been applied to other members of the c-C_3H_2 family such as cyclopropenylidenyl carbene (c-(C)C_3H_2; Agbaglo et al. 2019) and its protonated form (c-(CH)$C_3H_2^+$; Westbrook et al. 2020), along with disubstituted forms such as c-$C_3(C_2H)_2$, c-$C_3(CN)_2$, and

c-$C_3(C_2H)(CN)$ (Flint et al. 2023). Likewise the fundamental frequencies and spectroscopic constants of F-, Cl-, and CN-substituted c-C_3H_2 were calculated (Westbrook et al. 2021) as ethynyl-substituted c-C_3H_2 was recently discovered and Flint and Fortenberry (2022) showed that OH, NH_2, CN, and F, could react barrierlessly with c-C_3H_2 in a similar way to ethynyl (C_2H).

Other tricyclic species that contain nitrogen and are isoelectronic with c-C_3H_2 have also been investigated, but species like c-N_3^+, c-CNN, c-$HCNN^+$, and c-CNC^- are interesting in the context of Titan's atmosphere (Fortenberry et al. 2017, see also Sect. 9).

Molecules that are related to PAHs, either as a possible fragment from their dissociation or as a by-product of their formation, were also investigated. Fundamental vibrational frequencies of several small carbon species, including c-C_3H, c-CNC^-, c-$(C)C_3H_2$,c-$(CH)C_3H_2$ and substituted cyclopropenylidene, were derived (Bassett and Fortenberry 2017; Fortenberry et al. 2017, 2018; Agbaglo and Fortenberry 2019; Agbaglo et al. 2019; Westbrook et al. 2020, 2021; Flint and Fortenberry 2022), but there are still unsolved mysteries like the out-of-plane bending frequencies for C=C multiply bonded systems (Lee and Fortenberry 2021).

Other works on relevant small aromatic molecules submitted to AstroPAH has focused on the pyrylium cation (c-C_5H_5O) (Bera et al. 2013), tetrahadrane (Westbrook et al. 2022a), C_5H_2 isomers (Watrous et al. 2022), and SiC clusters (Sehring et al. 2022).

2.3.5 Emerging Methodologies

New methodologies have been investigated with the aim of increasing the speed of calculations. Besides their accuracy and new in-depth analysis have provided clues on the behavior of certain systems. Yang et al. (2017b) showed that using the less computationally expensive B3LYP DFT instead of MP2 perturbation theory, one can obtain the band strengths of PAHs by a simple scaling. Watrous et al. (2021) introduced the F12-TZ-cCR quartic force field (QFF) methodology as a cheaper and even more accurate alternative to more costly composite QFF methods like those containing complete basis set extrapolations within canonical coupled cluster theory. Semi-empirical methods can be reparameterized for computing anharmonic vibrational frequencies of multiply-bonded hydrocarbons (Westbrook et al. 2022b).

Machine learning methods were used to efficiently predict the IR spectra of PAHs with a computational cost many orders of magnitude lower than from first-principles calculations. The input to the neural network is based on the Morgan fingerprints extracted from the skeletal formulas of the molecules and does not require precise geometrical information such as interatomic distances (Kovács et al. 2020).

Machine learning features were also used to determine the molecular substructures that are responsible for mid- and far-IR emission features of neutral PAHs (Meng et al. 2021, 2023). Based in the spectra of 14,124 PAHs, a random forest model was trained to evaluate the importance of 10,632 molecular fragments for each band within the range of ∼2.8 to 1173 μm, using the extended-connectivity fingerprint as a descriptor of chemical structure. It was demonstrated that the results can be used to explore the relation between the PAH structure and the spectra of PANHs and superhydrogenated PAHs.

Geindre et al. (2021) performed a comprehensive study of the numerical aspects influencing the frequencies and intensities of the IR spectra of PAHs regarding the overestimate of the C–H stretching bands above 3000 cm^{-1}.

2.4 Modeling

2.4.1 The NASA Ames PAH IR Spectroscopic Database

Since the 1990's, much effort has been devoted to obtaining IR spectra of PAHs both experimentally and theoretically so that they can be made available to the astronomical, astrophysical, and astrochemical communities. The NASA Ames Research Center has devoted a considerable effort to obtain spectra of a sufficiently large number of PAHs to properly test the "PAH hypothesis" and develop it into a model and a new astronomical probe. During the past decade, the NASA Ames PAH IR Spectroscopic Database[10] has grown substantially.

The database contains a large number of computational and experimental spectra spanning the 2.5–4000 μm (2.5–4000 cm^{-1}) range (Boersma et al. 2014a; Bauschlicher et al. 2018). In addition to the spectra, the database portal also provide tools that allow (i) the analysis of spectra in the database and comparing them with imported astronomical spectra, (ii) the visualization of the molecular atomic motions corresponding to each vibrational mode, and (iii) the fitting of an imported astronomical spectrum with PAH spectra in the computational database Boersma et al. (2014a).

Several updates were made since its inception. Bauschlicher et al. (2018), for example, introduced the use of multiple scaling factors instead of a single scaling factor used previously to align the theoretical harmonic frequencies with the experimental fundamentals.

Mattioda et al. (2020b) presented a large increase in the PAH computed spectra available through the database, as well as specific tools developed to analyze and interpret astronomical spectra with the laboratory data, new updates to the website, documentation, and software tools. The authors also demonstrated how laboratory-measured data can be applied to explore absorption features in observations toward embedded sources and suggested that PAHs very likely contribute to the interstellar absorption spectra associated with dense clouds. Their work emphasizes the need for further IR spectroscopic studies of PAHs trapped in water ice. PAHs trapped in water are explored further in Sect. 4.2.4.

2.4.2 Search for PAH Size, Ionization, and Incident Radiation Field Diagnostics

By using the NASA Ames PAH IR database, Andrews et al. (2015) showed that PAH emission in the 5–15 μm range is rather insensitive to variations of the radiation field in several bright mid-IR locations like NGC 7023, NGC 2023, and NGC 1333 which already show a large variation in PAH band ratios. Their results suggested that the PAH populations must be remarkably similar at these different lines of sight considering that variations smaller than 30% in the PAH abundances would lead to noticeable spectral differences. Hence, Andrews et al. (2015) coined the "grandPAH" hypothesis which states that grandPAHs are a robust PAH population that results from intense processing of PAHs at the border limit between PDRs and their molecular clouds where they survive and emit at these bright points. Due to the UV radiation destroying the majority of the (smaller) PAH population the abundance of PAHs start decreasing toward the star, but, supposedly, larger and more symmetric PAHs survive the harsh radiation conditions.

The invariance observed in class A (the most prevalent of four classes of observed band profiles) 3.3 μm band profiles under a wide range of physical conditions was addressed in the work of Tokunaga and Bernstein (2021). To study a representative to the ISM range of

[10] https://www.astrochemistry.org/pahdb/theoretical/3.20/default/view.

PAH sizes — since the profile depends on the number of carbon atoms (besides the temperature) — the authors used laboratory data from the NASA Ames PAH IR Spectroscopic Database, with an extrapolation for the physics to a larger range of PAH sizes. Tokunaga and Bernstein (2021) extrapolated laboratory band shifts, widths, and profiles for smaller PAHs ($N_C < 33$) to larger PAHs ($N_C > 50$), Their study shows that the invariance in the band center wavelength and the full width at half maximum (FWHM) constraints the sizes of the putative PAH 3.3 μm carriers to a small range of sizes with invariant relative abundance and indicate that they are excited by the same average UV photon energy.

Rigopoulou et al. (2021) performed and explored the NASA Ames database and their own DFT spectral simulations of PAHs with varying number of carbons, charge, and harshness of the incident radiation field to investigate the potential of different band ratios as diagnostics. Their results indicate that the 6.2/7.1 and 11.3/3.3 ratios are tracers of the sizes of PAHs. However, the 11.3/3.3 band ratio also shows a dependence on the intensity of the radiation field. The 11.3/7.7 band ratio is a good indicator of PAH ionization, with higher values indicating a higher degree of ionization. By comparing their result with measured band ratios of a variety of galaxy types obtained with Spitzer, they demonstrated that the emission from galaxies indicate a spectrum produced by large PAHs exposed to a moderate intensity radiation field. Based on their results, they propose a three-dimensional diagnostic diagram (6.2/7.7 vs. 11.3/3.3 vs 11.3/7.7) to constrain size and physical conditions of PAHs.

The NASA Ames PAH IR database has also been used to study the PAH components of over 900 Spitzer galaxy spectra by Maragkoudakis et al. (2022). In that study, the authors found that the PAH population within galaxies consists of middle-sized PAHs with an average number of carbon atoms of 55 and a charge state distribution of 40% ionized and 60% neutral. The 6.2/11.2 ratio and γ (the ionization parameter) as well as the 8.6/11.2 ratio and its relation to the star-formation rate were described and a correlation between the 3.3/11.2 ratio and N_C (the number of carbon atoms in PAHs) therein was established.

In Maragkoudakis et al. (2023a), theoretical PAH spectra available in the NASA Ames database was used to understand and quantify the variations caused by the different PAH characteristics. According to them, small PAHs have a high impact on the PAH band strengths and also contribute significantly to the plateaus emission. They also concluded that the 3.3/(11.0+11.2) PAH band ratio can be used as PAH size tracer, which interestingly also allows the characterization of the dominant scenario of PAH processing (removal of small or large PAHs). On the other hand, the 7.7/(11.0+11.2) PAH band ratio is not sensitive to the PAH size and is a better choice as diagnostic of PAH charge. The authors also propose new diagnostic diagrams that helps evaluate the PAH average number of carbon atoms in astrophysical sources.

Continuing their efforts to understand the PAH size effect on the AIBs using the NASA Ames database, Maragkoudakis et al. (2023b) studied the variation of different band ratios with N_C. As in previous work, results indicate that ratios that involve the 3.3 μm PAH band as the best PAH size tracers for PAHs of small-to-intermediate sizes. They also found that band ratios that including the sum of the 15–20 μm PAH features and the 6.2 or 7.7 μm bands also serves as good tracers for PAH size in the case of small-to-intermediate sized PAHs, for objects under a similar PAH size distribution.

A follow up of the work by Mackie *et al.* on anharmonicity (see Sect. 2.3.2) based on recent experiments at FELIX by Lemmens *et al.* (see Sect. 2.2.3) investigated how computer simulated spectra compare to spectra obtained from experiments to reveal a consistent underestimation of the 11.2/3.3 PAH band ratio by 34% when not considering anharmonicity, simulated spectra based on higher level anharmonic calculations show very good agreement

with the experiments (Lemmens et al. 2023). The authors proposed an adjustment to the calculated intrinsic ratio for large molecules to compensate for the anharmonicity (which is still not reliable for large PAHs) and studied the indications that the 11.2/3.3 ratio increases systematically with the molecular size. Their recalculations of the PAH emission model as for NGC 7023 (see Sect. 3.1.1) corrected the typical PAH size in this object from 50 to 70 carbon atoms per PAH to 40 to 55. As the higher limit of this range is close to the size of the C_{60} fullerene, the authors argue that their result supports the hypothesis that large PAHs maybe converted into the more stable fullerenes in the ISM.

2.4.3 New Methods to Distinguish the Populations Contributing to the IR Spectrum

Multiple authors have delved into the development of new methods for the decomposition of the PAH IR features into their different components.

A new method of mid IR spectrum decomposition developed by Xie et al. (2018a) uses a composition of theoretical PAH templates with modified blackbody components to account for the underlying dust continuum, all multiplied by an extinction factor. The PAH template used was derived from the work of Draine and Li (2007). The technique was tested with the application to observations of different Galactic and extragalactic astronomical objects obtained with Spitzer. The fluxes of individual PAH bands derived with this method are consistent with those obtained using other popular decomposition tools. However, the total fluxes of all PAH features are as much as 30% higher than what is obtained by other tools. This is mainly due to the difference in the band profile in the template used, which incorporates the emission of PAHs associated with their skeletal vibrations at long wavelengths. A systematic difference is also seen in the comparison with fluxes obtained from spline fitting, as, according to the authors, it underestimates the wings of the PAH features.

Foschino et al. (2019) developed a method to analyze PAH populations in the mid IR spectra based on linear fitting and blind signal separation (BSS).[11] The method automatically extracts representative spectra from a spectral data set. In their application to ISO data, four representative spectra were obtained (whose characteristics were consistent with previous studies) with populations dominated by cationic PAHs, neutral PAHs, evaporating very small grains (VSGs), and large ionized PAHs. They included the 3 μm range, which revealed the presence of aliphatics connected to neutral PAHs. The authors highlight that their method can be readily applicable to JWST IFU data.

Maragkoudakis et al. (2020) developed a new method to accurately describe the PAHs ionization fraction and size distribution. Their method uses "measures" of band intensities from a sample of the DFT simulated PAH spectra available in the NASA Ames database. Their study showed that among the different PAH emission bands, the 3.3 μm band intensity has the strongest correlation with N_C. It is then not a surprise that they found that the intensity ratio of the solo C–H out-of-plane bending mode in PAH cations and anions (the 11.0 μm band) to the 3.3 μm emission scales with PAH size, and similarly the 11.2/3.3 ratio scales with N_C for neutral molecules. On the other hand, this new method shows that the 6.2/7.7 band ratio, which was previously used to track PAH size, does not seem to scale with N_C. The determined fluxes also allowed the authors to study and propose a new diagnostic to probe PAH charge and size by using the (11.2+11.0)/7.7 and (11.2+11.0)/3.3 intensity ratios. Its potential as diagnostic was demonstrated for M82, NGC 253, NGC 7027,

[11] BSS refers to a separation of multiple source signals from a set of mixed signals without any (or with very little) information about the source signals or the mixing process. It is commonly applied in digital signal processing.

NGC 2023, and NGC 7023. Quantitative relations for PAH size determination depending on the ionization fraction of the PAHs and the incident radiation field was also provided.

The mid-IR emission in the Orion Bar PDR was studied in terms of band flux ratios by Murga et al. (2022b). The authors used their code SHIVA (Murga et al. 2019), which was improved with new PAH formation and destruction processes for this work, to study the time evolution of PAHs. Assuming that the mid-IR emission arises primarily from PAHs and that a weak emission feature at 3.4 μm is related to hydrogenated PAHs, variations of the ratios were traced using a model for PAH evolution. They concluded that the best coincidence between modeling and observation is achieved if C loss of PAHs is limited by 60 C atoms and the 3.4 μm band is attributed to hydrogenated PAHs. They also confirmed that large cations dominate at the surface of the PDR but small neutral PAHs and anions are abundant deeper in the molecular cloud.

Sidhu et al. (2021, 2022a) applied PCA to study the PAH 6.2, 7.7, 8.6, 11.0, and 11.2 μm emission from the RNe NGC 2023 and NGC 7023, respectively. In both works they found that almost all the variance in the data could be explained with just the first two principal components. For NGC 2023, the first component is the primary driver of the variation and represents the amount of emission of a mixture of PAHs with ionized species dominating over neutral species. The second component traces variations in the ionization state of the PAHs across the nebula. For NGC 2023 PDR, the first component represented the total PAH emission, and the second component was related to the ionization state of PAHs across the nebula, which is consistent with the results for NGC 2023. A separate PCA was also carried out considering variations in the NGC 2023 cavity. In this case, the second component is not related to the charge state of the PAHs, but possibly to structural molecular changes. In both works, the study of correlations among the components with various PAH ratios show that the 6.2 and 7.7 μm bands behave differently than the 8.6 and 11.0 μm bands thereby forming two distinct groups of ionized bands. According to their results, for NGC 2023, the total amount of PAH emission does not depend on the strength of the radiation field.

Sidhu et al. (2022b) presented simulations of the PAH emission (PAH emission model) that account for the charge distribution to compute the IR spectrum of these molecules. These simulations consider the balance of the many mechanisms of PAH ionization and electron recombination to PAHs in a range of physical conditions. The model uses recent data measurements and theoretical calculations for these processes. The model was applied to a sample of well-studied PDRs with well-determined physical conditions (radiation field strength, electron density, and gas temperature). The work demonstrated that the charge distribution-based emission model could explain PAH observations in these objects. It also showed that without any prior knowledge of the ionization parameter, the 3.3/(11.0+11.2) ratio can predict PAH size, but the 6.2/(11.0+11.2) ratio cannot predict the ionization parameter of the astrophysical environment.

The work above was extended to include C_{60} and used the code to study the C_{60} and PAH IR emission in the cavity of NGC 7023 (Sidhu et al. 2023). The analysis shows that the relative intensity of the features in the 5–10 μm versus 15–20 μm can be used to probe the C_{60} charge state in interstellar spectra. A comparison of the model results with the observed band ratios showed that the γ values in the cavity do not vary significantly, suggesting that the emission in the cavity does not originate from locations at the projected distances. Furthermore, they found that the C_{60}-derived γ values are lower than the PAH-derived values by an order of magnitude, suggesting two possible reasons for this large difference: the uncertainties in the electron recombination rates of PAHs and C_{60}, or that PAHs and C_{60} are not co-spatial.

2.4.4 Graphene and Carbon Nanotubes

Inspired by reports of a potential detection of a graphene nanoflake in several Galactic and extragalactic PNe, Chen et al. (2017) used modeling to answer whether and how much graphene could exist in the ISM and how it would be revealed in the UV and IR. The UV absorption of graphene was calculated which allowed an upper limit of 1.9% of interstellar C to be placed on the interstellar graphene abundance.

Li et al. (2019a) expanded on this topic and examined the possible presence of graphene in space by comparing the interstellar extinction curve with the UV absorption of graphene as calculated from its dielectric functions that had been experimentally obtained. They placed an upper limit of 20 ppm of C/H on the interstellar graphene abundance, exceeding the previous limit (Chen et al. 2017).

Going even further and exploring the potential for the presence of carbon nanotubes was also done by the same authors (Li et al. 2020). They compared the observed interstellar extinction curve with the UV/optical absorption spectra obtained for single-walled carbon nanotubes of a wide range of diameters and chiralities and deduced an upper limit of approximately 10 ppm of C/H (i.e., around 4% of the total interstellar carbon).

2.4.5 Beyond the PAH Hypothesis

Although PAHs are the prime candidates to be the carriers of the IR emission bands observed throughout our Universe, there is also reason to be cautious to a degree.

Other species have been studied. Bernstein et al. (2017), for example, studied the possibility of the small fullerene C_{24} as a carrier of the 11.2 μm band in the PN NGC 7027. Those authors suggest that C_{24} this is a plausible result as it may be an abundant interstellar molecule due to its high photoionization energy (7.7 eV).

With the aim of testing the validity of the PAH hypothesis, Zhang and Kwok (2014) tested a variety of non-PAH spectra like silicates, HAC, coal, and even artificial spectra. They showed that the spectra of such compounds can be well fitted by mixtures of PAHs in the NASA Ames PAH IR Spectroscopic Database. Zhang and Kwok (2014) state that although a mixture of many PAHs can reproduce the AIB spectra, such a mixture is also able to produce non-PAH spectra, even randomly generated ones, and thus a general match between astronomical spectra and those of PAH mixtures does not necessarily provide definite support for the PAH hypothesis.

3 Photodissociation Regions, Planetary Nebulae, and Reflection Nebulae: UV-Driven PAH Processing

UV photons play a pivotal role in molecular astrophysics. They possess enough energy to dissociate and ionize molecules, and in doing so, reactive fragments — radicals and cations — are created which drive forward the chemistry in UV-irradiated regions. There are numerous types of UV-rich regions in space. In this section, PDRs, PNe, and RNe — which have all been found to be populated by fullerenes (Bernard-Salas et al. 2014) — will be highlighted, along with experimental and theoretical works dedicated to the processing and formation of PAHs, fullerenes, and HAC molecules.

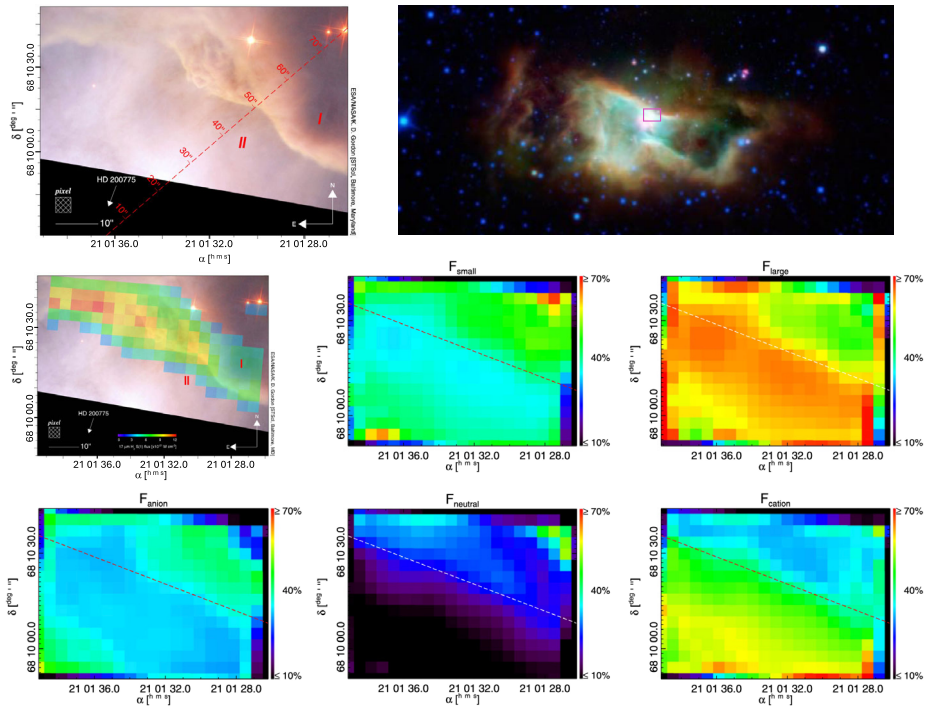

Fig. 6 Top right: Spitzer image of the central portion of the reflection nebula NGC 7023. Credits: NASA/JPL-Caltech. The pink rectangle roughly indicate the position of area shown in the remaining panels, which shows results from Boersma et al. (2013) and Boersma et al. (2014b)

3.1 Observations

3.1.1 NGC 7023: PAHs Processing in an Edge-on PDR

NGC 7023, also called the Iris Nebula, is a well studied and very bright reflection nebula, with intense PAH emission. This object is particularly interesting for studies related to UV processing, as we see part of its PDR practically edge on[12] (Fig. 6). This allows us to study different observational properties as a function of the distance from the illuminating source. In the period covered by this review, many studies have improved our knowledge about the PAH emission in this object.

Spectral maps of the mid IR emission from the northwest PDR in NGC 7023 were obtained with Spitzer. The data was analyzed in detail in a series of three papers by Boersma et al. (2013, 2014b, 2015). The authors investigated the emission as a function of the distance from the illuminating source with the aim to understand the processing of the different components responsible for the emission features. They decompose the emission into size, charge, composition, and structure with the help of the NASA Ames PAH database

[12] In astronomy, the terms "face-on" and "edge-on" refer to the viewing angle from which we observe an astrophysical object. The terms are usually applied to systems with a somewhat flat morphology, as, for example, spiral galaxies or accretion disks. If we are observing from the same plane defined by the object shape, we say that we see it "edge-on", whereas if we are observing it from one of the perpendicular directions of the plane, we say that we see it "face-on".

Fig. 6. Close to HD 200775, the stellar system that illuminates NGC 7023, there is indication of PAH photo-dehydrogenation and fragmentation. At 20 arcsec from HD 200775, the emission becomes dominated by a subclass of more stable, large, symmetric, compact PAH cations, while a subclass of smaller, neutral PAHs takes over along the lines-of-sight toward the more distant molecular cloud. The boundary between the PDR and the denser cloud material shows up as a distinct discontinuity. It is interesting to notice that in their procedure, the 6.2 and 11.0 μm features need PANH cations to a proper spectral fitting. As described above, work by Ricca et al. (2021) derived an upper limit of 12% for the contribution of PANH cations to the 6.2 μm emission band.

The AKARI telescope enabled observations of the 3.3 and 3.4 μm AIB features, which are associated with aromatic and aliphatic C-H bands. Pilleri et al. (2015) used AKARI observations to complement Spitzer data of the NGC 7023 northwest PDR and verified a previously proposed scenario where the evaporation of VSGs leads to PAH production. The 3.3 and 3.4 μm features and an underlying plateau centered at 3.45 μm are needed to explain the AKARI NGC 7023 northwest PDR spectrum. They found that the intensity of the 3.3 μm band relative to the total PAH emission increases with the intensity of the radiation field while the relative contribution of the 3.4 μm band decreases. The transition region between the aliphatic and aromatic material is found to spatially correspond with the transition zone between neutral PAHs and evaporating VSGs, that is, it delineates the PDR. The analysis indicated the presence of very small grains of mixed aromatic and aliphatic composition in the PDR, and the photo-processing of eVSGs produces PAHs with attached aliphatic sidegroups, responsible for the 3.4 μm emission band.

SOFIA was used to map PAH sizes in NGC 7023 northwest and south PDRs (Croiset et al. 2016). In this work, size is used as a proxy to understand the photochemical evolution of PAHs. Using an emission model and the vibrational spectra from the NASA Ames database to translate maps of the 11.2/3.3 band ratio to maps of PAH sizes, the authors found that in the NW PDR, PAHs bear on average 70 carbon atoms in the PDR cavity and 50 at the PDR surface. A factor of 2 variation in PAH size was observed in the northwest PDR, implying that small PAHs result from photoevaporation of VSGs as they reach the PDR surface, a conclusion similar to other studies discussed above. Inside the cavity, the PAH abundance drops as the smallest PAHs are broken down while the average PAH size increases, where only the largest species survive or are converted into other species such as C_{60} by photochemical processing (Croiset et al. 2016).

The multiple detailed investigations of the NGC 7023 PDR have made it an appropriate benchmark for comparisons with other irradiated regions. In this regard, several works have been dedicated to comparisons of NGC 7023 with regions such as H II regions, PNe, and RNe. For instance, correlations between ratios of band intensities of the 15–20 μm PAH emission bands were analyzed in a sample of 57 sources including Large Magellanic Cloud (LMC) point sources, nearby galaxies, two Galactic ISM cirrus sources[13] and the RNe NGC 2023 and NGC 7023 (Shannon et al. 2015). The study concluded that the 17.4 μm band is dominated by cations, the 15.8 μm band by neutral species, and the 12.7, 16.4, and 17.8 μm bands by a combination of the two.

The study of Spitzer spectral maps of NGC 7023, along with the RNe NGC 2023 and the star forming region M17, by (Shannon et al. 2016) supported the use of the 12.7/11.2 intensity ratio as a PAH charge proxy. In the work, the authors analyze the 11.0, 11.2, and

[13]Interstellar cirrus clouds are composed of dust grains smaller than a micrometer. These should not be confused with terrestrial cirrus clouds which are high-altitude atmospheric clouds composed of frozen water crystals.

12.7 μm bands decomposition into Gaussian components, which allowed them to study the spatial distribution and the contribution of components from different ionization states.

Boersma and collaborators extended their previous work on NGC 7023 (Boersma et al. 2013, 2014b, 2015) by analyzing the low-resolution Spitzer maps of another five RNe (Boersma et al. 2016) and the H II region M17 and the PN NGC 40 (Boersma et al. 2018) in terms of the PAH charge derived from their emission bands, using the NASA Ames PAH IR Spectroscopic Database. These works provide quantitative calibrations for the PAH band strength ratios traditionally considered as proxies for the charge state of the PAH population. They study, for example, the 6.2/(6.2+11.2) and 8.6/(8.6+11.2) band ratios.

Stock et al. (2016) analyzed spectral maps of galactic H II regions and PDRs between 5–15 μm obtained with Spitzer. The H II region PAH band ratios are different from those in RNe, which have ratios with a greater dynamic range than the H II regions. The authors separated their sample in two groups with similar PAH properties, the H II regions W49A, G11.94-0.62, G37.55-0.11, and IRAS 12063-6259, and the RNe NGC 1333, NGC 2023. However three objects could not fit in any of these groups: the Horsehead PDR,[14] M17, and NGC 7023. According to the authors, the differences could be explained by the faint radiation field incident in the Horsehead PDR and the very clean separation between the PDR and the diffuse gas region in the NGC 7023 observations. This shows the importance of the environment properties and the observed morphology to the PAH band ratios.

3.1.2 PAHs in Other PDRs, PNe, and RNe

The Orion Bar — the PDR prototype — and the region that surrounds it have been extensively studied in the literature. As for NGC 7023, the edge-on morphology of the Orion Bar is an advantage for studies related with the UV processing. Boersma et al. (2012) analyzed the PAH emission between 10 and 37 μm from the Orion Bar and outward in relation to θ^1 Ori C, the main ionizing star of the so-called Trapezium star cluster. They probe 3 zones, from the closest to the more distant from the Orion Bar: the interface between the PDR and the H II region immediately southeast of the bar; the shielded molecular material, and the interface between the H II region and PDR. Among the main observed results, they found that PAH erosion[15] and destruction were important within ∼5 arcsec from the Orion Bar. The ionized PAH fraction increases outward from the Orion Bar up to 6.5 arcsec, likely due to PAH dehydrogenation. The 11.2 μm PAH band shift from profile class from A to A(B) between 9 and 10 arcsec reveals a different environment in that region, probably shielded molecular material. The fullerene to PAH band ratio decreases outward from the bar to about 7 arcsec, but has a bump around 10 arcsec. The first region coincides with where PAHs are dehydrogenated and eroded whereas the second is the shielded molecular zone. Another result is that the different spatial behavior between the PAH bands and the 10-15 μm plateau emission suggests a separate carrier for these features.

Spatially resolved observations of NGC 7023, NGC 2023, and the southeast of the Orion Bar with SOFIA and Spitzer were analyzed to study the PAH size and ionizations distributions (Knight et al. 2021a). The results of this work confirm that PAH size is dependent on the radiation field intensity and, moreover, that the UV radiation strongly influences the evolution of PAHs, contributing to a rich carbon-based chemistry in the ISM. As in other works

[14] The interface between the H II region IC 434 and the Orion B molecular cloud.

[15] PAH erosion typically refers to PAHs being eroded by chemically processing, e.g., reacting with O atoms to form CO, similarly as the term erosion refers to geological processes in which materials are worn away and transported by natural forces like wind or water.

discussed above, the results show that the PAH ionization and average size decrease with the distance to the illuminating source in NGC 7023 and NGC 2023. They also show that the average PAH sizes in NGC 2023 are larger than those in NGC 7023 at all points. The Orion Bar did not show a significant variation in the average PAH size in the southeast region. Another difference in the Orion Bar is the PAH ionization radial profile that decreases away from the illuminating source up to 4.5 arcsec, but increases at ∼5 arcsec. This profile does not resemble that of the 11.0/11.2 band ratio.

Knight et al. (2021b) used observations from SOFIA (3.3 μm) and Spitzer (5-14 μm) to extend the study of PAHs (as well as dust, atomic and molecular emission) across the Orion Bar. The PAH-related emission is strongly peaked in the Orion Bar, where the average PAH size increases with the strength of the FUV radiation field. Once more we see that the intense UV field leads to the photoprocessing of PAHs (destruction of the smallest molecules). Outside the bar, the variations in the PAH emission and band ratios typically coincide with the radiation peaks. As noted in their previous work, the observed behavior of the PAH emission is influenced by the nebular structure as we view it.

Knight et al. (2022) used Spitzer, SOFIA and Herschel Space Observatory (hereafter just Herschel) spatially resolved observations of the RN NGC 1333 to characterize the PAH emission and the physical conditions in the emitting PDR to better calibrate the response of PAHs to their environment. Their study indicates multiple promising relationships between PAH ratios and the far-UV radiation field strength, although no clear correlation with the PAH ionization parameter was found. The 6–9 μm emission features vary strongly between the irradiated PDR and the diffuse outskirts of the nebula. This supports that multiple PAH sub-populations possessing different molecular properties, have different origins. The ionic PAH bands (i.e., 6.2, 7.7, 8.6, and 11.0) and the 7–9 μm features must be due to multiple PAH sub-populations.

PAHs have also been observed in oxygen-rich PNe toward the Galactic bulge (Guzman-Ramirez et al. 2014). This could be construed as counterintuitive from a chemical point of view given that AGB stars, their precursors, follow the oxygen/carbon duality expected due to the stability of CO. PNe, in addition to strictly O- or C-rich objects, can also exhibit these so-called mixed chemistry cases. In all of these mixed-chemistry objects observed by Guzman-Ramirez et al. (2014), they found a dense central torus and, in most of them, PAHs were located in the outer edge of this structure, surrounding the more ionized material. This supports their hypothesis that PAHs can be formed outside of what would be the CO photodissociation front. However, this is not the only reason invoked in the literature to explain mixed-chemistry. In Guzman-Ramirez et al. (2015), the same authors investigate further the hypothesis above and also the idea of a dredge-up bringing more carbon from the star's interior to its surface. For this, the authors used SOFIA to obtain images of a C-rich PN with filters that can be used to characterize PAHs and O-rich dust emissions. Comparing these and ISO's spectral observations with a 3D photoionization model,[16] they show that the C-rich material is located in the inner parts of the nebula favoring the recent dredge-up as the explanation for the double chemistry in this object.

Another example of mixed-chemistry object is the PN NGC 6720. Its atomic abundances indicated an O-rich nebula (Delgado-Inglada and Rodríguez 2014). Cox et al. (2016) used Spitzer spectral imaging observations to study this nearby object to reveal the presence of the 11.3 μm PAH emission band in the outer region of the ring that gives the name for this nebula. The PAH populations seem to be dominated by neutral and small PAHs, since no

[16] A photoionization model simulates the ionization structure of a gaseous (and usually dust) cloud subject to illumination by a close radiative source.

bands in the 7–8 μm range were observed. The ring is dominated by dense clumps. The authors suggested that in this environment the local conditions allows the *in situ* formation of large carbonaceous molecules such as PAHs, through a bottom-up chemical pathway such as those described in Sect. 3.2.2. Mixed-chemistry objects enrich the ISM with both O-rich dust and large carbonaceous molecules.

Data from Herschel and Spitzer and SOFIA were also used to analyze the radiation fields around two cometary shaped nebulae, IC 63 and IC 59 (Andrews et al. 2018). IR emission from PAHs is very similar at the tip of both nebulae and the derived band ratios are remarkably similar despite intensity variations between the two. While the intensity of the UV field in IC 63 is approximately ten times higher than that in IC 59, both of these are low-UV irradiated environments with significantly lower intensity radiation fields than previously assumed.

Ground-based high resolution near-IR imaging of the well known PNe NGC 7027 and BD +30°3639 were taken with the 3.6 m Devasthal Optical Telescope by Anand et al. (2020). Their analysis suggested the predominance of neutral PAHs in BD +30°3639, while in NGC 7027 the PAH population is more ionized and more processed.

3.1.3 Fullerenes in PDRs, PNe, and RNe

The presence of C_{60} in different interstellar and circumstellar environments led to a plethora of questions concerning the relation of buckminsterfullerenes to other carbonaceous compounds in the ISM, and their formation and excitation processes. Using both Spitzer and Herschel data, Castellanos et al. (2014) studied several PDRs where C_{60} and PAHs are detected and the local physical conditions are reasonably well constrained in order to provide observational insights into these questions. C_{60} was found to emit in PDRs where the dust is cool ($T_{\rm dust}$ = 20-40 K) and even in PDRs with cool stars. These results thus excluded the possibility for C_{60} to be locked in grains at thermal equilibrium in these environments. They observed that PAH and C_{60} emission are spatially uncorrelated and that C_{60} is present in PDRs where the physical conditions (in terms of radiation field and hydrogen density) allow for full dehydrogenation of PAHs, with the exception of Ced 201. Castellanos et al. (2014) also found trends indicative of an increase in C_{60} abundance within individual PDRs, but these trends are not universal. These results support models where the dehydrogenation of carbonaceous species is the first step toward C_{60} formation. However, this is not the only parameter involved and C_{60} formation is likely affected by shocks and PDR age.

Using archival Spitzer/IRS data, C_{60} was also identified through its characteristic 17.4 and 18.9 μm features in eleven different PNe (Otsuka et al. 2014). They found that PAH profiles over the 6–9 μm region in the C_{60}-bearing carbon-rich PNe is of the more chemically processed class A (see Sect. 2). The intensity ratio of the 3.3 to 11.3 μm PAH bands indicates that the number of C-atoms per PAH in C_{60}-containing PNe is small compared to that of non-C_{60} PNe. The locations of C_{60}-containing PNe on a face-on map of the Milky Way show that most of the PNe are outside the solar circle which is consistent with low metallicity values. The metallicity suggests that the progenitors are an older population.

The same authors later used the X-Shooter instrument at the Very Large Telescope (VLT) in tandem with Spitzer data of the C_{60}-containing PNe Lin49 in the Small Magellanic Cloud (SMC) to find that there might either be (i) very small particles present in the form of small carbon clusters, small graphite sheets or fullerene precursors or (ii) a high-density structure surrounding the central star (Otsuka et al. 2016). They found that SMC C_{60}-containing PNe show a near-IR excess component to a lesser or greater degree.

This suggests that these C_{60}-containing PNe might maintain a structure nearby their central star.

Peeters et al. (2017) obtained 5–20 μm spectral maps of the reflection nebula NGC 2023 with Spitzer/IRS which revealed PAHs, C_{60} and H_2 superimposed on a dust continuum. The observations were accompanied by DFT calculations of oval PAHs ranging in sizes from 66 to 210 carbon atoms which were used as testing grounds to relate the band positions and relative intensities as a function of PAH size, charge and geometry. They proposed a photochemical evolutionary scenario for the PAHs in NGC 2023 as they are exposed more and more to the radiation field.

Aleman et al. (2019) analyzed deep VLT/X-Shooter observations of Tc 1, the PN where C_{60} and C_{70} were first discovered, in detail to physically and chemically characterize it in an attempt to understand the conditions that lead to the fullerene presence and emission. Their results support the idea that the fullerene emission is related to the fast wind overtaking the slow wind and the development of an ionization front in the early stages of the PNe formation, thus consistent with the fullerene detection only in young PNe.

Díaz-Luis et al. (2018) obtained mid-IR images of the spatially extended fullerene-containing PN IC 418 to study the 17.4 μm C_{60} fullerene band, the PAH-like feature at 11.3 μm, the broad 9–13 μm feature and their adjacent continua at 9.8 and 20.5 μm, using the CanariCam instrument on the Gran Telescopio Canarias. The analyses implied that other fullerene-based species like hydrogenated fullerenes (i.e., fulleranes) with very low H-content may contribute to the observed 17.4 μm emission.

3.2 Experiments - VUV Photoprocessing

In PDRs, PAHs experience significant photoprocessing from a close intense source of far UV radiation. Such systems, as it was seen in the previous sections, are sites for the formation of large PAHs, and also for the destruction of small PAHs. Hence, PDRs are a unique dynamic astrochemical laboratory. Multiple state-of-the-art experiments have been developed since 2013 to better simulate conditions in space and to understand unique astrochemical laboratories such as PDRs which host the formation and destruction of PAHs. Much experimental work has been devoted to understanding the build-up and destruction of PAHs which all contributes to our understanding of the dynamic life cycle of PAHs in PDRs. Here follows an overview of different experimental techniques that have led to advancements in our understanding of how PAHs are destroyed, or processed, and formed in bottom-up reactions.

3.2.1 Photoelectron Spectroscopy: PAH Destruction

Photoelectron spectroscopy coupled with mass spectrometry can be a powerful method to elucidate ionization thresholds, products of dissociative ionization, and product yields.

The past decade has seen many experiments performed where the products of dissociative ionization and the relevant thresholds were obtained for substituted PAHs. These could include hydrogenated PAHs or PAHs substituted with various functional groups. Dissociative photoionization as well as collision-induced dissociation have already been studied for a large variety of PAHs. Generally speaking, the primary reaction is H loss apart from smaller species where C_2H_2 loss is observed to a varying extent (West et al. 2018).

Examples of hydrogenated PAHs are 1,2-dihydronaphthalene ($C_{10}H_{10}$) and 9,10-dihydrophenanhrene ($C_{14}H_{12}$), who both undergo isomerization when ionized. This leads to not only competing H-loss channels, but also a CH_3 loss channel (West et al. 2014a). Besides providing dissociative mechanistic insights, studies of superhydrogenated PAHs

like pyrene have also revealed that pyrene is probably too small to support catalytic H_2-formation, while trends in previously reported data suggest that larger PAHs may serve as catalysts up to a certain level of hydrogenation (Stockett et al. 2021). H_2 formation is further explored in Sect. 5.

Ethynyl-substituted PAHs are also of interest, as they appear as intermediates in the Hydrogen Abstraction-Acetylene Addition (HACA) mechanism (see Sect. 3.3.3). When alkynyl-substituted peri-condensed PAHs are attacked by free radicals, covalently bound compounds form which promote further clustering through repeated addition reactions with negligible energy barriers (Liu et al. 2021). Studies of the dissociative photoionization of 9-ethynylphenanthrene and 1-ethynylpyrene have revealed that H-losses are observed at energies close to the H-losses of the parent or unsubstituted PAHs. Furthermore, photostability indices were determined to be larger than measured values for smaller PAHs (Rouillé et al. 2015). The threshold photoionization of 1-ethynylpyrene was also investigated, where the observed fragmentation channels were losses of one and two H atoms, as well as minor channels of C_2H and C_2H_2 losses, which is similar to what was observed generally for PAHs (West et al. 2018), but including the loss of C_2H – the attached functional group. Thus, the cation of 1-ethynylpyrene behaves similarly to that of pyrene and is consequently more photostable than 1-methylpyrene (Rouillé et al. 2019).

Generally, in terms of the photostability of PAH cations, it has been shown through the in-depth study of (V)UV photoionization of several large PAHs that fragmentation and double ionization are highly competitive, but as the size of the carbon skeleton increases double (and eventually triple) ionization is dominant. This was shown in experiments on the fragmentation and double ionization of the benzobisanthene cation ($C_{30}H_{14}^+$) which are competitive up to 15 eV, but in the case of the dicoronylene cation ($C_{48}H_{20}^+$), fragmentation processes are entirely negligible (Wenzel et al. 2020).

In terms of PANHs, it has been shown that dissociative ionization of quinoline and isoquinoline exhibits clear HCN formation, which is found to be a main characteristic of PANHs that only include one N-atom (Bouwman et al. 2015b) while cyano-group-containing PAHs appear to be more resistant to dissociative photoionization like was shown for 1-cyanonaphthalene (Bull et al. 2023). The dissociative ionization of quinoline was further investigated to reveal two different HCN loss channels but also an acetylene loss channel for the first time from a PANH molecule (Kadhane et al. 2022). This work was then followed up with a comprehensive exploration of its potential energy surface showing that HNC loss is energetically competitive with HCN loss, and that five- and seven-membered rings appear to be prominent intermediates in the isomerization following the photoionization of quinoline (Ramanathan et al. 2022).

Dissociative ionization has also been studied in molecules related to PAHs such as that of adamantane ($C_{10}H_{16}$). Most important products identified included H, C_3H_7, and C_4H_8 which clearly sets adamantane apart from PAHs in terms of the fragmentation pathways accessible at just above the ionization threshold (Candian et al. 2018). Adamantane dissociation has also been studied with IRMPD (see Sect. 3.2.7) and X-rays (see Sect. 6.2.2), where each case showcases different fragmentation.

Besides the utility toward studying dissociative ionization, the recording of threshold photoelectron spectra (TPES) is also a powerful analytical technique. TPES are recorded by collecting the very slowest photoelectrons that are produced during photoionization of atoms and molecules. As they possess low kinetic energies (typically less than 20 meV), their collection to construct a TPES reveals the energy levels of the cation and makes a molecule's TPES a unique fingerprint to identify that molecule in complex mixtures, particularly ones where multiple isomers are formed. Therefore, recording and analyzing the

TPES of PAHs is important so that they can be uniquely identified through their cationic fingerprints (see below). In one example TPES were used to solve the issue of the thermal breakdown of phthalide ($C_8H_6O_2$) which yields fulvenallene and other C_7H_6 isomers like ethynylcyclopentadiene, but also shedding light of thermal-induced H loss from fulvenallene to form the fulvenallenyl radical (Bouwman et al. 2021a). Another example concerned the formation of PAHs in sooting flames. To identify cyclopentaring-fused PAHs, the TPES of species such as acenaphthylene ($C_{12}H_8$), acenaphthene ($C_{12}H_{10}$), fluoranthene ($C_{16}H_{10}$) and benzo(ghi)fluoranthene ($C_{18}H_{10}$) (all containing a pentaring in their PAH skeleton) were recorded, and subsequently identified as products in a sooting flame comprising CH_4, O_2 and N_2 (Mercier et al. 2020).

It should however be mentioned that although the TPES of individual isomers should be different, cases exist where isomer differentiation may not be possible through the cationic ground state. For example, in the case of the anilino radical (Hrodmarsson et al. 2019) and 4-picolyl radical (Reusch et al. 2017), both C_6H_6N isomers, the TPES of the respective ground states are exceedingly similar so the first excited states of the cations would have to be sampled to successfully disentangle them.

TPES have also been recorded of the C_{60} fullerene to investigate the symmetry of the C_{60}^+ ground state (Hrodmarsson et al. 2020). They also recorded the total ion yield of C_{60} in order to scale it and give a photoionization cross section, obtained partial photoionization cross sections of the individual photoelectron bands, and the kinetic energy distribution of photoelectrons of C_{60} irradiated with the Lyman-α line.

3.2.2 Photoelectron Spectroscopy: PAH Formation

Studying the PAH formation processes in different conditions is another essential step to understand the observed PAH behavior in astrophysical environments. The comprehensive review on this important subject was prepared by Reizer et al. (2022).

In this context, photoelectron spectroscopy plays a pivotal role when it comes to identifying larger species in complex mixtures. Here, photoelectron spectroscopy serves as an important analytical tool and multiple TPES and dissociative photoionization dynamics have been reported for PAH monomers and their dimers (Bréchignac et al. 2014), larger PAH clusters (Joblin et al. 2017), doubly-nitrogenated PAHs (Schleier et al. 2022), as well as oxygenated PAHs (Mayer and Bodi 2021).

In regards to preparation of more complex samples in which these PAHs could potentially be detected, instruments like pyrolysis microreactors have been built which are providing new insights into the formation of PAHs and other molecules by utilizing the aforementioned threshold photoelectron spectroscopy (Hemberger et al. 2022). Other instruments have also been developed where PAH formation is studied in ethylene-rich flames (Carpentier et al. 2013), graphite electrodes submerged in n-hexane (Cataldo et al. 2021), and electrical discharges (Levey et al. 2022).

TPES have also been utilized to discern products of individual reactions of resonantly stabilized radicals (RSRs) which are considered to be of pivotal importance to PAH formation at low temperatures. However, modeling work has found that odd-C-numbered PAHs embedding 5-membered rings rapidly lose a H atom to form RSRs while even-C-numbered PAHs react as open-shell rather than closed-shell molecules independently of temperature (Nobili et al. 2022) so the importance of RSRs is not solely expected at low temperatures. Table 2 contains examples of reactions involving RSRs that have been shown to form PAHs or monocyclic daughter species of PAHs, like benzene, cyclopentadiene, *etc*.

Table 2 Summary of reactions studied by the Bouwman group employing TPES for isomer identification

Reactant 1 (name)	Reactant 2 (name)	Products (isomers formed, yields)	References
C_3H_5 (allyl)	C_2H_2 (acetylene)	c-C_5H_6 (cyclopentadiene)	[1]
C_3H_5N (acrylonitrile)	c-C_6H_5 (phenyl)	C_9H_7N (Z- and E-3-phenylacrylonitril, o-cyanostyrene, and 2-phenyl acrylonitrile)	[2]
C_3H_5 (allyl)	c-C_6H_4 (ortho-benzyne)	C_9H_8 (indene)	[3]
c-C_6H_4 (ortho-benzyne)	C_2H_2 (acetylene)	c-C_5H_5-CCH (phenylacetylene)/C_8H_6 (benzocyclobutadiene)	[4]
c-C_6H_4 (ortho-benzyne)	CH_3 (methyl)	c-$C_6H_5-CH_2$ (benzyl)	[5]

References: [1]Bouwman et al. (2015a) [2]Bouwman et al. (2018a) [3]McCabe et al. (2020) [4]McCabe et al. (2022) [5]Bouwman et al. (2023)

The continued study of RSRs has also showed that subsequent H-atom loss from benzyl yields fulvenallene, 1-ethynylcyclopentadiene, and 2-ethynylcyclopentadiene (Bouwman et al. 2021a) and these results have been used in astrochemical simulations of the Taurus molecular cloud 1 (TMC-1) reproducing the abundances of the five-membered ring species 1-ethynylcyclopentadiene providing strong evidence for the *in-situ* bottom-up formation of small cyclic species in cold cores (Bouwman et al. 2023).

Regarding formation of PANHs, the reaction of acrylonitrile (C_3H_3N) and the phenyl radical (c-C_6H_5) did not produce quinoline (C_9H_7N), which is the most stable product, which is in stark contrast with the isoelectronic phenyl + vinylacetylene reaction which produces naphthalene. Rather, the reaction produces Z- and E-3-phenylacrylonitril, o-cyanostyrene, and 2-phenyl acrylonitrile as it is found that the stability of the nitrile group inhibits ring formation that includes the N atom. Hence, alternative mechanisms are required to for PANHs in the ISM and Titan's atmosphere (Bouwman et al. 2018a).

For identification purposes, recording photoelectron emission spectra of PAHs is also possible, though this method is better suited to investigating photoexcitation dynamics (Mishra et al. 2014a). However, the most utilized technique in the past decade involves using photoionization cross sections of different species, which involves recording photon energy-dependent photoion yield curves (Johansson et al. 2017). Although not as sensitive as the TPES, it is still widely applicable and has been used to showcase the formation of — sometimes fairly large — PAHs. Table 3 summarizes the vast body of work carried out mostly by the Kaiser group using photoionization cross sections to identify and quantify the products formed.

Although not relying on photoelectron spectroscopy, the Kaiser group at Manoa, Hawai'i has also employed sophisticated crossed molecular beam techniques in tandem with mass spectrometry to investigate multiple fundamental reactions leading to the formation of PAHs or PAH-precursors. The strength of these molecular beam studies coupled with electronic structure calculations is evident (Kaiser et al. 2015) and the couplings have elucidated key elementary mechanisms involved in PAH formation, namely, HACA, Hydrogen Abstraction-Vinylacetylene Addition (HAVA), Phenyl Addition-DehydroCyclization (PAC), Radical-Radical Reactions (RRR), and Methylidyne Addition-Cyclization-Aromatization (MACA)

Table 3 Summary of reactions studied by employing total ion yields for isomer identification

Reactant 1 (name)	Reactant 2 (name)	Products (isomers formed and yields where relevant)	References
C_3H_3 (propargyl)	C_3H_3 (propargyl)	C_6H_6 (2-ethynyl-1,3-butadiene / fulvene / 1,5-hexadiene / benzene)	1
c-C_6H_5-CCH (phenylacetylene)	C_2H_2 (acetylene)	$C_{10}H_8$ (naphthalene)	2
1-$C_{10}H_7$ (1-naphthyl)	$H_2CCHCCH$ (vinylacetylene)	$C_{14}H_{10}$ (phenanthrene)	3
2-$C_{10}H_7$ (2-naphthyl)	$H_2CCHCCH$ (vinylacetylene)	$C_{14}H_{10}$ (anthracene)	3
1-$C_{14}H_9$ (1-anthracenyl)	$H_2CCHCCH$ (vinylacetylene)	$C_{18}H_{12}$ (benz[a]anthracene)	4
2-$C_{14}H_9$ (2-anthracenyl)	$H_2CCHCCH$ (vinylacetylene)	$C_{18}H_{12}$ (benz[a]anthracene / tetracene)	4
2-$C_{14}H_9$ (2-phenanthrenyl)	$H_2CCHCCH$ (vinylacetylene)	$C_{18}H_{12}$ (benz[a]anthracene / chrysene)	4
3-$C_{14}H_9$ (3-phenanthrenyl)	$H_2CCHCCH$ (vinylacetylene)	$C_{18}H_{12}$ (benz[a]anthracene / [4]helicene)	4
4-$C_{14}H_9$ (4-phenanthrenyl)	$H_2CCHCCH$ (vinylacetylene)	$C_{18}H_{12}$ ([4]helicene)	5
5-C_9H_7 (5-indenyl)	$H_2CCHCCH$ (vinylacetylene)	$C_{13}H_{10}$ (3H-cylopenta[a]naphthalene / 1H-cyclopenta[b]naphthalene)	6
6-C_9H_7 (6-indenyl)	$H_2CCHCCH$ (vinylacetylene)	$C_{13}H_{10}$ (1H-cylopenta[a]naphthalene / 1H-cyclopenta[b]naphthalene)	7
1-$C_{10}H_7$ (1-naphthyl)	H_2CCCH_2 (allene)	$C_{13}H_{10}$ (1H-phenalene / 1-methylacenaphthylene)	7
1-$C_{10}H_7$ (1-naphthyl)	CH_3CCH (methylacetylene)	$C_{13}H_{10}$ (1-methylacenaphthylene / 3H-cyclopenta[a]naphthalene)	7
2-$C_{18}H_{11}$ (2-tetracenyl)	$H_2CCHCCH$ (vinylacetylene)	$C_{22}H_{14}$ (pentacene)	8
$CH_3-C_6H_5$ (o-methylphenyl)	H_2CCCH_2 (allene)	$C_{10}H_{10}$ (3-methylindene, 96%) or $C_{10}H_{10}$ (1,2-dihydronaphthalene, 58% + 1,4-dihydronaphthalene, 35%)	9
$CH_3-C_6H_5$ (o-methylphenyl)	CH_3CCH (propyne)	C_9H_8 (indene, 89%) or $C_{10}H_{10}$ (3-methylindene, (98%))	9
$CH_2-C_6H_5$ (benzyl)	$CH_2-C_6H_5$ (benzyl)	$C_{14}H_{10}$ (phenanthrene / anthracene)	10
c-C_5H_5 (cyclopentadiene)	CH_3 (methyl)	c-C_6H_6 (benzene)	11

Table 3 (*Continued*)

Reactant 1 (name)	Reactant 2 (name)	Products (isomers formed and yields where relevant)	References
c-C_5H_5 (cyclopentadiene)	c-C_5H_5 (cyclopentadiene)	$C_{10}H_8$ (naphthalene)	11
o-C_5H_4N (o-pyridinyl)	$H_2CCHCCH$ (vinylacetylene)	C_9H_7N (quinoline)	12
m-C_5H_4N (m-pyridinyl)	$H_2CCHCCH$ (vinylacetylene)	C_9H_7N (quinoline / isoquinoline)	12
p-C_5H_4N (p-pyridinyl)	$H_2CCHCCH$ (vinylacetylene)	C_9H_7N (isoquinoline)	12
$C_{18}H_{11}$ ([4]helicenyl)	$H_2CCHCCH$ (vinylacetylene)	$C_{22}H_{14}$ ([5]helicene)	13
$C_{22}H_{14}$ ([5]helicenyl)	$H_2CCHCCH$ (vinylacetylene)	$C_{26}H_{16}$ ([6]helicene)	13
$C_{16}H_9$ (7-fluoranthyl)	C_2H_2 (acetylene)	$C_{18}H_{10}$ (benzo[ghi]fluoranthene)	14
$C_{18}H_9$ (benzo[ghi]fluoranthen-5-yl)	C_2H_2 (acetylene)	$C_{20}H_{10}$ (corannulene)	14
C_7H_7 (benzyl)	C_6H_5 (phenyl)	$C_{13}H_{10}$ (9H-fluorene)	15
C_9H_7 (1-indenyl)	C_5H_5 (cyclopentadienyl)	$C_{14}H_{10}$ (anthracene, phenanthrene and benzofulvalene)	16
$C_{20}H_9$ (1-corannulenyl)	$H_2CCHCCH$ (vinylacetylene)	$C_{24}H_{12}$ (benzocorannulene)*	17

References: [1]Zhao et al. (2021b) [2]Parker et al. (2015) [3]Zhao et al. (2018) [4]Zhao et al. (2020d) [5]Zhao et al. (2019) [6]Zhao et al. (2020c) [7]Zhao et al. (2020b) [8]Zhao et al. (2020a) [9]Shiels et al. (2021) [10]Kaiser et al. (2022c) [11]Kaiser et al. (2022d) [12]Zhao et al. (2021c) [13]Kaiser et al. (2022b) [14]Zhao et al. (2021a) [15]He et al. (2023a) [16]He et al. (2023b) [17]Tuli et al. (2023)

*It was also shown *in silico* that this benzannulation mechanism can be expanded to pentabenzocorannulene ($C_{40}H_{20}$) followed by successive cyclodehydrogenation to C_{40} nanobowls ($C_{40}H_{10}$)

(see Fig. 7) (Kaiser and Hansen 2021). These are summarized in Table 4, but theoretical advances in the field of PAH formation are summarized in Sect. 3.3.3.

3.2.3 Photoelectron Spectroscopy: Photodetachment of PAH Anions

Although PAH anions have been studied to a much lesser extent than PAH cations, they are nonetheless very important to the physics and chemistry of PDRs as well as dark clouds (Buragohain et al. 2018; Maragkoudakis et al. 2020; Murga et al. 2022b).

Photoelectron spectroscopy has been applied to PAH anions, e.g., to study the photodetachment dynamics. As has been observed in the anthracenyl anion, several π^* resonances are active in the first 2.5 eV above the photodetachment threshold (Stanley et al. 2017). Hence, it was revealed that nuclear dynamics compete with autodetachment for one of the resonances, while higher-lying resonances were dominated by prompt autodetachment.

Photoelectron spectroscopy was also utilized to study the effect of solvation of H_2O molecules on electron capture of anionic anthracene and its nitrogen-substituted derivatives (Lietard et al. 2021). It was found that for incoming electrons, resonances redshift with

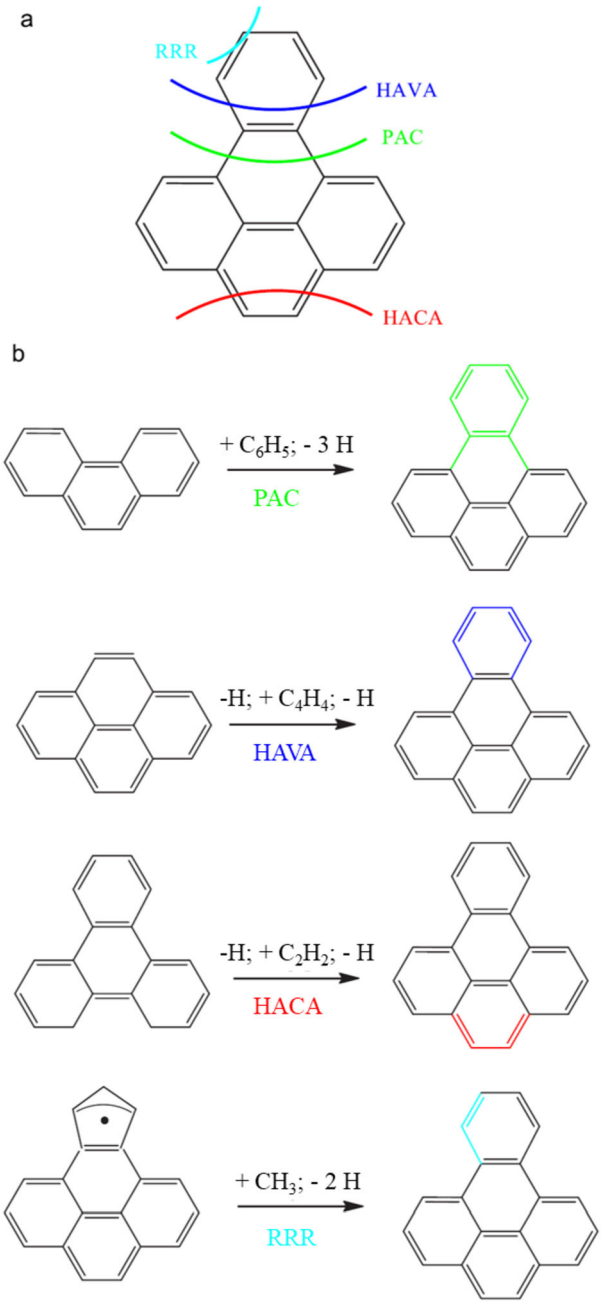

Fig. 7 Overview of the different mechanisms toward building PAHs with benzo[e]pyrene as an illustrated example. Adapted with permission from Kaiser and Hansen (2021). Copyright 2021 American Chemical Society

Table 4 Summary of the reactions studied by the Kaiser group employing a crossed molecular beam apparatus

Reactant 1 (name)	Reactant 2 (name)	Products (isomers formed)	References
C_6H_5 (phenyl)	C_4H_6 (1,2-butadiene & 1,3-butadiene)	$C_{10}H_{10}$ (2-phenyl-1,3-butadiene)	1
C_7H_7 (meta-tolyl)	C_4H_6 (1,3-butadiene)	$C_{11}H_{12}$ (5-methyl-1,4-dihydronaphthalene & 6-methyl-1,4-dihydronaphthalene*)	2
o-C_5H_4N (o-pyridinyl)	C_4H_6 (1,3-butadiene)	C_9H_9N (1,4-dihydroquinoline**)	3
m-C_5H_4N (o-pyridinyl)	C_4H_6 (1,3-butadiene)	C_9H_9N (1,4-dihydroquinoline**)	3
p-C_5H_4N (o-pyridinyl)	C_4H_6 (1,3-butadiene)	C_9H_9N (1,4-dihydroquinoline**)	3
CH (methylidyne)	C_6H_6 (benzene)	C_7H_7 (fulvenallene)	4
CH (methylidyne)	C_8H_8 (styrene)	C_9H_9 (indene)	5
C_2H_2 (acetylene)	$C_{11}H_9$ (1'-methylnaphthyl)	$C_{13}H_{10}$ (1H- & 3H-cyclopenta[a]naphthalene)	6
C_2H_2 (acetylene)	$C_{11}H_9$ (2'-methylnaphthyl)	$C_{13}H_{10}$ (3H-cyclopenta[a]naphthalene & 1H-cyclopenta[b]naphthalene)	6
C_2H_2 (acetylene)	$C_{11}H_9$ (2'-methylbiphenylyl)	$C_{13}H_{10}$ (fluorene)	6

References: [1]Yang et al. (2014) [2]Muzangwa et al. (2015) [3]Parker et al. (2015) [4]He et al. (2020) [5]Doddipatla et al. (2021) [6]Li et al. (2023)

Notes:

*5-, and 6-methyl-1,4-dihydronaphthalene were formed in 70.0% and 29.0% yields, respectively. The less stable thermodynamically 1-meta-tolyl-trans-1,3-butadiene was produced only in 0.8% yield

**Detected as a major product, while 1,4-dihydroisoquinoline was a minor product

increasing hydration, while, for the anion itself, the excitation energies of the resonances remain essentially the same. This compares well with the effects of microhydration on the electronic resonances of pyrene anions. The autodetachment of resonances shows that hydration has very little effect, showing that even the dynamics of most of the resonances are not impacted by hydration.

3.2.4 Laser-Induced (Optical Multiphoton) Fragmentation: i-POP

Among the earliest instruments to be introduced in the AstroPAH newsletter is the instrument for photodynamics of PAHs or i-POP for short (Zhen et al. 2014b). It comprises a quadrupole ion trap whose cationic PAH contents (that are prepared with an oven and elec-

tron gun) can be irradiated with a laser, but the mobility of the setup also allows its implementation at other light source facilities. It has been utilized at the SOLEIL synchrotron where a propensity of various PAHs to ionize rather than fragment upon exposure to (V)UV photons was observed (Zhen et al. 2015). i-POP has also been utilized at FELIX where PAH cations were excited with the FEL and dissociated via IRMPD (see Sect. 2.2.1). Symmetry, size, and structure were tested against the fragmentation patterns and IR spectra and it was found that a reduction in the molecular symmetry causes an activation in the 7–9 μm range (Bouwman et al. 2019).

Experiments using i-POP have been used to show that laser-induced multi-photon fragmentation of very large PAHs forms fullerenes (Zhen et al. 2014a), and by laser-activating clusters of smaller PAHs, covalent bonds can be fused and very large PAHs thusly formed (Zhen et al. 2018b). Laser-induced fragmentation of oxygenated PAHs like the bisanthenequinone cation ($C_{28}H_{12}O_2^+$) have been found to lose CO moieties, facilitating pentagon formation and bowling of the PAH skeleton (Chen et al. 2018b) and similar bowling mechanisms have been seen in laser-induced fragmentation of fluorene clusters (Zhang et al. 2019).

Experiments involving i-POP have also been conducted in tandem with Monte Carlo simulations to reveal that the formation of aliphatic side groups can be a critical first step in setting the stage for a competition between H and H_2 loss (Castellanos et al. 2018b). The presence of trio hydrogens, especially in combination with bay regions in small PAHs plays an important part in the experimentally established variations in the odd-to-even - atom loss ratios and as PAH sizes increase, H_2 formation becomes increasingly dominant, and sequential hydrogen loss is found to only play a marginal role.

More recently, experiments on i-POP have shown that the laser-induced fragmentation of three dibenzopyrene isomers showed almost identical products, namely, C_n^+ ($n = 11 - 15$) carbon clusters (Hrodmarsson et al. 2022). Interestingly, when the same methodology was applied to larger PAHs (isoviolanthrene and dicoronylene) the same carbon cluster cation products in almost the same branching ratios were observed, implying that PAH fragmentation might be a universal process, giving rise to essentially similar products, but also adding a new dimension to the universal fragmentation themes, i.e. formation of ionized cyclo[n]carbons in competition with H/H_2-losses and C_2(H_2) losses (Hrodmarsson et al. 2023).

A new experimental apparatus similar to i-POP utilizing two isolated ovens in order to form molecular clusters of species which sublimate at different temperatures, has been devised with the intent to investigate laser-induced fragmentation PAH clusters (Hu et al. 2021a; Zhen 2019), PAH-fullerene clusters, and PAH/fullerene clusters with various organic molecules such as amino acids (Hu et al. 2021c,b; Yang et al. 2021, 2022), and sugars (Zhang et al. 2021) to address a variety of issues relevant to dust growth, astrobiology, and processing of organics in meteorites.

Besides laser-induced fragmentation, this setup has also been used to study ion-molecule collisions. It was shown that collisions of C_{60}^+ and C_{70}^+ with 2,3-benzofluorene mostly yielded a charge exchange reaction, but in collisions of smaller fullerenes (C_{54}^+, C_{56}^+, and C_{58}^+), the dominant pathway involved formation of molecular adducts between the fullerene and PAH structures (Zhang et al. 2022b).

The laser has also been replaced with a D atom source. This allowed the study of deuteration of the HBC cation which was helped by a kinetic model describing how facile the deuterium process can be (Zhang et al. 2022a). Following these experiments, they also investigated the hydrogenation of photofragments of the HBC cation where a predominance of even-mass fragments are observed in the photofragmentation while no even-odd hydrogenated mass patterns are observed in the hydrogenation experiments (Zhang et al. 2023a),

but this also ties in with the theme of H_2 formation in Sect. 5. Along with modeling efforts to simulate the hydrogenation processes of the photofragments as a function of reaction time they infer that hydrogenation and photo-dehydrogenation channels are not reversible reaction channels. This means there is little chance that PAHs return to their initial state through hydrogenation following photodehydrogenation. Fulleranes are further explored in Sects. 3.1.3 and 10.

The same group also investigated the reactivity of C_{60}^+ and smaller cations (C_n^+, n = 54, 56, 58) with hydrogen and $C_{14}H_{10}$. H atoms are more likely to accumulate of the surface of the fullerenes than on $C_{14}H_{10}$, and the hydrogen will also expel already accreted $C_{14}H_{10}$ from the fullerene (Hu et al. 2023a). They also studied the hydrogenation and deuteration of C_{60}^+ and C_{70}^+ and their photodissociation (Hu et al. 2023b).

3.2.5 Fourier Transform - Ion Cyclotron Resonance Mass Spectrometer Techniques: PIRENEA

Another instrument that has been at the forefront of investigating fragmentation dynamics of PAHs of astronomical relevance is the Piège à Ions pour la Recherche et l'Etude de Nouvelles Espèces Astrochimiques or PIRENEA. It consists of a cold ion cyclotron resonance (ICR) cell to simulate interstellar environments and dissociation is achieved by processing the trapped PAHs with a Xe arc lamp, and more recently a 10.5 eV VUV source, for which the PAHs are prepared through laser ablation of a solid PAH sample.

PIRENEA has been used to study the gas-phase optical spectrum (in the 410–610 nm range) of a large PAH cation, $C_{78}H_{26}^+$ (Zhen et al. 2016b), which had been studied earlier with i-POP and shown to be a potential precursor of fullerenes (Zhen et al. 2014a). However, the optical spectrum of the $C_{78}H_{26}^+$ cation did not show any correspondence with known DIBs (Sect. 10).

Besides being used on its own it has also been used along with recording of TPES at the Swiss Light Source (SLS) synchrotron to study the full fragmentation map of pyrene cations and how they eventually dissociate to form an ionized cyclo[14]carbon ring (West et al. 2014b), which appears to be a principal product of PAH fragmentation along with ionized cyclo[*n*]carbons, $n = 11$–15 (Hrodmarsson et al. 2022, 2023).

Methyl- and ethyl-substituted coronene and pyrene cations were studied with PIRENEA where they were submitted to 10.5 eV VUV photons (Marciniak et al. 2021). It was found that aliphatic PAH derivatives have a higher fragmentation rate and a higher carbon to hydrogen loss compared to regular PAHs. This supports a scenario in which the evaporation of nanograins with a mixed aliphatic and aromatic composition followed by VUV photoprocessing results in both the production of the carriers of the 3.4 μm AIB by methyl side groups and in an abundant source of small hydrocarbons at the border of PDRs.

The PIRENEA setup in tandem with the Astrochemical Research of Organics using Molecular Analyzer (AROMA) setup (see Sects. 4.2.2 and 9.2) were used to show that coupling laser desorption ionization mass spectrometry with ion trapping allows the disentanglement of isomers by activating ion fragmentation via collisions or photon absorption (Vinitha et al. 2022a). As a proof of principle, isomer differentiation of pyrene, fluoranthene, and 9-ethynylphenanthrene was reported based on the parent dissociation curves as well as the ratio of dehydrogenation channels.

Other ICR setups apart from PIRENEA have also been utilized for work relevant to astrophysics, e.g., to study the growth of endofullerenes like $Na@C_{60}^+$. This may have implications for carbon condensation processes in supernova ejecta and the authors speculate these molecules could be present in various interstellar environments as well as explaining long-standing astrophysical puzzles such as the anomalous element enrichment of stardust (Dunk

et al. 2013). Later, DFT calculations of IR spectra of metallo-fullerenes along with a model built to predict the interstellar presence of endofullerenes concluded that metallo-fullerenes are potential emitters contributing to the observed IR spectra in circumstellar envelopes (Barzaga et al. 2023) which are known to be rich in fullerenes (Zhang et al. 2016).

3.2.6 UV-Vis / Laser Spectroscopy of PAHs

Many other studies of PAHs in the UV-visible range have been carried out, many of which have been dedicated to the electronic spectra of molecules of interest to the DIBs. These are detailed in Sect. 10.2.1. Here is a brief summary of work on spectroscopy and dynamics in the UV-Vis range.

Laser-desorbed coronene molecules were adiabatically expanded in a molecular jet, and subsequently exposed to 266 nm laser radiation. This yielded all sorts of fully dehydrogenated carbon, C_n^+, where $n_{max} = 24$. Although no detailed analysis is presented, the work does show the importance of understanding multiphoton dissociation processes so they can be appropriately compared with single photon dissociation events (Betancourt et al. 2015).

The photoionization and multiphoton dissociation/ionization of pyrene in a jet-cooled supersonic beam was studied in detail, particularly around its excited state, S_3 (Noble et al. 2019). This unraveled two different relaxation channels on the femtosecond (fs) timescale where one could be attributed to an initial interconversion to a dark state that is followed by relaxation via the first excited state. It has also been demonstrated that it is possible to prepare PAH cations with narrow internal energy distributions using a single UV nanosecond (ns) laser thanks to the unique excited state dynamics of PAHs. This has allowed the study of the ionization dynamics and wavelength-dependent internal energy distributions of small PAHs, such as naphthalene, azulene, and fluorene (Vinitha et al. 2020b). Furthermore, the internal photo-induced dynamics of H-loss of azulene cations has also been studied, but azulene cations are also found to isomerize rapidly to naphthalene cations (Vinitha et al. 2020a).

The same group has also shown that in the excitation region between 8.5 and 9.0 eV in the fluorene cation, there are three fragmentation channels where two or three H-atoms are lost (i.e., 2H, H + H_2, and H_2 + H) that are observed parallel to the emission of a single H atom (Vinitha et al. 2022b). Furthermore, two different internal energy distributions were found independently driving the single H loss reaction via H migration driven isomerization in the fluorene cation.

The REMPI technique has also been demonstrated as a useful tool in IR spectroscopy via the IR-UV ion-dip spectroscopic method which has been applied to acenaphthene, its dimer, and its complexes with H_2O (Lemmens et al. 2019), and many others (see Sect. 2.2.3). The same technique was later used to study the products from the electrical discharge chemistry of naphthalene and acetonitrile by Loru et al. (2022) who found that besides species already known to form in electric discharges of naphthalene, $-CH_3$ and $-CN$ substituted unsaturated hydrocarbons were formed as well. Most of them, particularly the ones containing an N atom, have a substantial dipole moment and could thus be considered as viable candidates for radio astronomical searches. Among the species they observed were 1- and 2-cyanonaphthalenes which have now been observed in TMC-1 (McGuire et al. 2018).

Besides the REMPI technique, CRDS has recently been successfully implemented to study the three-ringed PAHs anthracene, 9-methylanthracene, and 2-methylanthracene in UV absorption between 330 and 375 nm (26,666 to 30,303 cm^{-1}) (Bejaoui et al. 2023). These compare well with previous fluorescence spectra but CRDS offers unparalleled spectral resolution in the UV and has also been used as a hunting ground for DIBs in PAHs frozen in matrices (Bejaoui and Salama 2019) which are further explored in Sect. 10.2.1.

Laser-induced fragmentation of HACs and solid hexane have also been reported with links to benzene formation, c-C_3H_2 formation and other hydrocarbon radicals (Duley et al. 2015).

3.2.7 Fragmentation Using Infrared Multiphoton Dissociation

While IRMPD has shown itself to be a great tool to record IR spectra (see Sect. 2.2.1), it has also been widely used to identify fragmentation products and dynamical information following excitation via either photons or collisions.

IRMPD has been used to show that pentagon formation in the fragmentation of PAHs appears to be a commonality. This was found in the dissociation of naphthalene to form pentalene indicating a facile mechanism for pentagon formation in the acetylene loss from a PAH (Bouwman et al. 2016). IRMPD was also used to study the dissociative ionization of the nitrogen-containing PAHs, acridine and phenanthridine which showed that losing HCN leads to pentagon formation of the products which were identified as benzopentalene and acenaphthylene (de Haas et al. 2017).

The products of electron impact dissociative ionization of adamantane have also been studied with IRMPD where it was found that the protonated benzene isomers, dihydrotropylium, and benzylium were among the products formed (Bouwman et al. 2018b).

A common theme in the study of fragmentations of PAHs appears to be a commonality of particular fragment ions forming from the breakdown of PAHs. For instance, during the electron-ionization-induced fragmentation of three different three-ring PAHs, fluorene, 9,10-dihydrophenanthrene and 9,10-dihydroanthracene, the closed-shell fluorenyl cation was identified as the principal fragment ion (Petrignani et al. 2016). In this vein, the dissociative ionization of anthracene and phenanthrene ($C_{14}H_{10}$) forming the $C_{12}H_8^+$ ion from C_2H_2 loss, leads to a common product, namely the acenaphthylene cation (Banhatti et al. 2022). This ties in with the concept of universal fragmentations of PAHs which have been observed not only from losses of small fragments like C_2H_2, but also in multi-photon processes where PAHs break down into cyclo[*n*]carbons (Hrodmarsson et al. 2022, 2023).

The study of the dissociative ionization of aniline ($C_6H_5NH_2$) has also revealed, thanks to IRMPD, that cyanocyclopentadiene (c-C_5H_5CN) forms as a main product (Rap et al. 2022a), but cyanocyclopentadiene has recently been observed in the dark molecular cloud TMC-1 (see Sect. 7.1). In relation to aniline, IRMPD was also used to show that protonation of 4-bromoaniline forms an ammonium moiety, followed by C-Br cleavage and rearrangement forms the aniline cation (Finazzi et al. 2023).

The fragmentations of the dissociative ionization of pyridine (C_5H_5N) and benzonitrile ($C_6H_5(CN)$) have also been investigated (Rap et al. 2023). The loss of HCN/HNC is a major loss channel for both molecules. In the fragmentation of pyridine, multiple non-cyclic structures are formed, whereas fragmentation of benzonitrile dominantly leads to the formation of cyclic structures.

The viability or lack thereof, of H and H_2 losses from PAHs was also studied (Vala et al. 2017). Protonated tetralin (1,2,3,4-tetrahydronaphthalene) was studied to reveal a single fragment that neither H- nor H_2-losses could account for. The main ionic product appeared to resemble the benzylium ion, but with the extra hydrogen and methylene substituents in various ortho, meta, and para conformations.

IRMPD has been widely used to illuminate the underlying excitation dynamics and structural characteristics of astronomically relevant PAHs (Álvaro Galué et al. 2016). It was used to investigate the interaction of delocalized π-electrons with molecular vibrations where it

was shown that molecular edge topology in charged catacondensed aromatic molecules influences the Herzberg-Teller coupling[17] of π-electrons with vibrations. This was done by studying the radical cations of picene and pentacene (both $C_{22}H_{14}$) where picene with its armchair edges displayed a stronger charge π-flux that is generated in comparison to the pentacene with its zig-zag edges, which could justify the differences of electronic properties of armchair- versus zigzag-type families of PAHs in general.

PANH-copper complexes were studied by Gao et al. (2016) who confirmed that a σ-bond is formed between copper ions and the exoskeletal N atom. The experimental spectra suggest that the CNC stretching mode undergoes a small red shift of up to 20 cm^{-1}, with respect to the band position of the isolated PANH molecule, away from the 6.2 μm interstellar bands.

3.2.8 Collision-Induced PAH Processing

High-energy ions and atoms are expected to be omnipresent in the ISM as energetic cosmic rays as well as produced in shocks from, e.g., supernovae. Such particles are also capable of fragmenting PAHs. Here, a key question that has been addressed is whether the total excitation energy alone, or also the way energy is deposited in the interactions, dictates the subsequent dynamics (Gatchell and Zettergren 2022). It has been shown that atomic projectiles have the unique possibility to knock out single atoms in molecules through billiard ball type interactions. The formed fragments may be highly reactive and thus key intermediate steps, for example, in molecular growth processes. These are described here below.

Ionization and fragmentation of PAH molecules and their clusters by collisions with high-energy ions, typically keV alpha particles (He^{2+}), have been measured by Gatchell et al. (2013). In both cases of the monomers and clusters, singly-ionized PAHs are the dominant products, but as the charge state of the impacting high-energy ion increases, strong multiple ionization of PAH clusters and subsequent Coulomb explosions were observed.

For smaller PAHs such as naphthalene, collisions with 30 keV He^{2+} nuclei leads to extensive fragmentation (Reitsma et al. 2013). The ion-induced fragmentation of naphthalene is significantly more violent than corresponding photofragmentation with energetic photons as dozens of different products are observed including a variety of small hydrocarbon cations. Naphthalene has also been bombarded with high-energy protons (between 50 and 150 keV) in effort to measured the electron capture and electron emission cross sections of the process (Mishra et al. 2013). While multiple ionizations followed by H losses appear to be the dominant channels there are several nuances in the fragmentation process that are dependent on the charge states of the naphthalene cations. The experimental collision-induced fragmentation of naphthalene was subsequently followed up with Monte Carlo simulations, which showed results consistent with the experiments which revealed a velocity dependence on fragmentation yields (Mishra et al. 2014b). The impacts of such energetic ions are interesting to compare to those of X-rays in the energy range of hundreds of eV where multiple ionizations are observed as well, followed by fragmentations, but giving different sets of fragmentation products (see Sect. 6.2.2).

Ultimately, high-energy ions might be more efficient in producing H_2 from PAHs. PAH collisions with keV He^{2+} were found to effectively produce H_2 if the internal PAH temperature exceeds 2200 K (Chen et al. 2015). In comparison to UV radiation (i.e., single

[17] Certain vibronic (combined electronic and vibrational) transitions that are not expected in spectra on the grounds of being symmetry forbidden are frequently observed in large molecules. Herzberg-Teller effects are so-called "intensity borrowing" effects where the dipole transition moment for the electronic transition depends on the nuclear coordinate associated with the vibration. In the Franck-Condon approximation one assumes that there is no such dependence.

photons with energies below 13.6 eV), UV photons are incapable of producing such high internal temperatures in PAHs, and thus UV photons are not as effective in producing H_2 from PAHs. An overview of H_2 formation in the context of astronomicall relevant PAHs is given in Sect. 5.

Collisions of PAH clusters with keV ions (varying from high-energy protons, He^+, but likewise N^{3+}, O^{2+} and Ar^{2+}), however, appear to rather demonstrate efficient molecular growth (although fragmentation is also observed) (Delaunay et al. 2015). Similar growths in molecular complexity have been observed in collisions of high-energy ions with C_{60} clusters which lead to the formation of dumbbell C_{119}^+ and C_{118}^+ fullerenes (Seitz et al. 2013; Zettergren et al. 2013).

Pure coronene clusters and mixed C_{60} and coronene clusters have also been bombarded with 22.5 keV He^{2+} and 3 keV Ar^+ ions (Domaracka et al. 2018). While the heavier and slower Ar^+ projectiles induce prompt knockout-fragmentation of individual molecules and induce efficient secondary molecular growth reactions, the faster He^{2+} ions tend to ionize the clusters, which rather fragment the clusters without molecular growth.

Previously, evidence had been presented for the dominance of prompt single-atom knockout in fragmenting collisions between large PAHs and neutral He atoms at center-of-mass energies close to 100 eV, i.e., significantly lower collision energies in comparison to ionized projectiles (Stockett et al. 2014). These nonstatistical fragmentation processes are estimated to be the dominant decay pathway for interstellar PAHs containing more than 50 carbon atoms. Hence, more dynamical characteristics of PAH-He collisions have been measured, such as absolute cross sections for ultrafast single-carbon knockout from PAH cations as a function of the He-PAH center-of-mass collision energy in the 10–200 eV range (Stockett et al. 2015a). This work further evidenced the nonstatistical nature of PAH fragmentation induced by collisions, particularly single carbon-knockout.

Collisions of various PAH isomers with He nuclei at center-of-mass energies of 110 eV have also revealed significant differences in the fragmentation patterns than what is typically observed in pure statistical fragmentation processes (Stockett et al. 2015b). Most likely these differences stem from a competition between statistical and non-statistical fragmentation schemes at these collision energies. This suggests that the absolute cross sections for the loss of at least one carbon atom from different PAH isomers are nearly the same. However, threshold energies of single carbon knockout have been found to be similar in PAHs and C_{60} (Stockett et al. 2018).

3.2.9 PAH Dynamical Processing: Storage Ring Experiments

Among the dynamical information that can be obtained from experiments performed at storage rings are radiative cooling rates of excited PAHs. For instance, anthracene cations were prepared in an electron cyclotron resonance ion source and stored in an electrostatic storage ring, the so-called Mini-Ring, at the ILM[18] in Lyon (Chen et al. 2014a). While ion population distribution was dominated by unimolecular dissociation of the ions, fast radiative cooling rates (100 s^{-1}) were observed which could not be explained by vibrational IR emission. Rather, it was found that electronic fluorescence from thermally excited electronic states gave rise to the fast radiative cooling rates in anthracene cations (Brédy et al. 2015).

The radiative cooling rates of carbon cluster cations, C_N^+ ($N = 9, 11, 12, 17 - 27$) have also been measured in a storage ring (the TMU[19] E-ring in Tokyo, Japan), to values on the

[18] Institut de Lumière et Materière.

[19] Tokyo Metropolitan University.

order of 10^4 s^{-1} (Iida et al. 2022). These rates are even higher than those of the anthracene cation, and have a very strong stabilizing effect on the clusters. The underlying relaxation mechanism gives a high energy conversion efficiency with the potential to reach high quantum efficiencies in the emission process. The competing decay of unimolecular fragmentation defines upper limits for photon energies that can be downconverted to lower energy photons. Clusters absorbing photons below 10–14.5 eV cool down efficiently by emission of photons via electronic transitions and their fragmentation is strongly reduced, increasing the likelihood of their survival in HI regions.

Time-resolved spontaneous and laser-induced unimolecular fragmentation of PAH cations has also been studied on timescales up to 2 s. The competition between fragmentation and radiative cooling (both vibrational and electronic) in the perylene cation as a benchmark PAH cation was studied at the DESIREE[20] storage ring facility in Stockholm, Sweden, where the dominant electronic transition in the photoabsorption cross section was identified, and the vibrational cooling rate was found to be consistent with the simple harmonic cascade approximation (Stockett et al. 2020). These rates have also been measured in substituted pyrene cations, namely 1-hydroxy- and 1-bromo-pyrene. The substituted PAH cations exhibited no radiative cooling due to RF (see Sect. 2.3.3), but only vibrational cooling, which in part compromises the photostability of these substituted PAH cations (Zhu et al. 2022).

The radiative cooling rates of coronene cations following multiphoton absorption was also studied by the same group on time scales up to 10 s. The measurements revealed the absorption profile for the isolated coronene cations as well as the rate at which hot band absorptions are quenched by radiative cooling (Stockett et al. 2019b). The hot bands fade with a time constant of 200 ms which is consistent with radiative cooling via IR emission from vibrational bands. While the agreement between the simple harmonic cascade model and the experiment was satisfying, it is possible that at longer timescales, internal vibrational redistribution (IVR) may not be as efficient as assumed in the model, leading to population becoming trapped in IR inactive modes (Stockett et al. 2019a).

In terms of photostability of various PAHs, several studies have been performed at storage ring facilities. The photostability of hydrogenated and pristine pyrene cations was studied at the ELISA[21] ion storage ring at the Aarhus university in Denmark (Wolf et al. 2016). They showed that photo-induced carbon backbone fragmentation is more likely for hydrogenated pyrene than for pristine pyrene. Hence, carbon backbone fragmentation could be a viable competitor with H_2 formation at least for small and hydrogenated PAHs like pyrene.

The stability of PAH knockout fragments has been studied as well. The survival of reactive fragments of coronene where individual C atoms have been knocked out from collisions with He atoms was studied in DESIREE (Gatchell et al. 2021). They found that defective PAHs formed in energetic collisions with heavy particles may survive at thermal equilibrium in the ISM indefinitely and hence, could play an important role in the chemistry there due to their increased reactivity compared to intact or photo-fragmented PAHs.

The same group also reported on the radiative cooling rate coefficients of 1-cyanonaphthalene cation following their investigation of its single-photon VUV photoionization (Bull et al. 2023). They found that RF (see Sect. 2.3.3) efficiently stabilizes the cation owing to a large enhancement of the electronic transition probability by vibronic coupling. This result helps explain the anomalous abundance of 1-cyanonaphthalene in TMC-1 and challenge the widely accepted picture of rapid destruction of small PAHs in space (Stockett et al. 2023).

[20] The Double ElectroStatic Ion Ring ExpEriment.

[21] ELectrostatIc Storage ring for ions, Aarhus.

They also measured a radiative cooling rate which compares well with the RF rate (Navarro Navarrete et al. 2023).

PAH anions have been studied at storage ring facilities as well, but to a lesser extent. For instance, the spontaneous and photoinduced delayed electron detachment from pentacene anions were measured in the TMU-E storage ring. Radiative cooling rates in the time range of a few tens of milliseconds were obtained (Iida et al. 2021).

Carbon anions in and of themselves have also been studied. Examples include the radiative electron attachment to linear C_6 molecules (Chandrasekaran et al. 2017) and the isomerization of linear C_{10}^- to cyclo[10]carbon anions (Saha et al. 2018).

3.3 Theoretical

3.3.1 UV Excitation

Modeling the evolution of large molecules such as PAHs following the absorption of UV photons is an enormous challenge. It requires a description of how the energy spreads over multiple electronic and nuclear degrees of freedom. Understanding these processes is of primary interest to characterize photostability and photochemistry and the inherent competition between fluorescence and non-radiative relaxation channels, such as photodissociation and photoionization.

TD-DFTB calculations have been used to simulate the energy relaxation following the absorption of a UV photon by polyacenes (i.e., anthracene, tetracene, pentacene, hexacene, *etc.*; Posenitskiy et al. 2019). The intention was to study the size effect on the ultrafast dynamics in excited states for these PAH species, but the results showed a striking alternation in decay times of the brightest singlet state for neutral polyacenes with 3 to 6 aromatic cycles. The alternation corresponds to an order-of-magnitude variation between roughly 10 and 100 fs and is correlated with a qualitatively similar alternation of energy gaps between the brightest state and the state lying just below in energy. That is, larger energy gaps from the brightest excited states to the neighboring levels of lower energy lead to longer decay times.

DFT and TD-DFT are also widely used to describe excitation processes and photoionization. For example, the photoionization processes of naphthalene, 1-cyanonaphthalene, 2-cyanonaphthalene upon complexation with the water dimer to understand the photodissociation processes under ISM conditions were studied with DFT and TD-DFT (Queiroz et al. 2023). In strongly-irradiated regions of the ISM (above 8 eV), charge transfer excitations occur from localized occupied molecular orbitals (MOs) in the aromatic molecules to mixed unoccupied MOs in the complexes, favoring cationic species.

3.3.2 Fragmentation and Rearrangements

A common theme in the excitation and fragmentation of PAHs is that of intramolecular rearrangements. PAHs are such large molecules that upon excitation, their multiple degrees of freedom allow them to vibrationally relax, or to break bonds and form new ones by rearranging themselves to either a more compact, or a more energetically feasible product. Here, we present the theoretical work done in the past decade that has been devoted to understanding fragmentation and rearrangement dynamics of PAHs using various techniques.

DFT was used to investigate the structures of PAHs with internal energies in the range 1–10 eV (Trinquier et al. 2017a). In this energy range, where coronene and pyrene and

their multicationic forms were used as testing grounds, H-migrations are prevalent but H-shifted forms are common which both bear a carbene center and a saturated carbon. The H-shifted minima identified lie 4–5 eV above the regular all-conjugated forms, separated by barriers around 1 eV. In general, H-shifts are easier for cationic species as relative energies of the H-shifted minima are 1–1.5 eV lower than those for neutral species. The same authors followed up with a second entry that focused on the energetics involved in ring-opening mechanisms (Trinquier et al. 2017b). That is, opened forms containing ethynyl or 2-butynyl groups, vinylidene isomers, twisted forms, and bicyclobutane forms. Such arrangements should be ubiquitous in PAHs upon excitation but it is also possible that PAHs could be trapped into such higher-energy isomers followed by IR cooling in isolated environments such as the ISM.

Another aspect of these ring-openings concerns the formation of so-called Stone-Wales (SW) defects. A prime example of a SW defect has been studied in pyrene which comprises four hexagons. The defect is formed by rearranging the two central C atoms in pyrene to form two pentagons and two heptagons in place of hexagons. Campisi and Candian (2020) studied the SW defect in pyrene in effort to see whether reactivity of the defective species would be more or less catalytic in terms of H_2 formation through H-abstraction by a single impacting H atom. The formation of the SW defect requires overcoming an energy barrier of 8.4 eV, but the defective structure is also stable due to the high reverse reaction barrier which is approximately 6 eV. Campisi and Candian (2020) also showed that the presence of the defect decreases the sticking barrier for the first hydrogenation and promotes more stable singly and doubly hydrogenated intermediates with respect to the pristine pyrene and that H_2 can indeed be formed at low (2 eV) barriers through an extraction mechanism involving H atoms attached to distal carbon atoms.

Simon et al. (2017b) also investigated the molecular dynamics of the naphthalene, pyrene, and coronene cations in terms of ejected products when presented with up to 30 eV internal energy. The losses of H and C_2H_2 are the most prominent and the H/C_2H_2 ratio increases with PAH size and decreases with energy. While their calculations imply that decreasing the internal energy and increasing the PAH size will favor H-loss, they also state that prior to dissociation, many structural rearrangements occur, involving H migration, vinylidene type complexes and external ring openings, which is in line with several experimental observations investigating PAH dissociation.

Pyrene and coronene at various levels of dehydrogenation have also been studied in terms of isomerization and dehydrogenation using Monte Carlo MD simulations (Parneix et al. 2017). The authors found that hydrogenation significantly stabilizes the fully hydrogenated PAH structure, even though local dehydrogenation next to an aromatic ring favors ring opening, as was shown previously where H_2 formation competes with ring-opening (Wolf et al. 2016) (see Sect. 3.2.9). The formation of pentagonal rings is predicted to be competitive with the loss of a hydrogen atom. Hence the authors emphasized that these sorts of structural defects are likely present in astrophysical PAHs. But structural defects such as pentagons are of interest in the pursuit of both top-down and bottom-up fullerene formation as was shown in Sect. 3.2.2.

Following the experimental work of (Zhen et al. 2016a) on the VUV-induced fragmentation and ionization of PAH cations, DFT was used to study the fragmentation involving H-losses of two of the dibenzopyrene isomers, namely dibenzo[a,e]pyrene and dibenzo[al]pyrene (Rodriguez Castillo et al. 2018). The AL^+ isomer is chiral where two H atoms in a bay region distort the planarity of the PAH due to steric hindrance, leading to two enantiomers. Hence the $2H/H_2$ losses from the AL^+ cation appear at lower energies in comparison to AE^+, which lead to the formation of a planar PAH cation with an in-built

pentagon. This was also observed in the laser-induced fragmentation of these molecules (Hrodmarsson et al. 2022) and in the preparation of the cations to study their IR spectra (Bouwman et al. 2021b). Additionally, the authors showed that in AE^+ the H_2 loss channel is favored while AL^+ has favorable paths for both H and H+H losses.

Related to the dibenzopyrenes, the potential energy surfaces of $C_{24}H_x$ ($x = 0$, 6, 12, 18, 24) hydrocarbon clusters were investigated with a genetic algorithm approach to study the preferred structural arrangements of the hydrocarbons (Pla et al. 2021). The structural diversity was analyzed using parameters such as the total numbers of pentagons and hexagons in the structure, and the percentages of sp^2 hybridized carbon atoms to derive the so-called asphericity parameter. Different asphericities give rise to four types of structures, cages, flakes, pretzels, and branched. The most abundant and lowest energy population belongs in the flake category, but as the portion of H atoms to C atoms (n_H/n_C) increases, the fraction of pretzel structures increases. Cages are a minor population while branched structures are the highest energy population for all n_H/n_C ratios.

Considering that bare carbon clusters have been widely observed to be among the major products of PAH destruction (Zhen et al. 2014a; Hrodmarsson et al. 2022, 2023), the nucleation of bare carbon clusters in tenuous carbon gas is of interest in terms of dust formation. Patra et al. (2014) studied how the temperature, particle density, the presence of hydrogen, and carbon inflow affect the nucleation of different structural motifs leading to different types of carbon clusters. They did this by using reactive Molecular Dynamics (MD) calculations to simulate temperature-dependent carbon cluster growth at temperatures ranging from 500 to 3000 K. Patra et al. (2014) found that temperatures of 2000-3000 K were required to obtain fullerenes whereas graphene-type sheets and long chain molecules/structures were synthesized at relatively low temperatures.

Isomerization energies of fullerenes have been a particular center of attention concerning the prevalence of C_{60} in space. In this vein, Aghajamali and Karton (2021) evaluated the performance of carbon force fields at 1811 C_{60} isomerization energies. Several force fields exhibit a high statistical correlation with the DFT isomerization energies so linear scaling of the isomerization energies can significantly improve the accuracy. These force fields can thus offer a computationally economic way for exploring the relative energies of fullerenes.

On top of PAHs, clusters, and fullerenes, the fragmentation of ortho-benzyne has also been computationally studied at the multi-configurational second-order perturbative level (Ghigo et al. 2014). The fragmentation of o-benzyne yields C_2H_2, C_4H_2, and C_6H_2 as the main products, but the temperature-dependence on the product branching ratios and the mechanisms involved were elucidated as well.

3.3.3 PAH Formation Reactions

There are multiple different PAH formation schemes known. Among the earliest to be considered of astronomical relevance was the HACA mechanism (see also Sect. 3.2.2), which involves the addition of subsequent acetylene (C_2H_2) units to form aromatic systems. This requires abstracting an H-atom, but that is not a barrierless process which is a prerequisite for the viability of gas-phase reactions in interstellar space. However, Ghesquière et al. (2014) showed with high-level *ab initio* calculations that the addition of two C_2H_2 units to the benzene cation to form the naphthalene cation can proceed without H-abstraction in cold interstellar environments.

Besides the HACA mechanism, the Diels-Alder (DA) reaction can also lead to the formation of interesting PAH species. Neutral benzene and acetylene can react to form barrelene in this way by means of catalysis of an alkali cation. Vermeeren et al. (2020) studied this reaction quantum chemically using relativistic, dispersion-corrected DFT.

Intramolecular DA-type reactions can also lead to ring-closing in doubly-dehydrogenated polyacenes (Gupta et al. 2021). They used thermally assisted occupation (TAO)-DFT calculations to investigate the effectiveness of an intramolecular DA reaction in poly-*n*-acenes (n = 10-20) leading to ring closures to form *n*-cyclacenes followed by ejection of C_2H_2. In each case of C_2H_2 extrusions, they were found to be the step with the highest barrier, but the barrier heights were nonetheless smaller than C−H bond dissociation energies. Hence, Gupta et al. (2021) found the process to be energetically conceivable following multiple (V)UV photoabsorption.

On top of the HACA and DA mechanisms, there is also the Hydrogen Abstraction Ethynyl Radical Addition (HAERA) mechanism. The competition between HACA, DA, and HAERA were computationally studied in the formation of benzo(a)pyrene starting from chrysene or benzo(a)anthracene by using the ωB97XD/6-311++G(d,p) level of theory (Reizer et al. 2021). The DA mechanism was found to have the highest energy barriers in the formation of benzo(a)pyrene so the HACA and HAERA mechanisms can be considered more likely with HAERA as the least exergonic mechanism.

Reizer and Fiser (2022) also investigated the reaction initiation points of 16 PAHs by calculating the different C−H bond dissociation enthalpy values using multiple different DFT methods with varying basis sets. Their results showed that most of the hydrogen atoms are in zig-zag positions, and that most of the reaction initiation points are represented armchair and peak hydrogens.

Besides PAHs, the discovery of benzonitrile in TMC-1 (McGuire et al. 2018) also spurred quantum chemists to the study its formation under interstellar conditions. By employing quantum chemistry and *ab initio* molecular dynamics calculations, Jose et al. (2021) demonstrated that ionized clusters of cyanoacetylene rearrange to form a variety of different molecular species, including benzonitrile. They showed that a large amount of energy is made available to the system following ionization which makes barrier crossings more facile. On top of benzontrile, nitrile-containing molecules have also been shown computationally to be capable of reacting with partially dehydrogenated formamide (H_2NCHO) to form nucleobases (Lu et al. 2021). This is not the only viable route of nucleobase formation in space (e.g., Yang et al. 2023; Hamlin et al. 2017), but it is very significant to Astrobiology that the chemistry of PAHs and DNA are involved, as PAHs are an abundant and ubiquitous molecule.

Nitrogen atoms are not the only heteroatoms that can be inserted into PAHs. Phosphorous also holds a special place in the origin of life as it is an important biological component of life as we know it, and thus the insertion of P heteroatoms is worthy of investigation. The formation of phosphorous-containing PAHs (PAPHs) has been studied with various computational methods in a bottom-up approach, starting the CP diatomic and subsequent additions of acetylene (Fioroni et al. 2019). The results showed that formation of the first ring (phosphinine) is an energetically favorable process along with subsequent C_2H_2 additions to the radical phosphinine. Likewise, the addition of a single CP radical and acetylene units to a neutral benzene molecule generates a complex chemistry where the main product is 2-phospha-naphthalene, but single CP radical additions to PAHs also produces RSRs which are known to promote further growth of PAHs (see Sect. 3.2.2). Other potentially important PAH formation routes involve surfaces to catalyze reactions. To simulate reactions between dehydrogenated benzene molecules on a carbon nanoparticle, Hanine et al. (2020) used MD calculations to simulate these reactions. Multiple PAH structures were observed to form at temperatures up to 1000 K and the size of formed molecules was found to roughly increase with increasing temperature up to 800 K and was closely related with the level of dehydrogenation. Fullerene formation was not observed at these temperatures which verifies the findings of Patra et al. (2014) described above.

3.3.4 Collisions

In the ISM PAHs can interact with the energetic protons and atoms coming from cosmic rays and other sources and it is important to quantify the role of the interaction for the survival of the astronomical PAH population. Molecular dynamics simulations of H and He collisions with anthracene molecules were used to investigate the dynamic of C-atom knockout from the PAH structure and the energetic involved in the process (Postma et al. 2014). The authors found that for small PAHs such as anthracene, ion processing produce C_2H_2 loss rather than C-atom knockout (see Sects. 3.2.8 and 3.2.9).

The same year a study by Chen et al. (2014c) made use of DFT calculations and Monte Carlo simulations of C-atom knockout to simulate the energy transfer for a collection of PAH molecules when in collision with H and He atoms (0.05 – 10 keV center-of-mass energy). They showed that nuclear stopping dominates at low collision energies (below 1 keV) and that a substantial fraction of the total PAH destruction cross section is due to non-statistical atom knockout which agrees with experiments. At higher collision energies, electronic stopping dominates, leading to statistical fragmentation of isolated PAHs.

Fragmentation of cationic pyrene following a collision with energetic protons was extensively studied with DFTB-based molecular dynamics simulations by Simon et al. (2018). The good agreement they found between experimental and theoretical spectra globally validated the SCC-DFTB potential in giving the wide distribution of fragments corresponding to statistical dissociation and validated the assumed scenario for both the internal energy deposited distribution and the fast internal conversion. Using these assumptions, they showed that dissociation occurs within a few hundreds of picoseconds.

Finally, Mandal et al. (2022) developed a computationally affordable method to calculate cross sections and rate coefficients for collisional quenching and excitation of large molecules in space, such as PAHs. The method is successfully applied to benzene to compute cross sections for rotational excitation and quenching by collisions with He in a broad range of energies.

3.3.5 Clustering

The layered structure of PDRs offers some benign environments that can host clusters of carbon molecules (Rapacioli et al. 2011; Andrews et al. 2015) and several studies have addressed the formation and survival of these clusters in the ISM. Because of their size and the small amount of experiments available, different theoretical approaches have been used.

For instance, a microcanonical Phase Space Theory (PST) simulation, based on calculations using the DFTB combined with Configuration Interaction, was used to determine the dissociation energies of pyrene clusters by fitting the experimental breakdown curves (Zamith et al. 2019). Optimized potentials for liquid simulations (OPLS) calculations were used to predict the structures, stability and the formation sequence of PAH homoclusters containing from 2 up to 10 molecules per cluster (Takeuchi 2013). And Rodríguez-Cantano et al. (2015) used a basin-hopping algorithm and path-integral Monte Carlo calculations to investigate how coronene molecules form clusters with rare gas atoms such as He, Ne, Ar and Kr in very cold conditions.

Studies on clusters can also lead to the discovery of unexpected reactions, such as the barrieless formation of carbon chains from ionized clusters of HCN and HCN:HCCH (Stein et al. 2020) or clarify the mid-IR spectroscopy of clusters even when metals such as iron are included (Tarakeshwar et al. 2019).

In the early days of AstroPAH there were also highlighted some works on Boron molecules that are structurally similar to PAHs and fullerenes. These included the first evidence of the B_{40}^- fullerene (Zhai et al. 2014), planar B_{36} and B_{36}^- coronene analogues (Chen et al. 2014b), and boron nanostructures (Piazza et al. 2014).

3.3.6 Hydrogenation and Dehydrogenation

The (photo)chemistry of PAH molecules is closely linked to that of H, both in its atomic and molecular form (see also Sect. 3.3.2 and 5). DFT calculations have been employed to study the abstraction of H and H_2 from neutral, singly and multiply (up to a charge state $q = +9$) ionized coronene molecule (Paris et al. 2014). The study provided bond dissociation energies, reaction barriers, and energies for these processes. The study highlighted the strong charge dependent competition between the different channels. Coronene was also used as a prototype to study the diffusion of H atoms on neutral and charged PAHs by means of DFT and PM6 methods (Sánchez and Ruette 2015).

Binding energies, equilibrium distances, and strength of the long-range attraction were also evaluated for the H_2-coronene complex (Bartolomei et al. 2017). The system was revealed to not be too affected by the relative orientations of the H_2 molecule so its behavior can be approximated to that of a pseudoatom. The energy profiles confirmed the non-covalent nature of the bonding which is used to tune a new force field based on the atom-bond approach which correctly describes the main features of the H_2-coronene interaction.

H diffusion occurs mostly through C – C bonds and happens preferably on the edge sites. The same study also found that charged coronene has stronger adsorption energies than neutral systems. Fluorene is the smallest PAH molecule containing a pentagonal ring with 2 H atoms attached. Désesquelles et al. (2021) used a statistical fragmentation model to understand how the presence of the pentagon affects the dehydrogenation process (up to 3 H-losses) observed in VUV experiments of the fluorene cation. These types of calculations have the power to unveil information that experiments cannot give, such as effects of isomerization on fragmentation, competition between channels and more.

The hydrogenation reaction of several different aromatic molecules (benzene, pyridine, pyrrole, furan, thiophene, silabenzene, and phosphorine) was also investigated with quantum chemical methods, including instanton theory (Miksch et al. 2021). These reactions are all endothermic, but in same case the barrier can be overcome by quantum tunneling. It is then proposed that hydrogenated derivatives of furan and pyrrole, especially 2,3-dihydropyrrole, 2,5-dihydropyrrole, 2,3-dihydrofuran, and 2,5-dihydrofuran are promising candidates for future interstellar detection.

3.3.7 Structures and Physical Parameters

There are different ways in which the stability of PAHs can be studied. Poater et al. (2017) used DFT to look at the effect of non-bonded H...H interaction occurring in bay regions of kinked and armchair PAHs on the general stability of the molecule. DFT was also used to calculate the aromaticity index or Ring Current Strength (RCS), which influences stability, of known astronomically relevant aromatic molecules (Alvarez-Thon et al. 2022). Aromatic molecules with large RCS values have already been observed in space while those with smaller values have not yet been detected which implies that the RCS metric could be used to estimate the astronomical significance of future molecular targets.

Zhang et al. (2015) characterized the properties, including stability, of a new carbon-allotrope, pentagraphene which is composed entirely of carbon pentagons. The enthalpy of

formation and UV/Vis spectra of multiple PAHs have been computed with DFT and made available via the NIST PAH database (Allison and Burgess 2015).

Using high-level *ab initio* calculations to obtain heats of formation of PAHs, Karton and Chan (2021) showed that as the size of a PAH increases, the deviation between *ab initio* results and experiments increases as well. Hence, even high-level *ab initio* methods should only be used cautiously to obtain heats of formation for medium-to-large sized PAHs.

The discovery of ring-containing molecules in the ISM via rotational spectroscopy (see Sect. 7.1) inspired research on other small ring-containing molecules. For example, Simbizi et al. (2022), with high-level methods, computed proton affinities, enthalpy of formation and Gibbs free energy for 2- and 3-cyanofuran and their protonated forms. Also the viability of benzvalyne (C_6H_4) in the ISM, in particular in TMC-1, and its isomerization from o-benzyne was investigated (Poland et al. 2022a,b).

3.4 Modeling

The results on the photophysics and photochemistry of PAHs and hydrocarbons obtained by computational and experimental studies are fundamental ingredients not only to model the evolution of these molecules in regions of star formation and in the ISM of galaxies, but also to clarify the links between the different carbon species, including fullerenes.

Berné et al. (2015b) modeled the formation of C_{60} starting from the large PAH $C_{66}H_{20}$ in the environment of the reflection nebula NGC 7023. The model predicts that 100% of $C_{66}H_{20}$ is converted to C_{60} in 10^5 yrs, which is comparable to the age of the nebula. The model also showed that once C_{60} is formed it can survive much longer than other fullerenes because of its inherent stability. Finally, the model predicted a C_{60} abundance of 10^{-4} with respect to carbon (or less than 1% of PAH abundance), a value that matches well with the one derived by Spitzer observations.

A more sophisticated model, including also hydrogenation of PAHs and fullerenes, was applied to the conditions of two different PDRs, the Orion Bar and, as the study above, NGC 7023 (Murga et al. 2022a). The model showed that fullerenes can be efficiently formed from PAHs in a range of environments going from H-poor to ones with moderate (10^4 cm^{-3}) H densities. However, additional fullerene formation channels should operate to explain the observed amount of this molecule. The model also showed that hydrogenated fullerenes (fulleranes) can be formed, but in low abundances (see discussions in Sects. 2.3.3, 3.1.3, and 10).

Carbonaceous material can also participate in the carbon chemistry in PDRs by providing small hydrocarbons upon fragmentation. Murga et al. (2020) investigated the role of PAH photodissociation in producing smaller hydrocarbons molecules in the Orion bar and the Horsehead nebula as prototypical examples of PDRs irradiated by strong and weaker radiation fields, respectively. Acetylene is considered the main fragmentation product of PAHs in the model. It was found that acetylene production from PAHs may increase the abundances of small hydrocarbons in the Orion bar only at total extinction (A_V) larger than 3.5. In the Horsehead nebula, the contribution of PAH dissociation to hydrocarbon abundances is negligible.

The same authors investigated the link between HAC grains and the presence of small hydrocarbons (C_2H, C_2H_2, C_3H^+, C_3H, C_3H_2, C_4H) in the Orion bar and the Horsehead nebula PDRs (Murga et al. 2022c). They concluded that the contribution of the HAC destruction fragments to the chemistry is not enough to match the observed abundances of small hydrocarbons, although it increases the abundances by several orders of magnitude in the Orion Bar at $A_V = 0.1$. Additionally, they found that the process of carbonaceous

mantle formation on dust surface can inhibit the formation of observed small hydrocarbons in PDRs.

It is well-known that PAHs are a source of photoelectric heating for the neutral gas in the ISM. This have been verified in a range of environments, such as star-forming regions, galaxies, and protoplanetary disks, by Berné et al. (2022a). The authors made use of the recently updated measurements and calculations of PAH data (Zhen et al. 2016a; Wenzel et al. 2020) and, using a simple analytical model, found that the modeled PAH photoelectric heating rates are close to the observed cooling rates given by the observed gas emission in such regions.

The magnetic field present in astronomical environments can physically align the PAH molecules. Hoang (2017) showed that even a moderate degree of alignment can significantly increase the PAH emission polarization degree in comparison to the emission of a randomly oriented PAH population. The simulations also demonstrated that RNe are the most favorable environments to observe polarized PAH emission and to test the alignment of such small particles (see Sect. 11).

4 Dust

The importance of understanding the influence of dust in astronomical objects cannot be overstated. Dust can be produced in a variety of environments. The different physical conditions, compositions, and evolutionary timescales are reflected in the diverse types of dust observed in space. This diversity has been characterized through astronomical observations of dust spectral signatures and through detailed laboratory studies of dust grains (Tielens 2022). Dust grains are an important component of the interstellar and circumstellar matter as they absorb and scatter UV radiation, emit a large part of the absorbed UV radiation in the infrared and heat the gas via collisions and the photoelectric effect. The origin, evolution, composition, and spectral properties of dust are key themes within modern astrophysics and astrochemistry, deserving its own field entitled astromineralogy.

Dust is also an important catalyst for the formation of molecules such as water, molecular hydrogen, and multiple others, which stick to and diffuse upon interstellar dust grains as evidenced by multiple laboratory studies reviewed by Potapov and McCoustra (2021). Theoretical studies and observations also indicates that formation on dust surfaces and dust destruction must be an important route of molecular formation, in particular carbon based molecules, including PAHs, in different spatial environments and thus key for the Universe chemical complexity (e.g., Berné et al. 2015b; Bergin et al. 2016; Aleman et al. 2019; Anderson et al. 2021; Nickerson et al. 2023). Dust is included in this review, and also in AstroPAH, due to its close relation to PAHs and other carbon molecules.

It has been hypothesized that PAHs might be the building blocks for carbonaceous dust particles formed in the ISM, a mechanism of formation which is still not entirely understood (Potapov 2017). Hence, it is important to understand both the dynamics and structures of PAH clusters as well as PAHs clustered along with water molecules and other dust components such as silicates and amorphous (hydrogenated) carbon particulates. Experimental studies relevant to processes on dust grains such as adsorption, desorption, diffusion, and reactions have been recently reviewed (Potapov and McCoustra 2021).

Other carbon allotropes have also been predicted to be important dust components such as nanodiamonds (Chang 2016; Shiryaev et al. 2018b), graphene and carbon nanotubes (Mann et al. 2018; Chen et al. 2018a).

4.1 Observations

4.1.1 Dust and the Life Cycle of Matter and Stars

Dust is an important part of the cycle of matter in galaxies and partakes, in different capacities, in the beginning and the end of stellar evolution. Star formation starts with the gravitational collapse of a gaseous and dusty cloud. At the end of their lives, stars can produce copious amounts of dust grains that are ejected back to the ISM, where the cycle restarts, now with an enriched composition. Several examples of what we can observe and learn from about dust, especially in connection with PAHs during all of these phases, were printed in the pages of AstroPAH which we describe in the following.

The Carina nebula is a large complex of molecular clouds and star formation regions in our Galaxy. ISO observations in the mid- to far-IR were used to study the dust and PAH processing in this object (Onaka et al. 2015). While PAH bands (at 6.2, 7.7, 8.6, and 11.3 μm) are absent in the ionized region, emission are observed in the more neutral environments in the nebula. The observations also indicate that over 70% of the silicon which could be locked in grains is returned to the gas phase, suggesting that silicates cannot survive under the harsh conditions in this cloud. This result and the distinct behavior of the ionized and neutral PAH features indicate that active dust processing is taking place in this cloud.

A Herbig Ae/Be object is a figurative king of star formation. Gravitational contracting is still ongoing (pre-main sequence) and gas and dust still surrounds it, sometimes in the form of an accretion disk (see also Sect. 8.1.4.), where dust grains contribute to planet formation. Spatially extended features related to aromatic and aliphatic hydrocarbons were detected in disks around Herbig stars by (Boutéraon et al. 2019) using spatially resolved spectra obtained with the VLT. The 3.2-3.8 μm range spectrum allowed the authors to identify aromatic, olefinic, and aliphatic bands from sub-nanometer hydrocarbon grains surrounding Herbig Ae/Be stars in radius from 10 to 100 AU and in inner gaps that are devoid of large grains. Given their expected high destruction rates through UV photons, the authors further suggested that they are continuously replenished at the disk surfaces.

Once the pressure and temperature of a collapsing cloud is high enough, hydrogen starts being converted to helium by nuclear reactions and a *bona fide* star is created. Stars with more mass will spend most of their lives in a relatively stable phase called the main sequence, where the hydrogen nuclear reactions balance the gravitational force. Very low-mass stars ($M_\star < 0.08\ M_\odot$) will never ignite the hydrogen nuclear burning into helium and will die as a cool brown dwarf. Once the hydrogen is fully consumed in the star center, the star undergoes several phases of instability and nucleosynthesis of progressively heavier elements that leads to its final demise. What happens in these final chapters will depend mainly on the star's main sequence mass, but it usually involves significant mass-loss and dust formation. Low-mass stars ($0.08\ M_\odot < M_\star < 8\ M_\odot$) will evolve to become red giants and then eject most of its mass in the AGB and PN phases, ending their lives as a compact white dwarf which will cool down until it becomes a black dwarf. High-mass stars ($M_\odot > 8\ M_\odot$) will evolve to become red supergiants, which will end up exploding as a supernova with three possible fates: being totally destroyed, becoming neutron star, or collapsing as a black hole. This a very simplified description of the stellar evolution. The presence of companion stars, for example, can alter these simple scenarios (e.g., a binary system with an accreting white dwarf leading to novae explosions or type 1a supernovae).

As seen in previous sections, IR spectra of carbon-rich stars that have evolved off the AGB reveal a range of dust and molecular features, including fullerenes, PAHs, aliphatic hydrocarbons, and several unidentified features, including the 21 μm emission feature. As

complement to the Galactic objects already mentioned in the previous text, observations of post-AGB stars in the Magellanic Clouds were used to analyze PAH features in environments with lower metallicities than in the Milky Way. For example, (Matsuura et al. 2014) analyzed observations taken with Spitzer of carbon-rich post-AGB stars in the LMC. The study suggested that PAHs are gradually processed while the central stars evolve from the post-AGB phase to PNe, changing their composition before PAHs are incorporated into the ISM. Furthermore, although some metallicity dependence on PAH spectra exists, the evolutionary state of an object is more significant than its metallicity in determining the spectral characteristics of PAHs for LMC and Galactic post-AGB stars.

Sloan et al. (2014), also using Spitzer data of carbon-rich post-AGB objects in the Magellanic Clouds, successfully identified three new fullerene sources but in the process they also called three previous identifications into question. They confirmed that the strong 11 μm features in some sources primarily come from SiC which may exist as a coating around carbonaceous cores as a result of photo-processing.

The AGB carbon/oxygen-rich duality and the evolution to a possible mixed chemistry oxygen-rich in the subsequent phases, makes of interest to PAH researchers also understanding the production and evolution of dust and molecules in oxygen-rich environments. Furthermore, it can also reveal the physical conditions in zones with rich solid phases and helps us interpret the IR spectra of different sources. The relation of mass-loss and silicate crystallinity[22] in nearby oxygen-rich evolved stars was studied by Liu et al. (2017) using ISO data. The absence of correlation supports that stars with low mass-loss rates may not exhibit the characteristic crystalline silicate features in their emission spectra, even if they contain a significant fraction of crystalline silicates.

In the PNe phase the material of the star ejected and synthesized (remembering that dust is produced in the AGB envelopes) in the previous phases is, at least partially, processed by the star fast wind and ionizing radiation. Dust is interrelated to several aspects of the PNe nebular physics and chemistry. Delgado-Inglada and Rodríguez (2014) investigated PNe dust in terms of their iron content and C/O ratios in a sample of 56 PNe observed with Spitzer. Most of the PNe observed have abundance ratios C/O < 1. These objects, with the exception of one, show crystalline silicate features in their IR spectra. Most of the PNe where they observed C-rich dust features (SiC or the 30 μm feature) have C/O $\lesssim 0.8$. PAH features are seen in PNe in the full range of C/O values observed, including a few objects that also show silicates. The authors also inspected the gas phase iron abundances, with results suggesting that more than 90% of their iron can be depleted onto dust grains, but the iron depletion factors still vary by about two orders of magnitude. A weak but significant anti-correlation was found between the iron abundances and the C/O ratios as well. The largest depletion factors are found in C-rich objects, while the objects with the smallest depletion factors are the O-rich.

A born-again nebula is a rare case of PNe that have experienced a thermal pulse after their formation, resulting in a new large ejection of hydrogen-poor stellar material into the surrounding nebula. Sakurai's Object (V4334 Sgr) was the first object of this kind to be identified, but so far, only a few born-again nebulae have been identified. Spitzer spectra (6-14 μm) were used to determine temporal changes in dust features associated with Sakurai's Object (Bowey 2021). This object has been producing dust since its rebirth in 1996. Both SiC grain and PAH emission features were observed to change with time. The work monitored the appearance, growth, and possible disappearance of the 6-7 μm absorption features.

[22]Here, silicate crystallinity refers to the mass fraction of silicate dust in crystalline form in relation to the amorphous form.

The observed features can be well reproduced by a mix of PAHs, 10 to 20 micron-sized melilite and SiC grains, and the evolution of each component was studied. According to the authors, the use of these characteristics was convenient as otherwise these compounds would be undetectable due to their high opacity in the 10 μm Si-O and Si-C stretching bands. This study illustrates well the importance of continued monitoring of mass-loss and other properties in objects of such fast variability as Sakurai's Object.

Another example of born-again object is FG Sge, which has evolved from the hot central star of the young PN Hen 1-5 to a G-K supergiant in the last 100 yr. Signatures of PAH emission that disappeared from Spitzer and VLT (interferometry) observations in an interval of 20 months implied that it originated from an extended region of the optically thick dusty envelope (Ohnaka and Jara Bravo 2022). PAHs likely originated in the material ejected before the central star became H-deficient and were excited by the central star UV radiation escaping through the newly ejected material (suggesting to the authors the presence of gaps among dust clumps and/or a bipolar cavity of a disk-like structure).

CK Vul was proposed to be the oldest 'old nova', as its optical faintness ties in well with the 'hibernation' hypothesis for classical novae, but the true nature of this object is still a mystery. Evans et al. (2016) studied the dust content of this object. The CK Vul mid-IR Spitzer spectrum — which shows a warm dust continuum superimposed with ionic, H_2 and HCN lines, as well as PAH bands — together with literature data, allowed the authors to eliminate some of the previously suggestions for the nature of CK Vul. They excluded the possibility of CK Vul be a classical nova remnant in 'hibernation' after the event of 1670, a 'diffusion-induced' nova, a luminous red variable, and the occurrence of a very late thermal pulse (a born-again scenario).

So far, we focused on the post-main sequence low mass stars. They provide a great contribution to the dust galaxy budged, but so does the evolved high mass stars. Red supergiants are the most common final evolutionary stage of stars that have initial masses between 8 and 35 times that of the Sun. During this stage the stars experience substantial mass loss, but the mechanism for this mass loss is largely unknown. From November 2019 to March 2020, Betelgeuse — the second-closest red supergiant to Earth — experienced a historic dimming of its visible brightness (Montargès et al. 2021). Usually having an apparent magnitude between 0.1 and 1.0, its visual brightness decreased to 1.614 ± 0.008 magnitudes around 7-13 February 2020 — an event referred to as the Betelgeuse Great Dimming. Montargès et al. (2021) reported high-angular-resolution observations showing that the southern hemisphere of Betelgeuse was ten times darker than usual in the visible spectrum during its Great Dimming. Observations and modeling support a scenario in which a dust clump formed recently in the vicinity of the star, owing to a local temperature decrease in a cool patch that appeared on the photosphere. The directly imaged brightness variations of Betelgeuse evolved on a timescale of weeks. The findings of Montargès et al. (2021) suggested that a component of mass loss from red supergiants is inhomogeneous, linked to a very contrasted and rapidly changing photosphere.

Observations of absorption features toward bright sources reveals properties of the material present in the line of sight. Spectral observations were taken of the OH/IR supergiant 2MASS J17470898–2829561 (2M1747) covering key portions of the 2–5 μm wavelength interval (Geballe et al. 2021). The supergiant is located in the direction of the Sagittarius (Sgr) B molecular cloud complex that is within the central molecular zone of the Galaxy. Analysis of the spectra revealed that it is deeply embedded within Sgr B1 making it the only star within Sgr B for which IR spectra have been obtained so far. Thus, a unique probe of the dense ISM within the central molecular zone has been uncovered. Its 3.5–4.0 μm spectrum contains the strongest absorption lines of H_3^+ observed toward any object to date (Geballe et al. 2021).

Similarly, Spitzer spectra of five early-type (one O- and four B-type) stars were also compared with that of unreddened stars[23] of the same spectral type to estimate the interstellar extinction of silicate dust around 9.7 μm in the line of sight (Shao et al. 2018). The work resulted in an analytical formula that parametrizes the interstellar extinction in the IR in the 0.9–15 μm range.

ISO data and Spitzer data were used to analyze Cyg OB2 12, a luminous blue hypergiant star, to study interstellar dust on account of its large extinction and the fact that this extinction appears to be dominated by dust typical of the diffuse ISM (Hensley and Draine 2020). In addition to the prominent 9.7 and 18 μm silicate features, they robustly detected absorption features associated with PAHs, including the first identification of the 7.7 μm feature in absorption. The 3.3 μm aromatic feature was found to be much broader in absorption than is typically seen in emission and the 3.4 and 6.85 μm aliphatic hydrocarbon features were observed with relative strengths that are consistent with observations of these features on sight lines toward the Galactic center. Hensley and Draine (2020) identified and characterized more than 60 spectral lines in this wavelength range which may be useful in constraining models of the star and its stellar wind. Based on this analysis they presented an extinction curve that extrapolates smoothly to determinations of the mean Galactic extinction curve at shorter wavelengths, and to dust opacities inferred from emission at longer wavelengths, providing a new constraint on models of interstellar dust in the mid-IR.

The mid and far-IR spectra of the luminous blue variable (LBV) star R71, one of the most luminous stars in the LMC, clearly shows the presence of both silicates and PAHs indicates that dust has very mixed chemistry, as shown by (Guha Niyogi et al. 2014). The authors derived a mass-loss rate for this object around $10^{-5} M_{\odot}$ yr^{-1}, which is comparable to the values found for five other similar sources in the LMC. This value indicates that these few objects contribute to the mass budget of the ISM as all the AGB stars in the LMC.

Mid-IR spectra of five colliding-wind, massive, dust-producing Population I Wolf-Rayet (WR) binaries were investigated with ISO data (Marchenko and Moffat 2017). The WR binaries showed a wealth of absorption and emission details coming from the circumstellar dust envelopes, as well as from the ISM. It was suggested that the prominent absorption features arise from a mix of interstellar carbonaceous grains formed in high- and low-temperature environments while the broad emission complexes around 6.5, 8.0 and 8.8 μm could arise from ionized, small PAH clusters and/or amorphous carbonaceous grains. As such, these PAH emissions may represent the long sought-after precursors of amorphous carbon dust. Marchenko and Moffat (2017) also detected a strong 10 μm emission in the spectra of WR48a and WR112 which were tentatively linked to ionized PAHs and upon examining the available archival spectra of prodigious individual WR dust sources, a surprising lack of a 7.7 μm PAH band in the spectrum of the binary WR19 was observed, in contrast to the apparent strength of the 11.2, 12.7 and 16.4 μm PAH features. Strong PAH emissions were also detected beyond 10 μm in the spectrum of another dust-producing system, WR118, potentially pointing to the presence of large, neutral, presumably interstellar PAH molecules toward WR19 and WR118.

Dust can be produced in a wide variety of environments, but it is recognized that energetic supernovae and novae are considered one of the main sources of dust in space (together with AGB stars and ISM dense clouds). Observations of local supernovae over the past couple of decades have detected the presence of dust in supernovae ejecta and the reddening of high redshift quasars also indicates the presence of large dust masses in early galaxies (Sarangi et al. 2018). Newly formed dust initially resides in a cavity, which is crossed by a high

[23] Stars that are not subject to interstellar extinction.

velocity reverse shock generated by the pressure of the circumstellar material shocked by the initial supernova blast, so depending on the grain composition and initial size, processing by the reverse shock may lead to substantial dust erosion and even complete destruction (Micelotta et al. 2018). It is also worth noting that recently, maps built from Herschel and Spitzer images did not find conclusive evidence that supernova remnants (SNRs) destroyed swept-up dust (Matsuura et al. 2022).

4.1.2 Dust on Galactic Scales

PAH and dust emission toward the Galactic bulge were analyzed using Spitzer data by Shannon et al. (2018). Dust and PAH emissions are exceptionally similar in two regions as they reside on or near boundaries of a 7 Myr old Galactic outflow event and are partly shock-heated. It is likely that a transition zone of the outflow into the nascent environment is being traced where PAH abundances are slightly depressed relative to typical ISM values. Little variability in the PAH properties is found indicating that a stable population of PAHs dominates the overall spectral appearance; exceptionally similar to that of the M82 superwind, emphasizing that a local Galactic environment is being probed.

Spitzer data was also used to detect nanometer-sized dust grains that appear to be universally present in a wide variety of astronomical environments from Galactic high-latitude clouds to nearby star-forming galaxies and galaxies with low levels of nuclear activity (Xie et al. 2018b). The prevalence of such a grain population was revealed conclusively as prominent mid-IR continuum emission below 10 μm characterized by temperatures of 300-400 K that are significantly higher than the equilibrium temperatures of common, submicron-size grains in typical galactic environments. Xie et al. (2018b) suggested that the optimal carriers of this pervasive, featureless hot dust component are very small carbonaceous (e.g., graphite) grains of nanometer size that are transiently heated by single-photon absorption.

Previously, the same authors had studied the dust properties of 147 AGNs of various types paying special attention to the 93 AGNs that exhibit the 9.7 and 18 μm silicate emission features using Spitzer data (Xie et al. 2017). They found that 60/93 of the observed spectra can be well explained with "astronomical silicate" while the remaining sources favor amorphous olivine or pyroxene. Most notably, all sources require the dust to be micron-sized, much larger than the submicron-sized Galactic interstellar grains, implying a flat or "gray" extinction law for AGNs. AGNs are themselves explored further in Sect. 6.

Among the parameters that directly probe dust content is the metallicity which directly impacts the physics and chemistry of the constituent stars and the ISM of galaxies as different metallicities might result in different compositions of dust and molecules; changing the spectra of stars and the ISM as well as those of the integrated light of galaxies.

Data from Herschel, Spitzer and GALEX[24] were used in a detailed photometric study of star-forming regions in the galaxy Holmberg II to estimate both ages and metallicities (Wiebe et al. 2014). The fluxes at 8 μm and 24 μm characterizing the emission from PAHs and hot dust grains decrease with age, but their ratio increases implying that the relative contribution from PAHs to the total IR flux increases with age, i.e., the relative PAH fraction increases due to the destruction of larger grains.

Deep Herschel far-IR observations of the edge-on disc galaxy NGC 3079 revealed a dusty ring whose cool material directly interacts with the nuclear ionized and relativistic outflows that are traced by the Hα, X-ray and radio emission (Veilleux et al. 2021). The far-IR data trace the complex interplay of the cool gas/dust with the warm/hot ionized and

[24]Galaxy Evolution Explorer.

relativistic phases of the large-scale outflow detected at other wavelengths. The velocities of the cool gas entrained in the inner hot/relativistic outflow are modest relative to the escape velocity of the host. Eventually, the cool gas will be deposited in the halo of the galaxy and contribute to building up the gas, dust, and metal contents of the inner circumgalactic medium. A transition from neutral to ionized phases can occur due to AGN photoionization and/or shocks as the gas propagates outward into the halo. Without a sustained source of energy from the AGN or nuclear starburst, however, the material in the bicone will cool down and rain back on to the galaxy disc, closing the loop of a large-scale galactic fountain.

Finally, data from Herschel, Spitzer, and AKARI was used to combine mid-IR observations of PAHs with C II, O I and Si II fine-structure emission, i.e., the dominant heating mechanism and the strongest cooling channels in dense neutral gas (McKinney et al. 2021). The ratio of IR cooling line emission to PAH emission measures the photoelectric efficiency which dictates how much energy carried by UV photons gets transferred into the gas, e.g., see discussion on the work of Berné et al. (2022a) in Sect. 3.4. McKinney et al. (2021) found that IR-luminous galaxies with high IR surface densities have low photoelectric efficiencies which supports a scenario in which the most compact galaxies have more young star-forming regions per unit area that exhibit less efficient gas heating. These conditions may be more common at high redshift and may help explain the higher star formation rates at cosmic noon.

4.2 Experiments and Theory

Multiple types of experiments and theoretical works relating to dust have been developed and carried out in the past decade. Here we present an overview of the different works that involve dust processing, dust formation, the optical properties of dust, PAHs in ices, PAH formation on dust and in ices, and the roles PAHs can play in catalysis.

4.2.1 Dust Processing - UV/Electron/Ion Bombardment

Employing many similar techniques as described in Sects. 2.2 and 3.2, dust processing has also been studied in terms of UV-, electron-, and ion-bombardment.

Experiments have shown that HAC deposits are relatively stable under UV photon and electron bombardment (Maté et al. 2014). The decays in the IR intensity of the HAC samples were observed for comparatively high fluences (*ca.* 10^{19} cm^{-2}) and UV photons were found to induce a certain dehydrogenation of the hydrocarbon structure, probably leading to an increasing chain length. 2 keV bombardment by electrons was however less effective for depletion.

Maté et al. (2016) also studied the effects of cosmic-ray bombardment — simulated as 5 keV electrons — on carbonaceous dust that has been proposed to be the carrier of the 3.4 μm band. This band is widely observed in the diffuse ISM but disappears in dense clouds. The decay of the band is attributed to CH bond breaking and recombination of H atoms to form H_2. The estimated cosmic-ray destruction rate for the 3.4 μm band carriers lies in the 10^8 yr range which cannot account for the disappearance of this band in dense clouds which have characteristic lifetimes of 3×10^7 yr.

Nanodiamonds have been investigated as well with bombardment of Xe ions (Shiryaev et al. 2018a). A pronounced size effect of the radiation resistance of the nanodiamonds was observed. Particles larger than 8 nm behave similarly to macroscopic diamonds, and smaller particles can be completely destroyed by a single impact from an ion. These results are not limited to nanodiamonds, but can help place constraints on the survival of dust in astrophysical environments.

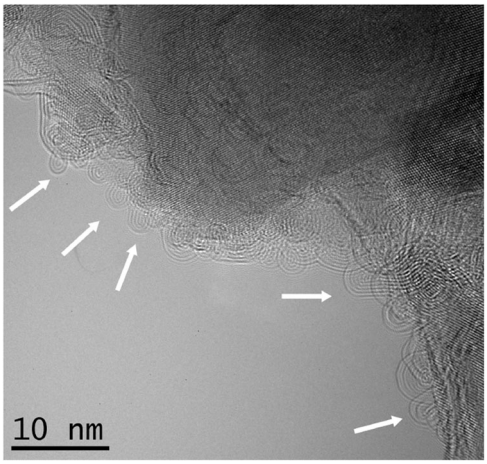

Fig. 8 High-resolution TEM image of SiC grains heated at 1050 °C. The surface is coated with MWCNTs as indicated by white arrows. Adapted with permission from Bernal et al. (2022). Copyright 2022 American Chemical Society

Laboratory experiments with analog crystalline silicon carbide (SiC) grains using transmission electron microscopy (TEM) and electron energy-loss spectroscopy (EELS) were performed using the 3C polytype of SiC — the type commonly produced in the envelopes of AGB stars (Bernal et al. 2019). By rapidly heating small (∼50 nm) synthetic SiC crystals under vacuum to *ca.* 1300 K and bombarding them with 150 keV Xe ions, TEM imaging and EELS spectroscopic mapping showed that silicon was leached from the SiC surface, creating layered graphitic sheets. The six-membered rings, characteristic of graphite, appeared to be distorted due to surface defects in the crystals, creating hemispherical structures with diameters matching that of C_{60}. Such nonplanar features require the formation of five-membered rings. Bernal et al. (2019) also identified a circumstellar grain, preserved inside the Murchison meteorite, that contains the remnant of an SiC core almost fully encased by graphite, contradicting long-standing thermodynamic predictions of material condensation. The combined laboratory data suggest that C_{60} can undergo facile formation from shock heating and ion bombardment of circumstellar SiC grains. Such heating/bombardment could occur in the PPNe phase, accounting for the observation of C_{60} in these objects, in PNe and other interstellar sources receiving PN ejecta. The synthesis of C_{60} in astronomical sources poses challenges, as the assembly of sixty pure carbon atoms in an H-rich environment is difficult. A viable mechanism could be the formation of C_{60} from the surface decomposition of SiC grains. This could readily occur in the heterogeneous, hydrogen-dominated gas of evolved circumstellar shells.

Bernal et al. (2022) also used the same technique to investigate the formation of fullerenes and carbon nanotubes. Their experimental findings revealed that heating the analog SiC grains to the point of decomposition initially yields hemispherical C_{60}-sized nanostructures, with five- and six-membered rings which transform into multiwalled carbon nanotubes (MWCNTs; Fig. 8) if held isothermally for longer than 2 min. These MWCNTs are larger, both in overall size and number of C atoms, than any of the fullerene species currently observed in the ISM. These experimental simulations suggest that such MWCNTs are likely to form in post-AGB circumstellar material, where the structures, along with the smaller fullerenes, are subsequently injected into the ISM.

4.2.2 Dust Formation

PAHs make excellent candidates as dust grain precursors as they are known to form ordered films when deposited on surfaces under ultrahigh vacuum conditions (Salomon et al. 2021).

Low-temperature condensation of carbonaceous materials was investigated where carbonaceous precursors were created by laser ablation of graphite and accreted on cold substrates (Fulvio et al. 2017). The condensation process is governed by carbon chains that first condense into small carbon clusters and eventually into more stable carbonaceous materials. Fullerene-like carbonaceous samples are also transformed into a more ordered material under VUV processing. The cold condensation mechanisms were discussed in relation to the balance between the cosmic timescales for dust injection, destruction, and reformation in the ISM.

Many novel experiments have been performed with the AROMA setup (introduced in Sects. 3.2.5 and also in 9.2) that combines laser desorption/ionization techniques with ion trap mass spectrometry (Sabbah et al. 2017).

To address the question of how metal is incorporated into dust for an environment rich in elements involved in stardust formation (C, H, O, and Si), silver atoms were injected into a plasma reactor containing organosilicon (Bérard et al. 2021). It is suggested that molecular Ag-C seeds promote the formation of Ag clusters and also catalyze hydrocarbon growth.

Molecules constituting nascent soot particles formed from ethylene/air samples were also analyzed with AROMA (Sabbah et al. 2021). Here, just-nucleated soot was found to be rich in PAHs with various sizes: mainly medium sizes containing 18–40 carbon atoms but some as large as 90 carbon atoms.

To mimic the bottom-up dust formation process in a laboratory, an ultra-high vacuum machine combining atomic gas aggregation with advanced *in situ* characterization techniques was built called "Stardust" (Martínez et al. 2020). They have shown that in an environment similar to evolved stars, carbonaceous dust analogues were formed in a hydrogen atmosphere from low-pressure gas-phase condensation of carbon atoms, and they led to the formation of amorphous carbon nanograins and aliphatic carbon clusters.

Around carbon-rich AGB stars, where interstellar dust is formed, carbon, diatomic carbon and acetylene are the most abundant species after H_2 and CO. As a follow-up work, Santoro et al. (2020) studied the chemistry of carbon with acetylene in the Stardust machine. Linear polyacetylenic chains, benzene and PAHs were shown to form as well as a nonnegligible amount of pure and hydrogenated carbon clusters and aromatics with aliphatic substitutions. All these species were incorporated into the nanometer-sized dust analogs.

Another instrument was constructed to study interstellar dust, namely the NASA Ames COsmic SImulation Chamber (COSmIC) (Contreras and Salama 2013), and it produced its first results on low-temperature solid-phase *ex situ* analysis of cosmic grain analogs (Sciamma-O'Brien and Salama 2020). In the experiment, small hydrocarbon precursors, methane and acetylene seeded in an Ar supersonic jet expansion were submitted to a discharge. The plasma-induced reactions produce larger and larger molecules, eventually solid particles that are collected *in situ*. Scanning electron microscopy (SEM) imaging was used to provide insight on the morphology and growth structure of the grains produced and to investigate how the precursors used to produce the grains affect these parameters.

Other experiments involve the simulation of carbonaceous dust with the inclusion of nitrogen in the form of quenched nitrogen-included carbonaceous composite (QNCC) (Endo et al. 2021). The dust was produced by quenched condensation of plasma gas generated from the nitrogen gas, and aromatic, and/or aliphatic hydrocarbon solids by applying a microwave (MW) discharge. The spectra of the generated dust bore close resemblance to the observed

IR spectra of novae and it was suggested that the inclusion of nitrogen plays an important role in the origin of the broad 8 μm feature detected in dusty novae.

Similarly, experimental results of band strengths of the C – D stretching modes relative to the C – H stretching modes were reported where a laboratory analog of interstellar carbonaceous dust, quenched carbonaceous composite (QCC), and synthesized deuterated QCC by replacing the QCC starting gas of CH_4 with mixtures of CH_4 and CD_4 with various ratios, were investigated (Mori et al. 2022). Relative strengths of aromatic and aliphatic C – D to C – H stretches were 0.56 and 0.38 per D/H, respectively. The results did not significantly deviate from the D/H ratios in interstellar PAHs that have been estimated previously.

4.2.3 Optical Properties of Dust

Laboratory analogs to interstellar carbonaceous dust characterized by their wide degree of hydrogenation and differences in polyaromatic structure were produced and analyzed (Gavilan et al. 2017). These were measured in the 120–210 nm range at the DISCO[25] beamline at the SOLEIL synchrotron, and also in the mid-IR (3–15 μm) in combination with 210 nm – 1 μm measurements. Optical gaps were derived from the visible spectra and a correlation between the optical gap and the positions of the π-π* electronic transitions was found. The results suggested that carriers of the UV bump should exhibit IR bands akin to the A/B classes of the aromatic IR bands while the circumstellar bump carriers should exhibit bands corresponding to the B/C classes (see Sect. 2).

Chou et al. (2020) also studied the photoabsorption of a graphene monolayer on a LiF substrate between 105 and 350 nm. They found an excitonic band near 130 nm and that the absorbance of the sample at 10 K was found to be 10% larger than that at 300 K. Upon far-UV excitation, the photoluminescence of the sample showed a broad band at 630 nm at 300 K and two adjacent bands at 560 and 634 nm at 10 K. The graphene monolayer exhibited photoluminescence similar to the ERE implying that graphene materials are promising candidates for the ERE carriers (see Sect. 2.1.3).

4.2.4 PAHs in Ices: Experiments and Theory

Within dense molecular clouds, volatile molecules freeze onto the low temperature (10 to 50 K) dust particles forming ice mantles around the dust grains. It is expected that PAH molecules will take part in this process and become embedded in the ice mantles. The apparent absence of PAH IR emission features from within molecular clouds is consistent with PAHs embedded in interstellar ices and hence, a wealth of studies of PAHs embedded in ice matrices have been carried out.

Two prototypical PAHs (pyrene and coronene), mixed in water ice showed that their abundance affects their ionization efficiency as well as their resulting spectra (Cuylle et al. 2014). The spectra of neutral and cationic PAHs have a tendency to broaden if the PAH:H_2O ratio is increased, probably due to clustering.

Hardegree-Ullman et al. (2014), on the other hand, measured the IR spectra of pyrene embedded in water ice. This was the first laboratory determination of the band strength of C – H stretching mode which was obtained near 3.25 μm in this system. Absolute IR band strengths for pyrene in both H_2O and D_2O were determined between 3-15 μm. Hardegree-Ullman et al. (2014) compared their results to spectra of YSOs to look for evidence of PAH

[25] Dichroism, Imaging, mass Spectrometry for Chemistry and biOlogy.

absorption at 3.25 μm and based on this comparison, neutral PAHs were estimated to account for 2-9% of the non-H_2O ice absorption from 5 to 8 μm.

Freidzon et al. (2014) used (TD-)DFT to study the vibrational and electronic spectrum of gas-phase pyrene and pyrene in a water ice matrix. They found that while the fluorescence spectrum of gas-phase pyrene cannot be reproduced by using Franck-Condon or Herzberg-Teller approximations, the vibronic profile of the absorption spectrum of pyrene in water are well reproduced within the Franck-Condon approximation. The calculations also reveal that bands become broader because of the translation and torque of pyrene in the solvent cage.

IR spectroscopy studies of UV irradiated water-rich ice analogs including anthracene, pyrene and benzo[ghi]perylene have been presented as well (Cook et al. 2015). Aromatic alcohols and ketones were identified as products and based on these findings it is expected that interstellar ices should contain neutral and ionized PAHs, alcohols, ketones and quinones at the 2-4% level relative to H_2O.

The interactions between coronene and water were also studied in an Ar matrix with FTIR spectroscopy and theoretical calculations by Simon et al. (2017a). They showed that in the solid phase, coronene:water$_n$ ($n \leq 6$) σ-type complexes, i.e., with water molecules coordinated on the edge of coronene, are formed, whereas in the gas phase, π-interactions are preferred.

In a follow up study, the photochemistry of the coronene:water complexes was studied with FTIR spectroscopy for low numbers of water molecules (Noble et al. 2017). In the experiment, coronene readily reacted with water upon irradiation with a mercury vapor lamp and produced oxygenated PAH photoproducts through a transfer Rydberg state mechanism. This could be indicative of oxygenated PAHs being widely abundant in the ISM.

The photochemistry of coronene irradiated in H_2O ices was further studied at different concentrations (de Barros et al. 2017). In addition to the coronene cation, hydroxy-, keto-, and protonated coronene were formed. The rate constant for the decay of neutral coronene and the formation of the byproducts was determined and it was suggested that oxygenated and hydrogenated coronene products could be present in UV-irradiated regions of the ISM where water-rich ices are important.

Oxygenated PAHs have themselves been irradiated in a water ice matrix by Potenti et al. (2018). They reported the photochemical behavior of 1-naphthol (1-HN), 1,6- and 1,8-dihydroxynaphthalene (DHN) either as pure powdered solids or adsorbed on forsterite or anatase surfaces. An extensive decrease of the main vibrational bands was observed for all the compounds and in the case of DHNs, new molecular species were formed. Irradiation of 1,8-DHN at 80 K resulted in the IR-detectable generation of CO_2 (2340 cm^{-1}), a process reported by other authors following irradiation of PAHs in water ice analogues at 14 K. These results indicated a high susceptibility of hydroxylated naphthalene derivatives to UV radiation leading to free radical and carbonyl-containing extended quinone intermediates with partial degradation and decarboxylation. In view of these results, the formation and photoprocessing of oxygenated PAHs on minerals could be a plausible pathway for PAHs to transform under astrochemical conditions to molecules of prebiotic relevance.

Electronic spectra of triphenylene and its cation were also recorded in a H_2O ice and solid Ar at 12 K (Kofman et al. 2017), but triphenylene is among the PAHs that have been detected mass spectrometrically in meteorites. Comparison was made to astronomical spectra near 400 nm which contain broad interstellar absorption features consistent with the predictions from the laboratory matrix spectra.

Molecular dynamics simulations were used to investigate the binding of PAHs to water ice surface (Michoulier et al. 2018b). This work represents a complete description of PAH-ice interactions in the ground electronic state and at low temperature, providing the

binding energies and barrier heights necessary for astrochemical models. Indeed, based on the adsorption energies calculated, a function is derived to predict the adsorption energy of any PAH on a given ice surface as a function of the number of C and H atoms. In a follow up study, the same authors investigated the lowest energy structure of a PAH in H_2O_n (n = 1-6, 13) matrices and the vertical ionization potential of a PAH adsorbed on water ice using DFTB (Michoulier et al. 2018a). Among their findings, there is a clear deviation of vertical ionization potential of up to 1.4 eV when the PAHs were absorbed on ice.

This led to further investigations of this significant lowering of the ionization energy of PAHs in H_2O ice matrices (Lignell et al. 2021). In this work, experiments showed that charge-mediated nucleation processes can now be understood in that impurities trapped in ice can efficiently be ionized, leading to charged ice particles even in low-energy photon environments. Previously where benzene: H_2O ices were exposed to UV and IR, showed that at the interfaces of the molecules, the electronically excited states of benzene were red-shifted (Dawes et al. 2018).

DFT calculations were also used in attempt to explain another puzzling behavior observed in experiments, i.e., the formation of PAH cations from UV irradiation of water-embedded PAHs while PAHs in ammonia lead to the formation of radical anions (ten Brinck et al. 2022). When interacting with PAHs, the lone pair-type highest occupied molecular orbital (HOMO) of water has poor orbital overlap and is too low in energy to mix with the filled π-orbitals of the PAH. As the lone-pair HOMO of ammonia is significantly higher in energy and has better overlap with filled π-orbitals of the PAH, the subsequent Pauli repulsion leads to mixed molecular orbitals with both PAH and ammonia character.

Isoviolanthrene was studied as well in both Ar and H_2O matrices where it was irradiated with different energy sources like UV photons, soft electron, protons and He^+ particles (Cruz-Diaz et al. 2019). Anions, cations, hydrogen- and oxygen-rich photoproducts were produced and observed, in line with previous findings.

Coronene and isoviolanthrene in H_2O were further studied under proton and electron bombardment and UV-irradiation (Mattioda et al. 2020a). Proton irradiation products appear to contain more oxygen-related species but electron irradiation generates more abundant, larger mass organic species. These results demonstrate the power of top-down synthesis of solar system COMs via irradiative processing of PAHs. The same group also studied the IR spectroscopy of anthracoronene embedded in H_2O (Korsmeyer et al. 2022).

The contribution of neutral PAHs and hydrogenated PAHs in H_2O ices to the 3 μm and 5-8 μm regions of the IR absorption spectrum of the YSO Mon R2 IRS 3 and the Taurus cloud were assessed (Chiar et al. 2021). Fractional contributions are in the area of a few percent. Using the best match (coronene in H_2O), it was estimated that neutral PAHs contribute up to 12.0% of the cosmic 3.47 μm absorption and very little to the 5 to 8 μm region. For neutral hydrogenated PAHs it is estimated that they contribute up to 0.6% of the cosmic carbon budget for Mon R2 IRS 3 and less than 1% for Elias 16, a highly reddened star in the Taurus Dark Cloud.

The corannulene:water complex has also been studied with a combination of theory and experiments to study the influence of the H_2O matrix on the photoreactivity of corannulene (Leboucher et al. 2022). Complexes with 2 and 3 H_2O molecules are energetically favored and in the case of the water trimer, where the water cluster is trapped "inside" the corannulene bowl, it may account for the difference in photoreactivity of non-planar compared to planar PAHs with water. Indeed, planar PAHs such as pyrene and coronene embedded in H_2O:Ar matrices react with water to form alcohols and quinones under low energy UV irradiation, whereas no photoreactivity was observed for corannulene under the same experimental conditions. This work compares well with the microwave spectroscopic work of

Pérez et al. (2017) who studied the structural properties of the corannulene:water complex with MW spectroscopy (Sect. 7.2).

The desorption of benzene from compact amorphous solid water and crystalline ice surfaces was investigated during irradiation of ultrathin solid films with low energy (250-300 eV) electrons (Marchione et al. 2016). Typically, two desorption components were observed with particularly large cross sections. There is a fast component attributed to desorption of isolated benzene molecules that are hydrogen bonded to small clusters of water molecules on the solid water surface, and there is a slow component attributed to desorption from larger islands of benzene molecules on the solid water surface. Adsorption of PAHs on a surface of amorphous solid water was also shown to perturb the "dangling" OH ice spectral feature where a redshift increasing with PAH size up to around 85 cm^{-1} is observed (Michoulier et al. 2020).

Leboucher et al. (2023) performed global explorations of the potential energy surface of neutral clusters made of two pyrene units solvated by water molecules, $(Pyrene)_2(H_2O)_n$ (n = 1-10). They showed that water clusters interacting with the pyrene dimer have larger cohesion energy than the pure water cluster of the same size and this energy increases as a function of the cluster size (n) until it reaches an asymptotic limit, close to that of pure water clusters. Ionization potential calculations show that in these systems the charge is mostly located on pyrene molecules.

The influence of water clusters' organization and size on the electronic spectrum of benzene was investigated with TD-DFT (Ben Amor et al. 2021). It was found that the position and energy of the strong $\pi \rightarrow \pi^*$ transitions were mostly unaffected, but when the size of the cluster increased, more weak transitions at both lower and higher energy than the intense transition were detected. Benzene was also used as a proxy for PAHs to evaluate how the anharmonicity of its vibrational spectrum is affected when adsorbed on an ordered water surface (Clark and Benoit 2021).

The influence of ice structure on reactivity under soft UV irradiation conditions was also investigated by Noble et al. (2020). They showed that the production of oxygenated PAHs is efficient only in amorphous water ice, while fragmentation can occur in both amorphous and crystalline ices. Reactivity is driven by PAH–water interactions in favorable geometries, notably where dangling bonds are available at the surface of pores.

Benzene and naphthalene molecules in amorphous solid water have also been shown to react with non-energetic H atoms (Tsuge et al. 2022). A portion of these molecules could thus be fully hydrogenated in astrophysical environments which ties in with the superhydrogenation of PAHs described in Sect. 5.

Finally, the IR spectrum of the 1H-phenalenyl radical isolated in Ar and Xe matrices was studied (Schneiker et al. 2020). Annealing the matrices revealed that the phenalenyl radicals can recombine with the H atoms at low temperatures so the H abstraction of 1H-phenalene could be observed from spectral changes between 40 and 50 K.

4.2.5 PAH Formation on Dust and in Ices

On top of dust processing and dust formation, dust can also play a key role in the synthesis of PAHs in interstellar environments. The work by Bernal et al. (2019, 2022) has already been showcased which showed the facile formation of fullerenes and carbon nanotubes through the processing of SiC dust grains, but SiC has been found to have other catalyzing qualities.

Merino et al. (2014) presented a top-down route to form PAHs through graphene etching[26] on the surface of SiC dust grains in the ISM. These were studied in a laboratory setting that simulated the environment in a circumstellar envelope. The aromatic species formed on the graphitized surface of the silicon carbide stardust were found to be large, and the mechanism proposed by Merino et al. (2014) includes several factors promoting a self-stopping of the etching of graphene into PAHs. DFT calculations have shown that the efficiency of the process is strongly dependent on the underlying interface and graphene etching is found to be efficient because it is supported on a SiC grain. Once the PAH is decoupled from the SiC, however, etching is no longer an efficient mechanism.

Acetylene on a solid SiC grain surface has also been shown to lead to the formation of PAHs (Zhao et al. 2016). The activation of acetylene correlates closely with the dangling bonds on the SiC surface, which interact with and break the C–C π bond. Acetylene addition to the resulting radical site results in the formation of a surface ring structure which can desorb from the surface.

Other potentially catalytic surfaces involve forsterite. Li et al. (2018) showed that catalytic conversion of methanol along with other organic intermediates on a forsterite surface leads to a variety of products that included PAHs like naphthalene, anthracene, and pyrene.

PAH precursors can also be frozen on surfaces and processed to form PAHs. This has been successfully shown through the irradiation of propargylalcohol ice which mostly yields benzene as a product via propargyl recombination (Sivaraman et al. 2014). Solid acetylene has also been irradiated by 5 keV energetic electrons resulted in formation of species like benzene, naphthalene and phenanthrene (Abplanalp et al. 2019) and solid acetylene has been photolyzed as well by low energy UV photons where it was shown that benzene and PAHs easily synthesize via excited state photochemistry (Kleimeier et al. 2022). Benzene ices have been irradiated at 4 K with 9 eV UV photons and then warmed up to room temperature which resulted in the formation of crystals of various shapes and sizes (Rahul et al. 2020). The authors suggested that such geometrically shaped dust particles might be a key component of interstellar dust.

Frozen PAH precursors have also been processed with X–rays while frozen in inert noble gas matrices. In this regard, frozen acetylene irradiated with X-rays showed the formation of benzene (Lukianova and Feldman 2021) and isolated styrene-acetylene complexes irradiated with X-rays were observed to form naphthalene radical cations (Lukianova and Feldman 2022).

Pressed-pellet samples of PAHs have been studied as well but via laser desorption mass spectrometry experiments. Covalently bonded dimers (e.g. dicoronylene from coronene) were conclusively identified as final products (Webster et al. 2022).

4.2.6 Theoretical Studies of Dust Grain Analogs

Molpeceres et al. (2017) performed DFT calculations to obtain the IR spectrum of interstellar hydrocarbon dust analogs, based on two proposed models in the literature, (i) small aromatic units linked by aliphatic chains and, (ii) polyaromatic cores with hydrogen atoms and methyl groups at the edges. The calculated spectra are in reasonable agreement with those of samples of HAC generated in the laboratory. This work shows that evaluation of hydrogen vs graphitic content on interstellar dust based on decomposition of IR features is often unreliable due to mode mixing. The comparison of the IR spectra with observation

[26] In nanotechnology, etching refers to a solid surface being processed to fabricate particular structures, such as p-n junctions in semiconductors.

suggests that the average type of carbonaceous dust in the ISM is likely representative of the two models considered, with a small preference toward the more aliphatic-rich structure.

Atomistic simulations can be used to characterize the adsorption of organic molecules on carbon nanoparticles. Qi et al. (2018) found that aromatic organics adsorb more readily than aliphatic ones, forming a monolayer over the nanoparticle surface before stacking up in aggregates. This study suggested that onion-like carbon nanostructures in the ISM can have a layer-by-layer formation process. This is also briefly addressed at the end of Sect. 2.3.3.

Improvements on the parameterization of the atomic polarizabilities for all the atomic species have allowed for a more precise evaluation of the UV-visible cross section for curved carbon structure, like that of fullerene (Rérat et al. 2022), but the grounds and applications of polarizability to the astrochemical studies on carbon-based compounds, including PAHs and fullerenes have been recently reviewed by Sabirov et al. (2022). More accurate values of binding energies for straight-chain and branched-chain alkyl cyanides on water ice have also been computed by (Srivastav et al. 2022) who found that the new values for the binding energies can lead to dramatic changes in the abundance of the branched form.

Our understanding of silicate dust also improved. DFT was used to investigate the reactivity of hydroxylated pyroxene nanoclusters $(Mg_4Si_4O_{12})(H_2O)_n$ (n = 1-4) toward hydrogen physisorption, chemisorption and H_2 formation (Kerkeni et al. 2017). Higher level of hydroxylation leads to significant reduction in the energy range for the physisorption and chemisorption of single H atoms in comparison with bare silicate grains and bare bulk silicate surfaces. The subsequent chemisorption of a second H atom is however little affected and barrierless. All recombination paths leading to H_2 formation are exothermic and could lead to formation of vibrationally excited H_2.

Finally, ground state candidate structures and binding energy for Mg-rich olivine clusters $(Mg_2SiO_4)_n$ (n = 2-13) where derived using computational chemistry and then used to evaluate the nucleation rates for these structures in stellar outflows of core-collapse supernovae (Mauney and Lazzati 2018). The study found that a the formation of silicate dust in these stellar environments is slower than previously assumed.

4.2.7 Catalysis Involving PAHs as Surfaces or Adsorbed Compounds

PAHs, alongside dust grains, can act as catalytic surfaces in the ISM. Coupled-Cluster calculations are frequently used to assess the role of PAHs in the formation of molecules containing noble gas atoms (Filipek and Fortenberry 2016). For instance, $ArCCH^+$, $ArOH^+$, $ArNH^+$, and $NeCCH^+$ are stable minima on the potential energy surface and they can form either in gas-phase reaction or through adsorption on PAHs. The spectroscopic features of these molecules were later computed as well (Novak and Fortenberry 2017).

Small PAHs with an imperfect aromatic system were studied with DFT to evaluate if they can catalyze the formation of H_2 (Jelenfi et al. 2023). The results reveal that the presence of these defects can increase the rate of the catalytic H_2 formation at 50 K.

Campisi et al. (2021) developed a robust theoretical method to describe the interaction of aromatic molecules such as PAHs with forsterite mineral surfaces for astronomical and planetary science applications. Using this model, they showed that forsterite surfaces with a vacancy show potential catalytic activity for the dissociation of aromatic CH.

4.3 Modeling

As mentioned previously, the evolution of interstellar dust is a key but a complex subject. Dust undergoes rather multiplexed, size-dependent evolution that principally arises from

photoprocessing, thermal processing, and incident ion and electron collisions in shock waves and in hot gas. Here is a brief overview of the successes in dust modeling over the past decade and its applications to understanding the evolution of various objects.

4.3.1 Dust Models

In the early days of AstroPAH, Jones et al. (2013) presented a dust model built on laboratory data on amorphous hydrocarbon species. It naturally explained the variations in the IR to FUV extinction, the 217 nm UV bump, the IR absorption and emission bands and the IR-mm dust emission. The most innovative aspect of this dust model was that most of the observed extinction and emission, and their evolution, could quite naturally be explained by the size- and composition dependent optical properties of amorphous hydrocarbon dust, with amorphous silicate dust playing only a subordinate role. Jones et al. (2013) proposed that the aliphatic-to-aromatic transformation would be accompanied by photofragmentation and that the evolution of large aliphatic grains formed around evolved stars and the mantles formed by accretion in the dense ISM would then be driven by UV photo-processing and photofragmentation in H II regions and PDRs. These processes are critical for understanding dust evolution in the ISM.

Jones et al. (2014) then explored the consequences of gas-phase carbon accretion onto the surfaces of grains in the transition regions between the diffuse ISM and molecular clouds using their newly built model (Jones et al. 2013). They found that significant carbonaceous dust re-processing and/or mantle accretion could occur in the outer regions of molecular clouds and that this dust would have significantly different optical properties from the dust in the adjacent diffuse ISM. They concluded that the (re-)processing and cycling of carbon into and out of dust is perhaps the key to advancing our understanding of dust evolution in the ISM.

In later years, Hensley and Draine (2021) presented a synthesis of astronomical observations constraining the wavelength-dependent extinction lines where sensitive new observations of polarized dust emission, provided by Planck, allowed to investigate dust polarimetry including continuum polarized extinction, polarization in the carbonaceous and silicate spectroscopic features, the wavelength dependent polarization fraction of the dust emission, and the connection between optical polarized extinction and far-IR polarized emission. Together these constituted a set of constraints that should be reproduced by models of dust in the diffuse ISM.

More recently a new dust model was developed by Hensley and Draine (2023). In this model, large grains are a single composite material "astrodust", and nanoparticle-sized grain come in distinct varieties including PAHs. They argued that a single-composition model for grains larger than 0.02 mm most naturally explains the lack of frequency dependence in the far-IR polarization fraction and the characteristic ratio of optical to FIR polarization. Hensley and Draine (2023) derived a size distribution and alignment function for 1.4:1 oblate astrodust grains, that with PAHs, reproduce the mean wavelength dependence and polarization of Galactic extinction and emission from the diffuse ISM while respecting constraints on solid-phase abundances. The success of the astrodust model in reproducing observations of dust in the diffuse ISM with depletion of selected elements from the gas phase to build new grain material. While pristine stardust grains in the ISM may be predominantly silicate or carbonaceous in nature, they argued that the vast majority of large grains are well-described by a single composition. While Hensley and Draine (2023) identified a number of refinements that could be made to the model, they concluded that an idealized model consisting of PAH nanoparticles plus a dominant population of grains with a uniform astrodust

composition is consistent with current constraints on dust in the ISM and future observations, particularly polarimetry, will be key for testing this hypothesis and further elucidating the nature of interstellar grains.

An update to a dust evolution model was presented that focuses on the grain size distribution in galaxies, whereby galaxies are treated as a one-zone object with five main processes included, i.e., stellar dust production, dust destruction in supernova shocks, grain growth by accretion and coagulation, and grain disruption by shattering (Hirashita 2023). They improved the predictions related to small carbonaceous grains, which are responsible for the 2175 Å bump in the extinction curve and the PAH emission features in the dust SED, both of which are underpredicted in a previous model. The new model assumes that small carbonaceous grains are not involved in interstellar processing which avoids them being lost by coagulation. The hypothetical model shows better matches to both the Milky Way extinction curve as well as the dust emission SED.

4.3.2 Models of Dust Properties

The porosity of dust has been modeled to investigate chemical effects resulting from different porosities (Christianson and Garrod 2021). On the porous grain surface, the build-up of ice mantles, mostly composed of water, can cover the pores and leave empty pockets underneath. The most prominent chemical effect of the presence of grain porosity is the trapping of molecular hydrogen within ices and voids inside the grain pores. Other volatiles could also be trapped within dust-grain porous structures when ices begin forming.

The amplitude and wavelength dependence on the absorption cross sections of needle-like metallic particles has been modeled to investigate whether metallic needles can explain a wide variety of astrophysical phenomena, ranging from the mid-IR interstellar extinction to the thermalization of starlight to generate the cosmic microwave background (CMB; Xiao et al. 2020). The work showed that the antenna approximation is not an appropriate representation of the absorption cross sections of metallic needles as it violates the Kramers-Kronig relation. They therefore demonstrated that rigorous calculations of the absorption cross sections of metallic needle-like particles are needed along with experimental studies of the formation and growth mechanisms of metallic needle-like particles as well as experimental measurements of the absorption cross sections of metallic needles of various aspect ratios over a wide wavelength range.

Somewhat related, extremely elongated, conducting dust particles (also known as metallic 'needles' or 'whiskers') are seen in carbonaceous chondrites and their formation in protostellar nebulae and subsequent inclusion in the ISM have been demonstrated, both experimentally and theoretically by Huang et al. (2021). They calculated the absorption cross sections of iron needles of various aspect ratios over a wide wavelength range, by exploiting the discrete dipole approximation and found that the antenna theory and the Rayleigh approximation, which are often taken to approximate the optical properties of metallic needles, are indeed inapplicable.

A molecular dynamics approach was developed to predict the thermal release pattern of implanted noble gases (He and Xe) in nanodiamonds (Aghajamali et al. 2021). The model showed that the thermal release process of noble gases is highly sensitive to the impact and annealing parameters as well as the position of the implanted ion in the crystal lattice and the morphology of the nanograin. The simulations confirmed that low-energy ion implantation is a viable way to incorporate noble gases into nanodiamonds.

4.3.3 Models of Dust Dynamics

Modeling of dust drift under the influence of stellar radiation pressure during the pressure-driven expansion of an H II region where dust size distribution is represented by four dust types: conventional PAHs, VSGs, big grains, and intermediate sized grains was performed by Akimkin et al. (2015). They concluded that accounting for charge dispersion is necessary to describe the dynamics of small grains.

Akimkin et al. (2017) then extended their previous study by modeling grain ensemble evolution in a dynamical model of an expanding H II region and checking the effects of momentum transfer from dust to gas. The radiation pressure on the dust, the dust drift, and the lug on the gas by the dust are all important processes that were considered simultaneously to describe the dynamics of H II regions. The momentum transfer from the dust to the gas resulted in a notably reduced expansion time of the H II region. When considering the common approximation of frozen dust, where there is no relative drift between the dust and gas, the radiation pressure from the ionizing star is shown to drive the formation of the very deep gas cavity near the star. Such a cavity is much less pronounced when the dust drift is taken into account as it leads to the two-peak morphology of the dust density distribution and significantly reduces the dust-to-gas ratio in the ionized region (by a factor of 2 to 10). The dust-to-gas ratio is larger for higher temperatures of the ionizing star since the dust grains have a larger electric charge and are more strongly coupled to the gas.

4.3.4 Applications of Dust Models to Various Astrophysical Objects

The IR features of dust illuminated in a reflection nebula have been modeled with respect to the PAH size and the radiation intensity (Gadallah and Ali 2021). The dust model contained PAHs, amorphous C and amorphous silicate, and various trends show the effect of varying both the PAH size and the radiation intensity on the aromatic mid-IR bands.

Extinction profiles in the SMC and LMC have been modeled with a synthetic population of dust grains consisting of core-mantle particles and a collection of free-flying PAHs (Zonca et al. 2015). All the different flavors of molecular cloud (MC) extinction curves can be described by this model. In both SMC and LMC the extinction produced by classical grains is generally larger than absorption by PAHs and the nonlinear far-UV rise observed is accounted for by PAHs, whose presence in turn is associated with a gap in the size distribution of classical particles. This hints at a physical connection between PAHs and the absence of middle-sized dust particles or the need for an additional component in the model that can account for the nonlinear far-UV rise without contributing to the UV bump at 217 nm such as, e.g., nanodiamonds.

To explain the properties of dust in the ISM, the presence of a refractory organic mantle is necessary. Among the main contributors of stellar dust to the ISM are the outflows of AGB stars. van de Sande et al. (2020) modeled the refractory organic contribution of AGB stars to the ISM. Based on laboratory experiments, they included a new reaction in their extended chemical kinetics model: the photoprocessing of volatile complex ices into inert refractory organic material. The refractory organic feedback of AGB outflows to the ISM was estimated using observationally motivated parent species and grids of models of C-rich and O-rich outflows. Refractory organic material is considered to be mainly inherited from the gas phase through accretion on to the dust and subsequent photoprocessing. Photodissociation of ices also initiates a grain-surface chemistry but it produces only a minor part or the organic refractory material and it takes place in a sub-monolayer regime in almost all outflows. The formation of refractory organic material increases with outflow density and

depends on the initial gas-phase composition. While O-rich dust is negligibly covered by refractory organics, C-rich dust has an average coverage of 3-9%, but can be as high as 8-22%. Although C-rich dust does not enter the ISM bare, its average coverage is too low to influence its evolution in the ISM or significantly contribute to the coverage of interstellar dust. This study opens up questions on the coverage of other dust-producing environments. van de Sande et al. (2020) highlighted the need for an improved understanding of dust formation and for models specific to density structures within the outflow.

Calculations using the CLOUDY model showed that the abundance of water ice in PNe, other conditions being equal, depends on the ionization rate of hydrogen, which depends on the flux of energetic particles in the MeV range (Yeghikyan 2017). The possibility of an increased flux of energetic particles in PNe under conditions of the standard interacting stellar winds scenario was discussed, and it was concluded that the flux may locally exceed by 1-3 orders of magnitude that of Galactic cosmic rays. This may have important implications for the chemistry of complex compounds under conditions of PNe, in particular, for models of the origin of fullerenes.

The pre- and post-shock dust masses in Cassiopeia A (Cas A – supernova remnant) were determined using a dust emission model (Priestley et al. 2021). Core-collapse supernovae produce large masses of dust, and are potentially the primary source of dust in the Universe, but much of this dust may be destroyed before reaching the ISM. Cas A is the only supernova remnant where an observational measurement of the dust destruction efficiency in the reverse shock is possible at present. Priestley et al. (2021) used an improved dust emission model to determine the pre- and post-shock dust masses in Cas A and their results support a mostly stellar origin for the cosmic dust budget.

Chen et al. (2021) meanwhile investigated the interstellar fate of SiC. The 11.3 μm absorption feature of SiC has never been seen in the ISM and it reveals that SiC dust grains are condensed in the outflows of carbon stars and could be a significant constituent of interstellar dust since it is generally believed that carbon stars inject a considerable amount of dust into the ISM. The destruction of interstellar SiC dust through oxidation was quantitatively explored and Chen et al. (2021) noted that since reactions with O atoms are exothermic, they could cause CO-loss. However, the destruction rate of SiC through oxidation could still be considerably smaller than the currently believed injection rate from carbon stars so the lack of a 11.3 μm absorption features in the ISM is still a mystery.

Finally, Shao et al. (2017) studied the role of dust in AGNs. Dust plays a central role in the unification theory of AGNs. The size of the dust particles that form the torus around an AGN, whether it is micron-sized, like interstellar grains, or much larger, has a large impact on modeling and correcting for the obscuration of the dust torus in order to recover the intrinsic spectrum and luminosity of the AGN. Shao et al. (2017) showed that the ratio of the optical extinction in the visual band (A_V) to the optical depth of the 9.7 μm silicate absorption feature could potentially be an effective probe of dust size. This ratio in AGNs compared to the Galactic diffuse ISM reveals that the dust in AGN tori could be substantially larger than the interstellar grains of the Milky Way and those of the SMC.

4.3.5 The Ultraviolet Extinction Curve

The UV extinction curve has also been found to be intricately linked with PAHs (Massa et al. 2022) as mentioned in Sect. 2.1.2.

The relation between the amount of silicon required to be locked up in silicates and the 2175 Å bump and the far-UV extinction rise were explored with a model built by Mishra and Li (2017). No correlations between the silicon content and the extinction curve was

found, but a correlation was found between carbon depletion and the 2175 Å bump as well as the far-UV extinction along with silicates. The study suggests the far-UV extinction is a combined effect of small carbon grains and silicates.

Zuo et al. (2021a) also examined the extinction and abundances of 10 interstellar sightlines quantitatively for which both the extinction curves and the gas-phase abundances of all the major dust-forming elements (C, O, Mg, Si, Fe) have been observationally determined. They did this to explore the viability of the abundance of B stars, the solar and protosolar abundances and the protosolar abundances augmented by Galactic chemical enrichment as an appropriate representation of the interstellar abundances. This work supports the Galactic chemical enrichment (GCE) augmented protosolar abundances as a viable representation of the interstellar abundances. The same authors also used a wealth of extinction and elemental abundance data to explore the dust properties of a large number of individual sight lines (Zuo et al. 2021b). The observed extinction curve was modeled of each sight line and abundances of the major dust-forming elements required to be tied up in dust were derived. The derived dust depletions were compared with observed gas-phase abundances to investigate the environmental effects on the dust properties and elemental depletions. It was found that for the majority of sight lines the interstellar oxygen atoms are fully accommodated by gas and dust and therefore there does not appear to be a "missing oxygen" problem as had been previously thought.

5 H_2 Formation from PAHs and Superhydrogenated PAHs

Molecular hydrogen is the most abundant molecular species in the universe. However, there still remain gaps in our understanding of how H_2 is formed in space. Its formation involves PAHs and dust as catalytic reactors and the micro-physics of this mechanism have been investigated intensively since the turn of the century (Wakelam et al. 2017).

The dust surfaces principally catalyzing H_2 formation are typically on particles that are sub-micron in size and are usually classified as either silicates or carbonaceous materials. In the carbonaceous class there are sp^3 (nanodiamonds), sp^2 (grapite, PAHs), and mixed sp^3-sp^2 (amorphous carbon) carbon bonded materials. Hence, understanding all the processes relevant to H_2 formation on carbonaceous materials such as sticking, binding, diffusion, reactions, and desorption, is of great importance.

5.1 Observations

Now with JWST launched, we are close to achieving low- to medium-resolution ($\lambda/\Delta\lambda$ 3000) spectroscopy of H_2 lines, with an increase of two orders of magnitude in spatial resolution and sensitivity compared to ISO or Spitzer. The gain in sensitivity and spatial resolution (0.3" at 10 μm) can potentially generate high quality maps of the H_2 rotational and ro-vibrational transitions with a wealth of moderately/highly excited rotational levels that may now be detectable in outer space for the first time. Such observations have the potential to cover a huge range of excitation energies, making them excellent probes of the excitation of H_2 and the associated gas (Wakelam et al. 2017).

The wavelength coverage of JWST can also allows to study the links between H_2 and the properties of small dust particles; how rapidly dust properties change at cloud edges via photo-processing, and how such changes impact the H_2 formation process (Wakelam et al. 2017). Likewise, as JWST can spatially and spectrally resolve H_2 at rest-frame near-IR and mid-IR wavelengths out to $z = 1.5 – 3.5$ so H_2 line emission can be studied in the distant, early Universe.

5.2 Experiments

5.2.1 Superhydrogenated PAHs

Understanding the mobility of H at the surface of carbon nano-structures is one of the essential conditions for understanding the catalytic formation of H_2 in interstellar clouds. Studies of local environments of H structures chemisorbed at the surface of disordered graphene have been carried out (Cavallari et al. 2016), but a greater number has focused on the capabilities of individual PAHs to become superhydrogenated to understand their role in H_2 formation in space. This has also spurred a wealth of theoretical studies such as the potentially catalytic role of Stone-Wales (SW) defects in pyrene (Campisi and Candian 2020). In this respect, important clues can also be found the fragmentation and dissociation of PAHs which have been detailed in Sects. 3.2 and 3.3.

The ability of PAHs to catalyze molecular hydrogen formation has been investigated greatly in the past decade. While simple abstraction of atoms from PAHs by incident H atoms is not an energetically favorable process, such reactions can be activated by the addition of additional H atoms to the PAH molecule, creating a superhydrogenated PAH (Skov et al. 2014). Multiple experiments into the superhydrogenation of PAHs have been spearheaded and their results are presented here below.

When coronene is exposed to sufficiently high D atom fluences it is driven toward the completely deuterated state ($C_{24}D_{36}$) (Skov et al. 2014). The authors stated that the findings indicate that the cross section for addition does not scale with the number of sites available for addition on the molecule, but rather has a fairly constant value over a large interval of superhydrogenation levels. It was also demonstrated that deuterium atoms adsorbed on graphite can react with adsorbed PAHs to form superhydrogenated species. PAHs adsorbed on hydrogenated carbonaceous grains in warm interstellar environments therefore might serve as a route to release H_2 on top of forming superhydrogenated PAHs (Thrower et al. 2014). Similarly, it has been shown that when PAHs adsorb onto a TiO_2 surface, they are capable of being hydrogenated from H_2O molecules chemisorbed on the TiO_2 surface, i.e., without the need of external energy or hydrogen sources (Cruz-Diaz et al. 2020), but water molecules adsorb strongly to silicate surfaces whose reactivities are greatly affected by structural defects such as those resulting from hydroxylation (Kerkeni et al. 2017).

It was also found that in the study of the superhydrogenation of coronene cations, there is a site-specific sequence leading to the appearance of magic-number hydrogenations (Cazaux et al. 2016). Namely, coronene cations with 5, 11, or 17 attached hydrogen atoms are all observed. This contrasts with the superhydrogenation of pentacene which showed that even-numbered hydrogenated species were highly favored with a penchant for particular hydrogenation states from 2–22 additional H atoms (Campisi et al. 2020).

H-attachment to PAH cations has also been studied where coronene radical cations were confined in a radio frequency ion trap where they were exposed to H atoms or D atoms (Foley et al. 2018). Monitoring attachment of D atoms allowed to distinguish attachment from competing abstraction reactions. The strong contribution observed of abstraction seemed to indicate that H_2 formation on PAHs via the Eley-Rideal mechanism[27] is an order of magnitude faster than previously thought, but this mechanism has also been studied with theoretical calculations on pyrene which found edge sites to be most kinematically favored while the recombination of hydrogen atoms is a barrier-less process no matter the adsorption site

[27] The Eley-Rideal mechanism is a unique reaction pathway in surface chemistry where a gas-phase reactant directly interacts with an adsorbed species on a solid surface to form a product in a single step.

(Barrales-Martínez et al. 2018). Both the chemisorption and the abstraction of the adsorbed hydrogen atom by an incoming H atom, throughout the entire surface, are highly exoergic processes.

Sequential hydrogenation of gas-phase coronene cations was furthermore studied with IRMPD (Cazaux et al. 2019). There it was uncovered that molecules with odd numbers of additional H atoms are found to have the highest binding energies, but along with reaction barriers, the binding energies strongly affect the hydrogenation sequence and the site specificity. With increasing hydrogenation, C_2H_2 losses were also observed to become more relevant and in the case of 9 and 11 attached H atoms, the carbon skeleton is substantially weakened with fragmentations distributed over a large number of channels (Cazaux et al. 2019).

Dissociations following H attachment to gas-phase coronene cations was also studied in a radiofrequency ion trap (Rapacioli et al. 2018). With increasing hydrogenation, C_2H_x loss and multifragmentation are identified as main de-excitation channels where the coronene fragmentation patterns depend on the balance between energy deposition by H-attachment and the extent of cooling between subsequent attachment processes. Dissociation products of superhydrogenated pyrene were also investigated with IRMPD where it was found that ethylene (C_2H_4) along with C_2H_2 and H_2 form readily from collisionally induced dissociation (Tang et al. 2022). This is consistent with what has been observed in experiments at different wavelength regimes, i.e., that upon hydrogenation, ring openings become more competitive (see Sects. 3.2.9 and 3.3.2).

In sharp contrast with regular PAHs, the superhydrogenation of the oxygen atom containing PAH 6,13-pentacenequinone showed little evidence of the O-containing species remaining following complete hydrogenation (Jaganathan et al. 2022). This work showed that superhydrogenation of oxygenated PAHs is likely to catalyze the release of smaller molecules such as H_2O or small O-containing COMs. Such results that exhibit the depletion of oxygenated PAHs compare well with those of PAHs in ices described in Sect. 4.2.4.

In a similar regard, superhydrogenated PAHs have been investigated as potential catalysts for hydrogenation reactions in the ISM. A computational study showed that neutral hydrogenated PAHs can also catalyze hydrogenation reactions by acting as a hydrogen source. In particular, interactions of OH and CO with hydrogenated anthracene to form H_2O and HCO was fully modeled assuming an Eley-Rideal mechanism (Ferullo et al. 2019). In comparison to H_2 formation (which displays barriers between 0.02 and 0.10 eV), the formation of H_2O is completely barrierless and HCO formation is very unfavorable.

However, small PAHs with an imperfect aromatic system may provide better catalysis in comparison to pristine PAHs, i.e., without defects in the aromatic system. The catalytic effect of small PAHs with an imperfect aromatic system in producing H_2 was investigated with quantum chemical calculations and the results revealed that defects in the aromatic system compared to benzene can increase the rate of the catalytic H_2 formation at a temperature of 50 K (Jelenfi et al. 2023).

The effects of UV-processing on superhydrogenated coronene has also been studied experimentally and theoretically (Mennella et al. 2021). The effects of UV irradiation were monitored with IR spectroscopy which showed the photodestruction of aliphatic C–D bonds which were found to be 55% weaker than aliphatic C–H bonds. The experimental results when compared with modeling suggest an extension of the region inside PDRs where superhydrogenated coronene can survive and contribute to H_2 formation.

The diffusion of physisorbed H atoms and the desorption energetics of H_2 molecules on an amorphous diamond-like carbon surface have also been studied (Tsuge et al. 2019). This was showed to be a very efficient H_2 formation mechanism, even at 20 K, and it was

suggested that in astrophysical environments, chemisorbed H atoms might play a role in H_2 formation at temperatures above 20 K.

The superhydrogenation of corannulene, the bowl-shaped non-planar PAH, has also been investigated (Leccese et al. 2023). It was found that adding a certain number of H-atoms afforded corannulene with greater stability than others but notably, it was found that the completely hydrogenated species was not formed as a dominant product at high H-fluences. This is in stark contrast to the likes of coronene and other PAHs. Hence, the stability of the superhydrogenated corannulene with 17 additional H-atoms, a departure from the odd-even alternation observed for other PAHs, is noteworthy.

Recently, highly efficient formation of H_2 has been reported for temperatures up to 250 K on carbonaceous surfaces (using coronene as a test-bed) mimicking interstellar dust, but previously it was thought that H_2 formation rates on PAHs reduced above 50 K and H atom recombination was believed to be highly efficient only below 20 K (Grieco et al. 2023). This experimental work, however, showed that H_2 molecules could start contributing substantially to the cooling of warmer gas (temperatures of roughly 50–250 K. This will have a marked impact on our scientific perception of H_2 formation in nearby galaxies and its efficiency in high-redshift galaxies, where the CMB increases dust temperatures to more than 20 K.

5.3 Modeling

5.3.1 H_2 Formation from PAHs

Multiple models of H_2 formation have been constructed. One such model of the H_2 formation in PDRs was constructed to include the known dust grain chemistry for the formation of H_2, and H_2 formation from PAHs (Boschman et al. 2015). As H_2 formation on PAHs is impeded by thermal barriers, this pathway can only be efficient at temperatures above 200 K. This is convenient as H_2 formation via physisorbed H atoms on dust grains is no longer feasible at such elevated temperatures so the PAH mechanism expands the region in PDRs where H_2 formation is possible. They found that PAHs have a significant influence on the structure of PDRs, particularly if the PDRs have a strong external radiation field. A sharp transition between fully dehydrogenated PAHs on the outside of the cloud and normally hydrogenated PAHs on the inside was found and by using experimental results derived from coronene as a benchmark PAH, it was shown that H_2 forms very efficiently on PAHs and this model reproduced the high H_2 formation rates derived in several PDRs.

This has been followed up by investigating the physical conditions inside the well-studied RN NGC 7023 which were modeled using the Meudon PDR code to test coronene, circumcoronene and circumcircumcoronene as test examples of PAHs forming H_2 (Andrews et al. 2016). Coronene was found to be easily destroyed down to the complete loss of all of its H atoms while circumcircumcoronene does not dehydrogenate at all. It was concluded that PAHs with extra H atoms are not the carriers of the 3.4 μm band in NGC 7023 as superhydrogenated PAHs are easily destroyed. Likewise, H_2 abstraction from PAHs with extra H atoms is an inefficient process compared to grains. Instead the authors propose that photodissociation of PAHs of small to intermediate sizes could contribute to H_2 formation in PDR surfaces but they alone cannot account for the inferred high H_2 formation rates in these regions.

These modeling efforts were subsequently expanded to include molecule dependent branching of H-/H_2-loss reactions from UV-irradiated PAHs (Castellanos et al. 2018a). Three PAH cations were considered, namely coronene, ovalene, and circumcoronene. It was

found that for ovalene the rate coefficient for H_2 formation reaches values of the same order as H_2 formation in dust grains which suggests that this hitherto disregarded mechanism can account, at least, partly, for the high level of molecular hydrogen formation in dense PDRs.

Besides H_2 formation from PAHs in PDRs, H_2 formation in diffuse and translucent clouds on grain surfaces have also been modeled with Monte Carlo calculations, specifically how the prior presence of H_2 molecules adsorbed onto grains affects the grains' catalytic efficiency (Zhao et al. 2022). It was found that the effect of the presence of H_2 molecules on the grains on the H_2 formation efficiency strongly depends on the diffusion barriers of H_2 on grain surfaces. While translucent cloud model results show that H_2 formation efficiency is not affected by surface-H_2 (assuming a low H_2 diffusion barrier), diffuse cloud models predict a range of recombination efficiencies between 10 and 15 K.

6 H II Regions, Galaxies, Active Galactic Nuclei - X-ray Driven Destruction and Dynamics

While a wealth of work has been dedicated to understanding the processing of PAHs (Sect. 3.2) and their IR emission (Sect. 2) in PDRs and the ISM, there are other regions which are sources of higher energy photons and could drive PAH destruction and dynamics.

H II regions are emission nebulae created when young massive stars ionize nearby gas clouds with high-energy UV radiation. They primarily comprise hydrogen, hence the name (the term H II is used to refer to ionized hydrogen, H I for neutral hydrogen), and have temperatures of around 10,000 K. They can extend over several hundred light years or be so compact that they do not even stretch 1 light year across. Correspondingly they have a large range of densities, from a few to millions of atoms cm^{-3}, for the most compact regions.

In our Galaxy, H II regions (or "Galactic H II regions") follow a distribution pattern similar to that of the molecular clouds from which stars are formed, and are similarly concentrated in the spiral arms of other galaxies. They are also found in association with newly formed stars throughout irregular galaxies which makes them highly visible tracers of active star formation.

An Active Galactic Nucleus (AGN) is the name given to the central region of galaxies with luminosities that are far greater than what is expected from their stars alone. Such regions can be more luminous than the whole remaining galaxy. Much of the energy output of AGNs is a non-thermal (non-stellar) type of emission, with many AGNs being strong emitters of X-rays, radio and UV radiation, as well as optical radiation. It is believed that a black hole exists in the core of each AGN. Its gravity attracts the surrounding material, forming an accretion disk. The disk can release a luminous distribution of high-energy photons, as well as matter in the form of energetic jets, while the black hole accretes the material in the inner part of the disc.

Carl Seyfert discovered the first class of AGN, whose nuclei display emission lines. These are now known collectively as Seyfert galaxies and are categorized in two types. Type 1 Seyfert galaxies have both narrow and broadened optical spectral emission lines. The broad lines imply gas velocities of 1000–5000 km s^{-1} very close to the nucleus. Seyfert type 2 galaxies have narrow emission lines only (but still wider than emission lines in normal galaxies) implying gas velocities around 500–1000 km s^{-1}. These narrow lines originate from low density gas clouds at larger distances (than the broad line clouds) from the nucleus.

Another type of AGNs are quasars which are the most luminous AGNs. The spectra of quasars are similar to Seyferts apart from stellar absorption features being weak or absent, and the narrow emission lines are weaker relative to broad lines as seen in Seyferts.

This section is devoted to the observations of H II regions, galaxies, and AGNs, along with X-ray spectroscopy and dynamics, whose energetic quanta are capable of multiply ionizing and subsequently fragmenting astronomical PAHs.

6.1 Observations

6.1.1 Galactic H II Regions

In the early days of AstroPAH, the spatial variations in PAH band intensities were usually attributed to the physical conditions of the emitting PAHs, but they could also be caused by extinction. To resolve this, Stock et al. (2013) obtained near-IR, mid-IR, and radio observations of the compact H II regions IRAS 12063-6259. They constructed multiple independent extinction maps which were used to deredden mid-IR observations and hence investigate how the spatial extinction varies with PAH intensity variations. The two radio sources in IRAS 12063-6259 possess remarkably different properties which were difficult to satisfactorily explain.

Khramtsova et al. (2014) presented an analysis of the optical spectroscopy and IR aperture photometry of over 100 H II regions in nine galaxies to infer a strength of PAH emission, properties of the UV radiation field and metallicity. Physical properties (age, radiation field parameters, metallicity) were related to the 8/24 μm ratio used as a proxy for the PAH abundance in order to reveal factors that may influence the PAH evolution in H II complexes. The well-known correlation between the 8/24 μm band ratio and metallicity was confirmed in the studied complexes. The analysis of various mechanisms of PAH formation and destruction in the context of the various correlations the authors found, they suggested that PAH abundance is likely altered by the UV radiation within H II complexes. This is, however, not necessarily due to their destruction. If PAHs can also form in H II complexes then there is an ongoing balancing act between processes that can be nuanced for different metallicities.

Mori et al. (2014) systematically investigated NIR spectra (2.5-5.4 μm) of Galactic H II regions and H II region-like objects in terms of PAH features. They identify the 5.25 μm band feature associated with C – H vibrations as a potential probe of PAH size distribution and they also speculated on using other band strength ratios to probe PAH ionization fraction and dust processing.

Spitzer observations were used to investigate H II regions in the Magellanic cloud by Stephens et al. (2014) who found that the PAH mass fraction increases significantly toward molecular clouds except when there is a very strong radiation field. PAHs are likely being destroyed by the radiation field and the PAH mass fraction increases upon leaving the central OB association. They also found that optically thin areas in the H II regions also have a diminished mass fraction.

Another H II region of interest is the northern part of W49A which represents one of the largest complexes of massive star formation present in the Milky Way. It contains at least 50 young massive stars still enshrouded in their natal molecular cloud. W49A was mapped in the mid-IR in terms of PAH bands, PAH plateau features, *etc.* PAH bands were found to reproduce known trends with the caveat that the 6.2 μm PAH band seems to decouple from the other ionized PAHs bands in the some of the two ultra-compact-H II regions found within (Stock et al. 2014). This effect has only been observed in one other object, namely the giant star forming region N66 in the LMC. Stock et al. (2014) found that the mid-IR appearance of W49A is that of a starburst of large scales, yet its individual components are consistent with other galactic H II regions.

Infrared bubbles are also ideal regions to investigate the effects of the expansion of an H II region on its surroundings and eventual triggering of star formation on its borders. The

N10 dust bubble was studied at multiple wavelengths. IR studies conducted by Gama et al. (2016) of the young stellar content suggested a scenario of ongoing star formation, possibly triggered at the edge of the H II region. They proposed that the dynamical age of this region and the fragmentation timescale favors the "Radiation-Driven Implosion" mechanism of star formation as N10 possesses gas structures in a narrow frontier between the H II region and the surrounding molecular material. There, a range of ages can be found in the YSOs situated therein, indicating light-triggered star formation.

AKARI was also used to perform a near-IR spectroscopic survey of 53 H II regions in the Milky Way, LMC, and SMC with the aim to search for features indicative of deuterated PAHs to better constrain the D/H ratio of PAHs (Doney et al. 2016). Emission features between 4.4 and 4.8 μm, which can be unambiguously attributed to deuterated PAHs, were only observed in six of the observed sources. In all cases, the aromatic C–D stretching feature was weaker than the aliphatic C–D stretching feature and, in the case of M17b, this feature was not observed at all. Doney et al. (2016) suggested that the mechanism for PAH deuteration in the ISM in our Milky Way is uncommon based on the weak or absent aromatic C–D features.

Chastenet et al. (2019) built maps of the dust properties in SMC and LMC from fitting Herschel and Spitzer observations with a dust model. They found that the global PAH fraction is smaller in SMC than in LMC and the PAH fraction is measured in different gas phases (H II regions, ionized gas outside H II regions, molecular gas, and diffuse neutral gas). H II regions appear as distinctive holes in the spatial distribution of the PAH fraction. In both clouds, the PAH fraction in the diffuse neutral medium is higher than in the ionized gas, but similar in the molecular gas. Plausible explanations for the higher PAH fraction in the diffuse neutral medium of LMC compared to SMC include more effective PAH production by fragmentation of large grains at higher metallicity and/or the growth of PAHs in molecular gas.

Herschel and Spitzer data were used as well to estimate fluxes from 99 H II regions around massive stars (Topchieva et al. 2018). They showed that the PAH mass fraction is much lower in these objects than the average Galactic value, implying effective destruction of aromatic particles in H II regions. The same authors later used data from Herschel and Spitzer to analyze the IR radiation in the 8–500 μm range in the outer and inner parts of 32 IR bubbles (which form around H II regions) to determine their morphology and possible dust evolution processes (Topchieva et al. 2019). Their results suggested that PAHs may be generated due to larger grain destruction.

Over 7000 mid-IR spectra of the ISM observed with Spitzer were used to decompose the 7.7 μm PAH emission complexes by Stock and Peeters (2017). They showed there is a strong environmental dependence on the interrelationship between the band fluxes – in the H II regions all four components are intercorrelated, while in the RNe the inner and outer parts of bands correlate in the same manner as that observed in NGC 2023 (see Sects. 3.1.2 and 3.1.3). This effect arises because the maps of RNe are dominated by emission from strongly irradiated PDRs while the much larger H II maps are dominated by emission from regions much more distant from exciting stars.

6.1.2 Galaxies and Active Galactic Nuclei

The behavior of the PAH luminosity at 8 μm was studied in 1868 galaxies with redshifts in the z = 0.3–1.4 range by (Murata et al. 2014) using AKARI observations. The AKARI photometric filters coverage in the 2–24 μm range enabled Murata et al. (2014) to measure the 8/4.5 μm ratio for the redshift range of interest. The study showed evidence that starburst

galaxies (galaxies with unusually high star formation rates) have deficient PAH emission when compared to galaxies with more normal star formation rates (galaxies in the so called 'main sequence'). Furthermore, galaxies with extremely high (8 to 4.5) luminosity ratios have only a moderate degree of star formation. Such behavior suggests that in starburst galaxies (i) PAHs can be destroyed by the intense radiation in compact star-forming regions and/or (ii) the dust present in the H II regions absorbs the ionizing photons.

Because of results such as the one mentioned above, PAH emission is often used as a proxy for star-formation activity in galaxies in the literature. In Castro et al. (2014), for example, using the 3.3 μm PAH emission as a proxy for star formation, the authors found that the star formation activity is larger in Seyfert 2 type AGNs than in Seyfert 1 AGNs, for the low Eddington ratio regime.[28] However, for the high Eddington ratio regimes, no difference was observed between AGN types.

A systematic IR 2.5-5 μm spectroscopic study of 22 nearby IR galaxies was performed by Ichikawa et al. (2014) over a wide luminosity range ($10^{10} - 10^{13} L_{\odot}$) with the IRC camera, using the 3.3 μm PAH emission feature to investigate the luminosity relation between star formation and AGNs. The unique band of the AKARI IRC instrument enabled access to both the 3.3 μm PAH emission feature from star-forming activity and the continuum of torus-dust emission heated by an AGN. Applying AGN diagnostics to the AKARI spectra, the authors discovered 14 buried AGNs. This large fraction of buried AGNs suggests that AGN activity behind the dust is ubiquitous in ultra/luminous infrared galaxies (U/LIRGs). It appears that these galaxies exhibit higher star formation rates than optically selected Seyfert galaxies with the same AGN luminosities, implying that U/LIRGs could be an early evolutionary phase of AGN.

Data from the AKARI-Spitzer Extragalactic Spectral Survey of a sample of 2.5–38 μm galaxy spectra were studied by Lai et al. (2020a) to investigate a subset of 113 star-forming galaxies with prominent PAH emission spanning a wide range of star formation properties using an extended version of the spectral decomposition tool PAHFIT available on the NASA Ames PAH IR spectral database. A calibration between 3.3 μm PAH emission and the star formation rate was established, however at high luminosity and low metallicity the calibration becomes less reliable. As the PAH feature with the shortest wavelength, the one at 3.3 μm is susceptible to attenuation, leading to differences of a factor of $\sim$3 in the inferred star formation rate at high obscuration with different assumed attenuation geometries. Lai et al. (2020a) suggested that PAH emission is shifted to shorter wavelengths in intense and high-energy radiation environments and provided a photometric surrogate for 3.3 μm PAH luminosity using JWST/NIRCam that was found to be highly reliable at low redshift.

Spitzer data along with Gemini mid-IR spectroscopic observations were also used to investigate the properties of the dusty torus and circumnuclear star formation in two active galaxies, NGC 7213 and NGC 1386 by Ruschel-Dutra et al. (2014). PAH emission was absent in the nuclear spectra but were ubiquitous in the Spitzer data at distances above 100 pc. This is consistent with the paradigm that PAHs are destroyed by the radiation field of the AGN.

Earlier theoretical and observational works indicated the presence of a correlation between the star-formation rate (SFR) and AGN luminosity (and, therefore, the black hole accretion rate) of Seyfert galaxies. This suggested a physical connection between the gas-forming stars on kpc scales and the gas on sub–pc scales that is feeding the black hole. Esquej et al. (2013) compiled a large sample of Seyfert galaxies with high angular resolu-

[28]The Eddington ratio is the ratio between the object bolometric (total across all wavelengths) luminosity and the so-called Eddington luminosity, which is the luminosity an object has to emit to support its gravity in hydrostatic equilibrium.

tion mid-IR (8–13 μm) spectroscopy. The sample included 29 Seyfert galaxies who showed no suppression of the 11.3 μm PAH emission band in the vicinity of AGN in Seyfert galaxies, which meant that this band could be used as a proxy for the star formation regions. They found that star formation activity per unit area of the central 65 pc region of Seyfert galaxies were much higher than at larger distances from their nuclei.

A sample of 155 predominantly starburst-dominated galaxies (including H II regions and Seyferts) were extracted from the Spitzer ATLAS project[29], to analyze the 6.2 μm PAH emission feature (Canelo et al. 2018). The analysis suggested that a significant presence of PANHs in the ISM of these galaxies could be related to their starburst-dominated emission. Secondly, PANHs could constitute another reservoir of nitrogen in the Universe, in addition to the nitrogen in the gas phase and ices of the ISM.

Spitzer data from the ATLAS project were used to analyze the 7.7 and 8.6 μm emission bands in 126 predominantly starburst-dominated galaxies which are classified in A, B, and C classes (see Sect. 2) (Canelo et al. 2021). Considering the redshift range covered in the sample, the distribution of the bands revealed a potential cosmological evolution of the molecular nature of the PAHs that dominate the ISM in these galaxies where B class objects seem to be more frequent at higher redshifts.

A sample of 50 Seyfert galaxies were studied to compare the circumnuclear (inner kpc) PAH emission of AGN to that of a control sample of star-forming galaxies (22 luminous IR galaxies and 30 H II galaxies), and investigate the differences between central and extended PAH emission (Garcia-Bernete et al. 2022a). Tentative evidence was found that PAH ratios in AGN-dominated systems are consistent with emission from larger molecules (300–400 C atoms) as well as neutral species. The study demonstrated that PAH ratios measured in the extended regions of both type 1 and type 2 Seyfert galaxies can be explained assuming similar PAH molecular size distribution and ionized fractions of molecules to those seen in central regions of star-forming galaxies (100–300 C atoms).

Galaxy mergers have also been observed with the AKARI IRC instrument (Onaka et al. 2018). NIR-to-MIR imaging of the galaxy mergers NGC 2782 and NGC 7727 revealed excess PAH emission as well as an SED decline longward of 24 μm which suggests that VSGs are deficient. These characteristics were interpreted as PAHs being formed via the destruction of VSGs during merger events and the star formation rate estimated from the MIR PAH emission was in fair agreement with those estimated from Hα and [C II] 158 μm emissions. The small PAH abundances observed might be related to the destruction of PAHs due to the presence of an AGN, however, the IR spectra did not show clear evidence of AGN; only recent X-ray observations indicate the presence of a low-luminosity AGN.

The superwind/halo region of the starburst galaxy M82, which includes PAH emission features, was mapped in the mid-IR with Spitzer by Beirão et al. (2015). The PAH features were used to estimate the average size and ionization state of the small grains in the superwind. Large PAH flux variations were observed throughout the outflow. Analyses of the 11.3/7.7 and the 6.2/7.7 ratios revealed that PAH emitters are larger and more ionized on average.

Spitzer data of three spectroscopically anomalous galaxies (IRAS F10398+1455, IRAS F21013-0739, and SDSS J0808+3948) were modeled in terms of a mixture of cold silicate dust, and warm and cold carbon dust by Xie et al. (2015). Their modeling analysis showed that the steep 5–8 μm continuum and strong PAH emissions suggest a dominance of starbursts, while the silicate emission is indicative of significant heating from AGNs.

[29]The ATLAS project is a compilation of spectroscopic and photometric data from extragalactic sources, in particular star-forming and active galaxies, that have been observed with Spitzer.

Dust temperature is the primary cause in regulating the steep 5–8 μm continuum and silicate emission, insensitive to silicate or carbon dust mineralogy and grain size. It appears that larger dust grains are preferred in quasars. The lower dust temperature and smaller grain sizes inferred for these three galaxies compared with that of quasars could be due to the fact that they may harbor a young/weak AGN that is not maturely developed yet.

Spitzer spectroscopic maps (5–21 μm) toward 12 regions in the Andromeda galaxy (M31) have been analyzed in terms of PAH emission features (Hemachandra et al. 2015), but previous data from Herschel and Spitzer were also used to construct detailed dust maps of the Andromeda galaxy (Draine et al. 2013). The 6.2 and 7.7 μm features compared to the 11.2 μm feature strongly correlate in all regions apart from the nucleus. Equivalent widths as a function of metallicity and radiation harshness are consistent with those observed in other nearby spiral and starburst galaxies. The nucleus does not show any PAH emission but does show strong silicate emission and a 9.7 μm feature.

Spitzer data was used to analyze the mid-IR spectra of H II regions within the star-forming galaxies M83 and M33 by Maragkoudakis et al. (2018). They demonstrated that the 6.2/7.7 ratio does not effectively track PAH size, but the 11.3/3.3 PAH ratio does. Variations on the 17 μm PAH band depend on object type, but there is no dependence on metallicity for both extragalactic H II regions and galaxies. It was argued that extragalactic H II regions are more suitable templates in modeling and interpreting the large-scale properties of galaxies compared to Galactic H II regions.

The C_2H emission in the starburst galaxy NGC 253 was mapped as part of the ALCHEMI[30] program (Holdship et al. 2021). They found high C_2H column densities toward the dense regions of NGC 253. They were so high that they cannot only be from the PDRs at the edge of the cloud. Probably, the C_2H emission remains high because of a high cosmic-ray ionization rate but if so, then the ionization rate in each GMC is only constrained to within a few orders of magnitude. A more sensitive probe of the cosmic-ray ionization rate should be utilized in these regions to confirm the presence of a high ionization rate and better constrain its value.

The effectiveness of PAH emission as a SFR indicator on sub-kpc scales was studied using Spitzer observations of the nearby grand-design spiral galaxy M51 (Zhang et al. 2020). A new approach was presented which analyzes the spatial elements of the spectral cube that simultaneously maximizes spatial resolution and spatial coverage, while yielding reliable measurements of the total, integrated 5–20 μm PAH emission. A strategy of extracting robust PAH emission using spectra with only partial spectral coverage, complementing missing spectral regions with properly combined mid-IR photometry was devised as well. Zhang et al. (2020) found that in M51 the PAH emission correlates tightly with the extinction-corrected far-UV, near-UV and Lyman-α emission, from scales of 0.4 kpc close to the nucleus to 6 kpc out in the disk of the galaxy, indicating that PAHs serve as an excellent tracer of SFR over a wide range of galactic environments.

The PAH emission features in the circumnuclear region and extranuclear regions of M51a using Spitzer observations were studied in detail (Zang et al. 2022). Among the findings was that the radiation field hardness has a higher impact on PAH emission than metallicity, with the latter regulating PAH variance as a function of the galactocentric distance. Specifically, the variance of PAH emission with respect to different physical parameters suggests a higher rate of small/medium PAH processing compared to large PAHs and a higher ratio of small-to-large PAHs formed with increasing galactocentric distance.

[30] ALMA Comprehensive High-resolution Extragalactic Molecular Inventory. ALMA is the Atacama Large Millimeter Array.

Spitzer data were combined with new CO(1–0) observations of 24 intermediate redshift galaxies along with literature data of galaxies (z = 0–4), to explore scaling relations between the dust and gas content using PAH emission at 6.2 μm, CO and IR luminosities (Cortzen et al. 2019). They found that on galaxy integrated scales, PAH emission is better correlated with cold rather than warm dust emission, suggesting that PAHs are associated with the diffuse cold dust, which is another proxy for the mass of molecular hydrogen. The proposed relation of the 6.2 μm PAH emission with the CO luminosity and the molecular hydrogen mass could serve as useful tools for the determination of the physical properties of high-z star-forming galaxies.

In most galaxies, the fluxes of rotational H_2 lines strongly correlate with star formation diagnostics (such as PAHs), suggesting that H_2 emission from warm molecular gas is a minor by-product of star formation. In this vein, Spitzer data were used to analyze the optical properties of a sample of 309 nearby galaxies derived from a sample of 2015 objects (Riffel et al. 2020). They conclude that the excess of H_2 emission seen in AGNs is produced by shocks due to AGN-driven outflows and in the same clouds that produce the [OI] emission. The results provided an indirect detection of neutral and molecular winds and suggest a new way to select galaxies that likely host molecular outflows. Further ground- and space-based spatially resolved observations of different phases of the molecular gas (cold, warm, and hot) are necessary to test this new selection method.

Galaxies with AGN were also studied and characterized in terms of their main types of PAH molecules, the local physical conditions of their irradiating sources and the characteristics of the residing ionized gas (Silva-Ribeiro et al. 2021). Species containing 20–82 C atoms are most abundant in the sample and it was suggested that families of species with only two or three fused rings and a hanging N atom such as aromatic amines might be important targets worthy of consideration in future experimental/theoretical as well as observational studies.

The 11.3 μm PAH emission features were detected in 13 nearby AGNs out of a sample of 27 (Jensen et al. 2017). The fluxes within each aperture were scaled to a luminosity-normalized distance from the nucleus to be able to compare intrinsic spatial scales of AGN radiation spanning about two orders of magnitude in luminosity. The results were interpreted as evidence of the profiles being caused by a common compact central physical process, either in the AGN itself or the circumnuclear star formation linked to the AGN power. A photoionization model was shown to confirm that the AGN radiation field is strong enough to explain the observed PAH surface fluxes within ∼10–500 pc of the nucleus. The results advise caution in the use of PAH emission as a star formation tracer within a kpc around AGN.

Six local systems known to contain AGN that host nuclear star formation were investigated to see whether the 11.3 μm PAH emission feature was destroyed in the close vicinity of the AGN (Alonso-Herrero et al. 2014). It was concluded that the molecules responsible for the 11.3 μm PAH emission survive in the nuclear environments as close as 10 pc from the AGN and for Seyfert-like AGN luminosities. Material in the dusty tori, nuclear gas disks, and/or host galaxies of AGN is likely to provide the column densities necessary to protect the PAH molecules from the AGN radiation field.

The mid-IR PAH emission from 19 local AGN was used to study star formation therein (Esparza-Arredondo et al. 2018). There is a PAH emission deficit in the 11.3 μm feature within the inner few tens of parsecs from the AGN which could be due to the destruction of PAHs or the lack of star formation at these distances.

Finally, data from Hubble Space Telescope (HST), Spitzer, Herschel, and VLT were used to study the OH megamaser galaxy IRAS 16399-0937 whose IR emission is dominated by

PAH features (Sales et al. 2015). The picture that emerges of IRAS 16399-0937 is that of a gas-rich merger of mass ratio of 1:1. The merger has triggered widespread star formation but massive gas flows into the still distinct nuclei have not yet fully developed. The North nucleus of IRAS 16399-0937 harbors an embedded AGN of relatively modest luminosity and is also the likely source of the OH megamaser emission, while the South nucleus is starburst dominated. The AGN is apparent almost entirely through the contribution of AGN-heated dust to the IR SED. The optical spectrum upon which the original classification was based is probably due to shocks, rather than AGN photoionization. This work also highlights the value of multiwavelength data and spatial resolution in establishing the nature of the buried power sources in U/LIRGs.

6.1.3 Quasars

Mid-IR (5–40 μm) Spitzer spectra of 86 low-redshift quasars were investigated in terms of their PAH emission and its utility as a star formation rate indicator for the host galaxies of luminous AGN (Xie and Ho 2022). While luminous quasars can severely dilute and affect the detectability of emission lines, PAHs are intrinsically weak in some sources that are otherwise gas-rich and vigorously forming stars, conclusively demonstrating that powerful AGNs destroy PAH molecules. Comparing PAH-based SFRs with independent SFRs derived from the mid-IR fine-structure neon lines and the total IR luminosity reveals that PAHs can trace star formation activity in quasars, but increasingly underestimate the SFR for more powerful quasars. The findings support that AGNs preferentially destroy small grains and enhance the PAH ionization fraction.

Mrk 477 is the closest type-2 quasar at a distance of 163 Mpc. New mid-IR imaging and spectroscopic data obtained with CanariCam was presented which featured no 8.6 or 11.3 μm PAH emission which are commonly used as tracers of recent star formation (Almeida et al. 2023). This is in stark contrast to the presence of a nuclear starburst as constrained by HST observations, so the authors argued that even the more resilient, neutral molecules that mainly produce the 11.3 μm PAH band are most likely being destroyed in the vicinity of the active nucleus despite the relatively large X-ray column density and modest X-ray luminosity. This highlights the importance of remaining cautious when using PAH features as star formation tracers in the central region of galaxies to evaluate the impact of feedback from AGN.

6.1.4 SPICA

Besides the multitudes of telescopes currently in use, the AstroPAH community also had hopes for the development of other large-scale instruments that unfortunately have since been cancelled due to budget restraints. One such was the Space Infrared Telescope for Cosmology and Astrophysics (SPICA) (van der Tak et al. 2018). SPICA would have operated in the mid- and far-IR and it was hoped SPICA would address fundamental issues in our understanding of star formation and the ISM physics in galaxies and in particular, help clarify the complex physical mechanisms which underlie the baryon cycle of galaxies where survey strategies toward PAHs and dust in galaxies were already planned (Kaneda et al. 2017).

6.1.5 First Successes with JWST

In the age of JWST we have already seen exciting developments in the study of galaxies, AGN, and H II regions built on the foundation laid out in the previous pages.

MIRI spectroscopy of three Seyferts were used to compare nuclear PAH emission with that of star-forming regions (Garcia-Bernete et al. 2022b). It has now been found that a suite of PAH features is present in the innermost parts of luminous Seyfert galaxies and that nuclear regions of AGNs lie at different positions of the PAH diagnostic diagrams, whereas the SFRs are concentrated around the average values of star-forming galaxies.

Lai et al. (2022) presented JWST MIRI integral–field spectroscopy of the nearby merging, LIRG, NGC 7469. This galaxy hosts a Seyfert type 1.5 nucleus, a highly ionized outflow, and a bright, circumnuclear star–forming ring, making it an ideal target to study AGN feedback in the local universe. The starburst ring exhibits prominent PAH emission, with grain sizes and ionization states varying by only ∼30%, and a total star formation rate of 10-30 $M_{\odot}$ yr^{-1} derived from fine structure and recombination emission lines. They found that all PAH bands get significantly weaker toward the central source, where larger and possibly more ionized grains dominate the emission, likely the result of the ionizing radiation and/or the fast wind emerging from the AGN. The small grains and warm molecular gas in the bright regions of the ring, however, display properties consistent with normal star-forming regions. The observations of Lai et al. (2022) exemplify the power of JWST to probe the inner regions of dusty, rapidly evolving galaxies for signatures of feedback and inform models that seek to explain the coevolution of supermassive black holes and their hosts.

The PAH band ratio framework for analysis was used to analyze a sample of three nearby galaxies, NGC 628, NGC 1365, and NGC 7496 observed with JWST in the PHANGS[31] survey (Chastenet et al. 2022). Based on the variations observed in the 3.3, 7.7, 11.3 μm features, changes to the average PAH sizes and ionization states could be inferred across the different galaxy environments. It was found that H II regions in all three galaxies were populated by hotter PAHs and/or that the PAH ionization fraction was larger. Additionally, the authors saw evidence of heating and/or changes in PAH size in regions with higher molecular gas content as well as increased ionization in regions with higher Hα intensities.

The next paper from PHANGS presented maps tracing the fraction of dust in form of PAHs in IC 5332, NGC 628, NGC 1365, and NGC 7496 (Chastenet et al. 2023). The PAH fraction was traced by combining the 7.7 μm and 11.3 μm filters to track ionized and neutral PAH emission, respectively and comparing the PAH emission to F2100W, which traces small, hot dust grains. It was found that H II regions show a systematically low PAH fraction, which remains relatively constant across other galactic environments, with slight variations. The results suggest that the process of PAH destruction in ionized gas operates similarly across the four targets.

Thereafter, another PHANGS paper focused on maps of the 3.3 μm PAH emission feature in NGC 628, NGC 1365, and NGC 7496 (Sandstrom et al. 2023). Starlight continuum was removed through a complicated procedure which revealed that between 5% and 65% of the F335M intensity comes from the 3.3 μm feature within the inner radii of the targets. This percentage varies systematically from galaxy to galaxy and shows radial trends within the galaxies related to each galaxy's distribution of stellar mass, ISM, and star formation. The average F335MPAH/F1130W ratio agrees with the predictions of recent models for PAHs with size and charge distributions shifted toward larger grains with normal or higher ionization.

Mid-IR PAH emission from Spitzer was spatially resolved from the central regions of 66 nearby galaxies, roughly evenly divided into star-forming systems and low-luminosity AGN (Zhang et al. 2022a). In conjunction with similar measurements available for quasars, the

[31] Physics at High Angular resolution in Nearby GalaxieS.

aim was to understand the physical properties of PAHs across a broad range of black hole accretion power, with the goal of identifying observational diagnostics that can be used to probe the effect of AGNs on the host galaxy. Whereas the PAH emission correlates tightly with far-UV luminosity in star-forming regions, the spatially resolved regions of AGNs tend to be PAH deficient. Moreover, AGN exhibit on average smaller 6.2/7.7 band ratios and larger 11.3/7.7 band ratios which is suggestive of these anomalous PAH band ratios not being explainable by the effects of the AGN radiation field alone. Instead, they hint that small grains may be destroyed by the combined effects of the radiative processes and shocks, which are plausibly linked to jets and outflows preferentially associated with radiatively inefficient AGNs. While quasars also present PAH deficits and unusual PAH band ratios, their characteristics differ in detail compared to those observed in more weakly accreting AGNs. This could be a possible indicator of fundamental differences in their modes of energy feedback.

The same authors also investigated the use of PAHs as tracers of the molecular gas content in galaxies (Zhang and Ho 2023b). A sample of 19 nearby galaxies with spatially resolved mid-IR spectra from Spitzer was used. PAH emission correlated strongly with CO emission on sub-kpc scales over the diverse environments probed by the sample of star-forming galaxies and low-luminosity AGN. The tight correlation, likely a consequence of photoelectric heating of the diffuse interstellar gas by PAHs, permits us to derive an empirical calibration to estimate molecular gas mass from the luminosity of the PAH emission.

They also analyzed 33 nearby galaxies to study the contribution of evolved stars to the PAH emission (Zhang and Ho 2023a), but PAH emission is also a promising tool for estimating the SFR in galaxies. They demonstrated that the traditional empirical correlation between PAH luminosity and SFR has a secondary dependence on specific SFR, or, equivalently, stellar mass. UV-faint regions with lower specific SFRs and hence a greater fraction of evolved stars emit stronger PAH emission at fixed SFR than UV-bright regions. The PAH-based SFR estimator is thus reformulated to account for mass as a second parameter to account for the contribution of evolved stars to PAH excitation, but the influence of evolved stars can be invoked to explain the sublinear correlation between PAH emission and SFR, and it can also partly account for the PAH deficit in dwarf galaxies and low-metallicity environments.

Finally, JWST observations detecting the 3.3 μm PAH feature in a galaxy observed less than 1.5 billion years after the Big Bang were presented (Spilker et al. 2023). The large equivalent widths of the PAH features indicated that star formation, rather than black hole accretion, dominates the IR emission throughout the galaxy. The emission of PAH molecules, hot dust and large dust grains and stars were observed to be spatially distinct from one another, leading to order-of-magnitude variations in PAH equivalent widths and ratios of PAHs to total IR luminosity across the galaxy. The spatial variations we observe suggest either a physical offset between PAHs and large dust grains or wide variations in the local UV radiation field. The observations demonstrated that differences in emission from PAH molecules and large dust grains are a complex result of localized processes within early galaxies.

6.2 Experiments

The X-ray regime of the electromagnetic spectrum is an experimentally challenging one. X-ray photons have the unique energetic quanta to excite electrons in the very core of the individual atoms in molecules. This can lead to multiple ionizations and/or so-called Auger cascades where the multiply charged species become increasingly unstable. This can lead

to so-called Coulomb explosions where the multiply charged species explode into different ionic and reactive fragments. Experiments in this regime that are relevant to astronomical PAHs then tend to be either dedicated to the excitation mechanism itself where PAHs, fullerenes, or dust analogs absorb an X-ray photon, or to the reactive fragments resulting from the X-ray induced explosions of PAHs.

6.2.1 XUV Excitation: Femtosecond Relaxation and Dissociation

Following electronic excitation in large molecules such as PAHs, nuclear dynamics verily occur which lead to a breakdown of the Born-Oppenheimer approximation as the timescales of electronic and nuclear motion become comparable. Utilizing high harmonic generation in rare gas atoms, XUV photons can be produced to interact with PAHs. This has been done at the *Institut Lumière Matière* where XUV-IR pump-probe experiments on naphthalene, anthracene, pyrene and tetracene showed the ultrafast relaxation following XUV excitation of the PAH cations (Marciniak et al. 2015). The rapid relaxation is due to the favorable topology of the seams of conical intersections corresponding to slight distortions of the rigid molecular backbone which relax within a fraction of the vibrational period. Later measurements comparing naphthalene and adamantane measured the relaxation timescales in the fs range and the findings indicate that the electronic lifetimes increase with both the molecular size and the cationic excitation energy, and that multi-electronic and non-Born-Oppenheimer effects must be accounted for to provide accurate theoretical calculations (Marciniak et al. 2019).

These measurements were followed up with time-resolved mass spectrometry combining XUV and IR pulses to investigate the underlying dynamics induced by high-energy photon excitation in PAHs of varying sizes (Boyer et al. 2021). It was demonstrated that excited cations relax through a progressive loss of vibrational selectivity, created at the early-stage dynamics, and which represents the first steps of a complete intramolecular vibrational energy redistribution. This process is found to be in competition with correlation-band dynamics found previously (Marciniak et al. 2015).

It is worthwhile expanding on the PAH correlation bands which are features created by electron correlation in PAHs and other molecules. By studying the ultrafast energy relaxation of size-scalable 2D molecules following ionization by an ultrashort UV pulse the same group observed that long lifetimes linearly increase with the number of valence electrons (Hervé et al. 2021) (Fig. 9). This allowed them to construct a general law based on solid-like electron-phonon scattering which explains the results and previous work.

Other experiments have been performed at the CFEL-ASG[32] Multi Purpose (CAMP) endstation at the beamline BL1 at FLASH1[33] in Hamburg, Germany, where three PAHs, fluorene, phenanthrene, and pyrene, were investigated in a similar XUV+IR pump-probe manner (Lee et al. 2021). Relaxation times for the electronically excited states of monomers, monocations, and dications were reported and were on the order of tens of fs for all the types of excited species studied. Secondly, using recoil-frame covariance analysis between ion images, it was demonstrated that the dissociation pathways of PAH dications favor two-body breakup processes and/or losses of neutral fragments totaling an even number of carbon atoms.

This work was followed up by using XUV (30.3 nm) radiation and visible photons from an optical laser to investigate the relaxation and fragmentation dynamics of fluorene ions (Garg et al. 2022). The relaxation lifetimes of the excited fluorene monocation and dication

[32] Center for Free-Electron Laser Science - Advanced Study Group.

[33] https://astropah-news.strw.leidenuniv.nl/AstroPAH_0036.pdf.

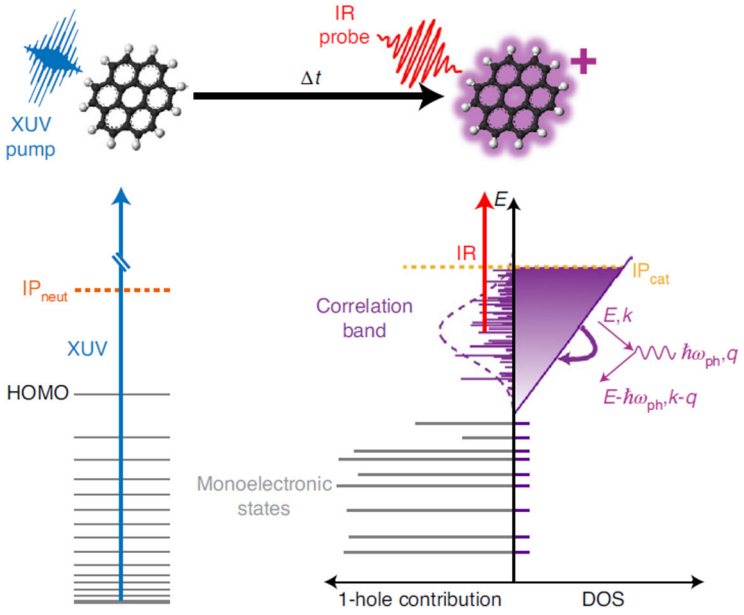

Fig. 9 Ionization of the inner valence shells of PAHs, well below the HOMO by an XUV pulse. This leads to the formation of a correlation band comprising strongly coupled multielectronic states below the double ionization threshold. The correlation bands can then be described as a solid-like band with a linear density of states. Adapted with permission from Hervé et al. (2021). Copyright 2021 under exclusive licence to Springer Nature Limited

obtained through the fragment formation channels were reported to be in the range of a few tens of fs to a few ps using visible radiation as a probe rather than IR. This difference in the lifetimes of the excited states when probed with a visible light pulse was attributed to its higher probe energy which is capable of exciting lower-lying states of doubly ionized fluorene to triply ionized fluorene, resulting in an increase in the observed relaxation lifetimes. Additionally, a longer lifetime corresponding to the $C_{11}H_x^+$ fragment ion in comparison to other fragments was reported which was attributed to the formation pathway leading to $C_{11}H_x^+$ involving acetylene loss from the parent species which is thought to proceed via a mechanism involving rearrangement of the rings to allow the C_2H_2 loss.

To further elucidate these X-ray induced fragmentation dynamics, the recoil-frame covariance analysis was further utilized to determine the total kinetic energy release (TKER) associated with multiple fragmentation channels with high precision (Lee et al. 2022). They measured TKER ranged from 1.94–2.60 eV for dications and 2.95–5.29 eV for trications. Multiple different fragments were observed in the dissociation of the dications and trications that were indicative of significant molecular and rearrangement and residual binding in the dissociation process.

Similar fragmentation dynamics have also been studied for the adamantane dication (Maclot et al. 2020). There it was demonstrated that the dissociation is a two-step process involving opening up the adamantane cage, which is then followed by Coulomb repulsion-driven fragmentation. Likewise have similar fragmentation dynamics and products been observed in the 70 eV electron impact double ionization of PAHs like anthracene (van der Burgt and Gradziel 2022).

6.2.2 X-ray Spectroscopy and Fragmentation Dynamics

Work with X-rays at significantly higher energies ($E_{ph} \geq 100$ eV) has also been reported. X-ray photoelectron spectroscopy is an important tool to investigate the chemical and electronic structures of molecules but in high-resolution X-ray photoelectron spectroscopy it is possible to resolve fine structures in the spectra that are a manifestation of the vibronic coupling effect, i.e., the coupling between nuclear vibrations and the electronic degrees of freedom. Besides experimental work described here below, XP spectra have also been theoretically computed for a number of PAHs (Cheng et al. 2022).

Examples of experimental results include the response of superhydrogenated gas-phase coronene cations upon soft X-ray absorption has been reported with primarily dications forming upon resonant excitation at 285 eV (Reitsma et al. 2014).

Much work has been done at the Brazilian Synchrotron Light Source Laboratory (LNLS) into the interaction of PAHs and related molecules with soft X-rays. The ionization and subsequent fragmentation of toluene into $C_nH_x^+$ ions and doubly ionized hydrocarbons using 280–320 eV photons were also studied with photoelectron photoion photoion coincidence (PEPIPICO) schemes (Monfredini et al. 2016). The authors also measured absorption, single photoionization and double photoionization cross sections at these energies. This has been followed up with detailed work comparing the VUV and soft X-ray induced ionization and dissociation (covering photon energies from 10.8 to 307 eV) of benzene and cyclohexane where absolute cross sections and partial ion yields were measured (Quitián-Lara et al. 2018). The authors also computed photo-rates using the radiation field relevant to the well-studied PDR of the PN NGC 7023.

The same authors have also reported on the photoionization and photodissociation of biphenyl upon its interaction with soft X-ray photons at energies around the inner-shell C1s resonance, i.e., 275 and 310 eV (Quitián-Lara et al. 2020). While the recorded mass spectra before the C1s resonance is dominated by single photoionization processes leading to $C_6H_5^+$, $C_6H_4^+$ and $C_{12}H_{10}^+$, after the resonance it was observed that multiple photoionization processes are more dominant. The authors also compared the results of biphenyl dissociation with that of benzene and naphthalene and discussed them in the context of four PNe featuring PAH IR emission: BD+30°3639, NGC 7027, NGC 5315, and NGC 40. They also suggest the presence of long-lived doubly charged ions $C_6H_3^{2+}$ and $C_6H_5^{2+}$.

The same authors also carried out a computational study of the dissociation of naphthalene following absorption of 2.5 keV photons (Santos et al. 2022). At such higher energies, naphthalene can be formed in various charge states, q, namely $q = 0, +1, +2, +3$, and $+4$. Contextualizing the dissociations and formations of multiply charged hydrocarbon species, the authors computed IR spectra of the fragments and compared them to the IR emission spectra of an AGN region, NGC 7582.

High-energy X-ray absorption spectroscopy has also been used to study implantation and behavior of heavy noble gases in few-layer graphene sheets and in nanodiamonds where the noble gas atoms distort the layers, forming bulges (Shiryaev et al. 2021). If the atom is trapped in the curved domain, considerable additional energy is required to displace it. DFT methods were also used to calculate the carbon K-edge X-ray absorption spectra of two large tetrahedral nanodiamonds, $C_{26}H_{32}$ and $C_{51}H_{52}$ where the authors propose a possible detection of nanodiamonds from X-ray spectra by future telescopes (Bilalbegović et al. 2018). Ionization and fragmentation of the metallo-endohedral fullerene $SC_3N@C_{80}$ using ultrashort (10 fs) X-ray pulses at 5.0 keV have also been reported (Obaid et al. 2019).

The fragmentation dynamics of adamantane dications produced following core-ionization at the carbon edge following Auger decay were also studied with the coincidence

technique (Ganguly et al. 2022). Detailed coincidence maps of the fragments formed provide intricate details of the dissociation processes where $C_2H_3^+$ and $C_3H_3^+$ ions are found to be particularly abundant with branching ratios totaling 36.7% and 23.1%, respectively.

6.3 Modeling

PAHs have shown themselves to be probes of the evolution of the Milky Way as well as galaxies at high redshift. Here we briefly summarize the progresses of galactic modeling which involves PAHs.

As PAHs are among the major dust components in the ISM, the evolution of PAH abundances in the ISM on a galactic evolutionary timescale was studied by Seok et al. (2014). Their models consider turbulence-induced dust grain shattering as the major formation mechanism of PAHs and coagulation onto dust grains, destruction by supernova shocks, and incorporation into nascent stars as the principal depletion mechanisms. The models accurately replicate both the paucity of PAHs in low-metallicity galaxies and the metallicity dependence on the PAH abundance in high-metallicity galaxies. This dependence on metallicity is the result of metal accretion onto dust grains, which increases the mass of dust and eventually causes it to shatter into PAHs. Seok et al. (2014) conclude that the observational trends of PAH abundances may be a natural consequence of shattering of carbonaceous grains being the sources of PAHs.

While the metallicity-dependence on PAH abundance in high-metallicity galaxies may be sensitive, it also opened new avenues to explore further how this dependence relates to PAH destruction on galactic scales. Priestley et al. (2022) showed that incorporating a sufficiently strong metallicity dependence into models of galaxy evolution removes the need for low stellar dust yields. The contribution of stellar sources to the overall dust budget may hence be significantly underestimated, and that of grain growth overestimated by models assuming a constant destruction efficiency.

In some cases of gas-rich galaxies at high redshift, the presence of extremely strong damped lyman α absorber may obscure PAH emission from nearby galaxies. In the case of QSO SDSS J1143+1420, there is no direct detection of PAH emission due to the limited observations of IR spectra along this sightline (Shaw and Ranjan 2022). Hence, indirect methods to detect PAHs in gas-rich absorption-selected galaxies at high redshift were explored. The CLOUDY numerical simulation was used to indirectly probe the presence of PAHs in the nearby extremely strong damped lyman α absorber and the presence of PAHs were indirectly inferred with an abundance of PAH/H $= 10^{-7}$. As a result, Shaw and Ranjan (2022) successfully highlighted the usage of CLOUDY modeling to indirectly detect PAHs in high-redshift gas-rich absorption-selected galaxies.

Another way to use PAHs indirectly to deepen our understanding of galactic process is to use their presence to shed more light on the cosmic-ray ionization rate (ξ) in our Galaxy. The value of ξ is determined by matching observed column densities of H_3^+ and H_2, but the presence of PAHs affects the electron density in the region under scrutiny which in turn changes the H_3^+ density and the derived value of ξ. To study the effects of the PAHs on ξ. Shaw and Ferland (2021) built a grid of calculations using the CLOUDY code to determine the cosmic ray ionization rate to match the column densities of H_3^+ and H_2. They found that models with average Galactic PAH abundances give a value of ξ an order of magnitude smaller than models without PAHs in our Galaxy so care must be taken when ξ is estimated along different sightlines.

7 Cold Molecular Clouds - Microwave Spectroscopy

While PAHs are considered as the primary source of the AIBs, these emission features fall in the mid-IR frequency range and while they are indicative of the vibrational modes involving C – C and C – H stretching and bending vibrational modes of aromatic species, assignments to individual PAHs is next to impossible, mainly due to the structural similarities among diverse PAHs which lead to differences in vibrational frequencies smaller than the width of the interstellar band profile (Sect. 2). As a consequence, the IR spectra of most PAHs are indistinguishable at the resolving power that can be achieved by astronomical observations.

Meanwhile, radio astronomy offers clear means to detect interstellar molecules although it also brings challenges when it comes to detecting individual PAHs. This is mainly attributed to the low or even absent dipole moment of several PAHs, alongside with their unfavorably large rotational partition functions, even at low temperatures. The latter typically results in the population distribution spread among several rotational levels which subsequently leads to a decrease in intensity of any given rotational transition. Nevertheless, radio astronomy can still be used for the detection of PAHs which are characterized by a sizeable dipole moment and relatively low rotational partition functions. Nitrogen substituted PAHs, for instance, have well-distinguishable rotational spectra, rendering them promising candidates for radio astronomy searches. The first search for quasi-asymmetric interstellar PAHs using rotational spectroscopy and matched filtering was carried out on data recorded with the Green Bank Observatory (GBO) in the star-forming region IC-348 within the Perseus molecular cloud, a known source of dust-correlated AME (Ali-Haïmoud et al. 2015). The noise level was not sufficient to allow detection of PAHs. However, it was still possible to gain information about upper bounds on the abundance of quasi-symmetric PAHs.

7.1 Observations

Evidence of benzonitrile, one of the smallest nitrogen-containing aromatic molecules, was found in TMC-1, a cold molecular cloud, through data collected by the Nobeyama 45-m telescope. Its detection in the TMC-1 was confirmed with the observation of nine of its individual transitions using the 100-m telescope at GBO (McGuire et al. 2018). In the same work, the authors documented the non-detection in the TMC-1 of various aromatic molecules, including several PA(N)Hs and nitriles. These encompassed molecules like cyclopropylcyanide, furan, pyrrole, pyridine, phenol, anisole, benzaldehyde, azulene, fluorene, acenaphthene, and acenaphthylene.

The detection of benzonitrile is seen as an indirect detection of the radio-invisible benzene. Therefore, if its presence can be confirmed in other astronomical sources, benzonitrile holds the potential to serve as a radio probe for aromatic chemistry. In line with this perspective, efforts were undertaken to search for benzonitrile in four additional astronomical sources: Serpens 1A, Serpens 1B, Serpens 2, and MC27/L1521F (Burkhardt et al. 2021b). These investigations yielded radio astronomical evidence of benzonitrile with the detection of three out of the four targeted rotational transitions across all four astronomical sources, thus suggesting that aromatic molecules are ubiquitous in interstellar environments. The abundance of benzonitrile in these interstellar sources far exceeds the predictions made by chemical models that are known to accurately reproduce the abundance of carbon chains like HC_7N, a cyanopolyyne with the same number of heavy atoms as benzonitrile. Additionally, noticeable variations in abundance are observed among clouds of comparable ages. These observations imply that the chemistry of small planar aromatic molecules is favorable but still poorly understood and that more laboratory and theoretical studies are needed.

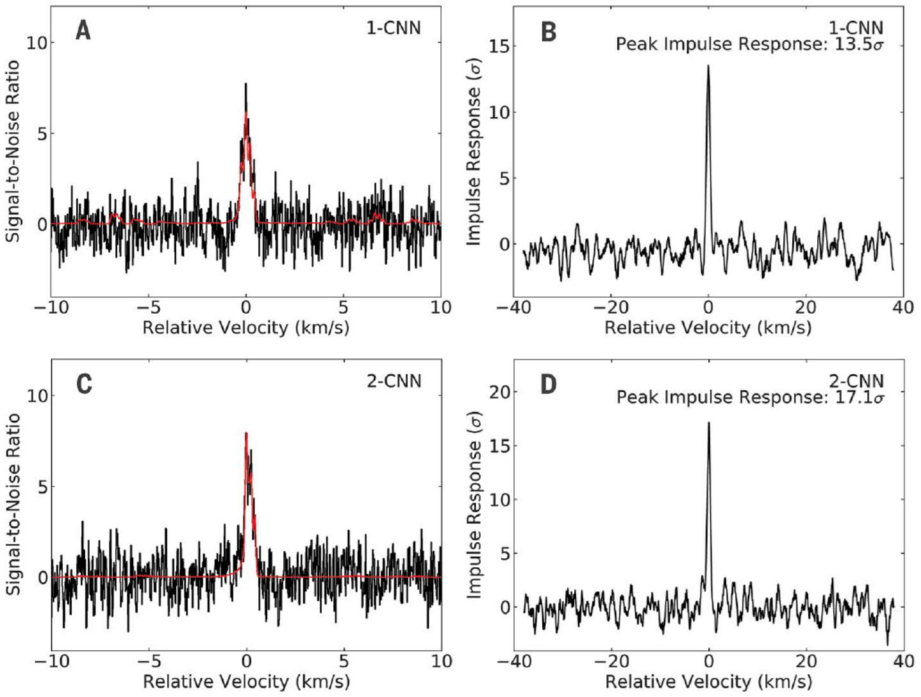

Fig. 10 Stacked spectra for the matched filtering analyses of both 1- and 2-cyanonaphthalene isomers in the interstellar molecular cloud TMC-1. Stacked spectra from the GOTHAM data are shown in black for 1-CNN (A) and 2-CNN (C) overlaid with the line profile in red. Peak impulse responses functions of the stacked spectra are shown for 1-CNN in (B) and 2-CNN in (D). Adapted with permission from McGuire et al. (2021). Reprinted with permission from AAAS. Copyright 2021

In the same year, Loomis et al. (2021) introduced a new approach to enhance detection efficiency and mitigate the impact of rotational dilution in molecules possessing relatively large rotational partition functions, like PAHs. This method involves combining Markov chain Monte Carlo (MCMC) inference with spectral line stacking and matched filtering techniques. The application of this new method on data recorded using the 100-m Green Bank telescope resulted in the detection in the TMC-1 molecular cloud of several species, including $HC_{11}N$, the largest cyanopolyyne detected so far and the first two interstellar polycyclic aromatic hydrocarbons: the two cyano-functionalized isomers of cyanonaphthalene (1-, and 2-cyanonaphthalene) in the TMC-1 molecular cloud (McGuire et al. 2021) (see Fig. 10).

Two possible routes were proposed to explain the formation of cyanonaphthalene, one involving a bottom-up approach and one a top-down approach. However, neither of these routes could account for the abundances derived for the two isomers (McGuire et al. 2021). The detection of the two isomers of cyanonaphthalene was then followed by the discovery of the first pure polycyclic aromatic hydrocarbon indene, within the TMC-1 molecular cloud. Employing MCMC method to derive the column density revealed that indene stands as the most abundant detected molecule containing a five- or six-membered ring in the TMC-1 (Burkhardt et al. 2021a). Its cyano derivative, the 2-cyanoindene, was later detected in the same molecular cloud. Its detection allowed for the first observation of the ratio of a cyano-substituted PAHs to its pure hydrocarbon counterpart (Sita et al. 2022).

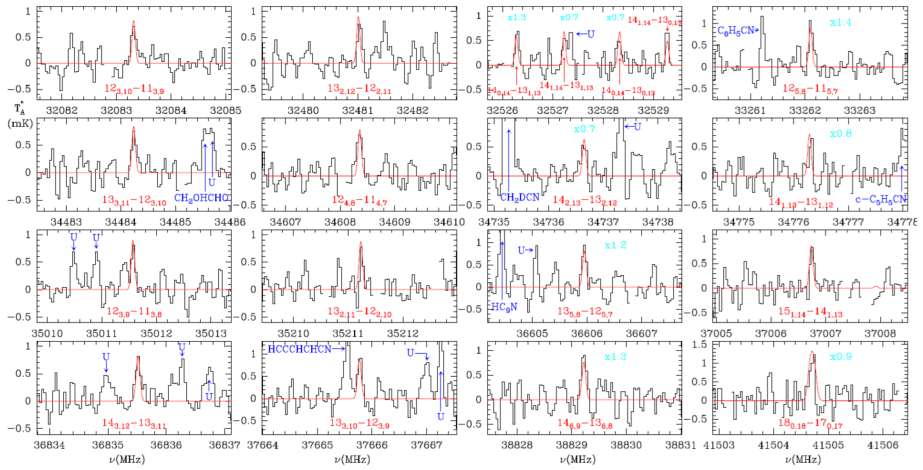

Fig. 11 Selected transitions of indene detected in the interstellar molecular cloud TMC-1. The abscissa correspond to the rest frequency. The quantum numbers for each transition are indicated in red in the lower part of each panel. Red lines show the computed synthetic spectrum of indene for a rotational temperature of 10 K. Cyan labels refer to the multiplicative factor applied to the best fit model that matches the observations. Adapted with permission from Cernicharo et al. (2021b). Copyright 2021. Reproduced with permission from Astronomy & Astrophysics, © ESO

Using data, also collected with the 100-m Green Bank Telescope, Shingledecker et al. (2021) reported on the discovery of cyanoacetyleneallene in TMC-1. This molecule holds the potential to bridge the gap between chains and rings in the TMC-1. Following the discovery of pure and CN- and CH_2- functionalized aromatic molecules, the logical step to undertake was to explore the presence of heterocycles. In line with this direction, Barnum et al. (2022) undertook a search for several heterocycles within TMC-1. Their investigation was focused on heterocycle compounds like pyrrole, imidazole, pyridine, pyrimidine, quinoline, isoquinoline, and furan. None of these species could be detected in TMC-1.

Along with observations at the GBO, new receivers built within the Nanocosmos project and installed at the Yebes 40m telescope have been used for observations of TMC-1 and the subsequent discoveries of dozens of new molecules in the past few years. Among these new discoveries are the PAH indene (see Fig. 11), and the aromatic monoringed species ethynyl-cyclopropenylidene, cyclopentadiene (Cernicharo et al. 2021a) and orthobenzyne (Cernicharo et al. 2021b). These aromatic species only represent the tip of the iceberg of recent molecule discoveries.[34]

7.2 Experiments

7.2.1 Microwave / Rotational Spectroscopy

The basics of rotational spectroscopy of PAHs was reviewed in one of the first papers submitted to AstroPAH (Ali-Haïmoud 2014). The work showcased that the asymmetry of planar, nitrogen-substituted symmetric PAHs is small enough that their rotational spectrum when observed with MHz resolution has the appearance of a 'comb' of evenly spaced stacks of

[34] https://astropah-news.strw.leidenuniv.nl/AstroPAH_0078.pdf.

Table 5 Examples of published rotational spectra of PAHs and aromatic molecules

Molecule	Spectral range	Reference
9-Fluoreneone ($C_{13}H_8O$)	52 – 74.4 GHz	Maris et al. (2015)
Corannulene:water ($C_{20}H_{10}-H_2O$)	2 – 8 GHz	Pérez et al. (2017)
Acenaphthene:water ($C_{20}H_{10}$-H_2O_n, n = 1-4)	2 – 8 GHz	Steber et al. (2017)
Acenaphthene ($C_{12}H_{10}$)	75 – 110 GHz	Gruet et al. (2020)
Phenanthrene:water ($C_{14}H_{10}$-H_2O_n, n = 1-3)	2 – 8 GHz	Loru et al. (2021)
Phenanthridine:water ($C_{13}H_9N$-H_2O_n, n = 1-3)	2 – 8 GHz	Loru et al. (2021)
Imidazole ($C_3H_4N_2$)	75 – 110 GHz	Arenas et al. (2021)
Iso-pentane (C_5H_{12})	84 – 111 GHz	Pandey et al. (2023)

lines and that this simple pattern allows for the use of matched-filtering techniques which results in a significantly enhanced signal-to-noise ratio. This exact technique was then later used when the first individual PAH was detected in TMC-1 (McGuire et al. 2021).

Ali-Haïmoud (2014) also discussed the possibility of PAHs being the originators of the AME, which at the time was believed to originate from collective PAH rotation or spinning dust grains. The AME is discussed further in Sect. 11.

Multiple groups worldwide are dedicated to rotational spectroscopy and many works have been performed on PAHs and aromatic molecules in the past decade. Table 5 showcases the examples published in the first ten years of AstroPAH.

Microwave spectroscopy offers a powerful tool, not only to search for the fingerprints of PAH molecules in space, but also to determine structural configurations. Previous studies have elucidated two structural forms of the corannulene-water complex (Pérez et al. 2017), and how water molecules arrange themselves on PAH surfaces (Steber et al. 2017; Loru et al. 2021). This forms strong links with ongoing investigations dedicated to the solubility of PAHs in water and PAHs frozen in ice matrices (see Sect. 4.2.4).

Rotational spectra of several PAHs have also been computed such as those of N- and CN-containing pyrene and coronene molecules (Vats and Pathak 2022) as well as naphthalene in all of its N-substituted forms (Vats et al. 2023b).

8 Star and Planet Formation - Herbig Ae Objects and Protoplanetary Disks

The IR signatures of PAHs are not only observed in the regions like PDRs, around H II regions, and high-redshift galaxies. They can also be found in protoplanetary disks and around Herbig Ae/Be stars, i.e., stars in their infancy. The presence of PAHs can also be assumed in these regions from products that are formed by the photo-induced destruction of PAHs. This section briefly showcases work relevant to such regions.

8.1 Observations

8.1.1 Intergalactic Star-Forming Objects

Spitzer data were used to analyze 10 intergalactic star-forming objects (Higdon et al. 2014). The majority of them have relative PAH band strengths similar to those of nearby spiral and

starburst galaxies. In contrast to what is observed in blue compact dwarfs and local H II regions in the Milky Way (e.g., NGC 3603) and the Magellanic clouds (30 Doradus and N 66), these bands correspond to models with a significant PAH ion fraction (less than 50%) and a bright emission from large (over 100 C atoms) PAHs. Most of the intergalactic star-forming objects have approximately 10^6 solar masses of warm H_2 that likely originates from PDRs, and they have a bright 8 μm, mostly likely due to PAHs, relative to normal spirals, dwarf irregulars and blue compact dwarf galaxies.

8.1.2 Herbig Ae/Be Stars

Mid-IR polarimetric images and spectra of WL 16, a Herbig Ae star at a distance of 125 pc were analyzed by Zhang et al. (2017c). The Herbig Ae star is surrounded by a protoplanetary disk of ∼900 AU in diameter, making it one of the most extended Herbig Ae/Be disks as seen in the mid-IR. Furthermore, it is behind or embedded in the ρ Ophiuchus molecular cloud. It has PAH emission bands with an anticorrelation between the PAH surface brightness and the PAH ionization fraction between the north-west and south-west side of the disk.

Polarized PAH emission at 11.3 μm was detected in the nebula associated with the Herbig Be star MWC 1080 (Zhang et al. 2017b). A polarization degree of 1.9% ± 0.2% is measured which is unexpectedly high compared to models. This challenges the current understanding of the alignment of PAHs, which is required to polarize the PAH emission, but this is thought to be substantially suppressed. Such a high level polarization might be due to the PAH alignment with a magnetic field via a resonance paramagnetic relaxation process.

The mid-IR PAH emissions have also been investigated in the disk of HD 179218 which is an intermediate-mass Herbig star (Taha et al. 2018). The radiative transfer modeling of the SED suggests that the resolved emission should result from PAH molecules on the disk atmosphere being UV excited by the central star. Based on the spatial and spectroscopic considerations a scenario in which PAHs extend out to large radii across the flared disk surface is favored. Simultaneously, the PAHs are ionized due to the strong UV radiation field of the central star.

Deep IR (10–20 μm) images have also been recorded of the immediate environments of the Herbig Be stars MWC 1080 and HD 259431 (Li et al. 2014). These are two very young objects but both also exhibit diffuse nebulosities. It was demonstrated that the well-extended emission around MWC 1080 traces neither a disk nor an envelope, but rather the surfaces of a cavity created by the outflow from MWC 1080A, the primary star of the MWC 1080 system. Li et al. (2014) confirmed that the environment around MWC 1080, where a small cluster is forming, is strongly affected by the outflow of the central Herbig Be star and similarities between the two objects suggest that the filamentary emission around HD 259431 may also arise from a similar outflow cavity structure.

8.1.3 Photodissociation Region with Moderate Ultraviolet Field

Emission lines of small hydrocarbons and complex organic molecules (COMs) precursors were studied in PDRs in the S235A star-forming complex with relatively weak radiation fields (smaller than 50 Habing[35]) using the IRAM[36] 30-m telescope (Kirsanova et al. 2021).

[35] 1 Habing = 1.6×10^{-3} erg cm^{-2} s^{-1} is the energy density of the average interstellar UV field (Habing 1968).

[36] Institut de radioastronomie millimétrique.

The abundance ratio of C_2H to CH_3OH is lower by a factor of few or an order of magnitude in comparison to the Horsehead and Orion nebula PDRs which is similar to values in hot corinos in the Perseus cloud. They concluded that ion–molecular and grain–surface chemical routes rule the molecular abundances in the PDRs and that they inherit molecular abundances from the previous dark stage of molecular cloud evolution in spite of massive stars already emitting in the optical (Kirsanova et al. 2021).

8.1.4 Protoplanetary Disks

The VISIR[37] camera at VLT was used to image "Gomez's hamburger" which is thought to be a potential protoplanet in the protoplanetary disk which exhibits bright PAH emission that is commonly observed in Herbig Ae/Be stars (Berné et al. 2015a). Analyzing this emission, the physical characteristics are consistent with Gomez's hamburger having a clumpy region between the edges of the PAH emission and the CO emission which could correspond to a planet in its infancy.

Resolved C_2H emission within the protoplanetary disks of TW Hya and DM Tau has been studied along with C_3H_2 emission that is also found with an identical spatial resolution (Bergin et al. 2016). Reproducing the emission of these important hydrocarbons that are intimately related to UV-processed PAHs requires a strong UV field in the upper disk atmosphere and outer disk beyond the edge of the pebble disk. This arises in a disk where the ice coated dust mass is spatially stratified because of the combined effects of coagulation, gravitational settling and drift. This stratification causes the disk surface and outer disk to have a greater permeability to UV photons. These hydrocarbons are thus assumed to appear from the photodissociation of small PAHs.

How much carbon can be delivered to young planets is still an open question and an important one as the chemical characterization of planet-forming disks is a crucial step in our understanding of the diversity and habitability of exoplanets. Tabone et al. (2023) presented the JWST detection of abundant hydrocarbons in the disk of a very low-mass star obtained as part of the Mid-InfraRed Instrument mid-INfrared Disk Survey (MINDS). In addition to very strong and broad emission from C_2H_2 and its $^{13}C_{12}CH_2$ isotopologue, C_4H_2, benzene, and possibly CH_4 were identified, but water, PAHs and silicate features were weak or absent (see Fig. 12). These detections testified to an active warm hydrocarbon chemistry with a high C/O ratio larger than unity in the inner 0.1 astronomical units (AU) of this disk, perhaps due to destruction of carbonaceous grains and the exceptionally high C_2H_2/CO_2 and C_2H_2/H_2O column density ratios indicated that oxygen is locked up in icy pebbles and planetesimals outside the water iceline.

8.2 Experiments and Theory

Experimental and theoretical works directly relating to subjects of star- and planet formation are difficult to categorize. In fact, to harmonize the observations of protoplanetary disks and Herbig Ae/Be stars, models are often constructed that take into account the same input parameters as models of PDRs and other highly irradiated regions. However, these objects can be significantly hotter than cold molecular gas which can lead to significant changes in the physical chemical parameters of the molecules present in models, such as absorption cross sections (Tennyson and Yurchenko 2017).

[37] Very large telescope Imager and Spectrometer for the mid-InfraRed.

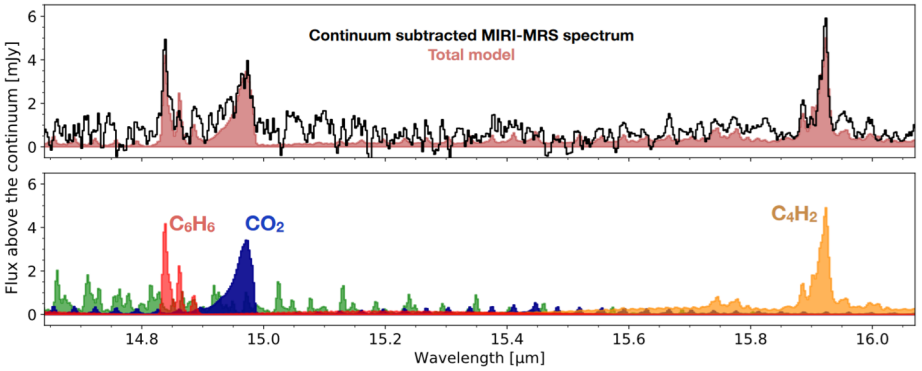

Fig. 12 Detection of key molecular transitions of C_6H_6, CO_2, and C_4H_2 in the 14.7 - 16.0 μm spectral region of the low-mass star J160532 using the MIRI instrument on JWST. The lower panel displays the best fit slab models of C_6H_6, CO_2, and C_4H_2 emission. Adapted with permission from Tabone et al. (2023). Copyright 2023 under exclusive licence to Springer Nature Limited

8.3 Modeling

8.3.1 Protoplanetary Disks

As planet-forming disks of gas and dust around young stars are known to contain PAHs, several models have been constructed to understand how the presence of PAHs can be used to understand star- and planet-formation to a greater extent.

A model has been built to characterize the charge state of PAHs so it could be used as a probe of flows of gas through protoplanetary gaps (Maaskant et al. 2014). PAH ionization is most sensitive to UV radiation and electron density so ionized PAHs trace low-density optically thin disk regions where the UV field is high and electron density is low. In optically thick disks, however, PAHs are predominantly neutral. It was found that PAH spectra of transitional disks can be understood as superpositions of neutral and ionized PAHs where it was demonstrated that fitting the PAH spectra of 4 transitional disks requires a contribution of ionized PAHs in gas flows through the gap. For the disk in HD 97048, neutral PAHs in the optically thick disk dominated the spectrum, while in the cases of HD 169142, HD 135344B and Oph IRS 48, small amounts of ionized PAHs located in gas flows through the gap are strong contributors to the total PAH luminosity. The observed trend in the sample of Herbig stars between the disk mass and PAH ionization may imply that lower-mass disks have larger gaps so ionized PAHs in the gas flows contribute more strongly to their spectra.

Data from various telescopes (AKARI, Spitzer, *etc.*) were used to model dust and PAH emission in the HD 34700 debris disk with the aim of exploring its dust and PAH properties (Seok and Li 2015). They found that porous dust together with a mixture of neutral and ionized PAHs closely explains the dust IR SED and PAH emission features in the disk. Substantial removal of dust and PAHs has occurred in the disk and continuous replenishment of these materials is required to maintain their abundances. This implies that these are not primitive materials but are the secondary products that probably originate from mutual collisions among planetesimals, asteroids and comets.

The same authors also modeled the dust in the pre-transitional disk around the Herbig Ae star HD 169142 to replicate the SED and the PAH emission features of the disk simultaneously with porous dust and astronomical PAHs taking into account the spatially resolved

disk structure (Seok and Li 2016). The accretion of ice mantles onto porous dust aggregates occurs between 16 and 60 AU which overlaps with the spatial extent (50 AU) of the observed PAH emission features.

Larger data sets of protoplanetary disks have also been modeled. The PAH emission bands (3.3, 6.2, 7.7 8.6, 11.3, and 12.7 μm) were modeled for 69 protoplanetary disks around 14 T Tauri stars and 55 Herbig Ae/Be stars (Seok and Li 2017). A size distribution and charge state was determined for the PAH populations and correlations of the PAH properties were investigated with the stellar properties. The characteristic PAH size tends to correlate with the stellar effective temperature which is interpreted in terms of the photodissociation of small PAHs in systems with higher effective temperatures. Interestingly, the ionization fraction does not seem to correlate with any stellar parameters. The marginally negative correlation between PAH size and stellar age suggests that continuous replenishment of PAHs via outgassing of cometary bodies and/or the collisional grinding of planetesimals and asteroids is required to maintain the abundance of smaller PAHs against full destruction by photodissociation.

The physical and chemical structure of a T Tauri disk has also been modeled to predict the abundances of mid-IR fluxes of observable molecules in anticipation of JWST (Anderson et al. 2021). Photon-driven chemistry in the inner disk surface layers largely destroys the initial carbon and oxygen carriers, which causes models with the same physical structure and C/O ratio to have similar steady-state surface compositions, regardless of the initial chemical abundances. Finally, initial disk compositions are better preserved in the shielded inner disk midplane.

9 The Solar System - Meteorites, Comets, and Titan

Since the first exploration of the outer solar system and beyond by the Voyager spacecraft, the insights we have gained from its chemical inventory have largely contributed to a better understanding of the solar system and Earth's own evolution. In particular, these cold and distant environments have made it possible to indirectly access the protosolar composition. In these regions, PAHs are expected to be found on comets and icy moon surfaces and/or in atmospheres. They are thought to be incorporated into comets and icy moons during their formation, through UV radiation and microphysical agglomeration.

To date, PAHs have been detected in the *comae* of comets, such as 67P/Churyumov-Gerasimenko and 103P/Hartley 2, some meteorites, and they are predicted to be involved in the organic growth of aerosols of Titan's atmosphere. In this section, major PAH and PAH-related detections in the outer solar system, from meteorites to comets, will be presented.

9.1 Observations

9.1.1 67P/Churyumov-Gerasimenko

The Rosetta Orbiter Spectrometer for Ion and Neutral Analysis (ROSINA) was a mass spectrometer instrument on the Rosetta spacecraft. It was designed to study the composition of the atmospheres and ionospheres of comets, asteroids, and other small bodies in the solar system. In particular, ROSINA highlighted a panorama of carbon-rich molecules present in the 67P/Churyumov-Gerasimenko comet. Hydrocarbon-based compounds with individual molecular masses of up to 140 Da were identified, corresponding to an average composition of $C_1H_{1.56}O_{0.134}N_{0.046}S_{0.017}$ (Hänni et al. 2022). In this study, the authors found that carbon

chain-based molecules were six times more abundant than cyclic molecules, themselves three times more abundant than PAHs. These turned out to have structural and elemental composition properties consistent with Solar System organic reservoirs, i.e., they kept their presolar signature. This study pointed to the presence of several aromatic molecules and their hydrogenated derivatives, such as cyclohexane, naphthalene, dihydronaphthalene, tetrahydronaphthalene, and decahydronaphthalene. These discoveries are in agreement with previous tentative detections of small PAHs by Quirico et al. (2016), wherein analyses showed the association of PAHs with opaque refractory surface materials. Low albedo can thus in part be explained by this carbon-rich composition of PAHs. Finally, a strong 3.2 μm band is visible in every spectra of 67P/CG which can be explained by the presence of aromatic C−H. Along with other ions, an aliphatic and/or aromatic presence is consistent with the strong 3.2 μm feature.

9.1.2 ISS Sample Return

In 2014, the ORGANIC experiment on the European Space Agency's EXPOSE-R multi-user facility on the International Space Station exposed 14 samples (11 PAHs and 3 fullerenes) to an irradiation dose of 14000 MJ m^{-2} over 2900 hours of unshadowed solar illumination (Ehrenfreund et al. 2007; Bryson et al. 2015). This platform, in low-Earth orbit, enables long-term exposure simulations subject to UV radiation under vacuum conditions. In Bryson et al. (2015), few spectral changes were observed, indicating that PAHs and fullerenes under space exposure conditions are relatively stable. The authors found that the more compact PAHs were, the more stable they were. These include, for example, perylene, corenene, ovalene, circobiphenyl, dinaphtocoronene, dicoronylene and the fullerenes. Less-compact PAHs (branched and linear) such as tetracene, chrysene, dibenzooctacene and tetrabenzoheptacene were found to show sustained levels of degradation. PAHs that include a heteroatom in their molecular structure such as diphenanthrothiophene showed in this study the highest level of degradation due to UV radiation.

Along with the ORGANIC experiment (Bryson et al. 2015), another simultaneous experiment named AMINO to investigate carbonaceous processing in the solar system was conducted by Cottin et al. (2015). This complementary study focused on applications to small bodies (asteroids and comets), the atmosphere of Titan, and, more broadly, the primitive Earth composition.

9.1.3 The Cassini Mission

Saturn's satellite Iapetus was imaged with the Cassini probe in the IR and major computational analyses of the detected bands indicated a presence of PANHs and hydrogenated PAHs. The PAHs on Iapetus exist in a H_2O-rich environment and are consequently subject to UV destruction by hydrogenation on short time-scales. The occurrence of this material is consistent with the assertion that the deposition of PAH-bearing dust is occurring at the present time (Cruikshank et al. 2014).

A spectral signature at 682 cm^{-1} was observed in Nadir and Limb geometry observations of Titan's southern stratospheric polar region. It is identified as, at least partially, the benzene ν_4 C−H bending mode (Vinatier et al. 2018). This study was the first to detect benzene ice signatures in Titan's atmosphere, and has since consolidated the importance of benzene-based solid-state chemistry therein. The nucleation and photochemical evolution of these ices could potentially involve other cyclic molecules in Titan's atmosphere but future observations will be needed to support the presence of ringed molecules in the atmosphere and their expected involvement in the formation of photochemical hazes.

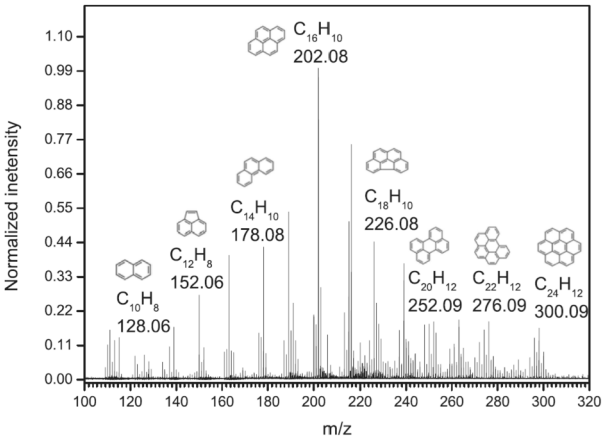

Fig. 13 PAHs recorded using the AROMA setup from a sample of the Murchison meteorite. Possible isomeric structures are shown for specific peaks. Adapted with permission from Sabbah et al. (2017). Copyright 2017 The American Astronomical Society

9.2 Experiments

9.2.1 Small Bodies of the Solar System

Our overview of meteoric laboratory studies starts with measurements of silicon impurities present in the lattice of some nanodiamonds extracted from chondrites of various groups (Shiryaev et al. 2015). These silicon defects were observed using the photoluminescence spectra of the diamond lattices. Shiryaev et al. (2015) highlighted how the relative luminescence intensities can be linked to temperature variations initiated by metamorphism of the parent bodies. Through this thermal history, silicon impurities get preferentially incorporated into small nanosized grains. As a result, the authors argue that such silicon defects could be used as a key proxy to identify nanodiamonds in the outer solar system.

A number of prebiotic molecules have been detected in carbonaceous chondrites, particularly in the Murchison meteorite. Sabbah et al. (2017) utilized the AROMA setup (see Sects. 3.2.5 and 4.2.2), followed by an actual detection of PAHs in samples from the Murchison meteorite (see Fig. 13). These included identification of pyrene and its methylated derivatives, and were obtained using collision-induced dissociation experiments. The use of atomic force microscopy has also been complementarily used by Kaiser et al. (2022a). This high-resolution technique is a unique way to unveil large individual organic molecules present in the soluble fraction of meteoritic samples. Also in carbonaceous-chondrite material from the Kapoeta achondritic meteorite, nanodiamonds were found to coexist with amorphous carbon (Abdu et al. 2018).

Naphtalene-benzene-based compounds such as fluoranthene crystal surfaces were investigated in terms of their solubility in aqueous solutions of different ionic strengths (Giese et al. 2018) where it was found that the physical properties of fluoranthene (i.e., its surface roughness) influence its sublimation and dissolution rate. This result can have important consequences on the interpretation of ionic strengths and chemical compositions as measured in meteorites and asteroids. These chemical compositions are intrinsically linked to the parent body interiors, as studied by Giese et al. (2019). In particular, this study found that smaller PAHs in the right conditions (i.e., within the aqueous alteration temperature of carbonaceous chondrites) can form carbonaceous spherules in the presence of water.

Much larger PAHs and fullerenes from C_{30} to at least C_{100}, however, were detected in the Almahata Sitta meteorite (Sabbah et al. 2022). This is in stark contrast with the non-detection of fullerenes in any of the Allende or Murchison materials and suggested that a

carbon-rich source was less abundant in the primitive samples. In addition, the question of material sources becomes even more intriguing with the analysis of isotopic measurements under asteroidal hydrothermal conditions. In these conditions (150°C), PAHs are stable, and their carbon isotopic composition remains unaltered (Lecasble et al. 2023). The hydrogen isotopic composition, however, changes in the presence of water. The stability of the PAHs studied by Lecasble et al. (2023) is also affected by the presence of phyllosilicates, which are major constituents of carbonaceous chondrites.

Laboratory radiation experiments have also explored organic syntheses by ion irradiation, assessing the radiolytic origins of polyaromatic IOM recovered from primitive chondrites and organics at the surface of reddish Trans-Neptunian Objects (Faure et al. 2021). It was shown that heavy ion irradiation of aromatic-rich precursors lead to simple icy organic compounds, and did thus not provide a viable process to synthesize IOM. Rather, in the case of aromatic rich precursors, they preferentially lead to polyaromatic materials over the ion irradiation of more simple icy organic materials. These findings resonate with other experiments in the synthesis of amino acids using fluoranthene with ammonium bicarbonate as a precursor. By studying 36 pathways involving the PAHs e.g. naphthalene, anthracene, fluoranthene, pyrene, and amino acids such as glycine, alanine, valine, leucine, Giese et al. (2022) found that experimental simulations did not lead to the formation of amino acids. Theoretical calculations, however, indicate that PAHs could act as precursors of some amino acids in carbonaceous chondrites, albeit at low temperatures.

9.2.2 Saturn's Largest Moon Titan

Photolysis and UV radiation experiments have long been part of the laboratory simulations to mimick Titan's atmospheric reactivity. Before the detection of benzene by Vinatier et al. (2018) in the stratospheric clouds of the south pole of Titan, Yoon et al. (2014) highlighted the influence of benzene on the gas-phase products formed in an N_2-CH_4 mixture. The presence of benzene in low ppm amounts led to a higher aromaticity in solid phase (tholin) compounds as well as a lower nitrogen incorporation into the tholins (Trainer et al. 2013). The optical properties of tholins formed under far-UV photolysis are also affected by the presence even in low amounts of benzene. Consequently, both the condensation and radiative properties of these organic aerosols will be affected by a higher compositional aromaticity. Unique broad emission features in the far-IR observed in the stratosphere of Titan have also lead Sebree et al. (2014) to assess the sensitivity of precursors such as benzene, naphthalene, pyridine, quinoline and isoquinoline on the far-IR spectroscopic signatures, which partially captured the observed features by Cassini's far-IR spectrometers. Photochemical kinetics, more broadly, were shown to be highly dependent on the photon flux utilized in the laboratory using VUV actinometry (Sebree et al. 2018b). The same group has recently been developing a new experimental GC/MS/MS operation where tholins are generated by either cold plasma or photochemical irradiation of CH_4-CO-N_2-based mixtures. Their technique reaches high sensitivity limits (down to 1 picomole) and points to the presence of several prebiotic species such as glycine, glycolic acid and urea (Sebree et al. 2018a).

Much higher in Titan's atmosphere in the ionospheric plasma region above 900 km in altitude, plasma laboratory facilities such as the Titan Haze Simulation experiment with COSmIC Simulation Chamber have been able to simulate the low-temperature and low-pressure conditions found in Titan's upper atmosphere (Sciamma-O'Brien et al. 2014). A pulsed plasma jet expansion enables to cool down the gas and initiate the plasma chemistry around 150 K. Scanning electron microscope and IR spectroscopy measurements of the tholins produced in the experiment in N_2-CH_4-based mixtures (with additions of ethane

and benzene) generated a spectrum of different grain morphologies and aggregates. The mid-IR spectra revealed the changes in nitrogen chemistry and the abundance of aromatic compounds (Sciamma-O'Brien et al. 2014, 2017; Nuevo et al. 2022).

Recently, other experiments relevant to Titan (and beyond) include the development of a UV/vis spectrometer to determine the refractive index and thicknesses of ice films of benzene (Stubbing et al. 2018). Benzonitrile ices, on the other hand, were exposed to VUV irradiation by (Sivaraman et al. 2023). The irradiated ice was observed to leave a residue upon warming to room temperature. When removed, the residue was analyzed with an electron microscope to reveal quantum dots and nitrogen-doped graphene with its detailed crystalline structure when coupled with diffraction and energy-dispersive X-ray spectroscopy (Sivaraman et al. 2023). The irradiation of organic materials by Galactic cosmic rays (an energy source capable of reaching the deeper parts of Titan's atmosphere) was studied by combining ultrahigh-vacuum irradiation experiments with a spectroscopic analysis to examine their color evolution during Galactic cosmic ray processing (Zhang et al. 2023b). Aromatic units such as phenanthrene, phenalene, and acenaphthylene were found to play a key role in producing reddish colors.

9.3 Modeling

The presence of PAHs in Titan's atmosphere, although inferred by some laboratory results discussed above, has never been directly confirmed. In Titan's high-altitude daytime atmosphere, the 3.28 μm emission feature was seen as an important potential candidate for the presence of PAHs. Using the NASA Ames PAH database, López-Puertas et al. (2013) inferred the presence of neutral PAHs with 9-96 carbons and an average of 34 carbons below 1300 km, with a peak up to 1250 km of $(2-3) \times 10^4$ particles cm^{-3}.

Furthermore, fully coupled updated ion-neutral photochemical models (Dobrijevic et al. 2016; Loison et al. 2019) have integrated a large number of reactions leading to the precursors of the haze macromolecular compounds. These models emphasize the importance of ionic chemistry in the formation of benzene as a basis precursor to putative PAHs and cyclic molecules in the atmosphere, e.g. toluene and ethylbenzene (Loison et al. 2019).

Finally, Sittler et al. (2020) discussed the formation of aerosols within Titan's thermosphere-ionosphere and the different chemical pathways involved. While there appears to be no direct observational evidence for large neutral molecule growth in Titan's thermosphere-ionosphere, hydrocarbon cations are expected to form PAHs and PANHs. They theorized that anion carbon chains could eventually become long enough to fold into fullerenes of various charge states which eventually form into larger onion fullerenes which condense into larger embryo aerosols, eventually falling onto Titan's surface and potentially precipitating to the bottom of its hydrocarbon lakes. Sittler et al. (2020) developed a model of Galactic cosmic ray irradiation of Titan's atmosphere, surface, subsurface and bottoms of Titan lakes which showed that Galactic cosmic ray secondary particles can penetrate ~100 m below the ice surface and produce chemically significant dosages over very long timescales. The Galactic cosmic ray model was combined with laboratory data from experiments in which dry methyl ices were irradiated to doses producing prebiotic amino acids such as glycine. The model calculations showed that glycine can form to ~2.5 ppb levels near the surface after ~450 Myrs of Galactic cosmic ray proton irradiation and potentially to 5 ppb if heavy-ion Galactic cosmic rays up through Fe are included.

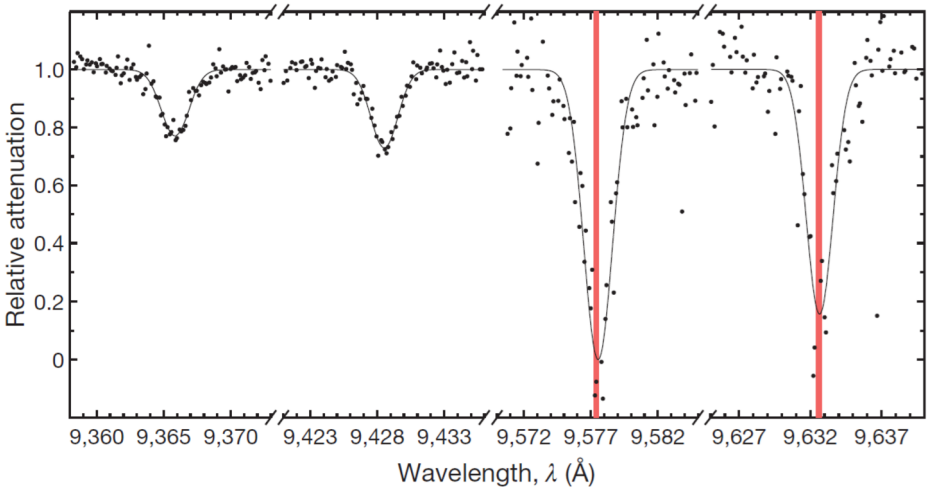

Fig. 14 Gas-phase laboratory spectra of C_{60}^+ at 5.8 K that was used for the confirmation of C_{60}^+ being the carrier of at least two of the DIBs. Adapted with permission from Campbell et al. (2015). Copyright 2015 Springer Nature

10 Diffuse Interstellar Bands

Heger (1922) reported two unknown absorption features in the spectra of stars. Those lines where later recognized as the first DIBs observed. The absorption bands collectively known as DIBs cover the UV/Vis and near-IR spectral range. Since their first detection, many different compounds have been proposed as carriers of the DIBs. Among other suggestions, the products of amorphous hydrocarbon grains and their doped variants were theorized to be potential molecular carriers (Jones 2014). In 2015, laboratory experiments confirmed the C_{60}^+ as a carrier of two of the DIBs, making the Buckminsterfullerene cation the only identified species responsible for some of the interstellar absorption features to date (Fig. 14; Campbell et al. 2015; Linnartz et al. 2020).

Among other large carbon-based molecules, other fullerenes, fulleranes (Omont 2016), their fragments (Omont and Bettinger 2021), as well as polyacenes and larger conjugated elongated molecules have been proposed as potential DIB carriers (Omont et al. 2019; Omont and Bettinger 2020), but recently helicenes were suggested to be a potential carrier of the 4502 Å DIB, i.e., [26]helicene ($C_{106}H_{56}$) (Oña-Ruales et al. 2021).

10.1 Observations

In the last decade, new DIBs have been detected, collectively reaching more than 600 lines, and various new candidates have been proposed as well.

Using the X-Shooter instrument mounted on the VLT, Cox et al. (2014) confirmed 9 of 13 near-IR DIBs predicted previously and presented a further 11 new DIB candidates. The UVES instrument mounted on VLT was used to survey interstellar features in the near-UV range (3050–3700 Å). In this study, seven new interstellar absorption lines were tentatively detected and upper limits to column densities of small neutral PAHs were revisited (Bhatt and Cami 2015).

Using the High Accuracy Radial Velocity Planet Searcher (HARPS) instrument, the 6614 Å DIB was recorded along the sightlines toward HD 179406 and HD 147889. The difference in band shapes was attributed to the degree of internal excitation of the carrier. The band shapes themselves were interpreted in terms of the population distribution among the rotational, vibrational, and potentially low-lying electronic states of a medium-sized ($N_C \sim 20$) planar PAH-type molecule (Marshall et al. 2015).

Based on the accurate laboratory data by Campbell et al. (2015), the presence of C_{60}^+ was confirmed in the diffuse ISM, using Spitzer a couple of years later. Neutral Buckminsterfullerene was also detected in the diffuse ISM via its 17.4 and 18.9 μm emission bands (Berné et al. 2017), and based on classical models computing the charge state of large molecules in space, it was expected that C_{60} is mostly neutral in the diffuse ISM.

The conclusive confirmation of interstellar C_{60}^+ was then presented by HST spectra covering the 9348, 9365, 9428, and 9577 Å absorption bands of C_{60}^+ (Cordiner et al. 2019). The spectra observed toward seven heavily reddened stars are the ultimate confirmation that C_{60}^+ is the carrier of these DIBs. In later work, the C_{60}^+ DIBs were identified in a sample of 25 stars using the data from the VLT/X-shooter instrument. The two strongest DIBs were unambiguously detected and further support for C_{60}^+ as the carrier of the 9632 Å and 9577 Å DIBs was given (Nie et al. 2021).

Two other fullerene-containing PNe in our Galaxy (Tc 1 and M 1–20) were studied using the VLT in the 2.9–4.1 μm spectral range in search for fulleranes (Díaz-Luis et al. 2016). From the observations, it was evident that the Tc 1 spectrum is likely due to only C_{60} and C_{70} and other kinds of fulleranes or fullerene/PAH adducts but fulleranes themselves were detected in neither source. Díaz-Luis et al. (2015) also reported the presence of diffuse circumstellar bands (DCBs) at 4428 and 5780 Å in the fullerene-rich circumstellar environment around the PN Tc 1.

One of the strongest near-IR DIBs at 15273 Å was recorded using the K-band Multi Object Spectrograph (KMOS) on VLT in the H-band (1.46–1.85 μm) spectral range to probe the presence and properties of visual extinction in the dark cloud Barnard 68 (Elyajouri et al. 2017). The results showed an increase of the DIB equivalent width with increasing A_V, but the increase is slighter than expected from what has been established for this DIB in the Galactic diffuse ISM.

The MUSE[38] instrument on VLT was used to map the ISM in absorption toward the globular cluster NGC 6397. It was demonstrated that MUSE is effective at mapping the local ISM on very small scales which provides a new window for ISM observations (Wendt et al. 2017). Data from VLT/MUSE was then used for the first time to derive maps for the DIBs at 5780 and 5797 Å in galaxies outside the Local Group (Monreal-Ibero et al. 2018).

High spectral resolution IR spectra were obtained of four reddened background supergiant stars and an unreddened comparison star (Ebenbichler et al. 2022). Seventeen known near-IR DIBs were confirmed and 12 previously unknown and generally weaker DIBs were identified. Three DIBs showed uniform profiles along all sight lines which might be connected to transitions from a common lower state of the carrier.

Lai et al. (2020b) also performed observations of a background star seen through the region between the ionization front and the dissociation front of the IC 63 nebula. Strong DIBs were detected in the stellar spectrum and the PDR exhibited strong ERE. However, observations of the nebular spectrum of the PDR of IC 63 at locations immediately adjacent to where the DIBs were detected, failed to reveal any presence of sharp emission features

[38] Multi Unit Spectroscopic Explorer.

seen in the spectrum of the Red Rectangle Nebula suggesting that the carriers of the Red Rectangle feature and nearby DIBs are not the same.

More recently, Smoker et al. (2023) performed a high-resolution study of near-IR DIBs, searching for small scale structure, time variability and stellar features. 76 early-type stars using CRIRES were observed and correlations between several DIBs were investigated. They concluded that the NIR DIBs observed occur in more UV-irradiated regions than the 5797 Å DIB, allowing the study of heavily reddened sightlines. Smoker et al. (2023) went on to suggest that future searches for time variability in DIBs may require higher quality data and/or larger intervals between epochs.

10.2 Experiments

10.2.1 Electronic Spectra

In order to answer one of the longest standing questions of astrochemistry and identify the carriers of the observed DIBs, high quality laboratory experiments are necessary. The potential candidates for DIB carriers are numerous, ranging from PAHs to fullerenes, smaller molecules to molecular clusters, *etc*. The wavelength range spanning the known DIBs traces from the near-IR to the UV, but this wavelength range typifies electronic transitions in molecules. Hence the term 'electronic spectroscopy' is usually the most relevant to characterizing spectroscopic work relevant to DIBs.

Besides the previously detailed work of Campbell et al. (2015), electronic absorption spectra of multiple species have been reported. The electronic absorption spectra of 1- and 2-methylnaphthalene cations were measured using an argon tagging photodissociation spectroscopic technique (Friha et al. 2013) as well as electronic spectra of substituted naphthalene anions with an ion mobility setup (Bull et al. 2019). Electronic spectra of protonated nitrogen-substituted PAHs have also been inspected (Noble et al. 2015) and although the spectra of protonated acridine and phenanthridine do not correspond to known DIBs, Noble et al. (2015) proposed that larger protonated PANHs could be responsible for DIBs.

Visible absorption spectra of C_9H_5 and C_9H_9 radicals were measured in a supersonic expansion of a hydrocarbon discharge source (Steglich et al. 2016). The main detected features are assigned to acetylenic-substituted cyclopentadienyl and vinyl-substituted isomers, respectively, and the strongest C_9H_9 feature appears to coincide with a very weak DIB toward HD183143 and HD204827, but more line coincidences are typically required for solid identifications as in the case of C_{60}^+.

Other relevant electronic absorption spectra include those of gas-phase cationic and protonated anthracene (Meyer et al. 2021), but those spectra showed no coincidence with known DIBs. Likewise, the electronic spectra of ionized cyclo[n]carbons tagged by He atoms were measured and might be interesting candidates for astrophysical consideration (Buntine et al. 2021; Rademacher et al. 2022).

The gas-phase electronic spectrum of the HBC cation has also been measured with an origin band at 8281 Å via messenger-tagging spectroscopy in a cryogenic ion trap (Campbell and Maier 2017). The measured absorption cross section in the trap allowed to estimate for the upper limits to the column density which indicated that PAH cations of this size ($N_C \sim 40$) should be excluded as candidates for the strong DIBs.

Electronic spectra of phenanthrene and phenanthridine were recorded with CRDS (see Sect. 2.2.9) and were compared with spectra recorded in solid Ar matrices at 10 K (Bejaoui and Salama 2019). While the CRDS spectra show much greater resolution, Bejaoui and Salama (2019) also state that since the gas-phase spectra are significantly hotter than

conditions in the cold ISM, the cold matrix spectra may be more appropriate for direct comparisons with astronomical spectra.

A new apparatus which combines a cryogenic radio frequency ion trap and a laser vaporization source was developed to obtain electronic spectra through messenger-tagging spectroscopy (Campbell and Dunk 2019). The technique was demonstrated by recording a spectrum of an electronic transition in cyclic C_6^+ in the gas phase but the electronic spectrum of endohedral fullerene $He@C_{60}^+$ was also recorded using messenger-tagging spectroscopy (Campbell et al. 2020).

The optical spectrum of the adamantane radical cation was measured as well in the 310–1000 nm range (Crandall et al. 2020). The main fragmentation channels that were observed were H and C_3H_7 losses, where a Jahn-Teller effect was observed in a band originated at 345 nm, exemplifying significant geometrical changes upon electronic excitation.

Electronic absorption spectra of oxygen-functionalized PAHs (OPAHs) were also measured in the context of searching for potential carriers of the ERE (Rasmussen et al. 2023). Their results demonstrate the ability of OPAHs to absorb in the UV/Vis spectral region. Among the four studied OPAHs, two revealed very broad absorption features at wavelengths up to 700 nm, which makes them suitable candidates to contribute to a part of the ERE spectrum. Moreover, these two OPAHs could dissociate into oxygen-bearing molecules and smaller functionalized PAHs in PDRs.

Recently, the IR (6–25 μm) spectra of gas-phase fullerene-metal complexes, $[C_{60}\text{-M}]^+$ (M = Fe and V), were recorded (Hou et al. 2023). These showed with the help of DFT calculations that complexes of C_{60} with cosmically abundant metals, including Li, Na, K, Mg, Ca, Al, V, and Fe, all have similar IR spectral patterns. Comparisons with observations from several fullerene-rich PNe demonstrate a strong positive correlation as the experimental features coincide with four bands attributed to neutral C_{60} bands in addition to several to date unexplained bands. Abundances and collision theory estimate that these complexes could survive in astrophysical environments. It is also noteworthy that previously, the electronic spectra of $Fe[C_6H_6]^+$ complexes were investigated with multireference wavefunction calculations and compared with DIBs (Lanza et al. 2015). This work laid the foundation for studies of PAHs complexed to Fe cations that are more likely to possess transitions relevant to the DIBs domain.

10.2.2 He Nanodroplets

Using He nanodroplets has become a relatively widespread method to study ions with mass spectrometry methods. Using a supersonic nozzle, tiny, superfluid helium nanodroplets can be produced with temperatures of less than one degree Kelvin. They can very effectively be doped with atoms and molecules and in the case of ionized droplets, the particles of interest are attracted to the charges, which are then measured in the mass spectrometer.

For instance, coronene-doped He clusters have been studied using classical and quantum mechanical approaches where liquid He nanodroplets were used to investigate the reactivity of PAHs with atomic carbon (Rodríguez-Cantano et al. 2015). The results showed that all small and large catacondensed PAHs react barrierlessly with the carbon atom and should therefore be efficiently destroyed in a broad temperature range. At the same time, large compact pericondensed PAHs should be more inert to these reactions which means that (also accounting for their high photostability) much higher abundances of pericondensed PAHs should be expected in various astrophysical environments. Since the reactions are barrierless, they could be a source of bottom-up PAH formation in space (Krasnokutski et al. 2017).

Superfluid helium nanodroplets doped with corannulene to prepare their cations were investigated spectroscopically as well (Gatchell et al. 2019). Protonated corannulene ions were also studied whose spectra differ significantly from the radical cations as the numerous narrow bands are replaced with a broad absorption feature that spans nearly 2000 Å in width.

Adsorption of He on charged HBC was investigated by a combination of high-resolution mass spectrometry and classical and quantum computational methods (Kappe et al. 2022) and similar works were also presented on triphenylene and 1,3,5-triphenylbenzene (Bergmeister et al. 2022) which elucidated nuances in the solvation dynamics of PAHs in superfluid He.

10.3 Theory

Computational chemistry can be used to characterize the electronic spectra of molecules. Unfortunately the different theories are not accurate enough yet to be able to definitively assign a specific DIB to a molecule. Nevertheless, theory can be used to assess the presence of Rydberg and dipole-bound electronic states or propose molecules for further experimental characterization.

Calculated optical properties of PAHs with different concavities and π-connectivities have revealed that the interplay between these characteristics shifts the optical lines and introduces symmetry forbidden dark excitations at low energy (Cocchi et al. 2013). Hartree-Fock semi-empirical configuration interaction methods have been used to investigate the effects of symmetry on the electronic/optical spectra/properties of PAHs related to coronene and circumbi-, tri-, and tetraphenyls (Cocchi et al. 2014).

Larger nitrogen-substituted PAH neutral and cations were also investigated by TD-DFT calculations (Shukla et al. 2022). Therein it was suggested that PANHs could be prospective carriers of some DIBs as previously suggested by Noble et al. (2015).

Electronic spectroscopy and excited states of negatively charged PANHs and deprotonated PAH anions have been studied with equation of motion calculations (Theis et al. 2015a,b). A follow up of this work investigating excited states of PANH anions found that once seven six-membered rings make up a PAH/PANH, valence excited states are present in the deprotonated anionic forms. Meanwhile for most PAHs/PANHs, the number of six-membered rings is closer to four. Considering the sheer amounts of PAHs in space these could be significant contributors to astronomical spectra despite the excited states being weak absorbers (Fortenberry et al. 2016).

The Rydberg states of various PAHs, cyclic alkanes and adamantanes have been studied by TD-DFT calculations (Bohl et al. 2017). There, systematic variations in binding energies and photoelectron angular distributions have been predicted for the first members of the s, p and d Rydberg series with increasing molecular complexity. Bohl et al. (2017) found that Dyson orbitals for small "hollow" carbon structures such as cubane, adamantane, and dodachedrane, have close similarities to atomic s, p and d orbitals, similar to the superatom molecular orbitals (SAMOs) reported for fullerenes, indicating that these low-lying, diffuse states are not restricted to p-conjugated molecules.

The electronic properties of deprotonated cyano-functionalized PAHs were investigated quantum chemically as well (Santaloci and Fortenberry 2021). It was found that the absorption and emission energies of the larger anions possess both valence and dipole bound states in the 450–900 nm with oscillator strengths of larger than 10^{-4} for both types. The valence and dipole bound excited state transitions produce slightly altered substructures from one another making them appear to originate with different molecules.

10.4 Modeling

For the multitudes of sight-lines where DIBs are observed, modeling can be exceedingly helpful in sorting out and locating correlations with different properties.

For instance, a million and a half extragalactic spectra were used to study the properties of DIBs in the Milky Way by Baron et al. (2015) who found that DIB strengths correlate with extinction and each other. They also showed that DIBs can exist in dust-free areas and that the correlation with dust varies significantly over the sky. The four DIBs studied are shown to likely originate from different carriers.

Modeling was also used to showcase that DIBs and the AME (see Sect. 11) may come from the same set of carriers, i.e., the physical properties of DIB carriers (composition, size, temperature, *etc.*) are consistent with those necessary to produce the AME. The results favor small, cold carriers with an average size around $N_C = 8$–15, and an average temperature between 3 and 10 K, depending on the type of carrier (Bernstein et al. 2015). Later work by Bernstein et al. (2018) deconvolved and modeled the 6196 and 6614 Å DIBs, deriving spectroscopic constants for potential carriers. The analysis suggested the carrier to be a puckered oblate symmetric top that can be consistent with corannulene or one of its derivatives (Bernstein et al. 2018).

The relationship between FUV extinction and 40 DIBs along 97 sightlines were investigated by Xiang et al. (2017) who found that the wavelength-integrated 2175 Å bump extinction does not correlate with the FUV extinction.

Ensor et al. (2017) then carried out a detailed PCA on a selection of DIBs and found that the majority of DIB variations can be attributed to four parameters: the amount of DIB-producing material in the line of sight, the level of UV exposure, the dust properties in the line of sight, and the depletion in the line of sight.

Later, the relation between the DIB strength and the total-to-selective extinction ratio (R_v) which characterizes how the extinction varies with wavelength were also investigated (Li et al. 2019b). It revealed that the DIB strength and R_v are not related if the strength of a DIB is represented by its reddening-normalized equivalent width, in contrast to earlier findings. The authors argued that the hydrogen column density is a more appropriate normalization than extinction and reddening.

High quality stellar spectra from the ESO[39] Diffuse Interstellar Bands Large Exploration Survey (EDIBLES) were studied by Lallement et al. (2018) in terms of the detectability of C_{60}^+ in DIBs. The study examined carefully the points made against the assignments of C_{60}^+ transitions to DIBs and showed how the high-resolution EDIBLES data can assist in detecting C_{60}^+ absorption bands.

The EDIBLES consortium also researched the so-called C_2-DIBs, a class of weak bands that fall in the blue part of the optical spectrum and are associated with high column densities of the C_2 molecule (Elyajouri et al. 2018). Three new weak DIB candidates were reported and it was shown that at least fourteen C_2-DIBs exhibit spectral sub-structures which are consistent with unresolved rotational branches of molecular carriers. The variability of their peak separations among the bands for a given sightline implied that their carriers are different molecules with quite different sizes.

More recently, the 5797, 6379 and 6614 DIB profiles were studied by the EDIBLES consortium (MacIsaac et al. 2022). They found systematic variations in these DIB profiles that provide means to constrain the molecular properties of the carriers. They estimated

[39] European Southern Observatory.

that the molecule sizes range from 7–9 C atoms (λ6614 carrier, linear) to 77–114 C atoms (λ6379, spherical).

The C_{60}/C_{60}^+ abundance ratio in diffuse and translucent clouds has been modeled as well using available spectroscopic and observational data by Rouillé et al. (2021) who derived an upper limit of 1.3 for the C_{60}/C_{60}^+ ratio.

11 The Anomalous Microwave Emission

The AME is a mysterious component of microwave radiation emitted from the diffuse ISM. It was discovered in the late 1990's from sensitive experiments dedicated to the CMB. It has since been detected in numerous sources in the frequency range 10–100 GHz. Its intensity is closely correlated with thermal radiation at mid-IR and far-IR wavelengths associated with interstellar dust grains. However, thermal dust grains cannot account for the observed microwave excess.

Although the AME occurs in the microwave regime it is not related to cold dark cloud chemistry where the first individual PAHs have now been detected (see Sect. 7). The most plausible models built to explain the AME assume it stems from electric dipole radiation from ultra-small rapidly spinning dust grains, but there is still ambiguity and several mysteries associated with the AME, which were reviewed by Dickinson et al. (2015).

11.1 Observations

The main reason for why the AME deserves its own section is the incompleteness of our understanding of its origin. Work by Hensley et al. (2015) followed up on the first extragalactic detection of AME in an extranuclear region of the nearby face-on spiral galaxy NGC 6946. Although the spectral shape and peak frequency of the AME in this region appears to be consistent with models of spinning dust emission, the strength of the emission far exceeds the Galactic AME emissivity given the abundance of PAHs in that region. To investigate the discrepancy Hensley et al. (2015) probed the relationships between the detected AME and factors such as dust surface density, PAH emission, and radiation fields, but no strong correlations were found. On the basis of these data and previous AME observations, Hensley et al. (2015) determined that the AME emissivity per unit dust mass is highly variable and that the spinning dust hypothesis (which predicts that the AME power is approximately proportional to the PAH mass) is incomplete.

Following this work, foreground component maps from Planck were combined with modified blackbody dust parameter maps and WISE 12 μm maps to test predictions of spinning PAHs as the source of the AME (Hensley et al. 2016). The study showed that while AME is highly correlated with all tracers of the dust emission, the best predictor of AME strength is the dust radiance. Fluctuations in the AME intensity per dust radiance appear to be uncorrelated with fluctuations in the emission from PAHs which casts doubt on the association between the two. The PAH abundance appears to be strongly correlated with the dust optical depth and dust radiance, consistent with PAH destruction in low density regions. It was found that the AME intensity increases with increasing radiation field strength, at variance with predictions of the spinning dust hypothesis. The temperature dependence on the AME per dust radiance also disfavors the interpretation of the AME as thermal emission so the authors argued that other AME carriers are more likely to be, e.g., ultrasmall silicates through magnetic dipole emission.

Later, AME was observed in several protoplanetary disks which are the only known systems that host hydrogenated nanodiamonds, like adamantane (Greaves et al. 2018). The

nanodiamonds were spectroscopically located close to the host stars, at physically well-constrained temperatures. Disk models were developed which reproduced the emission with diamonds 0.75–1.1 nm in radius, holding 1–2% of the carbon budget. The ratios of microwave emission to stellar luminosity are approximately constant which allows nanodiamonds to be ubiquitous but emitting below the detection threshold in many star systems. This result is compatible with the findings of similar-sized diamonds within Solar System meteorites. As nanodiamonds spectral absorption is seen in interstellar sightlines, these particles are also candidates for generating galaxy-scale AME.

Although the correlations between nanodiamonds and the AME was found to be strong in these protoplanetary disks, many unexplained and mixed links between the AME and PAHs still remain. Hensley et al. (2022) investigated the relationship between the cold neutral medium (CNM), the PAH abundance, and the AME. The fraction of CNM was found to be strongly correlated with the fraction of dust in PAHs as estimated from mid- and far-IR dust emission. But in contrast, no correlations between the CNM and the AME were found. These results suggested that PAHs preferentially reside in cold, relatively dense gas, perhaps owing to enhanced destruction in more diffuse media. The lack of a positive correlation between the CNM and the AME peak frequency appeared to be at odds with the expectations of different spectral energy distributions of AME in the cold versus warm neutral medium, as posited from theoretical models. Hensley et al. (2022) suggested that different PAH abundances and emission physics in different interstellar environments may explain the weaker-than-expected correlation between the 12 μm PAH emission and AME even if PAHs were AME carriers.

The link between PAHs and the AME was also explored in the λ-Orionis region by Chuss et al. (2022) who used archival data from COBE/DIRBE to construct a map of PAH emission to trace small PAHs through the 3.3 μm PAH emission band. These findings also contended with the hypothesis that AME is due to spinning PAHs. However, the expected correlation between mid-IR and the AME could potentially be degraded by different sensitivities of each emission mechanism to local environmental conditions even if PAHs are the carriers of both. The authors stressed that the work is a stepping stone and that future directions toward extending their technique over the entirety of the sky will enable more aggressive masking which will aid in determining if residual starlight in their PAH map is responsible for depressing the AME-PAH correlation coefficient.

11.2 Theory

Theory behind spinning PAHs originally comes from rotational spectroscopy (Ali-Haïmoud 2014). However, the study of spinning PAHs in the context of the AME requires further theoretical grounding, particularly regarding the alignment of PAHs by anisotropic radiation (Hoang and Lazarian 2018), even though the polarizabilities of non-planar PAHs have also been computed (Lukmanov et al. 2022). Hoang and Lazarian (2018) calculated the degree of PAH alignment for different environments and physical parameters, including the illumination direction, ionization fraction, and magnetic field strength. Interestingly, for conditions in RNe, the degree of alignment tends to increase with increasing angle, ϕ, between the illumination direction and the magnetic field as a result of the decrease of the cross section of photon absorption with the angle ϕ. As a result, the polarization of spinning PAH emission from RNe can be large, between 5–20% at frequencies above 20 GHz, in comparison to 3% for PDRs. Overall, the results demonstrate that RNe are the favored environments to observe the polarization of spinning dust emission and polarized mid-IR emission from PAHs.

11.3 Modeling

In attempt to explain previous observations of AME from protoplanetary disks, Hoang et al. (2018) modeled AME from spinning PAHs from disks around Herbig Ae/Be and T Tauri stars where PAH emission features have been observed as well as AME features from spinning nanosilicates. The numerical results demonstrated that microwave emission from either spinning PAHs or spinning nanosilicates dominates over thermal dust emission at frequencies below 60 GHz, even in the presence of significant grain growth.

The authors also attempted to fit mm-cm observational data with both thermal dust and spinning dust for several disks around Herbig Ae/Be stars and found that spinning dust can successfully reproduce the observed excess microwave emission.

Hoang et al. (2019) then modeled a newly discovered effect called the Radiative Torque Disruption (RATD) which can act as an important dynamical constraint for dust models. This was used to derive the maximum size of dust grains that survive in the ISM for different dust models. The RATD mechanism describes dust destruction based on centrifugal stress within extremely fast-rotating grains spun-up by radiative torques (Hoang 2019). RATD can disrupt large grains located within a distance of about a pc from a massive star. This disruption increases the abundance of small grains relative to large grains and successfully reproduces the observed NIR-MIR excess and anomalous dust extinction/polarization.

The AME was also investigated by Bell et al. (2019) who compared AME from the Planck Collaboration astrophysical component separation product with IR dust emission. They found that dust mass certainly correlates with AME, and that PAH-related emission correlates slightly more strongly, which lends support for the spinning PAH hypothesis.

Finally, Hoang and Tram (2019) modeled the microwave emission from spinning nanoparticles in continuous- or C-shocks. They found that suprathermally rotating nanoparticles can emit strong microwave radiation, and both peak flux and peak frequency increase with increasing shock velocity. They suggested spinning dust as a new method to constrain nanoparticles and trace shock velocity in shock dense regions.

12 Outlook and Final Words

The first ten years of AstroPAH saw an extraordinary amount of scientific advances that have deepened our understanding of the roles PAHs play in the Cosmos. These advances have been made thanks to combined efforts and collaborations across multiple disciplines where diverse expertise has been a prerequisite for the development and evolution of instruments for both laboratory and observational studies, as well as computational developments in terms of both applied quantum chemical methods and physical chemical modeling of objects in space.

JWST started to reveal new answers and new questions and, as Zettergren et al. (2021) noted, we expect that JWST will be the primary source to revolutionize our view of the carbonaceous universe. The advances we have detailed herein that pertain to JWST certainly testify to its incredible sensitivity and its capabilities to unravel cosmic mysteries of our time.

The recent wealth of data from state-of-the-art telescopes like Spitzer, Herschel, AKARI, GBO, VLT, ALMA, and HST, has certainly helped advancing the field. However, this review reminds us that the most expensive and state-of-the-art equipment is not the sole prerequisite to obtain important results. Creativity, hard work, diversity, and collaboration are still the best tools! The same is certainly true for the numerous dedicated experimental techniques

that have been devised and utilized which are uncovering an incredible wealth of data detailing the intricate and rich spectra and dynamics of PAHs and their molecular families.

Often, it is impossible to predict exactly what the future brings. However, reading through this overview, there are certain themes that appear to be consistently vying for the reader's attention, and we can make educated guesses to what the next decade of AstroPAH research will bring.

- Going beyond the cyano-functionalized PAHs detected in cold clouds, will oxygen-containing PAHs be detected? Or will they remain frozen in water-rich matrices on dust grains as has been observed in laboratory settings?
- Will PAHs be observed in IR ice features with JWST?
- What will be the next molecular carrier of the DIBs to be identified?
- Will PAH complexes with water or other polar molecules be observed in cold clouds?
- Can fullerenes smaller than C_{60} be detected in space? Or cyclo[n]carbons?
- What are the principal precursors of interstellar dust? Are they or are they not related to DIB carriers?
- Will very large PAHs ($N_C \geq 100$) become measurable in laboratory settings?
- Will PAHs play a role in exoplanet atmospheres?
- Are PAHs at the root of the anomalous microwave emission?

Acronyms

AGB	Asymptotic Giant Branch
AGN/s	Active Galactic Nucleus/Nuclei
AIB/s	Aromatic Infrared Band/s
AKARI	Japanese infrared astronomical satellite, its name means "light"
ALMA	Atacama Large Millimeter Array
AME	Anomalous Microwave Emission
AROMA	Astrochemical Research of Organics using Molecular Analyzer
BSS	Blind Signal Separation
CMB	Cosmic Microwave Background
CNM	Cold Neutral Medium
COM	complex organic molecules
CRDS	Cavity Ring Down Spectroscopy
DA	Diels-Alder
DFT	Density Functional Theory
DFTB	Density Functional Tight Binding
DIB/s	Diffuse Interstellar Band/s
EELS	Electron Energy-Loss Spectroscopy
ERE	Extended Red Emission
ESO	European Space Observatory
FT-ICR	Fourier Transform Ion Cyclotron Resonance
GALEX	Galactic Evolution Explorer
GBO	Green Bank Observatory
HAC	Hydrogenated Amorphous Carbon
HACA	Hydrogen Abstraction-Acetylene Addition
HAERA	Hydrogen Abstraction Ethynyl Radical Addition
HAVA	Hydrogen Abstraction-Vinylacetylene Addition
HBC	Hexa-peri-hexabenzocoronene
Herschel	Herschel Space Observatory

HOMO	Highest Occupied Molecular Orbital
HST	Hubble Space Telescope
IOM	Insoluble Organic Matter
IR	Infrared
IRMPD	Infrared Multiple Photon Dissociation
IRPD	Infrared Photodissociation
ISM	Interstellar Medium
ISO	Infrared Space Observatory
JWST	James Webb Space Telescope
LMC	Large Magellanic Cloud
MACA	Methylidyne Addion-Cyclization-Aromatization
MCMC	Markov Chain Monte Carlo
MS	Mass Spectrometry
MW	Microwave
MWCNT/s	Multiwalled Carbon Nanotube/s
OPAH/s	Oxygen-containing Polycyclic Aromatic Hydrocarbon/s
OPO	Optical Parametric Oscillator
QCC	Quenched Carbonaceous Composite
QCL	Quantum Cascade Laser
QNCC	Quenched Nitrogen-included Carbonaceous Composite
PAH/s	Polycyclic Aromatic Hydrocarbon/s
PANH/s	Polycyclic Aromatic Nitrogen-containing Hydrocarbon/s
PAPH/s	Polycyclic Aromatic Phosphorous-containing Hydrocarbon/s
pc	parsec
PCA	Principal Component Analysis
PDR	Photon-dominated region or Photodissociation region
PEPICO	Photoelectron Photoion Coincidence
PEPIPICO	Photoelectron Photoion Photoion Coincidence
PN/e	Planetary Nebula/e
PPN/e	Protoplanetary Nebula/e
SPICA	Space Infrared Telescope for Cosmology and Astrophysics
Spitzer	Spitzer Space Telescope
RATD	Radiative Torque Disruption
REMPI	Resonance Enhanced Multiphoton Ionization
RF	Recurrent Fluorescence
RN/e	Reflection Nebula/e
RSR/s	Resonantly Stabilized Radical/s
SED	Spectral Energy Distribution
SEM	Scanning Electron Microscope
SFR	Star Formation Rate
Sgr	Sagittarius
SMC	Small Magellanic Cloud
SOLEIL	*Source Optimisée de Lumière d'énergie Intermédiaire du LURE*, in English LURE optimised intermediary energy light source (LURE is the *Laboratoire pour l'Utilisation du Rayonnement électromagnétique*).
TEM	Transmission Electron Microscopy
TKER	Total Kinetic Energy Release
TMC-1	Taurus Molecular Cloud 1
TPES	threshold photoelectron spectra

UIB/s	Unidentified Infrared Band/s
UIE	Unidentified Infrared Emission
(U)LIRG	(Ultra-) Luminous Infrared Galaxy
VLT	Very Large Telescope
VSG/s	Very Small Grain/s
(V)UV	(Vacuum) Ultraviolet
YSO/s	Young Stellar Object/s

Acknowledgements We thank the anonymous referees for their constructive comments on the manuscript.

We thank Els Peeters, Aigen Li, Christian Boersma, Ralf Kaiser, Jacob Bernal, Christine Joblin, Hassan Sabbah, Brett McGuire, José Cernicharo, Benoit Tabone, and Ewen K. Campbell for granting us permission to reprint their figures for this review. We also thank Els Peeters for her comments on Fig. 4.

We thank the former AstroPAH editors that were not able to co-author this paper, Elisabetta Micelotta, Rijutha Jaganathan, Annemieke Petrignani, Amanda Steber, and Kin Long Kelvin Lee, for all the work and time they devoted to the AstroPAH newsletter. We also thank all the researchers who contributed to AstroPAH along the years. A special thanks to Lou Allamandola for his encouragement when we started AstroPAH.

This work has made use of the NASA's Astrophysics Data System.

Funding Information Open access funding provided by Université Paris-Est Créteil.

Declarations

Competing Interests The authors have no competing interests, either financial or non-financial, to declare.

References

Abdu YA, Hawthorne FC, Varela ME (2018) Infrared spectroscopy of carbonaceous-chondrite inclusions in the Kapoeta meteorite: discovery of nanodiamonds with new spectral features and astrophysical implications. Astrophys J 856(1):L9. https://doi.org/10.3847/2041-8213/aab433

Abplanalp MJ, Frigge R, Kaiser RI (2019) Low-temperature synthesis of polycyclic aromatic hydrocarbons in Titan's surface ices and on airless bodies. Sci Adv 5(10):eaaw5841. https://doi.org/10.1126/sciadv.aaw5841

Adjizian JJ, Vlandas A, Rio J, et al (2016) Ab initio infrared vibrational modes for neutral and charged small fullerenes (C_{20}, C_{24}, C_{26}, C_{28}, C_{30} and C_{60}). Philos Trans R Soc A 374(2076):20150323. https://doi.org/10.1098/rsta.2015.0323

Agbaglo D, Fortenberry RC (2019) The performance of explicitly correlated wavefunctions [CCSD(T)-F12b] in the computation of anharmonic vibrational frequencies. Chem Phys Lett 734:136720. https://doi.org/10.1016/j.cplett.2019.136720

Agbaglo D, Lee TJ, Thackston R, et al (2019) A small molecule with PAH vibrational properties and a detectable rotational spectrum: c-(C)C_2H_2, cyclopropenylidenyl carbene. Astrophys J 871(2):236. https://doi.org/10.3847/1538-4357/aaf85a

Aghajamali A, Karton A (2021) Can force fields developed for carbon nanomaterials describe the isomerization energies of fullerenes? Chem Phys Lett 779:138853. https://doi.org/10.1016/j.cplett.2021.138853

Aghajamali A, Shiryaev AA, Marks NA (2021) Molecular dynamics approach for predicting release temperatures of noble gases in presolar nanodiamonds. Astrophys J 916(2):85. https://doi.org/10.3847/1538-4357/ac06cf. https://iopscience.iop.org/article/10.3847/1538-4357/ac06cf

Akimkin VV, Kirsanova MS, Pavlyuchenkov YN, et al (2015) Dust dynamics and evolution in expanding H II regions. I. Radiative drift of neutral and charged grains. Mon Not R Astron Soc 449(1):440–450. https://doi.org/10.1093/mnras/stv187

Akimkin VV, Kirsanova MS, Pavlyuchenkov YN, et al (2017) Dust dynamics and evolution in H II regions. II. Effects of dynamical coupling between dust and gas. Mon Not R Astron Soc 469(1):630–638. https://doi.org/10.1093/mnras/stx797

Aleman I, Leal-Ferreira ML, Cami J, et al (2019) Characterization of the planetary nebula Tc 1 based on VLT X-shooter observations. Mon Not R Astron Soc 490(2):2475–2494. https://doi.org/10.1093/mnras/stz2654

Ali-Haïmoud Y (2014) Rotational spectroscopy of interstellar PAHs. Mon Not R Astron Soc 437(3):2728–2743. https://doi.org/10.1093/mnras/stt2083

Ali-Haïmoud Y, Pérez LM, Maddalena RJ, et al (2015) Search for polycyclic aromatic hydrocarbons in the Perseus molecular cloud with the Green Bank Telescope. Mon Not R Astron Soc 447(1):315–324. https://doi.org/10.1093/mnras/stu2476

Allamandola LJ, Tielens AG, Barker JR (1989) Interstellar polycyclic aromatic hydrocarbons: the infrared emission bands, the excitation/emission mechanism, and the astrophysical implications. Astrophys J Suppl Ser 71:733–775. https://doi.org/10.1086/191396

Allamandola LJ, Boersma C, Lee TJ, et al (2021) PAH spectroscopy from 1 to 5 μm. Astrophys J Lett 917(2):L35. https://doi.org/10.3847/2041-8213/ac17f0

Allison TC, Burgess DR (2015) High-quality thermochemistry data on polycyclic aromatic hydrocarbons via quantum chemistry. Polycycl Aromat Compd 35(1):16–31. https://doi.org/10.1080/10406638.2014.892890

Almeida CR, Esparza-Arredondo D, González-Martín O, et al (2023) Absence of nuclear polycyclic aromatic hydrocarbon emission from a compact starburst: the case of the type-2 quasar Mrk 477. Astron Astrophys 669:L5. https://doi.org/10.1051/0004-6361/202245409

Alonso-Herrero A, Ramos Almeida C, Esquej P, et al (2014) Nuclear 11.3 μm PAH emission in local active galactic nuclei. Mon Not R Astron Soc 443(3):2766–2782. https://doi.org/10.1093/mnras/stu1293

Alvarez-Thon L, Lee TJ, Fortenberry RC, et al (2022) Quantification of molecular aromaticity as a predictive factor of astrophysical significance. Astron Astrophys 662:A106. https://doi.org/10.1051/0004-6361/202243253

Álvaro Galué H (2014) Decoding the infrared signatures of pyramidal carbons in graphenic molecular nanostructures of interstellar origin. Chem Sci 5(7):2667. https://doi.org/10.1039/c4sc00890a

Álvaro Galué H, Díaz Leines G (2017) Origin of spectral band patterns in the cosmic unidentified infrared emission. Phys Rev Lett 119(17):171102. https://doi.org/10.1103/PhysRevLett.119.171102

Álvaro Galué H, Oomens J, Buma WJ, et al (2016) Electron-flux infrared response to varying π-bond topology in charged aromatic monomers. Nat Commun 7(1):12633. https://doi.org/10.1038/ncomms12633

Anand RK, Rastogi S, Kumar B, et al (2020) Detection of PAH and nbL features in planetary nebulae NGC 7027 and BD +30° 3639 with TIRCAM2 instrument on 3.6 m DOT. J Astrophys Astron 41(1):27. https://doi.org/10.1007/s12036-020-09644-9

Anand RK, Rastogi S, Kumar B (2023) PAH emission features in star-forming regions and late type stars. J Astrophys Astron 44(1):47. https://doi.org/10.1007/s12036-023-09941-z

Anderson DE, Blake GA, Cleeves LI, et al (2021) Observing carbon and oxygen carriers in protoplanetary disks at mid-infrared wavelengths. Astrophys J 909(1):55. https://doi.org/10.3847/1538-4357/abd9c1

Andrews H, Boersma C, Werner MW, et al (2015) PAH emission at the bright locations of PDRs: the grand-PAH hypothesis. Astrophys J 807(1):99. https://doi.org/10.1088/0004-637X/807/1/99

Andrews H, Candian A, Tielens AGGM (2016) Hydrogenation and dehydrogenation of interstellar PAHs: spectral characteristics and H_2 formation. Astron Astrophys 595:A23. https://doi.org/10.1051/0004-6361/201628819

Andrews H, Peeters E, Tielens AGGM, et al (2018) Whipping IC 63/IC 59. Astron Astrophys 619:A170. https://doi.org/10.1051/0004-6361/201832808

Arenas BE, Batra G, Steber AL, et al (2021) Rotational spectroscopy of imidazole: accurate spectroscopic information for three vibrationally excited states and the heavy-atom isotopologues up to 295 GHz. J Mol Spectrosc 378:111452. https://doi.org/10.1016/j.jms.2021.111452

Banhatti S, Palotás J, Jusko P, et al (2021) Infrared action spectroscopy of doubly charged PAHs and their contribution to the aromatic infrared bands. Astron Astrophys 648:A61. https://doi.org/10.1051/0004-6361/202039744

Banhatti S, Rap DB, Simon A, et al (2022) Formation of the acenaphthylene cation as a common C_2H_2-loss fragment in dissociative ionization of the PAH isomers anthracene and phenanthrene. Phys Chem Chem Phys 24(44):27343–27354. https://doi.org/10.1039/D2CP03835H

Barnum TJ, Siebert MA, Lee KLK, et al (2022) A search for heterocycles in GOTHAM observations of TMC-1. J Phys Chem A 126(17):2716–2728. https://doi.org/10.1021/acs.jpca.2c01435

Baron D, Poznanski D, Watson D, et al (2015) Dusting off the diffuse interstellar bands: DIBs and dust in extragalactic Sloan Digital Sky Survey spectra. Mon Not R Astron Soc 447(1):545–558. https://doi.org/10.1093/mnras/stu2448

Barrales-Martínez C, Cortés-Arriagada D, Gutiérrez-Oliva S (2018) Molecular hydrogen formation in the interstellar medium: the role of polycyclic aromatic hydrocarbons analysed by the reaction force and activation strain model. Mon Not R Astron Soc 481(3):3052–3062. https://doi.org/10.1093/mnras/sty2215

Bartolomei M, Pérez de Tudela R, Arteaga K, et al (2017) Adsorption of molecular hydrogen on coronene with a new potential energy surface. Phys Chem Chem Phys 19(38):26358–26368. https://doi.org/10.1039/C7CP03819D

Barzaga R, García-Hernández DA, Díaz-Tendero S, et al (2023) On the presence of metallofullerenes in fullerene-rich circumstellar envelopes. Astrophys J 942(1):5. https://doi.org/10.3847/1538-4357/aca529

Bassett MK, Fortenberry RC (2017) Symmetry breaking and spectral considerations of the surprisingly floppy c-C_3H radical and the related dipole-bound excited state of c-C_3H^-. J Chem Phys 146(22):224303. https://doi.org/10.1063/1.4985095

Bauschlicher CW, Ricca A (2014) The infrared spectra of $C_{96}H_{25}$ compared with that of $C_{96}H_{24}$. Theor Chem Acc 133(4):1454. https://doi.org/10.1007/s00214-014-1454-0

Bauschlicher CW, Peeters E, Allamandola LJ (2008) The infrared spectra of very large, compact, highly symmetric, polycyclic aromatic hydrocarbons (PAHs). Astrophys J 678(1):316–327. https://doi.org/10.1086/533424

Bauschlicher CW, Peeters E, Allamandola LJ (2009) The infrared spectra of very large irregular polycylic aromatic hydrocarbons (PAHs): observational probes of astronomical PAH geometry, size, and charge. Astrophys J Suppl Ser 697(1):311. https://doi.org/10.1088/0004-637X/697/1/311

Bauschlicher CW, Ricca A, Boersma C, et al (2018) The NASA ames PAH IR spectroscopic database: computational version 3.00 with updated content and the introduction of multiple scaling factors. Astrophys J Suppl Ser 234(2):32. https://doi.org/10.3847/1538-4365/aaa019

Beirão P, Armus L, Lehnert MD, et al (2015) Spatially resolved Spitzer-IRS spectral maps of the superwind in M82. Mon Not R Astron Soc 451(3):2640–2655. https://doi.org/10.1093/mnras/stv1101

Bejaoui S, Salama F (2019) Cavity ring down spectroscopy of cold neutral phenanthrene and phenanthridine in supersonic jets. AIP Adv 9(8):085021. https://doi.org/10.1063/1.5100152

Bejaoui S, Bera PP, Salama F, et al (2023) Cavity ring-down spectroscopy of anthracene, 9-methylanthracene, and 2-methylanthracene in supersonic expansion. J Phys Chem A 127(12):2717–2730. https://doi.org/10.1021/acs.jpca.2c08994

Bell AC, Onaka T, Galliano F, et al (2019) Investigation of the origin of the anomalous microwave emission in Lambda Orionis. Publ Astron Soc Jpn 71(6):123. https://doi.org/10.1093/pasj/psz110

Ben Amor N, Michoulier E, Simon A (2021) Electronic excited states of benzene in interaction with water clusters: influence of structure and size. Theor Chem Acc 140(6):70. https://doi.org/10.1007/s00214-021-02764-7

Bera PP, Head-Gordon M, Lee TJ (2013) Relative energies, structures, vibrational frequencies, and electronic spectra of pyrylium cation, an oxygen-containing carbocyclic ring isoelectronic with benzene, and its isomers. J Chem Phys 139(17):174302. https://doi.org/10.1063/1.4826138

Bérard R, Makasheva K, Demyk K, et al (2021) Impact of metals on (star)dust chemistry: a laboratory astrophysics approach. Front Astron Space Sci 8. https://doi.org/10.3389/fspas.2021.654879

Bergin EA, Du F, Cleeves LI, et al (2016) Hydrocarbon emission rings in protoplanetary disks induced by dust evolution. Astrophys J 831(1):101. https://doi.org/10.3847/0004-637X/831/1/101

Bergmeister S, Kollotzek S, Calvo F, et al (2022) Adsorption of helium and hydrogen on triphenylene and 1,3,5-triphenylbenzene. Molecules 27(15):4937. https://doi.org/10.3390/molecules27154937

Bernal JJ, Haenecour P, Howe J, et al (2019) Formation of interstellar C_{60} from silicon carbide circumstellar grains. Astrophys J 883(2):L43. https://doi.org/10.3847/2041-8213/ab4206

Bernal JJ, Zega TJ, Ziurys LM (2022) Destructive processing of silicon carbide grains: experimental insights into the formation of interstellar fullerenes and carbon nanotubes. J Phys Chem A 126(34):5761–5767. https://doi.org/10.1021/acs.jpca.2c01441

Bernard-Salas J, Cami J, Jones A, et al (2014) Interstellar and circumstellar fullerenes. Proc Sci LCDU2013:032. https://doi.org/10.22323/1.207.0032

Berné O, Fuente A, Pantin E, et al (2015a) Very Large Telescope observations of Gomez's Hamburger: insights into a young protoplanet candidate. Astron Astrophys 578:L8. https://doi.org/10.1051/0004-6361/201526041

Berné O, Montillaud J, Joblin C (2015b) Top-down formation of fullerenes in the interstellar medium. Astron Astrophys 577:A133. https://doi.org/10.1051/0004-6361/201425338

Berné O, Cox NLJ, Mulas G, et al (2017) Detection of buckminsterfullerene emission in the diffuse interstellar medium. Astron Astrophys 605:L1. https://doi.org/10.1051/0004-6361/201630325

Berné O, Foschino S, Jalabert F, et al (2022a) Contribution of polycyclic aromatic hydrocarbon ionization to neutral gas heating in galaxies: model versus observations. Astron Astrophys 667:A159. https://doi.org/10.1051/0004-6361/202243171

Berné O, Habart E, Peeters E, et al (2022b) PDRs4All: a JWST early release science program on radiative feedback from massive stars. Publ Astron Soc Pac 134(1035):054301. https://doi.org/10.1088/1538-3873/ac604c

Bernstein LS, Clark FO, Cline JA, et al (2015) The diffuse interstellar bands and anomalous microwave emission may originate from the same carriers. Astrophys J 813(2):122. https://doi.org/10.1088/0004-637X/813/2/122

Bernstein LS, Shroll RM, Lynch DK, et al (2017) A small fullerene (C_{24}) may be the carrier of the 11.2 μm unidentified infrared band. Astrophys J 836(2):229. https://doi.org/10.3847/1538-4357/aa5c89

Bernstein LS, Shroll RM, Galazutdinov GA, et al (2018) Spectral deconvolution of the 6196 and 6614 Å diffuse interstellar bands supports a common-carrier origin. Astrophys J 859(2):174. https://doi.org/10.3847/1538-4357/aabd85

Betancourt F, Poveda JC, Alvarez I, et al (2015) Carbon/hydrogen clusters $C_nH_x^+$ formation from laser irradiation of coronene. J Phys Conf Ser 605:012021. https://doi.org/10.1088/1742-6596/605/1/012021

Bhatt NH, Cami J (2015) A sensitive spectral survey of interstellar features in the Near-UV [3050-3700 Å]. Astrophys J Suppl Ser 216(2):22. https://doi.org/10.1088/0067-0049/216/2/22

Bilalbegović G, Maksimović A, Valencic LA (2018) Tetrahedral hydrocarbon nanoparticles in space: X-ray spectra. Mon Not R Astron Soc 476(4):5358–5364. https://doi.org/10.1093/mnras/sty607

Boersma C, Rubin RH, Allamandola LJ (2012) Spatial analysis of the polycyclic aromatic hydrocarbon features southeast of the Orion bar. Astrophys J 753(2):168. https://doi.org/10.1088/0004-637X/753/2/168

Boersma C, Bregman JD, Allamandola LJ (2013) Properties of polycyclic aromatic hydrocarbons in the northwest photon dominated region of NGC 7023. I. PAH size, charge, composition, and structure distribution. Astrophys J 769(2):117. https://doi.org/10.1088/0004-637X/769/2/117

Boersma C, Bauschlicher CW, Ricca A, et al (2014a) The NASA AMES PAH IR spectroscopic database version 2.00: updated content, website, and on(off)line tools. Astrophys J Suppl Ser 211(1):8. https://doi.org/10.1088/0067-0049/211/1/8

Boersma C, Bregman J, Allamandola LJ (2014b) Properties of polycyclic aromatic hydrocarbons in the northwest photon dominated region of NGC 7023. II. Traditional PAH analysis using k -means as a visualization tool. Astrophys J 795(2):110. https://doi.org/10.1088/0004-637X/795/2/110

Boersma C, Bregman J, Allamandola LJ (2015) Properties of polycyclic aromatic hydrocarbons in the northwest photon dominated region of NGC 7023. III. Quantifying the traditional proxy for PAH charge and assessing its role. Astrophys J 806(1):121. https://doi.org/10.1088/0004-637X/806/1/121

Boersma C, Bregman J, Allamandola LJ (2016) The charge state of polycyclic aromatic hydrocarbons across reflection nebulae: PAH charge balance and calibration. Astrophys J 832(1):51. https://doi.org/10.3847/0004-637X/832/1/51

Boersma C, Bregman J, Allamandola LJ (2018) The charge state of polycyclic aromatic hydrocarbons across a reflection nebula, an H II region, and a planetary nebula. Astrophys J 858(2):67. https://doi.org/10.3847/1538-4357/aabcbe

Bohl E, Mignolet B, Johansson JO, et al (2017) Low-lying, Rydberg states of polycyclic aromatic hydrocarbons (PAHs) and cyclic alkanes. Phys Chem Chem Phys 19(35):24090–24099. https://doi.org/10.1039/C7CP03913A

Boschman L, Cazaux S, Spaans M, et al (2015) H_2 formation on PAHs in photodissociation regions: a high-temperature pathway to molecular hydrogen. Astron Astrophys 579:A72. https://doi.org/10.1051/0004-6361/201323165

Boutéraon T, Habart E, Ysard N, et al (2019) Carbonaceous nano-dust emission in proto-planetary discs: the aliphatic-aromatic components. Astron Astrophys 623:A135. https://doi.org/10.1051/0004-6361/201834016

Bouwman J, Bodi A, Oomens J, et al (2015a) On the formation of cyclopentadiene in the $C_3H_5 + C_2H_2$ reaction. Phys Chem Chem Phys 17(32):20508–20514. https://doi.org/10.1039/C5CP02243F

Bouwman J, Sztáray B, Oomens J, et al (2015b) Dissociative photoionization of quinoline and isoquinoline. J Phys Chem A 119(7):1127–1136. https://doi.org/10.1021/jp5121993

Bouwman J, de Haas AJ, Oomens J (2016) Spectroscopic evidence for the formation of pentalene$^+$ in the dissociative ionization of naphthalene. Chem Commun 52(12):2636–2638. https://doi.org/10.1039/C5CC10090A

Bouwman J, Bodi A, Hemberger P (2018a) Nitrogen matters: the difference between panh and PAH formation. Phys Chem Chem Phys 20(47):29910–29917. https://doi.org/10.1039/C8CP05830J

Bouwman J, Horst S, Oomens J (2018b) Spectroscopic characterization of the product ions formed by electron ionization of adamantane. ChemPhysChem 19(23):3211–3218. https://doi.org/10.1002/cphc.201800846

Bouwman J, Castellanos P, Bulak M, et al (2019) Effect of molecular structure on the infrared signatures of astronomically relevant PAHs. Astron Astrophys 621:A80. https://doi.org/10.1051/0004-6361/201834130

Bouwman J, Hrodmarsson HR, Ellison GB, et al (2021a) Five birds with one stone: photoelectron photoion coincidence unveils rich phthalide pyrolysis chemistry. J Phys Chem A 125(8):1738–1746. https://doi.org/10.1021/acs.jpca.1c00149

Bouwman J, Linnartz H, Tielens AGGM (2021b) Mid-infrared spectroscopic signatures of dibenzopyrene cations – the effect of symmetry on PAH IR spectroscopy. J Mol Spectrosc 378:111458. https://doi.org/10.1016/j.jms.2021.111458

Bouwman J, McCabe MN, Shingledecker CN, et al (2023) Five-membered ring compounds from the ortho-benzyne + methyl radical reaction under interstellar conditions. Nat Astron 7(4):423–430. https://doi.org/10.1038/s41550-023-01893-2

Bowey JE (2021) Dust changes in sakurai's object: new PAHs and sic with coagulation of submicron-sized silicate dust into 10 μm-sized melilite grains. Mon Not R Astron Soc 505(1):568–581. https://doi.org/10.1093/mnras/stab1305

Bowey JE, Hofmeister AM (2022) Sakurai's object revisited: new laboratory data for carbonates and melilites suggest the carrier of 6.9-μm excess absorption is a carbonate. Mon Not R Astron Soc 513(2):1774–1784. https://doi.org/10.1093/mnras/stac993

Boyer A, Hervé M, Despré V, et al (2021) Ultrafast vibrational relaxation dynamics in XUV-excited polycyclic aromatic hydrocarbon molecules. Phys Rev X 11(4):041012. https://doi.org/10.1103/PhysRevX.11.041012

Bréchignac P, Garcia GA, Falvo C, et al (2014) Photoionization of cold gas phase coronene and its clusters: autoionization resonances in monomer, dimer, and trimer and electronic structure of monomer cation. J Chem Phys 141(16):164325. https://doi.org/10.1063/1.4900427

Brédy R, Ortéga C, Ji M, et al (2015) PAH radiative cooling and fragmentation kinematics studied within an electrostatic ring. J Phys Conf Ser 583:012042. https://doi.org/10.1088/1742-6596/583/1/012042

Brieva AC, Gredel R, Jaeger C, et al (2016) C_{60} as a probe for astrophysical environments. Astrophys J 826(2):122. https://doi.org/10.3847/0004-637X/826/2/122

Bryson K, Salama F, Elsaesser A, et al (2015) First results of the organic experiment on EXPOSE-R on the ISS. Int J Astrobiol 14(1):55–66. https://doi.org/10.1017/S1473550414000597

Bull JN, Buntine JT, Scholz MS, et al (2019) Photodetachment and photoreactions of substituted naphthalene anions in a tandem ion mobility spectrometer. Faraday Discuss 217:34–46. https://doi.org/10.1039/C8FD00217G

Bull JN, Bolognesi P, Anstöter CS, et al (2023) Autoionization from the plasmon resonance in isolated 1-cyanonaphthalene. J Chem Phys 158(24):241101. https://doi.org/10.1063/5.0153058

Buntine JT, Cotter MI, Jacovella U, et al (2021) Electronic spectra of positively charged carbon clusters–$C_{2n}{}^+$ (n = 6–14). J Chem Phys 155(21):214302. https://doi.org/10.1063/5.0070502

Buragohain M, Pathak A, Sarre P, et al (2015) Theoretical study of deuteronated PAHs as carriers for IR emission features in the ISM. Mon Not R Astron Soc 454:193–204. https://doi.org/10.1093/mnras/stv1946

Buragohain M, Pathak A, Sarre P, et al (2016) Mid-infrared vibrational study of deuterium-containing PAH variants. Planet Space Sci 133:97–106. https://doi.org/10.1016/j.pss.2016.05.001

Buragohain M, Pathak A, Sarre P, et al (2018) Interstellar dehydrogenated PAH anions: vibrational spectra. Mon Not R Astron Soc 474(4):4594–4602. https://doi.org/10.1093/mnras/stx3060

Buragohain M, Pathak A, Sakon I, et al (2020) DFT study on interstellar PAH molecules with aliphatic side groups. Astrophys J 892(1):11. https://doi.org/10.3847/1538-4357/ab733a

Burkhardt AM, Long K, Lee K, Bryan Changala P, et al (2021a) Discovery of the pure polycyclic aromatic hydrocarbon indene (c-C_9H_8) with gotham observations of TMC-1. Astrophys J Lett 913(2):L18. https://doi.org/10.3847/2041-8213/abfd3a

Burkhardt AM, Loomis RA, Shingledecker CN, et al (2021b) Ubiquitous aromatic carbon chemistry at the earliest stages of star formation. Nat Astron 5(2):181–187. https://doi.org/10.1038/s41550-020-01253-4

Calvo F, Simon A, Parneix P, et al (2021) Infrared spectroscopy of chemically diverse carbon clusters: a data-driven approach. J Phys Chem A 125(25):5509–5518. https://doi.org/10.1021/acs.jpca.1c03368

Campbell EK, Dunk PW (2019) LV-DIB-s4PT: a new tool for astrochemistry. Rev Sci Instrum 90(10):103101. https://doi.org/10.1063/1.5116925

Campbell EK, Maier JP (2017) Gas-phase absorptions of $C_{42}H_{18}{}^+$ near 8300 Å below 10 K: astronomical implications. Astrophys J 850(1):69. https://doi.org/10.3847/1538-4357/aa9274

Campbell EK, Holz M, Gerlich D, et al (2015) Laboratory confirmation of $C_{60}{}^+$ as the carrier of two diffuse interstellar bands. Nature 523(7560):322–323. https://doi.org/10.1038/nature14566

Campbell EK, Reedy ES, Rademacher J, et al (2020) Electronic spectroscopy of He@$C_{60}{}^+$ for astrochemical consideration. Astrophys J 897(1):88. https://doi.org/10.3847/1538-4357/ab8dba

Campisi D, Candian A (2020) Do defects in PAHs promote catalytic activity in space? Stone–Wales pyrene as a test case. Phys Chem Chem Phys 22(12):6738–6748. https://doi.org/10.1039/C9CP06523G
Campisi D, Simonsen FDS, Thrower JD, et al (2020) Superhydrogenation of pentacene: the reactivity of zigzag-edges. Phys Chem Chem Phys 22(3):1557–1565. https://doi.org/10.1039/C9CP05440E
Campisi D, Lamberts T, Dzade NY, et al (2021) Interaction of aromatic molecules with forsterite: accuracy of the periodic DFT-D4 method. J Phys Chem A 125(13):2770–2781. https://doi.org/10.1021/acs.jpca.1c02326
Candian A, Mackie CJ (2017) Anharmonic interstellar PAH molecules. Int J Quant Chem 117(2):146–150. https://doi.org/10.1002/qua.25292
Candian A, Sarre PJ (2015) The 11.2 μm emission of PAHs in astrophysical objects. Mon Not R Astron Soc 448(3):2960–2970. https://doi.org/10.1093/mnras/stv192
Candian A, Kerr TH, Song IO, et al (2012) Spatial distribution and interpretation of the 3.3 μm PAH emission band of the red rectangle: 3.3 μm PAH emission of the red rectangle. Mon Not R Astron Soc 426(1):389–397. https://doi.org/10.1111/j.1365-2966.2012.21760.x
Candian A, Sarre PJ, Tielens AGGM (2014) Polycyclic aromatic hydrocarbons with armchair edges and the 12.7 μm band. Astrophys J 791(1):L10. https://doi.org/10.1088/2041-8205/791/1/L10
Candian A, Bouwman J, Hemberger P, et al (2018) Dissociative ionisation of adamantane: a combined theoretical and experimental study. Phys Chem Chem Phys 20(8):5399–5406. https://doi.org/10.1039/C7CP05957D
Candian A, Gomes Rachid M, MacIsaac H, et al (2019) Searching for stable fullerenes in space with computational chemistry. Mon Not R Astron Soc 485(1):1137–1146. https://doi.org/10.1093/mnras/stz450
Canelo CM, Friaça ACS, Sales DA, et al (2018) Variations in the 6.2 μm emission profile in starburst-dominated galaxies: a signature of polycyclic aromatic nitrogen heterocycles (PANHs)? Mon Not R Astron Soc 475(3):3746–3763. https://doi.org/10.1093/mnras/stx3351
Canelo CM, Sales DA, Friaca ACS, et al (2021) Profile comparison of the 6-9 mu m polycyclic aromatic hydrocarbon bands in starburst-dominated galaxies. Mon Not R Astron Soc 507(4):6177–6195. https://doi.org/10.1093/mnras/stab2552
Carpentier Y, Pino T, Bréchignac P (2013) R2PI spectroscopy of aromatic molecules produced in an ethylene-rich flame. J Phys Chem A 117(39):10092–10104. https://doi.org/10.1021/jp400913n
Castellanos P, Berne O, Sheffer Y, et al (2014) C_{60} in photodissociation regions. Astrophys J 794(1):83. https://doi.org/10.1088/0004-637X/794/1/83
Castellanos P, Candian A, Andrews H, et al (2018a) Photoinduced polycyclic aromatic hydrocarbon dehydrogenation. Molecular hydrogen formation in dense PDRs. Astron Astrophys 616:A167. https://doi.org/10.1051/0004-6361/201833221
Castellanos P, Candian A, Zhen J, et al (2018b) Photoinduced polycyclic aromatic hydrocarbon dehydrogenation. The competition between H- and H_2-loss. Astron Astrophys 616:A166. https://doi.org/10.1051/0004-6361/201833220
Castro A, Miyaji T, Shirahata M, et al (2014) AKARI infrared camera observations of the 3.3 μm PAH feature in Swift/BAT AGNs. Publ Astron Soc Jpn 66(6):110. https://doi.org/10.1093/pasj/psu096
Cataldo F, Garcia-Hernandez AD, Torres AM (2021) Vinylacetylene synthesis with a low power submerged carbon arc in n-hexane. Fuller Nanotub Carbon Nanostructures 29(12):956–965. https://doi.org/10.1080/1536383X.2021.1920580
Cavallari C, Pontiroli D, Jiménez-Ruiz M, et al (2016) Hydrogen motions in defective graphene: the role of surface defects. Phys Chem Chem Phys 18(36):24820–24824. https://doi.org/10.1039/C6CP04727K
Cazaux S, Boschman L, Rougeau N, et al (2016) The sequence to hydrogenate coronene cations: a journey guided by magic numbers. Sci Rep 6(1):19835. https://doi.org/10.1038/srep19835
Cazaux S, Arribard Y, Egorov D, et al (2019) The sequence of coronene hydrogenation revealed by gas-phase ir spectroscopy. Astrophys J 875(1):27. https://doi.org/10.3847/1538-4357/ab0e01
Cernicharo J, Agúndez M, Cabezas C, et al (2021a) Pure hydrocarbon cycles in TMC-1: discovery of ethynyl cyclopropenylidene, cyclopentadiene, and indene. Astron Astrophys 649:L15. https://doi.org/10.1051/0004-6361/202141156
Cernicharo J, Agúndez M, Kaiser RI, et al (2021b) Discovery of benzyne, o-C_6H_4, in TMC-1 with the QUIJOTE line survey. Astron Astrophys 652:L9. https://doi.org/10.1051/0004-6361/202141660
Chakraborty S, Mulas G, Demyk K, et al (2019) Experimental approach to the study of anharmonicity in the infrared spectrum of pyrene from 14 to 723 K. J Phys Chem A 123(19):4139–4148. https://doi.org/10.1021/acs.jpca.8b11016
Chakraborty S, Demyk K, Biennier L, et al (2020) Absorption spectroscopy of solid-phase fullerene C_{60} between 1.65 and 2.78 μm. ACS Earth Space Chem 4(9):1540–1548. https://doi.org/10.1021/acsearthspacechem.0c00123
Chakraborty S, Mulas G, Rapacioli M, et al (2021) Anharmonic infrared spectra of thermally excited pyrene ($C_{16}H_{10}$): a combined view of DFT-based GVPT2 with AnharmonicCaOs, and approximate DFT

molecular dynamics with demonNano. J Mol Spectrosc 378:111466. https://doi.org/10.1016/j.jms.2021.111466
Chandrasekaran V, Prabhakaran A, Kafle B, et al (2017) Formation and stabilization of C_6^- by radiative electron attachment. J Chem Phys 146(9):094302. https://doi.org/10.1063/1.4977059
Chang HC (2016) Diamonds in space: a brief history and recent laboratory studies. J Phys Conf Ser 728:062004. https://doi.org/10.1088/1742-6596/728/6/062004
Chastenet J, Sandstrom K, Chiang ID, et al (2019) The polycyclic aromatic hydrocarbon mass fraction on a 10 pc scale in the Magellanic Clouds. Astrophys J 876(1):62. https://doi.org/10.3847/1538-4357/ab16cf
Chastenet J, Sutter J, Sandstrom K, et al (2022) PHANGS-JWST first results: Measuring PAH properties across the multiphase ISM. https://doi.org/10.48550/arXiv.2212.10512
Chastenet J, Sutter J, Sandstrom K, et al (2023) PHANGS-JWST first results: variations in PAH fraction as a function of ISM phase and metallicity. Astrophys J Lett 944(2):L11. https://doi.org/10.3847/2041-8213/acadd7
Chatterjee K, Dopfer O (2017) Infrared spectroscopy of hydrated polycyclic aromatic hydrocarbon cations: naphthalene$^+$–water. Phys Chem Chem Phys 19(48):32262–32271. https://doi.org/10.1039/C7CP06893J
Chatterjee K, Dopfer O (2018a) Infrared signatures of protonated benzonitrile. Astrophys J 865(2):114. https://doi.org/10.3847/1538-4357/aad462
Chatterjee K, Dopfer O (2018b) Microhydration of PAH$^+$ cations: evolution of hydration network in naphthalene$^+$–$(H_2O)_n$ clusters (n $\leq$ 5). Chem Sci 9(8):2301–2318. https://doi.org/10.1039/C7SC05124G
Chatterjee K, Dopfer O (2020a) Microhydration of protonated biomolecular building blocks: protonated pyrimidine. Phys Chem Chem Phys 22(23):13092–13107. https://doi.org/10.1039/D0CP02110E
Chatterjee K, Dopfer O (2020b) Protonation of naphthalene–$(water)_n$ nanoclusters: intracluster proton transfer to hydration shell revealed by infrared photodissociation spectroscopy. J Phys Chem A 124(6):1134–1151. https://doi.org/10.1021/acs.jpca.9b11779
Chawananon S, Pirali O, Goubet M, et al (2022) Characterizing centrosymmetric two-ring PAHs using jet-cooled high resolution mid-infrared laser spectroscopy and anharmonic quantum chemical calculations. J Chem Phys 157(6):064301. https://doi.org/10.1063/5.0096777
Chen T, Gatchell M, Stockett MH, et al (2014c) Absolute fragmentation cross sections in atom-molecule collisions: scaling laws for non-statistical fragmentation of polycyclic aromatic hydrocarbon molecules. J Chem Phys 140(22):224306. https://doi.org/10.1063/1.4881603
Chen L, Ji M, Bernard J, et al (2014a) Time evolution of internal energy distribution of anthracene studied in an electrostatic storage ring, the Mini-Ring. J Phys Conf Ser 488(1):012039. https://doi.org/10.1088/1742-6596/488/1/012039
Chen Q, Wei GF, Tian WJ, et al (2014b) Quasi-planar aromatic B_{36} and B_{36}^- clusters: all-boron analogues of coronene. Phys Chem Chem Phys 16(34):18282–18287. https://doi.org/10.1039/C4CP02032D
Chen T, Gatchell M, Stockett MH, et al (2015) Formation of H_2 from internally heated polycyclic aromatic hydrocarbons: excitation energy dependence. J Chem Phys 142(14):144305. https://doi.org/10.1063/1.4917021
Chen XH, Li A, Zhang K (2017) On graphene in the interstellar medium. Astrophys J 850(1):104. https://doi.org/10.3847/1538-4357/aa93d5
Chen X, Xiao Z, Li A, et al (2018a) Graphene and carbon nanotubes in space. Proc Int Astron Union 14(A30):403–404. https://doi.org/10.1017/S1743921319004940
Chen T, Zhen J, Wang Y, et al (2018b) From planes to bowls: photodissociation of the bisanthenequinone cation. Chem Phys Lett 692:298–303. https://doi.org/10.1016/j.cplett.2017.12.043
Chen T, Xiao CY, Li A, et al (2021) Where have all the interstellar silicon carbides gone? Mon Not R Astron Soc 509(4):5231–5236. https://doi.org/10.1093/mnras/stab3175
Cheng X, Wei M, Tian G, et al (2022) Vibrationally-resolved X-ray photoelectron spectra of six polycyclic aromatic hydrocarbons from first-principles simulations. J Phys Chem A 126(33):5582–5593. https://doi.org/10.1021/acs.jpca.2c04426
Chiar JE, de Barros ALF, Mattioda AL, et al (2021) Assessment of the presence of PAHs and hydrogenated PAHs in the young stellar object Mon R2 and the Taurus dense cloud toward Elias 16. Astrophys J 908(2):239. https://doi.org/10.3847/1538-4357/abd6e8
Chou SL, Lin MY, Lin SY, et al (2020) Far-ultraviolet absorption and photoluminescence of monolayer graphene and its implications for extended red emission. Astrophys J 901(2):103. https://doi.org/10.3847/1538-4357/abb0e6
Christianson DA, Garrod RT (2021) Chemical kinetics simulations of ice chemistry on porous versus non-porous dust grains. Front Astron Space Sci 8:643297. https://doi.org/10.3389/fspas.2021.643297
Chuss DT, Hensley BS, Kogut AJ, et al (2022) Tracing PAH emission in λ-Orionis using COBE/DIRBE data. Astrophys J 940(1):59. https://doi.org/10.3847/1538-4357/ac9b24

Clark VHJ, Benoit DM (2021) The vibrational properties of benzene on an ordered water ice surface. Mon Not R Astron Soc 508(3):3239–3250. https://doi.org/10.1093/mnras/stab2670
Cloutis E, Szymanski P, Applin D, et al (2016) Identification and discrimination of polycyclic aromatic hydrocarbons using Raman spectroscopy. Icarus 274:211–230. https://doi.org/10.1016/j.icarus.2016.03.023
Cocchi C, Prezzi D, Ruini A, et al (2013) Concavity effects on the optical properties of aromatic hydrocarbons. J Phys Chem C 117(24):12909–12915. https://doi.org/10.1021/jp4036259
Cocchi C, Prezzi D, Ruini A, et al (2014) Anisotropy and size effects on the optical spectra of polycyclic aromatic hydrocarbons. J Phys Chem A 118(33):6507–6513. https://doi.org/10.1021/jp503054j
Contreras CS, Salama F (2013) Laboratory investigations of polycyclic aromatic hydrocarbon formation and destruction in the circumstellar outflows of carbon stars. Astrophys J Suppl Ser 208(1):6. https://doi.org/10.1088/0067-0049/208/1/6
Cook AM, Ricca A, Mattioda AL, et al (2015) Photochemistry of polycyclic aromatic hydrocarbons in cosmic water ice: the role of PAH ionization and concentration. Astrophys J 799(1):14. https://doi.org/10.1088/0004-637X/799/1/14
Cordiner MA, Linnartz H, Cox NLJ, et al (2019) Confirming interstellar C_{60}^+ using the Hubble Space Telescope. Astrophys J 875(2):L28. https://doi.org/10.3847/2041-8213/ab14e5
Cortzen I, Garrett J, Magdis G, et al (2019) PAHs as tracers of the molecular gas in star-forming galaxies. Mon Not R Astron Soc 482(2):1618–1633. https://doi.org/10.1093/mnras/sty2777
Cottin H, Saiagh K, Guan YY, et al (2015) The AMINO experiment: a laboratory for astrochemistry and astrobiology on the EXPOSE-R facility of the International Space Station. Int J Astrobiol 14(1):67–77. https://doi.org/10.1017/S1473550414000500
Cox NLJ, Cami J, Kaper L, et al (2014) VLT/X-Shooter survey of near-infrared diffuse interstellar bands. Astron Astrophys 569:A117. https://doi.org/10.1051/0004-6361/201323061
Cox NLJ, Pilleri P, Berné O, et al (2016) Polycyclic aromatic hydrocarbons and molecular hydrogen in oxygen-rich planetary nebulae: the case of NGC 6720. Mon Not R Astron Soc Lett 456(1):L89–L93. https://doi.org/10.1093/mnrasl/slv184
Crandall PB, Müller D, Leroux J, et al (2020) Optical spectrum of the adamantane radical cation. Astrophys J 900(2):L20. https://doi.org/10.3847/2041-8213/abafbd
Croiset BA, Candian A, Berné O, et al (2016) Mapping PAH sizes in NGC 7023 with SOFIA. Astron Astrophys 590:A26. https://doi.org/10.1051/0004-6361/201527714
Cruikshank DP, Dalle Ore CM, Clark RN, et al (2014) Aromatic and aliphatic organic materials on Iapetus: analysis of Cassini VIMS data. Icarus 233:306–315. https://doi.org/10.1016/j.icarus.2014.02.011
Cruz-Diaz GA, Erickson SE, da Silveira EF, et al (2019) PAH products and processing by different energy sources. Astrophys J 882(1):44. https://doi.org/10.3847/1538-4357/ab311f
Cruz-Diaz GA, Ricca A, Mattioda AL (2020) Polycyclic aromatic hydrocarbons and dust particle surface interactions: catalytic hydrogenation of polycyclic aromatic hydrocarbon molecules under vacuum conditions. ACS Earth Space Chem 4(10):1730–1742. https://doi.org/10.1021/acsearthspacechem.0c00145
Cuylle SH, Allamandola LJ, Linnartz H (2014) Photochemistry of PAHs in cosmic water ice - the effect of concentration on UV-Vis spectroscopy and ionization efficiency. Astron Astrophys 562:A22. https://doi.org/10.1051/0004-6361/201322495
Dawes A, Pascual N, Mason NJ, et al (2018) Probing the interaction between solid benzene and water using vacuum ultraviolet and infrared spectroscopy. Phys Chem Chem Phys 20(22):15273–15287. https://doi.org/10.1039/C8CP01228H
de Barros ALF, Mattioda AL, Ricca A, et al (2017) Photochemistry of coronene in cosmic water ice analogs at different concentrations. Astrophys J 848(2):112. https://doi.org/10.3847/1538-4357/aa8c71
de Haas AJ, Oomens J, Bouwman J (2017) Facile pentagon formation in the dissociation of polyaromatics. Phys Chem Chem Phys 19(4):2974–2980. https://doi.org/10.1039/C6CP08349H
Delaunay R, Gatchell M, Rousseau P, et al (2015) Molecular growth inside of polycyclic aromatic hydrocarbon clusters induced by ion collisions. J Phys Chem Lett 6(9):1536–1542. https://doi.org/10.1021/acs.jpclett.5b00405
Delgado-Inglada G, Rodríguez M (2014) C/O abundance ratios, iron depletions, and infrared dust features in galactic planetary nebulae. Astrophys J 784(2):173. https://doi.org/10.1088/0004-637X/784/2/173
Désesquelles P, Van-Oanh NT, Xu L, et al (2021) Multiple dehydrogenation of fluorene cation and neutral fluorene using the statistical molecular fragmentation model. Phys Chem Chem Phys 23(16):9900–9910. https://doi.org/10.1039/D0CP06100J
Devi G, Buragohain M, Pathak A (2020) DFT study of five-membered ring PAHs. Planet Space Sci 183(September 2018):104593. https://doi.org/10.1016/j.pss.2018.09.003
Díaz-Luis JJ, García-Hernández DA, Kameswara Rao N, et al (2015) A search for diffuse bands in fullerene planetary nebulae: evidence of diffuse circumstellar bands. Astron Astrophys 573:A97. https://doi.org/10.1051/0004-6361/201424710

Díaz-Luis JJ, García-Hernández DA, Manchado A, et al (2016) A search for hydrogenated fullerenes in fullerene-containing planetary nebulae. Astron Astrophys 589:A5. https://doi.org/10.1051/0004-6361/201527727

Díaz-Luis JJ, García-Hernández DA, Manchado A, et al (2018) GTC/CanariCam mid-IR imaging of the fullerene-rich planetary nebula IC 418: searching for the spatial distribution of fullerene-like molecules. Astron J 155(3):105. https://doi.org/10.3847/1538-3881/aaa75c

Dickinson C, Ali-Hamoud Y, Beswick RJ, et al (2015) Studies of anomalous microwave emission (AME) with the SKA. In: Proceedings of Advancing Astrophysics with the Square Kilometre Array – PoS(AASKA14), p 124. https://doi.org/10.22323/1.215.0124

Dobrijevic M, Loison JC, Hickson KM, et al (2016) 1D-coupled photochemical model of neutrals, cations and anions in the atmosphere of Titan. Icarus 268:313–339. https://doi.org/10.1016/j.icarus.2015.12.045

Doddipatla S, Galimova GR, Wei H, et al (2021) Low-temperature gas-phase formation of indene in the interstellar medium. Sci Adv 7(1):eabd4044. https://doi.org/10.1126/sciadv.abd4044

Domaracka A, Delaunay R, Mika A, et al (2018) Ion collision-induced chemistry in pure and mixed loosely bound clusters of coronene and C_{60} molecules. Phys Chem Chem Phys 20(22):15052–15060. https://doi.org/10.1039/C8CP01179F

Doney KD, Candian A, Mori T, et al (2016) Deuterated polycyclic aromatic hydrocarbons: revisited. Astron Astrophys 586:A65. https://doi.org/10.1051/0004-6361/201526809

Dontot L, Spiegelman F, Rapacioli M (2019) Structures and energetics of neutral and cationic pyrene clusters. J Phys Chem A 123(44):9531–9543. https://doi.org/10.1021/acs.jpca.9b07007

Dontot L, Spiegelman F, Zamith S, et al (2020) Dependence upon charge of the vibrational spectra of small polycyclic aromatic hydrocarbon clusters: the example of pyrene. Eur Phys J D 74(11):216. https://doi.org/10.1140/epjd/e2020-10081-0

Draine BT, Li A (2007) Infrared emission from interstellar dust. IV. The silicate-graphite-PAH model in the post-Spitzer era. Astrophys J 657(2):810–837. https://doi.org/10.1086/511055. arXiv:astro-ph/0608003 [astro-ph]

Draine BT, Aniano G, Krause O, et al (2013) Andromeda's dust. Astrophys J 780(2):172. https://doi.org/10.1088/0004-637X/780/2/172

Dubosq C, Falvo C, Calvo F, et al (2019) Mapping the structural diversity of C_{60} carbon clusters and their infrared spectra. Astron Astrophys 625:L11. https://doi.org/10.1051/0004-6361/201834943

Dubosq C, Pla P, Dartois E, et al (2023) Spectroscopic investigation of interstellar hydrogenated carbon clusters – infrared and optical spectra of $C_{24}H_n$ populations. Astron Astrophys 670:A175. https://doi.org/10.1051/0004-6361/202245472

Duley WW, Zaidi A, Wesolowski MJ, et al (2015) Small molecules from the decomposition of interstellar carbons. Mon Not R Astron Soc 447(2):1242–1246. https://doi.org/10.1093/mnras/stu2508

Dunk PW, Adjizian JJ, Kaiser NK, et al (2013) Metallofullerene and fullerene formation from condensing carbon gas under conditions of stellar outflows and implication to stardust. Proc Natl Acad Sci 110(45):18081–18086. https://doi.org/10.1073/pnas.1315928110

Ebenbichler A, Postel A, Przybilla N, et al (2022) CRIRES high-resolution near-infrared spectroscopy of diffuse interstellar band profiles: detection of 12 new DIBs in the YJ band and the introduction of a combined ISM sight line and stellar analysis approach. Astron Astrophys 662:A81. https://doi.org/10.1051/0004-6361/202142990

Ehrenfreund P, Ruiterkamp R, Peeters Z, et al (2007) The ORGANICS experiment on BIOPAN V: UV and space exposure of aromatic compounds. Planet Space Sci 55(4):383–400. https://doi.org/10.1016/j.pss.2006.07.001

Elyajouri M, Cox NLJ, Lallement R (2017) The 15273 Å diffuse interstellar band in the dark cloud Barnard 68. Astron Astrophys 605:L10. https://doi.org/10.1051/0004-6361/201731437

Elyajouri M, Lallement R, Cox NLJ, et al (2018) The EDIBLES survey: III. C_2-DIBs and their profiles. Astron Astrophys 616:A143. https://doi.org/10.1051/0004-6361/201833105

Endo I, Sakon I, Onaka T, et al (2021) On the nature of organic dust in novae. Astrophys J 917(2):103. https://doi.org/10.3847/1538-4357/ac0cf1

Ensor T, Cami J, Bhatt NH, et al (2017) A principal component analysis of the diffuse interstellar bands. Astrophys J 836(2):162. https://doi.org/10.3847/1538-4357/aa5b84

Esparza-Arredondo D, González-Martín O, Dultzin D, et al (2018) Circumnuclear star formation and AGN activity: clues from surface brightness radial profile of PAHs and [S_{IV}]. Astrophys J 859(2):124. https://doi.org/10.3847/1538-4357/aabcbc

Esquej P, Alonso-Herrero A, González-Martín O, et al (2013) Nuclear star formation activity and black hole accretion in nearby Seyfert galaxies. Astrophys J 780(1):86. https://doi.org/10.1088/0004-637X/780/1/86

Evans A, Gehrz RD, Woodward CE, et al (2016) CK Vul: a smorgasbord of hydrocarbons rules out a 1670 nova (and much else besides). Mon Not R Astron Soc 457(3):2871–2876. https://doi.org/10.1093/mnras/stw352

Faure M, Quirico E, Faure A, et al (2021) A radiolytic origin of organic matter in primitive chondrites and trans-Neptunian objects? New clues from ion irradiation experiments. Icarus 364:114462. https://doi.org/10.1016/j.icarus.2021.114462

Ferullo RM, Zubieta CE, Belelli PG (2019) Hydrogenated polycyclic aromatic hydrocarbons (H_nPAHs) as catalysts for hydrogenation reactions in the interstellar medium: a quantum chemical model. Phys Chem Chem Phys 21(22):12012–12020. https://doi.org/10.1039/C9CP02329A

Filipek GT, Fortenberry RC (2016) Formation of potential interstellar noble gas molecules in gas and adsorbed phases. ACS Omega 1(5):765–772. https://doi.org/10.1021/acsomega.6b00249

Finazzi L, Martens J, Berden G, et al (2023) Probing radical versus proton migration in the aniline cation with IRMPD spectroscopy. Mol Phys 0(0):e2192307. https://doi.org/10.1080/00268976.2023.2192307

Fioroni M, Savage RE, DeYonker NJ (2019) On the formation of phosphorous polycyclic aromatics hydrocarbons (PAPHs) in astrophysical environments. Phys Chem Chem Phys 21(15):8015–8021. https://doi.org/10.1039/C9CP00547A

Flint AR, Fortenberry RC (2022) The formation of monosubstituted cyclopropenylidene derivatives in the interstellar medium via neutral-neutral reaction pathways. Astrophys J 938(1):15. https://doi.org/10.3847/1538-4357/ac8f4a

Flint AR, Watrous AG, Westbrook BR, et al (2023) Gas-phase formation and spectroscopic characterization of the disubstituted cyclopropenylidenes c-$C_3(C_2H)_2$, c-$C_3(CN)_2$, and c-$C_3(C_2H)(CN)$. Astron Astrophys 671:A95. https://doi.org/10.1051/0004-6361/202245643

Foley N, Cazaux S, Egorov D, et al (2018) Molecular hydrogen formation on interstellar PAHs through eley-rideal abstraction reactions. Mon Not R Astron Soc. https://doi.org/10.1093/mnras/sty1528

Fortenberry RC, Moore MM, Lee TJ (2016) Excited state trends in bidirectionally expanded closed-shell PAH and PANH anions. J Phys Chem A 120(37):7327–7334. https://doi.org/10.1021/acs.jpca.6b06654

Fortenberry RC, Lee TJ, Huang X (2017) Towards completing the cyclopropenylidene cycle: rovibrational analysis of cyclic N_3^+, CNN, $HCNN^+$, and CNC^-. Phys Chem Chem Phys 19(34):22860–22869. https://doi.org/10.1039/C7CP04257D

Fortenberry RC, Novak CM, Layfield JP, et al (2018) Overcoming the failure of correlation for out-of-plane motions in a simple aromatic: rovibrational quantum chemical analysis of c-C_3H_2. J Chem Theory Comput 14(4):2155–2164. https://doi.org/10.1021/acs.jctc.8b00164

Foschino S, Berné O, Joblin C (2019) Learning mid-IR emission spectra of polycyclic aromatic hydrocarbon populations from observations. Astron Astrophys 632:A84. https://doi.org/10.1051/0004-6361/201935085

Freidzon AY, Valiev RR, Berezhnoy AA (2014) Ab initio simulation of pyrene spectra in water matrices. RSC Adv 4(79):42054–42065. https://doi.org/10.1039/C4RA05574H

Friha H, Féraud G, Troy T, et al (2013) Visible photodissociation spectra of the 1- and 2-methylnaphthalene cations: laser spectroscopy and theoretical simulations. J Phys Chem A 117(50):13664–13672. https://doi.org/10.1021/jp407627x

Fulvio D, Góbi S, Jäger C, et al (2017) Laboratory experiments on the low-temperature formation of carbonaceous grains in the ISM. Astrophys J Suppl Ser 233(1):14. https://doi.org/10.3847/1538-4365/aa9224

Gadallah KA, Ali AA (2021) Impacts of the PAH size and the radiation intensity on the IR features of illuminated dust within the reflection nebulae. Adv Space Res 67(12):4222–4237. https://doi.org/10.1016/j.asr.2021.02.025

Gama DRG, Lepine JRD, Mendoza E, et al (2016) CO observations and investigation of triggered star formation toward the N10 infrared bubble and surroundings. Astrophys J 830(2):57. https://doi.org/10.3847/0004-637X/830/2/57

Ganguly S, Gisselbrecht M, Eng-Johnsson P, et al (2022) Coincidence study of core-ionized adamantane: site-sensitivity within a carbon cage? Phys Chem Chem Phys 24(47):28994–29003. https://doi.org/10.1039/D2CP04426A

Gao J, Berden G, Oomens J (2014) Laboratory infrared spectroscopy of gageous negatively charged polyaromatic hydrocarbons. Astrophys J 787(2):170. https://doi.org/10.1088/0004-637X/787/2/170

Gao J, Bouwman J, Berden G, et al (2016) The influence of metal ion binding on the IR spectra of nitrogen-containing PAHs. J Phys Chem A 120(40):7800–7809. https://doi.org/10.1021/acs.jpca.6b05060

Garcia-Bernete I, Rigopoulou D, Alonso-Herrero A, et al (2022a) A high angular resolution view of the PAH emission in Seyfert galaxies using JWST/MRS data. Astron Astrophys 666:L5. https://doi.org/10.1051/0004-6361/202244806

Garcia-Bernete I, Rigopoulou D, Alonso-Herrero A, et al (2022b) Polycyclic aromatic hydrocarbons in Seyfert and star-forming galaxies. Mon Not R Astron Soc 509(3):4256–4275. https://doi.org/10.1093/mnras/stab3127

Garg D, Lee JWL, Tikhonov DS, et al (2022) Fragmentation dynamics of fluorene explored using ultrafast XUV-Vis pump-probe spectroscopy. Front Phys 10. https://doi.org/10.3389/fphy.2022.880793
Gatchell M, Zettergren H (2022) Open questions on the interaction dynamics of molecules and clusters in the gas phase. Commun Chem 5(1):1–4. https://doi.org/10.1038/s42004-022-00646-y
Gatchell M, Zettergren H, Seitz F, et al (2013) Ions colliding with polycyclic aromatic hydrocarbon clusters. Phys Scr T 156:014062. https://doi.org/10.1088/0031-8949/2013/T156/014062
Gatchell M, Martini P, Laimer F, et al (2019) Spectroscopy of corannulene cations in helium nanodroplets. Faraday Discuss 217:276–289. https://doi.org/10.1039/C8FD00178B
Gatchell M, Ameixa J, Ji M, et al (2021) Survival of polycyclic aromatic hydrocarbon knockout fragments in the interstellar medium. Nat Commun 12(1):6646. https://doi.org/10.1038/s41467-021-26899-0
Gatchell M, Zettergren H, Hansen K (2023) The largest fullerene. Phys Chem Chem Phys 25(25):16790–16795. https://doi.org/10.1039/D3CP01716H
Gavilan L, Le KC, Pino T, et al (2017) Polyaromatic disordered carbon grains as carriers of the UV bump: Far-UV to mid-IR spectroscopy of laboratory analogs. Astron Astrophys 607:A73. https://doi.org/10.1051/0004-6361/201730712
Gavilan L, Ricketts CL, Bejaoui S, et al (2022) Raman spectroscopic study of pyrene in cosmic dust analogues: evolution from the gas to the solid phase. ACS Earth Space Chem 6(9):2215–2225. https://doi.org/10.1021/acsearthspacechem.2c00136
Geballe TR, Pendleton Y, Chiar J, et al (2021) The interstellar medium toward the galactic center source 2mass j17470898–2829561. Astrophys J 912(1):47. https://doi.org/10.3847/1538-4357/abee12
Geindre H, Allouche A, Peláez D (2021) Non long-range corrected density functionals incorrectly describe the intensity of the C-H stretching band in polycyclic aromatic hydrocarbons. J Comput Chem 42(14):1018–1027. https://doi.org/10.1002/jcc.26520
Ghesquière P, Talbi D, Karton A (2014) The reaction of the benzene cation with acetylenes for the growth of PAHs in the interstellar medium. Chem Phys Lett 595(596):13–19. https://doi.org/10.1016/j.cplett.2014.01.040
Ghigo G, Maranzana A, Tonachini G (2014) o-benzyne fragmentation and isomerization pathways: a CASPT2 study. Phys Chem Chem Phys 16(43):23944–23951. https://doi.org/10.1039/C4CP02582B
Giese CC, King HE, van den Ende MP, et al (2018) In situ nanoscale investigation of step retreat on fluoranthene crystal surfaces. ACS Earth Space Chem 2(12):1301–1311. https://doi.org/10.1021/acsearthspacechem.8b00120
Giese CC, Ten Kate IL, Plümper O, et al (2019) The evolution of polycyclic aromatic hydrocarbons under simulated inner asteroid conditions. Meteorit Planet Sci 54(9):1930–1950. https://doi.org/10.1111/maps.13359
Giese CC, ten Kate IL, van den Ende MPA, et al (2022) Experimental and theoretical constraints on amino acid formation from PAHs in asteroidal settings. ACS Earth Space Chem 6(3):468–481. https://doi.org/10.1021/acsearthspacechem.1c00329
Goubet M, Pirali O (2014) The far-infrared spectrum of azulene and isoquinoline and supporting anharmonic density functional theory calculations to high resolution spectroscopy of polycyclic aromatic hydrocarbons and derivatives. J Chem Phys 140(4):044322. https://doi.org/10.1063/1.4862828
Greaves JS, Scaife AMM, Frayer DT, et al (2018) Anomalous microwave emission from spinning nanodiamonds around stars. Nat Astron 2(8):662–667. https://doi.org/10.1038/s41550-018-0495-z
Grieco F, Theulé P, De Looze I, et al (2023) Enhanced star formation through the high-temperature formation of H_2 on carbonaceous dust grains. Nat Astron 7(5):541–545. https://doi.org/10.1038/s41550-023-01902-4
Gruet S, Goubet M, Pirali O (2014) High resolution measurements supported by electronic structure calculations of two naphthalene derivatives: [1, 5]- and [1, 6]-naphthyridine–estimation of the zero point inertial defect for planar polycyclic aromatic compounds. J Chem Phys 140(23):234308. https://doi.org/10.1063/1.4882652
Gruet S, Steber AL, Schnell M (2020) Reconnaissance of the uncharted low energy vibrational motions of acenaphthene. J Mol Spectrosc 371:111296. https://doi.org/10.1016/j.jms.2020.111296
Guha Niyogi S, Min M, Meixner M, et al (2014) Dust composition and mass-loss return from the luminous blue variable R71 in the LMC. Astron Astrophys 569:A80. https://doi.org/10.1051/0004-6361/201423746
Gupta D, Omont A, Bettinger HF (2021) Energetics of formation of cyclacenes from 2,3-didehydroacenes and implications for astrochemistry. Chem Eur J 27(14):4605–4616. https://doi.org/10.1002/chem.202003045
Guzman-Ramirez L, Lagadec E, Jones D, et al (2014) PAH formation in o-rich planetary nebulae. Mon Not R Astron Soc 441(1):364–377. https://doi.org/10.1093/mnras/stu454
Guzman-Ramirez L, Lagadec E, Wesson R, et al (2015) Witnessing the emergence of a carbon star. Mon Not R Astron Soc Lett 451(1):L1–L5. https://doi.org/10.1093/mnrasl/slv055

Habing HJ (1968) The interstellar radiation density between 912 Å and 2400 Å. Bull Astron Inst Neth 19:421
Hamlin TA, Poater J, Fonseca Guerra C, et al (2017) B-DNA model systems in non-terran bio-solvents: implications for structure, stability and replication. Phys Chem Chem Phys 19(26):16969–16978. https://doi.org/10.1039/C7CP01908D
Hammonds M, Mori T, Usui F, et al (2015) Variations in the 3.3μm feature and carbonaceous dust in AKARI data. Planet Space Sci 116:73–83. https://doi.org/10.1016/j.pss.2015.05.010
Hanine M, Meng Z, Lu S, et al (2020) Formation of interstellar complex polycyclic aromatic hydrocarbons: insights from molecular dynamics simulations of dehydrogenated benzene. Astrophys J 900(2):188. https://doi.org/10.3847/1538-4357/abab06
Hänni N, Altwegg K, Combi M, et al (2022) Identification and characterization of a new ensemble of cometary organic molecules. Nat Commun 13(1):3639. https://doi.org/10.1038/s41467-022-31346-9
Hardegree-Ullman EE, Gudipati MS, Boogert ACA, et al (2014) Laboratory determination of the infrared band strengths of pyrene frozen in water ice: implications for the composition of interstellar ices. Astrophys J 784(2):172. https://doi.org/10.1088/0004-637X/784/2/172
He C, Thomas AM, Galimova GR, et al (2020) Gas-phase formation of fulvenallene (C_7H_6) via the Jahn–Teller distorted tropyl (C_7H_7) radical intermediate under single-collision conditions. J Am Chem Soc 142(6):3205–3213. https://doi.org/10.1021/jacs.9b13269
He C, Kaiser RI, Lu W, et al (2023a) Unconventional pathway in the gas-phase synthesis of 9H-fluorene ($C_{13}H_{10}$) via the radical–radical reaction of benzyl (C_7H_7) with phenyl (C_6H_5). Angew Chem, Int Ed 62(6):e202216972. https://doi.org/10.1002/anie.202216972
He C, Kaiser RI, Lu W, et al (2023b) Exotic reaction dynamics in the gas-phase preparation of anthracene ($C_{14}H_{10}$) via spiroaromatic radical transients in the indenyl–cyclopentadienyl radical–radical reaction. J Am Chem Soc 145(5):3084–3091. https://doi.org/10.1021/jacs.2c12045
Heger ML (1922) The spectra of certain class B stars in the regions 5630A-6680A and 3280A-3380A. Lick Obs Bull 10(337):146–147
Hemachandra D, Barmby P, Peeters E, et al (2015) Mid-infrared spectroscopy of the Andromeda Galaxy. Mon Not R Astron Soc 454(1):818–830. https://doi.org/10.1093/mnras/stv2001
Hemberger P, Wu X, Pan Z, et al (2022) Continuous pyrolysis microreactors: hot sources with little cooling? New insights utilizing cation velocity map imaging and threshold photoelectron spectroscopy. J Phys Chem A 126(14):2196–2210. https://doi.org/10.1021/acs.jpca.2c00766
Hensley BS, Draine BT (2020) Detection of PAH absorption and determination of the mid-infrared diffuse interstellar extinction curve from the sight line toward Cyg OB2-12. Astrophys J 895(1):38. https://doi.org/10.3847/1538-4357/ab8cc3
Hensley BS, Draine BT (2021) Observational constraints on the physical properties of interstellar dust in the post-Planck era. Astrophys J 906(2):73. https://doi.org/10.3847/1538-4357/abc8f1
Hensley BS, Draine BT (2023) The Astrodust+PAH model: a unified description of the extinction, emission, and polarization from dust in the diffuse interstellar medium. Astrophys J 948:55. https://doi.org/10.3847/1538-4357/acc4c2
Hensley B, Murphy E, Staguhn J (2015) Characterizing extragalactic anomalous microwave emission in NGC 6946 with CARMA. Mon Not R Astron Soc 449(1):809–819. https://doi.org/10.1093/mnras/stv287
Hensley BS, Draine BT, Meisner AM (2016) A case against spinning PAHs as the source of the anomalous microwave emission. Astrophys J 827(1):45. https://doi.org/10.3847/0004-637X/827/1/45
Hensley BS, Murray CE, Dodici M (2022) Polycyclic aromatic hydrocarbons, anomalous microwave emission, and their connection to the cold neutral medium. Astrophys J 929(1):23. https://doi.org/10.3847/1538-4357/ac5cbd
Hervé M, Despré V, Castellanos Nash P, et al (2021) Ultrafast dynamics of correlation bands following xuv molecular photoionization. Nat Phys 17(3):327–331. https://doi.org/10.1038/s41567-020-01073-3
Higdon SJU, Higdon JL, Smith BJ, et al (2014) Star formation and the interstellar medium in nearby tidal streams (SAINTS): spitzer mid-infrared spectroscopy and imaging of intergalactic star-forming objects. Astrophys J 787:103. https://doi.org/10.1088/0004-637X/787/2/103
Hirashita H (2023) Evolution of grain size distribution with enhanced abundance of small carbonaceous grains in galactic environments. Mon Not R Astron Soc 518:3827–3837. https://doi.org/10.1093/mnras/stac3394
Hirsch A, Chen ZF, Jiao HJ (2000) Spherical aromaticity in I_h symmetrical fullerenes: the $2(N+1)^2$ rule. Angew Chem, Int Ed 39(21):3915–3917. https://doi.org/10.1002/1521-3773(20001103)39:21<3915::AID-ANIE3915>3.0.CO;2-O
Hoang T (2017) Effect of alignment on polarized infrared emission from polycyclic aromatic hydrocarbons. Astrophys J 838(2):112. https://doi.org/10.3847/1538-4357/aa65cf
Hoang T (2019) A dynamical constraint on interstellar dust models from radiative torque disruption. Astrophys J 876(1):13. https://doi.org/10.3847/1538-4357/ab1075

Hoang T, Lazarian A (2018) Cross-sectional alignment of polycyclic aromatic hydrocarbons by anisotropic radiation. Astrophys J 860(2):158. https://doi.org/10.3847/1538-4357/aac6e7

Hoang T, Tram LN (2019) Dust rotational dynamics in C-shocks: rotational disruption of nanoparticles by stochastic mechanical torques and spinning dust emission. Astrophys J 877(1):36. https://doi.org/10.3847/1538-4357/ab1845

Hoang T, Lan NQ, Vinh NA, et al (2018) Spinning dust emission from circumstellar disks and its role in excess microwave emission. Astrophys J 862(2):116. https://doi.org/10.3847/1538-4357/aaccf0

Hoang T, Tram LN, Lee H, et al (2019) Rotational disruption of dust grains by radiative torques in strong radiation fields. Nat Astron 3(8):766–775. https://doi.org/10.1038/s41550-019-0763-6

Holdship J, Viti S, Martín S, et al (2021) The distribution and origin of C_2H in NGC 253 from ALCHEMI. Astron Astrophys 654:A55. https://doi.org/10.1051/0004-6361/202141233

Hou GL, Lushchikova OV, Bakker JM, et al (2023) Buckyball-metal complexes as promising carriers of astronomical unidentified infrared emission bands. Astrophys J 952(1):13. https://doi.org/10.3847/1538-4357/accf1b

Hrodmarsson HR, Garcia GA, Nahon L, et al (2019) Threshold photoelectron spectrum of the anilino radical. J Phys Chem A 123(42):9193–9198. https://doi.org/10.1021/acs.jpca.9b07273

Hrodmarsson HR, Garcia GA, Linnartz H, et al (2020) VUV photoionization dynamics of the C_{60} buckminsterfullerene: 2D-matrix photoelectron spectroscopy in an astrophysical context. Phys Chem Chem Phys 22:13880–13892. https://doi.org/10.1039/D0CP01210F

Hrodmarsson HR, Bouwman J, Tielens AGGM, et al (2022) Similarities and dissimilarities in the fragmentation of polycyclic aromatic hydrocarbon cations: a case study involving three dibenzopyrene isomers. Int J Mass Spectrom 476:116834. https://doi.org/10.1016/j.ijms.2022.116834

Hrodmarsson HR, Bouwman J, Tielens AGGM, et al (2023) Fragmentation of the PAH cations of isoviolanthrene and dicoronylene: a case made for interstellar cyclo[n]carbons as products of universal fragmentation processes. Int J Mass Spectrom 485:116996. https://doi.org/10.1016/j.ijms.2022.116996

Hu X, Yang Y, Zhang C, et al (2021a) Gas-phase laboratory formation of large, astronomically relevant PAH-organic molecule clusters. Astron Astrophys 656:A80. https://doi.org/10.1051/0004-6361/202141407

Hu X, Zhang D, Yang Y, et al (2021b) Gas-phase formation of cationic fullerene/amino acid clusters: evidence for the "magic number" chemical reactivity of fullerene cations. Astrophys J 918(2):81. https://doi.org/10.3847/1538-4357/ac0f06

Hu X, Zhang D, Zhang C, et al (2021c) Gas-phase formation of cationic fullerene/9-aminoanthracene clusters: an indicator for interstellar dust growth. Mon Not R Astron Soc 508(4):4758–4766. https://doi.org/10.1093/mnras/stab2823

Hu X, Dong Z, Ge Y, et al (2023a) Gas phase hydrogenated and deuterated fullerene cations. Res Astron Astrophys 23:085021. https://doi.org/10.1088/1674-4527/acd994

Hu X, Dong Z, Liu J, et al (2023b) Coevolution of the interstellar chemistry: gas-phase laboratory formation of hydrogenated fullerene-PAH clusters. Mon Not R Astron Soc 522:4626–4638. https://doi.org/10.1093/mnras/stad1297

Huang XM, Li Q, Li A, et al (2021) Optical properties of elongated conducting grains. Mon Not R Astron Soc 503(3):4544–4550. https://doi.org/10.1093/mnras/stab765

Hudgins DM, Allamandola LJ (1999a) Interstellar PAH emission in the 11-14 micron region: new insights from laboratory data and a tracer of ionized PAHs. Astrophys J 516(1):L41–L44. https://doi.org/10.1086/311989

Hudgins DM, Allamandola LJ (1999b) The spacing of the interstellar 6.2 and 7.7 micron emission features as an indicator of polycyclic aromatic hydrocarbon size. Astrophys J 513(1):L69–L73. https://doi.org/10.1086/311901

Hudgins DM, Bauschlicher CW, Sandford SA (2004) The impact of deuteration on the infrared spectra of interstellar polycyclic aromatic hydrocarbons. Astrophys J 614(2):770–780. https://doi.org/10.1086/423930

Ichikawa K, Imanishi M, Ueda Y, et al (2014) AKARI IRC 2.5-5 μm spectroscopy of infrared galaxies over a wide luminosity range. Astrophys J 794(2):139. https://doi.org/10.1088/0004-637X/794/2/139

Iida S, Kuma S, Kuriyama M, et al (2021) Ir-photon quenching of delayed electron detachment from hot pentacene anions. Phys Rev A 104(4):043114. https://doi.org/10.1103/PhysRevA.104.043114

Iida S, Hu W, Zhang R, et al (2022) Thermal radiative cooling of carbon cluster cations C_N^+, N = 9, 11, 12, 17-27. Mon Not R Astron Soc 514(1):844–851. https://doi.org/10.1093/mnras/stac1349

Izawa M, Applin D, Norman L, et al (2014) Reflectance spectroscopy (350–2500 nm) of solid-state polycyclic aromatic hydrocarbons (PAHs). Icarus 237:159–181. https://doi.org/10.1016/j.icarus.2014.04.033

Jaganathan R, Simonsen FDS, Thrower JD, et al (2022) Enhanced reactivity of oxygen-functionalised PAHs with atomic hydrogen – a route to the formation of small oxygen-carrying molecules. Astron Astrophys 663:A136. https://doi.org/10.1051/0004-6361/202243312

Jakobsen P, Ferruit P, Alves de Oliveira C, et al (2022) The Near-Infrared Spectrograph (NIRSpec) on the James Webb Space Telescope. I. Overview of the instrument and its capabilities. Astron Astrophys 661:A80. https://doi.org/10.1051/0004-6361/202142663

Jelenfi DP, Schneiker A, Tajti A, et al (2023) Polyaromatic hydrocarbons with an imperfect aromatic system as catalysts of interstellar H_2 formation. Mol Phys 121:e2142168. https://doi.org/10.1080/00268976.2022.2142168

Jensen JJ, Hönig SF, Rakshit S, et al (2017) PAH features within few hundred parsecs of active galactic nuclei. Mon Not R Astron Soc 470(3):3071–3094. https://doi.org/10.1093/mnras/stx1447

Joblin C, Dontot L, Garcia GA, et al (2017) Size effect in the ionization energy of PAH clusters. J Phys Chem Lett 8(15):3697–3702. https://doi.org/10.1021/acs.jpclett.7b01546

Johansson KO, Campbell MF, Elvati P, et al (2017) Photoionization efficiencies of five polycyclic aromatic hydrocarbons. J Phys Chem A 121(23):4447–4454. https://doi.org/10.1021/acs.jpca.7b02991

Jones A (2014) A framework for resolving the origin, nature and evolution of the diffuse interstellar band carriers? Planet Space Sci 110:26–31. https://doi.org/10.1016/j.pss.2013.11.011

Jones AP, Fanciullo L, Köhler M, et al (2013) The evolution of amorphous hydrocarbons in the ISM: dust modelling from a new vantage point. Astron Astrophys 558:A62. https://doi.org/10.1051/0004-6361/201321686

Jones AP, Ysard N, Köhler M, et al (2014) The cycling of carbon into and out of dust. Faraday Discuss 168:313–326. https://doi.org/10.1039/C3FD00128H

Jose J, Zamir A, Stein T (2021) Molecular dynamics reveals formation path of benzonitrile and other molecules in conditions relevant to the interstellar medium. Proc Natl Acad Sci 118(19):e2101371118. https://doi.org/10.1073/pnas.2101371118

Jusko P, Simon A, Banhatti S, et al (2018) Direct evidence of the benzylium and tropylium cations as the two long-lived isomers of $C_7H_7^+$. ChemPhysChem 19(23):3182–3185. https://doi.org/10.1002/cphc.201800744

Kadhane UR, Vinitha MV, Ramanathan K, et al (2022) Comprehensive survey of dissociative photoionization of quinoline by pepico experiments. J Chem Phys 156(24):244304. https://doi.org/10.1063/5.0092158

Kaiser RI, Hansen N (2021) An aromatic universe – A physical chemistry perspective. J Phys Chem A 125(18):3826–3840. https://doi.org/10.1021/acs.jpca.1c00606

Kaiser RI, Parker DS, Mebel AM (2015) Reaction dynamics in astrochemistry: low-temperature pathways to polycyclic aromatic hydrocarbons in the interstellar medium. Annu Rev Phys Chem 66(1):43–67. https://doi.org/10.1146/annurev-physchem-040214-121502

Kaiser K, Schulz F, Maillard JF, et al (2022a) Visualization and identification of single meteoritic organic molecules by atomic force microscopy. Meteorit Planet Sci 57(3):644–656. https://doi.org/10.1111/maps.13784

Kaiser RI, Zhao L, Lu W, et al (2022b) Gas-phase synthesis of racemic helicenes and their potential role in the enantiomeric enrichment of sugars and amino acids in meteorites. Phys Chem Chem Phys 24(41):25077–25087. https://doi.org/10.1039/D2CP03084E

Kaiser RI, Zhao L, Lu W, et al (2022c) Unconventional excited-state dynamics in the concerted benzyl (C_7H_7) radical self-reaction to anthracene ($C_{14}H_{10}$). Nat Commun 13(1):786. https://doi.org/10.1038/s41467-022-28466-7

Kaiser RI, Zhao L, Lu W, et al (2022d) Formation of benzene and naphthalene through cyclopentadienyl-mediated radical–radical reactions. J Phys Chem Lett 13(1):208–213. https://doi.org/10.1021/acs.jpclett.1c03733

Kaneda H, Ishihara D, Oyabu S, et al (2017) Unbiased large spectroscopic surveys of galaxies selected by SPICA using dust bands. Publ Astron Soc Aust 34:e059. https://doi.org/10.1017/pasa.2017.56

Kappe M, Calvo F, Schöntag J, et al (2022) Solvation of large polycyclic aromatic hydrocarbons in helium: cationic and anionic hexabenzocoronene. Molecules 27(19):6764. https://doi.org/10.3390/molecules27196764

Karri VL, Kaluva S, Chaudhari A, et al (2022) Theoretical study of infrared and ultraviolet spectra of 14 isomers of C_{24} and comparison with astronomical observations. Mon Not R Astron Soc 519(2):2186–2197. https://doi.org/10.1093/mnras/stac2767

Karton A, Chan B (2021) Accurate heats of formation for polycyclic aromatic hydrocarbons: a high-level ab initio perspective. J Chem Eng Data 66(9):3453–3462. https://doi.org/10.1021/acs.jced.1c00256

Kerkeni B, Bacchus-Montabonel MC, Bromley ST (2017) How hydroxylation affects hydrogen adsorption and formation on nanosilicates. Mol Astrophys 7:1–8. https://doi.org/10.1016/j.molap.2017.04.001

Kerkeni B, García-Bernete I, Rigopoulou D, et al (2022) Probing computational methodologies in predicting mid-infrared spectra for large polycyclic aromatic hydrocarbons. Mon Not R Astron Soc 513(3):3663–3681. https://doi.org/10.1093/mnras/stac976

Khramtsova MS, Wiebe DS, Lozinskaya TA, et al (2014) Optical and infrared emission of H II complexes as a clue to the PAH life cycle. Mon Not R Astron Soc 444(1):757–775. https://doi.org/10.1093/mnras/stu1482

Kirsanova MS, Punanova AF, Semenov DA, et al (2021) Dark cloud-type chemistry in photodissociation regions with moderate ultraviolet field. Mon Not R Astron Soc 507(3):3810–3829. https://doi.org/10.1093/mnras/stab2361

Kleimeier NF, Liu Y, Turner AM, et al (2022) Excited state photochemically driven surface formation of benzene from acetylene ices on Pluto and in the outer Solar System. Phys Chem Chem Phys 24(3):1424–1436. https://doi.org/10.1039/D1CP04959C

Knight C, Peeters E, Stock DJ, et al (2021a) Tracing PAH size in prominent nearby mid-infrared environments. Astrophys J 918(1):8. https://doi.org/10.3847/1538-4357/ac02c6

Knight C, Peeters E, Tielens AGGM, et al (2021b) Characterizing the pah emission in the Orion bar. Mon Not R Astron Soc 509(3):3523–3546. https://doi.org/10.1093/mnras/stab3047

Knight C, Peeters E, Wolfire M, et al (2022) Characterizing spatial variations of PAH emission in the reflection nebula NGC 1333. Mon Not R Astron Soc 510(4):4888–4908. https://doi.org/10.1093/mnras/stab3295

Kofman V, Sarre P, Hibbins R, et al (2017) Laboratory spectroscopy and astronomical significance of the fully-benzenoid PAH triphenylene and its cation. Mol Astrophys 7:19–26. https://doi.org/10.1016/j.molap.2017.04.002

Korsmeyer JM, Ricca A, Cruz-Diaz GA, et al (2022) Infrared spectroscopy and photochemistry of anthracoronene in cosmic water ice. ACS Earth Space Chem 6(1):165–180. https://doi.org/10.1021/acsearthspacechem.1c00337

Kovács P, Zhu X, Carrete J, et al (2020) Machine-learning prediction of infrared spectra of interstellar polycyclic aromatic hydrocarbons. Astrophys J 902(2):100. https://doi.org/10.3847/1538-4357/abb5b6

Krasnokutski SA, Huisken F, Jäger C, et al (2017) Growth and destruction of PAH molecules in reactions with carbon atoms. Astrophys J 836(1):32. https://doi.org/10.3847/1538-4357/836/1/32

Kwok S (2022) The mystery of unidentified infrared emission bands. Astrophys Space Sci 367(2):16. https://doi.org/10.1007/s10509-022-04045-6

Lacinbala O, Calvo F, Dubosq C, et al (2022a) Radiative relaxation in isolated large carbon clusters: vibrational emission versus recurrent fluorescence. J Chem Phys 156(14):144305. https://doi.org/10.1063/5.0080494

Lacinbala O, Féraud G, Vincent J, et al (2022b) Aromatic and acetylenic C–H or C–D stretching bands anharmonicity detection of phenylacetylene by UV laser-induced vibrational emission. J Phys Chem A 126(30):4891–4901. https://doi.org/10.1021/acs.jpca.2c01436

Lacinbala O, Calvo F, Dartois E, et al (2023a) A plausible molecular mechanism to explain near-infrared continuum emission: recurrent fluorescence. Astron Astrophys 671:A89. https://doi.org/10.1051/0004-6361/202245421

Lacinbala O, Calvo F, Falvo C, et al (2023b) Emission spectra of fullerenes: computational evidence for blackbody-like radiation due to structural diversity and electronic similarity. Phys Rev A 107(6):062808. https://doi.org/10.1103/PhysRevA.107.062808

Lagadec E, Zijlstra AA (2008) The trigger of the asymptotic giant branch superwind: the importance of carbon. Mon Not R Astron Soc 390(1):L59–L63. https://doi.org/10.1111/j.1745-3933.2008.00535.x. arXiv:0807.3730 [astro-ph]

Lai TSY, Witt AN, Crawford K (2017) Extended red emission in IC59 and IC63. Mon Not R Astron Soc 469(4):4933–4948. https://doi.org/10.1093/mnras/stx1124

Lai TSY, Smith JDT, Baba S, et al (2020a) All the PAHs: an AKARI–Spitzer cross-archival spectroscopic survey of aromatic emission in galaxies. Astrophys J 905(1):55. https://doi.org/10.3847/1538-4357/abc002

Lai TSY, Witt AN, Alvarez C, et al (2020b) Are the carriers of diffuse interstellar bands and extended red emission the same? Mon Not R Astron Soc 492(4):5853–5864. https://doi.org/10.1093/mnras/staa223

Lai TSY, Armus L, U V, et al (2022) GOALS-JWST: tracing AGN feedback on the star-forming interstellar medium in NGC 7469. Astrophys J Lett 941(2):L36. https://doi.org/10.3847/2041-8213/ac9ebf

Lallement R, Cox NLJ, Cami J, et al (2018) The EDIBLES survey II. The detectability of C_{60}^+ bands. Astron Astrophys 614:A28. https://doi.org/10.1051/0004-6361/201832647

Lanza M, Simon A, Ben Amor N (2015) Electronic spectroscopy of $[FePAH]^+$ complexes in the region of the diffuse interstellar bands: multireference wave function studies on $[FeC_6H_6]^+$. J Phys Chem A 119(23):6123–6130. https://doi.org/10.1021/acs.jpca.5b00438

Leboucher H, Mascetti J, Aupetit C, et al (2022) Water clusters in interaction with corannulene in a rare gas matrix: structures, stability and IR spectra. Photochem 2(2):237–262. https://doi.org/10.3390/photochem2020018

Leboucher H, Simon A, Rapacioli M (2023) Structures and stabilities of PAH clusters solvated by water aggregates: the case of the pyrene dimer. J Chem Phys 158(11):114308. https://doi.org/10.1063/5.0139482

Lecasble M, Bernard S, Viennet JC, et al (2023) Influence of hydrothermal asteroidal conditions on the molecular structure and isotopic compositions of polycyclic aromatic hydrocarbons. Icarus 401:115603. https://doi.org/10.1016/j.icarus.2023.115603

Leccese M, Jaganathan R, Slumstrup L, et al (2023) Bending the rules of PAH hydrogenation: the case of corannulene. Mon Not R Astron Soc 519(4):5567–5578. https://doi.org/10.1093/mnras/stad054
Lee TJ, Fortenberry RC (2021) The unsolved issue with out-of-plane bending frequencies for CC multiply bonded systems. Spectrochim Acta, Part A, Mol Biomol Spectrosc 248:119148. https://doi.org/10.1016/j.saa.2020.119148
Lee JWL, Tikhonov DS, Chopra P, et al (2021) Time-resolved relaxation and fragmentation of polycyclic aromatic hydrocarbons investigated in the ultrafast XUV-IR regime. Nat Commun 12(1):6107. https://doi.org/10.1038/s41467-021-26193-z
Lee JWL, Tikhonov DS, Allum F, et al (2022) The kinetic energy of PAH dication and trication dissociation determined by recoil-frame covariance map imaging. Phys Chem Chem Phys 24(38):23096–23105. https://doi.org/10.1039/D2CP02252D
Lemmens AK, Gruet S, Steber AL, et al (2019) Far-IR and UV spectral signatures of controlled complexation and microhydration of the polycyclic aromatic hydrocarbon acenaphthene. Phys Chem Chem Phys 21(7):3414–3422. https://doi.org/10.1039/C8CP04480E
Lemmens AK, Rap DB, Thunnissen JMM, et al (2020) Far-IR absorption of neutral polycyclic aromatic hydrocarbons (PAHs): light on the mechanism of IR-UV ion dip spectroscopy. J Phys Chem Lett 11(21):8997–9002. https://doi.org/10.1021/acs.jpclett.0c02714
Lemmens AK, Chopra P, Garg D, et al (2021a) High-resolution infrared spectroscopy of naphthalene and acenaphthene dimers. Mol Phys 119(1–2):e1811908. https://doi.org/10.1080/00268976.2020.1811908
Lemmens AK, Rijs AM, Buma WJ (2021b) Infrared spectroscopy of jet-cooled "GrandPAHs" in the 3–100 μm region. Astrophys J 923(2):238. https://doi.org/10.3847/1538-4357/ac2f9d
Lemmens AK, Rap DB, Brunken S, et al (2022) Polycyclic aromatic hydrocarbon growth in a benzene discharge explored by IR-UV action spectroscopy. Phys Chem Chem Phys 24(24):14816–14824. https://doi.org/10.1039/d2cp01631a
Lemmens AK, Mackie CJ, Candian A, et al (2023) Size distribution of polycyclic aromatic hydrocarbons in space: an old new light on the 11.2/3.3 μm intensity ratio. Faraday Discuss. https://doi.org/10.1039/D2FD00180B
Levey ZD, Laws BA, Sundar SP, et al (2022) PAH growth in flames and space: formation of the phenalenyl radical. J Phys Chem A 126(1):101–108. https://doi.org/10.1021/acs.jpca.1c08310
Li A (2020) Spitzer's perspective of polycyclic aromatic hydrocarbons in galaxies. Nat Astron 4(4):339–351. https://doi.org/10.1038/s41550-020-1051-1
Li AG, Draine BT (2001) Infrared emission from interstellar dust. II. The diffuse interstellar medium. Astrophys J 554(2):778–802. https://doi.org/10.1086/323147
Li D, Mariñas N, Telesco CM (2014) The immediate environments of two Herbig BE stars: MWC 1080 and HD 259431. Astrophys J 796(2):74. https://doi.org/10.1088/0004-637X/796/2/74
Li Q, Dai W, Liu B, et al (2018) Catalytic conversion of methanol to larger organic molecules over crystalline forsterite: laboratory study and astrophysical implications. Mol Astrophys 13:22–29. https://doi.org/10.1016/j.molap.2018.09.002
Li Q, Li A, Jiang BW (2019a) How much graphene in space? Mon Not R Astron Soc 490(3):3875–3881. https://doi.org/10.1093/mnras/stz2740
Li K, Li A, Xiang FY (2019b) Probing the missing link between the diffuse interstellar bands and the total-to-selective extinction ratio R_v I. Extinction versus reddening. Mon Not R Astron Soc 489(1):708–713. https://doi.org/10.1093/mnras/stz2103
Li Q, Li A, Jiang BW, et al (2020) On carbon nanotubes in the interstellar medium. Mon Not R Astron Soc 493(2):3054–3059. https://doi.org/10.1093/mnras/staa467
Li W, Zhao L, Kaiser RI (2023) A unified reaction network on the formation of five-membered ringed polycyclic aromatic hydrocarbons (PAHs) and their role in ring expansion processes through radical–radical reactions. Phys Chem Chem Phys 25(5):4141–4150. https://doi.org/10.1039/D2CP05305E
Lietard A, Mensa-Bonsu G, Verlet JRR (2021) The effect of solvation on electron capture revealed using anion two-dimensional photoelectron spectroscopy. Nat Chem 13(8):737–742. https://doi.org/10.1038/s41557-021-00687-1
Lignell A, Tenelanda-Osorio LI, Gudipati MS (2021) Visible-light photoionization of aromatic molecules in water-ice: organic chemistry across the universe with less energy. Chem Phys Lett 778:138814. https://doi.org/10.1016/j.cplett.2021.138814
Linnartz H, Cami J, Cordiner M, et al (2020) C_{60}^+ as a diffuse interstellar band carrier; a spectroscopic story in 6 acts. J Mol Spectrosc 367:111243. https://doi.org/10.1016/j.jms.2019.111243
Liu J, Jiang BW, Li A, et al (2017) On the silicate crystallinities of oxygen-rich evolved stars and their mass-loss rates. Mon Not R Astron Soc 466(2):1963–1986. https://doi.org/10.1093/mnras/stw3165
Liu P, Jin H, Chen B, et al (2021) Rapid soot inception via α-alkynyl substitution of polycyclic aromatic hydrocarbons. Fuel 295:120580. https://doi.org/10.1016/j.fuel.2021.120580

Loison J, Dobrijevic M, Hickson K (2019) The photochemical production of aromatics in the atmosphere of Titan. Icarus 329:55–71. https://doi.org/10.1016/j.icarus.2019.03.024

Loomis RA, Burkhardt AM, Shingledecker CN, et al (2021) An investigation of spectral line stacking techniques and application to the detection of $HC_{11}N$. Nat Astron 5(2):188–196. https://doi.org/10.1038/s41550-020-01261-4

López-Puertas M, Dinelli BM, Adriani A, et al (2013) Large abundances of polycyclic aromatic hydrocarbons in Titan's upper atmosphere. Astrophys J 770(2):132. https://doi.org/10.1088/0004-637X/770/2/132

Loru D, Steber AL, Pinacho P, et al (2021) How does the composition of a PAH influence its microsolvation? A rotational spectroscopy study of the phenanthrene–water and phenanthridine–water clusters. Phys Chem Chem Phys 23(16):9721–9732. https://doi.org/10.1039/D1CP00898F

Loru D, Steber AL, Thunnissen JMM, et al (2022) New potential candidates for astronomical searches discovered in the electrical discharge of the PAH naphthalene and acetonitrile. J Mol Spectrosc 386:111629. https://doi.org/10.1016/j.jms.2022.111629

Lu S, Meng Z, Xie P, et al (2021) Gas-phase formation of interstellar nucleobases from dehydrogenated formamide and vinyl cyanide. Astron Astrophys 656:A84. https://doi.org/10.1051/0004-6361/202140744

Lukianova MA, Feldman VI (2021) Direct evidence for a single-step radiation-induced assembling of benzene ring from acetylene trimer at cryogenic temperatures. Radiat Phys Chem 183:109417. https://doi.org/10.1016/j.radphyschem.2021.109417

Lukianova MA, Feldman V (2022) Radiation-induced closure of the second aromatic ring: possible way to PAH starting from a styrene-acetylene complex. Radiat Phys Chem 191:109847. https://doi.org/10.1016/j.radphyschem.2021.109847

Lukmanov T, Akhmetov AF, Sabirov DS (2022) Polarizability of kekulene, septulene, and nearest non-planar polycyclic aromatic hydrocarbons. Carbon 8(4):61. https://doi.org/10.3390/c8040061

Maaskant KM, Min M, Waters LBFM, et al (2014) Polycyclic aromatic hydrocarbon ionization as a tracer of gas flows through protoplanetary disk gaps. Astron Astrophys 563:A78. https://doi.org/10.1051/0004-6361/201323137

MacIsaac H, Cami J, Cox NLJ, et al (2022) The EDIBLES survey: V. line profile variations in the λλ 5797, 6379, and 6614 diffuse interstellar bands as a tool to constrain carrier sizes. Astron Astrophys 662:A24. https://doi.org/10.1051/0004-6361/202142225

Mackie CJ, Peeters E, Bauschlicher CW Jr, et al (2015) Characterizing the infrared spectra of small, neutral, fully dehydrogenated polycyclic aromatic hydrocarbons. Astrophys J 799(2):131. https://doi.org/10.1088/0004-637X/799/2/131

Mackie CJ, Candian A, Huang X, et al (2016) The anharmonic quartic force field infrared spectra of five non-linear polycyclic aromatic hydrocarbons: benz[a]anthracene, chrysene, phenanthrene, pyrene, and triphenylene. J Chem Phys 145(8):084313. https://doi.org/10.1063/1.4961438

Mackie CJ, Candian A, Huang X, et al (2018a) The anharmonic quartic force field infrared spectra of hydrogenated and methylated PAHs. Phys Chem Chem Phys 20(2):1189–1197. https://doi.org/10.1039/C7CP06546A

Mackie CJ, Chen T, Candian A, et al (2018b) Fully anharmonic infrared cascade spectra of polycyclic aromatic hydrocarbons. J Chem Phys 149(13):134302. https://doi.org/10.1063/1.5038725

Maclot S, Lahl J, Peschel J, et al (2020) Dissociation dynamics of the diamondoid adamantane upon photoionization by XUV femtosecond pulses. Sci Rep 10(1):2884. https://doi.org/10.1038/s41598-020-59649-1

Maltseva E, Petrignani A, Candian A, et al (2015) High-resolution IR absorption spectroscopy of polycyclic aromatic hydrocarbons: the realm of anharmonicity. Astrophys J 814(1):23. https://doi.org/10.1088/0004-637X/814/1/23

Maltseva E, Petrignani A, Candian A, et al (2016) High-resolution IR absorption spectroscopy of polycyclic aromatic hydrocarbons in the 3 μ m region: role of periphery. Astrophys J 831(1):58. https://doi.org/10.3847/0004-637X/831/1/58

Maltseva E, Mackie CJ, Candian A, et al (2018) High-resolution IR absorption spectroscopy of polycyclic aromatic hydrocarbons in the 3 μm region: role of hydrogenation and alkylation. Astron Astrophys 610:A65. https://doi.org/10.1051/0004-6361/201732102

Mandal B, Joy C, Semenov A, et al (2022) Mixed quantum/classical theory for collisional quenching of PAHs in the interstellar media. ACS Earth Space Chem 6(3):521–529. https://doi.org/10.1021/acsearthspacechem.1c00418

Mann I, Li A, Tanaka KK (2018) Nano dust in space and astrophysics. Proc Int Astron Union 14(A30):379–381. https://doi.org/10.1017/S1743921319004666

Maragkoudakis A, Ivkovich N, Peeters E, et al (2018) PAHs and star formation in the H II regions of nearby galaxies M83 and M33. Mon Not R Astron Soc 481(4):5370–5393. https://doi.org/10.1093/mnras/sty2658

Maragkoudakis A, Peeters E, Ricca A (2020) Probing the size and charge of polycyclic aromatic hydrocarbons. Mon Not R Astron Soc 494(1):642–664. https://doi.org/10.1093/mnras/staa681

Maragkoudakis A, Boersma C, Temi P, et al (2022) Linking characteristics of the polycyclic aromatic hydrocarbon population with galaxy properties: a quantitative approach using the NASA Ames PAH IR spectroscopic database. Astrophys J 931(1):38. https://doi.org/10.3847/1538-4357/ac666f
Maragkoudakis A, Peeters E, Ricca A (2023a) Spectral variations among different scenarios of PAH processing or formation. Mon Not R Astron Soc 520(4):5354–5372. https://doi.org/10.1093/mnras/stad465
Maragkoudakis A, Peeters E, Ricca A, et al (2023b) Polycyclic aromatic hydrocarbon size tracers. Mon Not R Astron Soc 524(3):3429–3436. https://doi.org/10.1093/mnras/stad2062
Marchenko SV, Moffat AFJ (2017) Search for polycyclic aromatic hydrocarbons in the outflows from dust-producing Wolf–Rayet stars. Mon Not R Astron Soc 468(2):2416–2428. https://doi.org/10.1093/mnras/stx563
Marchione D, Thrower JD, McCoustra MRS (2016) Efficient electron-promoted desorption of benzene from water ice surfaces. Phys Chem Chem Phys 18(5):4026–4034. https://doi.org/10.1039/C5CP06537B
Marciniak A, Despré V, Barillot T, et al (2015) XUV excitation followed by ultrafast non-adiabatic relaxation in PAH molecules as a femto-astrochemistry experiment. Nat Commun 6(1):7909. https://doi.org/10.1038/ncomms8909
Marciniak A, Despré V, Loriot V, et al (2019) Electron correlation driven non-adiabatic relaxation in molecules excited by an ultrashort extreme ultraviolet pulse. Nat Commun 10(1):337. https://doi.org/10.1038/s41467-018-08131-8
Marciniak A, Joblin C, Mulas G, et al (2021) Photodissociation of aliphatic PAH derivatives under relevant astrophysical conditions. Astron Astrophys 652:A42. https://doi.org/10.1051/0004-6361/202140737
Maris A, Calabrese C, Melandri S, et al (2015) Accurate spectroscopy of polycyclic aromatic compounds: from the rotational spectrum of fluoren-9-one in the millimeter wave region to its infrared spectrum. J Chem Phys 142(2):024317. https://doi.org/10.1063/1.4905134
Marshall CCM, Krełowski J, Sarre PJ (2015) The λ6614 diffuse interstellar absorption band: evidence for internal excitation of the carrier. Mon Not R Astron Soc 453(4):3913–3918. https://doi.org/10.1093/mnras/stv1838
Martin-Drumel MA, Pirali O, Falvo C, et al (2014) Low-energy vibrational spectra of flexible diphenyl molecules: biphenyl, diphenylmethane, bibenzyl and 2-, 3- and 4-phenyltoluene. Phys Chem Chem Phys 16(40):22062–22072. https://doi.org/10.1039/C4CP03278K
Martínez L, Santoro G, Merino P, et al (2020) Prevalence of non-aromatic carbonaceous molecules in the inner regions of circumstellar envelopes. Nat Astron 4(1):97–105. https://doi.org/10.1038/s41550-019-0899-4
Massa D, Gordon KD, Fitzpatrick EL (2022) Relations between mid-infrared dust emission and UV extinction. Astrophys J 925(1):19. https://doi.org/10.3847/1538-4357/ac3825
Maté B, Tanarro I, Moreno MA, et al (2014) Stability of carbonaceous dust analogues and glycine under uv irradiation and electron bombardment. Faraday Discuss 168:267–285. https://doi.org/10.1039/C3FD00132F
Maté B, Molpeceres G, Jiménez-Redondo M, et al (2016) High-energy electron irradiation of interstellar carbonaceous dust analogs: cosmic-ray effects on the carriers of the 3.4 μm absorption band. Astrophys J 831(1):51. https://doi.org/10.3847/0004-637X/831/1/51
Matsuura M, Bernard-Salas J, Lloyd Evans T, et al (2014) Spitzer Space Telescope spectra of post-AGB stars in the Large Magellanic Cloud – polycyclic aromatic hydrocarbons at low metallicities. Mon Not R Astron Soc 439(2):1472–1493. https://doi.org/10.1093/mnras/stt2495
Matsuura M, Ayley V, Chawner H, et al (2022) Spitzer and Herschel studies of dust in supernova remnants in the small magellanic cloud. Mon Not R Astron Soc 513(1):1154–1174. https://doi.org/10.1093/mnras/stac583
Mattioda AL, Cruz-Diaz GA, Ging A, et al (2020a) Formation of complex organic molecules (COMs) from polycyclic aromatic hydrocarbons (PAHs): Implications for ISM IR emission plateaus and Solar System organics. ACS Earth Space Chem 4(12):2227–2245. https://doi.org/10.1021/acsearthspacechem.0c00165
Mattioda AL, Hudgins DM, Boersma C, et al (2020b) The NASA Ames PAH IR spectroscopic database: the laboratory spectra. Astrophys J Suppl Ser 251(2):22. https://doi.org/10.3847/1538-4365/abc2c8
Mauney CM, Lazzati D (2018) The formation of astrophysical Mg-rich silicate dust. Mol Astrophys 12:1–9. https://doi.org/10.1016/j.molap.2018.03.002
Maurya A, Rastogi S (2015) Vibrational spectroscopic study of vinyl substituted polycyclic aromatic hydrocarbons. Spectrochim Acta, Part A, Mol Biomol Spectrosc 151:1–10. https://doi.org/10.1016/j.saa.2015.06.069
Maurya A, Singh R, Rastogi S (2023) Study of vibrational spectra of polycyclic aromatic hydrocarbons with phenyl side group. J Mol Spectrosc 391:111720. https://doi.org/10.1016/j.jms.2022.111720
Mayer PM, Bodi A (2021) VUV photoprocessing of oxygen-containing polycyclic aromatic hydrocarbons: threshold photoelectron spectra. J Mol Spectrosc 377:111446. https://doi.org/10.1016/j.jms.2021.111446

McCabe MN, Hemberger P, Reusch E, et al (2020) Off the beaten path: almost clean formation of indene from the ortho -benzyne + allyl reaction. J Phys Chem Lett 11(8):2859–2863. https://doi.org/10.1021/acs.jpclett.0c00374

McCabe MN, Hemberger P, Campisi D, et al (2022) Formation of phenylacetylene and benzocyclobutadiene in the ortho-benzyne + acetylene reaction. Phys Chem Chem Phys 24(3):1869–1876. https://doi.org/10.1039/D1CP05183K

McGuire BA, Burkhardt AM, Kalenskii S, et al (2018) Detection of the aromatic molecule benzonitrile (c-C_6H_5CN) in the interstellar medium. Science 359(6372):202–205. https://doi.org/10.1126/science.aao4890

McGuire BA, Loomis RA, Burkhardt AM, et al (2021) Detection of two interstellar polycyclic aromatic hydrocarbons via spectral matched filtering. Science 371(6535):1265–1269. https://doi.org/10.1126/science.abb7535

McKinney J, Armus L, Pope A, et al (2021) Regulating star formation in nearby dusty galaxies: low photoelectric efficiencies in the most compact systems. Astrophys J 908(2):238. https://doi.org/10.3847/1538-4357/abd6f2

Meng Z, Zhu X, Kovács P, et al (2021) Machine-learning interpretation of the correlation between infrared emission features of interstellar polycyclic aromatic hydrocarbons. Astrophys J 922(2):101. https://doi.org/10.3847/1538-4357/ac2c78

Meng Z, Zhang Y, Liang E, et al (2023) Machine-learning identified molecular fragments responsible for infrared emission features of polycyclic aromatic hydrocarbons. Mon Not R Astron Soc Lett 525(1):L29–L35. https://doi.org/10.1093/mnrasl/slad089

Mennella V, Suhasaria T, Hornekær L, et al (2021) Ly α irradiation of superhydrogenated coronene films: Implications for H_2 formation. Astrophys J 908(1):L18. https://doi.org/10.3847/2041-8213/abddb9

Mercier X, Faccinetto A, Batut S, et al (2020) Selective identification of cyclopentaring-fused PAHs and side-substituted PAHs in a low pressure premixed sooting flame by photoelectron photoion coincidence spectroscopy. Phys Chem Chem Phys 22(28):15926–15944. https://doi.org/10.1039/d0cp02740e

Merino P, Švec M, Martinez JI, et al (2014) Graphene etching on SiC grains as a path to interstellar polycyclic aromatic hydrocarbons formation. Nat Commun 5(1):3054. https://doi.org/10.1038/ncomms4054

Meyer M, Martini P, Schiller A, et al (2021) Electronic spectroscopy of anthracene cations and protonated anthracene in the search for carriers of diffuse interstellar bands. Astrophys J 913(2):136. https://doi.org/10.3847/1538-4357/abf93e

Micelotta ER, Matsuura M, Sarangi A (2018) Dust in supernovae and supernova remnants II: Processing and survival. Space Sci Rev 214(2):53. https://doi.org/10.1007/s11214-018-0484-7

Michoulier E, Ben Amor N, Rapacioli M, et al (2018a) Theoretical determination of adsorption and ionisation energies of polycyclic aromatic hydrocarbons on water ice. Phys Chem Chem Phys 20(17):11941–11953. https://doi.org/10.1039/C8CP01175C

Michoulier E, Noble JA, Simon A, et al (2018b) Adsorption of PAHs on interstellar ice viewed by classical molecular dynamics. Phys Chem Chem Phys 20(13):8753–8764. https://doi.org/10.1039/C8CP00593A

Michoulier E, Toubin C, Simon A, et al (2020) Perturbation of the surface of amorphous solid water by the adsorption of polycyclic aromatic hydrocarbons. J Phys Chem C 124(5):2994–3001. https://doi.org/10.1021/acs.jpcc.9b09499

Miksch AM, Riffelt A, Oliveira R, et al (2021) Hydrogenation of small aromatic heterocycles at low temperatures. Mon Not R Astron Soc 505(3):3157–3164. https://doi.org/10.1093/mnras/stab1514

Mishra A, Li A (2017) Interstellar silicon depletion and the ultraviolet extinction. Astrophys J 850(2):138. https://doi.org/10.3847/1538-4357/aa937a

Mishra PM, Rajput J, Safvan CP, et al (2013) Electron emission and electron transfer processes in proton-naphthalene collisions at intermediate velocities. Phys Rev A 88(5):052707. https://doi.org/10.1103/PhysRevA.88.052707

Mishra PM, Avaldi L, Bolognesi P, et al (2014a) Valence shell photoelectron spectroscopy of pyrene and fluorene: photon energy dependence in the far-ultraviolet region. J Phys Chem A 118(17):3128–3135. https://doi.org/10.1021/jp502445d

Mishra PM, Rajput J, Safvan CP, et al (2014b) Velocity dependence of fragmentation yields in proton–naphthalene collision and comparison with electronic energy loss calculation. J Phys B, At Mol Opt Phys 47(8):085202. https://doi.org/10.1088/0953-4075/47/8/085202

Mishra A, Li A, Jiang BW (2015) A tale of three mysterious spectral features in carbon-rich evolved stars: the 21 μm, 30 μm, and "Unidentified infrared" emission features. Astrophys J 802(1):39. https://doi.org/10.1088/0004-637X/802/1/39

Mishra A, Li A, Jiang BW (2016) On the relation between the mysterious 21 μm emission feature of post-asymptotic giant branch stars and their mass-loss rates. Astrophys J 825(1):68. https://doi.org/10.3847/0004-637X/825/1/68

Molpeceres G, Timón V, Jiménez-Redondo M, et al (2017) Structure and infrared spectra of hydrocarbon interstellar dust analogs. Phys Chem Chem Phys 19(2):1352–1360. https://doi.org/10.1039/C6CP06043A
Monfredini T, Fantuzzi F, Nascimento MAC, et al (2016) Single and double photoionization and photodissociation of toluene by soft X-rays in a circumstellar environment. Astrophys J 821(1):4. https://doi.org/10.3847/0004-637X/821/1/4
Monreal-Ibero A, Weilbacher PM, Wendt M (2018) Diffuse interstellar bands λ5780 and λ5797 in the Antennae Galaxy as seen by MUSE. Astron Astrophys 615:A33. https://doi.org/10.1051/0004-6361/201732178
Montargès M, Cannon E, Lagadec E, et al (2021) A dusty veil shading Betelgeuse during its great dimming. Nature 594(7863):365–368. https://doi.org/10.1038/s41586-021-03546-8
Mori TI, Onaka T, Sakon I, et al (2014) Observational studies on the near-infrared unidentified emission bands in galactic H II regions. Astrophys J 784(1):53. https://doi.org/10.1088/0004-637X/784/1/53
Mori T, Onaka T, Sakon I, et al (2022) Laboratory measurements of stretching band strengths of deuterated quenched carbonaceous composites. Astrophys J 933(1):35. https://doi.org/10.3847/1538-4357/ac71ae
Mulas G, Falvo C, Cassam-Chena P, et al (2018) Anharmonic vibrational spectroscopy of polycyclic aromatic hydrocarbons (PAHs). J Chem Phys 149(14):144102. https://doi.org/10.1063/1.5050087
Murakami H, Baba H, Barthel P, et al (2007) The infrared astronomical mission AKARI. Publ Astron Soc Jpn 59:S369–S376. https://doi.org/10.1093/pasj/59.sp2.S369
Murata K, Matsuhara H, Inami H, et al (2014) Polycyclic aromatic hydrocarbon feature deficit of starburst galaxies in the AKARI North ecliptic pole deep field. Astron Astrophys 566:A136. https://doi.org/10.1051/0004-6361/201423744
Murga MS, Wiebe DS, Sivkova EE, et al (2019) SHIVA: a dust destruction model. Mon Not R Astron Soc 488(1):965–977. https://doi.org/10.1093/mnras/stz1724. arXiv:1906.11308 [astro-ph.GA]
Murga MS, Kirsanova MS, Vasyunin AI, et al (2020) Impact of PAH photodissociation on the formation of small hydrocarbons in the Orion bar and the horsehead PDRs. Mon Not R Astron Soc 497(2):2327–2339. https://doi.org/10.1093/mnras/staa2026
Murga MS, Akimkin VV, Wiebe DS (2022a) Efficiency of the top-down polycyclic aromatic hydrocarbon-to-fullerene conversion in ultraviolet irradiated environments. Mon Not R Astron Soc 517(3):3732–3748. https://doi.org/10.1093/mnras/stac2926
Murga MS, Kirsanova MS, Wiebe DS, et al (2022b) Orion bar as a window to the evolution of PAHs. Mon Not R Astron Soc 509(1):800–817. https://doi.org/10.1093/mnras/stab3061. arXiv:2111.05583 [astro-ph.GA]
Murga MS, Vasyunin AI, Kirsanova MS (2022c) Impact of hac evolution on the formation of small hydrocarbons in the Orion Bar and the Horsehead PDRs. Mon Not R Astron Soc 519(2):2466–2474. https://doi.org/10.1093/mnras/stac3656
Muzangwa LG, Yang T, Parker DSN, et al (2015) A crossed molecular beam and ab initio study on the formation of 5- and 6-methyl-1, 4-dihydronaphthalene ($C_{11}H_{12}$) via the reaction of meta-tolyl (C_7H_7) with 1, 3-butadiene (C_4H_6). Phys Chem Chem Phys 17(12):7699–7706. https://doi.org/10.1039/C5CP00311C
Navarro Navarrete JE, Bull JN, Cederquist H, et al (2023) Experimental radiative cooling rates of a polycyclic aromatic hydrocarbon cation. Faraday Discuss. https://doi.org/10.1039/D3FD00005B
Nickerson S, Rangwala N, Colgan SWJ, et al (2023) The mid-infrared molecular inventory toward Orion IRc2. Astrophys J 945(1):26. https://doi.org/10.3847/1538-4357/aca6e8
Nie TP, Xiang FY, Li A (2021) C_{60} cation as the carrier of the λ 9577 Å and λ 9632 Å diffuse interstellar bands: further support from the VLT/X-Shooter spectra. Mon Not R Astron Soc 509(4):4908–4915. https://doi.org/10.1093/mnras/stab3296
Nobili A, Maffei LP, Baggioli A, et al (2022) On the radical behavior of large polycyclic aromatic hydrocarbons in soot formation and oxidation. Combust Flame 235:111692. https://doi.org/10.1016/j.combustflame.2021.111692
Noble JA, Dedonder C, Jouvet C (2015) The electronic spectra of protonated nitrogen-substituted polycyclic aromatic hydrocarbon molecules. Astron Astrophys 577:A79. https://doi.org/10.1051/0004-6361/201425493
Noble JA, Jouvet C, Aupetit C, et al (2017) Efficient photochemistry of coronene: water complexes. Astron Astrophys 599:A124. https://doi.org/10.1051/0004-6361/201629613
Noble JA, Aupetit C, Descamps D, et al (2019) Ultrafast electronic relaxations from the S_3 state of pyrene. Phys Chem Chem Phys 21(26):14111–14125. https://doi.org/10.1039/C8CP06895J
Noble JA, Michoulier E, Aupetit C, et al (2020) Influence of ice structure on the soft UV photochemistry of PAHs embedded in solid water. Astron Astrophys 644:A22. https://doi.org/10.1051/0004-6361/202038568
Novak CM, Fortenberry RC (2017) Vibrational frequencies and spectroscopic constants of three, stable noble gas molecules: $NeCCH^+$, $ArCCH^+$, and $ArCN^+$. Phys Chem Chem Phys 19(7):5230–5238. https://doi.org/10.1039/C6CP08140A

Nuevo M, Sciamma-O'Brien E, Sandford SA, et al (2022) The Titan Haze Simulation (THS) experiment on COSmIC. Part III. XANES study of laboratory analogs of Titan tholins. Icarus 376:114841. https://doi.org/10.1016/j.icarus.2021.114841

Obaid R, Schnorr K, Wolf TJA, et al (2019) Photo-ionization and fragmentation of $Sc_3N@C_{80}$ following excitation above the Sc K-edge. J Chem Phys 151(10):104308. https://doi.org/10.1063/1.5110297

Ohnaka K, Jara Bravo BA (2022) Spatially resolved mid-infrared observations of the circumstellar environment of the born-again object FG Sge. Astron Astrophys 668:A119. https://doi.org/10.1051/0004-6361/202244921. arXiv:2212.07448 [astro-ph.SR]

Oliveira RR, Molpeceres G, Fantuzzi F, et al (2020) Gas-phase spectroscopic characterization of neutral and ionic polycyclic aromatic phosphorus heterocycles (PAPHs). Mon Not R Astron Soc 500(2):2564–2576. https://doi.org/10.1093/mnras/staa3460

Omont A (2016) Interstellar fullerene compounds and diffuse interstellar bands. Astron Astrophys 590:A52. https://doi.org/10.1051/0004-6361/201527685

Omont A, Bettinger HF (2020) Correlation between UV resilience and wavelength of narrow diffuse interstellar bands. Astron Astrophys 637:A74. https://doi.org/10.1051/0004-6361/201937071

Omont A, Bettinger HF (2021) Intermediate-size fullerenes as degradation products of interstellar polycyclic aromatic hydrocarbons. Astron Astrophys 650:A193. https://doi.org/10.1051/0004-6361/202140675

Omont A, Bettinger HF, Tönshoff C (2019) Polyacenes and diffuse interstellar bands. Astron Astrophys 625:A41. https://doi.org/10.1051/0004-6361/201834953

Oña-Ruales JO, Ruiz-Morales Y, Alvarez-Ramírez F (2021) The helicenes: potential carriers of diffuse interstellar bands. ACS Earth Space Chem 5(2):381–390. https://doi.org/10.1021/acsearthspacechem.0c00235

Onaka T, Mori TI, Sakon I, et al (2013) Search for the infrared emission features from deuterated interstellar polycyclic aromatic hydrocarbons. Astrophys J 780(2):114. https://doi.org/10.1088/0004-637X/780/2/114

Onaka T, Mori TI, Okada Y (2015) Dust processing in the Carina nebula region. Planet Space Sci 116:84–91. https://doi.org/10.1016/j.pss.2015.03.025

Onaka T, Nakamura T, Sakon I, et al (2018) Near-infrared to mid-infrared observations of galaxy mergers: NGC 2782 and NGC 7727. Astrophys J 853(1):31. https://doi.org/10.3847/1538-4357/aaa004

Onaka T, Sakon I, Shimonishi T (2022) Near-infrared spectroscopy of a massive young stellar object in the direction toward the galactic center: XCN and aromatic C–D features. Astrophys J 941(2):190. https://doi.org/10.3847/1538-4357/ac9b15

Oomens J (2011) Laboratory infrared spectroscopy of PAHs. In: Joblin C, Tielens AGGM (eds) PAHs and the Universe. EAS Publications Series, pp 61–73. https://doi.org/10.1051/eas/1146007

Otsuka M, Kemper F, Cami J, et al (2014) Physical properties of fullerene-containing galactic planetary nebulae. Mon Not R Astron Soc 437(3):2577–2593. https://doi.org/10.1093/mnras/stt2070

Otsuka M, Kemper F, Leal-Ferreira ML, et al (2016) XSHOOTER spectroscopy of the enigmatic planetary nebula Lin49 in the Small Magellanic Cloud. Mon Not R Astron Soc 462(1):12–34. https://doi.org/10.1093/mnras/stw1615

Palotás J, Martens J, Berden G, et al (2019) The infrared spectrum of protonated buckminsterfullerene $C_{60}H^+$. Nat Astron 4(3):240–245. https://doi.org/10.1038/s41550-019-0941-6

Palotás J, Martens J, Berden G, et al (2021a) The infrared spectrum of protonated C_{70}. Astrophys J Lett 909(2):L17. https://doi.org/10.3847/2041-8213/abe874

Palotás J, Martens J, Berden G, et al (2021b) Laboratory IR spectroscopy of protonated hexa-peri-hexabenzocoronene and dicoronylene. J Mol Spectrosc 378:111474. https://doi.org/10.1016/j.jms.2021.111474

Palotás J, Martens J, Berden G, et al (2022) Laboratory ir spectra of the ionic oxidized fullerenes $C_{60}O^+$ and $C_{60}OH^+$. J Phys Chem A 126(19):2928–2935. https://doi.org/10.1021/acs.jpca.2c01329

Panchagnula S, Bouwman J, Rap DB, et al (2020) Structural investigation of doubly-dehydrogenated pyrene cations. Phys Chem Chem Phys 22(38):21651–21663. https://doi.org/10.1039/D0CP02272A

Pandey A, Srivastav S, Vats A, et al (2023) A comprehensive rotational study of astronomical iso-pentane within 84 to 111 GHz. Spectrochim Acta, Part A, Mol Biomol Spectrosc 290:122299. https://doi.org/10.1016/j.saa.2022.122299

Paris C, Alcamí M, Martín F, et al (2014) Multiple ionization and hydrogen loss from neutral and positively-charged coronene. J Chem Phys 140(20):204307. https://doi.org/10.1063/1.4875805

Parker DSN, Yang T, Dangi BB, et al (2015) Low temperature formation of nitrogen-substituted polycyclic aromatic hydrocarbons (PANHs)—barrierless routes to dihydro(iso)quinolines. Astrophys J 815(2):115. https://doi.org/10.1088/0004-637X/815/2/115

Parneix P, Gamboa A, Falvo C, et al (2017) Dehydrogenation effects on the stability of aromatic units in polycyclic aromatic hydrocarbons in the interstellar medium: a computational study at finite temperature. Mol Astrophys 7:9–18. https://doi.org/10.1016/j.molap.2017.05.001

Patra N, Král P, Sadeghpour HR (2014) Nucleation and stabilization of carbon-rich structures in interstellar media. Astrophys J 785(1):6. https://doi.org/10.1088/0004-637X/785/1/6
Peeters E, Allamandola LJ, Bauschlicher CW, et al (2004) Deuterated interstellar polycyclic aromatic hydrocarbons. Astrophys J 604(1):252–257. https://doi.org/10.1086/381866
Peeters E, Bauschlicher CW, Allamandola LJ, et al (2017) The PAH emission characteristics of the reflection nebula NGC 2023. Astrophys J 836(2):198. https://doi.org/10.3847/1538-4357/836/2/198
Peeters E, Mackie C, Candian A, et al (2021) A spectroscopic view on cosmic PAH emission. Acc Chem Res 54(8):1921–1933. https://doi.org/10.1021/acs.accounts.0c00747
Pérez C, Steber AL, Rijs AM, et al (2017) Corannulene and its complex with water: A tiny cup of water. Phys Chem Chem Phys 19(22):14214–14223. https://doi.org/10.1039/C7CP01506B
Petrignani A, Vala M, Eyler JR, et al (2016) Breakdown products of gaseous polycyclic aromatic hydrocarbons investigated with infrared ion spectroscopy. Astrophys J 826(1):33. https://doi.org/10.3847/0004-637X/826/1/33
Piazza ZA, Hu HS, Li WL, et al (2014) Planar hexagonal B_{36} as a potential basis for extended single-atom layer boron sheets. Nat Commun 5(1):3113. https://doi.org/10.1038/ncomms4113
Pilleri P, Joblin C, Boulanger F, et al (2015) Mixed aliphatic and aromatic composition of evaporating very small grains in NGC 7023 revealed by the 3.4/3.3 μm ratio. Astron Astrophys 577:A16. https://doi.org/10.1051/0004-6361/201425590
Pirali O, Kisiel Z, Goubet M, et al (2015) Rotation-vibration interactions in the spectra of polycyclic aromatic hydrocarbons: quinoline as a test-case species. J Chem Phys 142(10):104310. https://doi.org/10.1063/1.4913750
Pla P, Dubosq C, Rapacioli M, et al (2021) Hydrogenation of C_{24} carbon clusters: structural diversity and energetic properties. J Phys Chem A 125(24):5273–5288. https://doi.org/10.1021/acs.jpca.1c02359
Poater J, Sola M (2011) Open-shell spherical aromaticity: the $2N^2 + 2N+1$ (with $S = N+1/2$) rule. Chem Commun 47(42):11647–11649. https://doi.org/10.1039/c1cc14958j
Poater J, Paauwe J, Pan S, et al (2017) Kekulene: structure, stability and nature of H•••H interactions in large PAHs. Mol Astrophys 8:19–26. https://doi.org/10.1016/j.molap.2017.05.003
Poland KN, Westbrook BR, Magers DH, et al (2022a) Benzvalyne: real or imaginary? J Chem Phys 156(2):024302. https://doi.org/10.1063/5.0077033
Poland KN, Yang W, Fortenberry RC, et al (2022b) The thermal isomerization of benzvalyne to benzyne. Phys Chem Chem Phys 24(23):14573–14578. https://doi.org/10.1039/D2CP00794K
Posenitskiy E, Rapacioli M, Lepetit B, et al (2019) Non-adiabatic molecular dynamics investigation of the size dependence of the electronic relaxation in polyacenes. Phys Chem Chem Phys 21(23):12139–12149. https://doi.org/10.1039/C9CP00603F
Postma J, Hoekstra R, Tielens AGGM, et al (2014) A molecular dynamics study on slow ion interactions with the polycyclic aromatic hydrocarbon molecule anthracene. Astrophys J 783(1):61. https://doi.org/10.1088/0004-637X/783/1/61
Potapov A (2017) Weakly bound molecular complexes in the laboratory and in the interstellar medium: A lost interest? Mol Astrophys 6:16–21. https://doi.org/10.1016/j.molap.2017.01.001
Potapov A, McCoustra M (2021) Physics and chemistry on the surface of cosmic dust grains: A laboratory view. Int Rev Phys Chem 40(2):299–364. https://doi.org/10.1080/0144235X.2021.1918498
Potenti S, Manini P, Fornaro T, et al (2018) Solid state photochemistry of hydroxylated naphthalenes on minerals: probing polycyclic aromatic hydrocarbon transformation pathways under astrochemically-relevant conditions. ACS Earth Space Chem 2(10):977–1000. https://doi.org/10.1021/acsearthspacechem.8b00060
Preitschopf T, Hirsch F, Lemmens AK, et al (2022) The gas-phase infrared spectra of the 2-methylallyl radical and its high-temperature reaction products. Phys Chem Chem Phys 24(13):7682–7690. https://doi.org/10.1039/D2CP00400C
Priestley FD, Arias M, Barlow MJ, et al (2021) Dust destruction and survival in the Cassiopeia A reverse shock. Mon Not R Astron Soc 509(3):3163–3171. https://doi.org/10.1093/mnras/stab3195
Priestley FD, De Looze I, Barlow MJ (2022) The impact of metallicity-dependent dust destruction on the dust-to-metals ratio in galaxies. Mon Not R Astron Soc 509(1):L6–L10. https://doi.org/10.1093/mnrasl/slab114
Puget J, Leger A (1989) A new component of the interstellar matter - small grains and large aromatic molecules. Annu Rev Astron Astrophys 27:161–198. https://doi.org/10.1146/annurev.aa.27.090189.001113
Qi H, Picaud S, Devel M, et al (2018) Adsorption of organic molecules on onion-like carbons: insights on the formation of interstellar hydrocarbons. Astrophys J 867(2):133. https://doi.org/10.3847/1538-4357/aae4e4
Queiroz MH, Alves TV, Rivelino R (2023) Photoabsorption of microhydrated naphthalene and its cyano-substituted derivatives: probing prereactive models for photodissociation in molecular clouds. J Phys Chem A 127(19):4317–4327. https://doi.org/10.1021/acs.jpca.3c00487

Quirico E, Moroz LV, Schmitt B, et al (2016) Refractory and semi-volatile organics at the surface of comet 67P/Churyumov-Gerasimenko: insights from the VIRTIS/Rosetta imaging spectrometer. Icarus 272:32–47. https://doi.org/10.1016/j.icarus.2016.02.028

Quitián-Lara HM, Fantuzzi F, Nascimento MAC, et al (2018) Hydrogenated benzene in circumstellar environments: insights into the photostability of super-hydrogenated PAHs. Astrophys J 854(1):61. https://doi.org/10.3847/1538-4357/aaa977

Quitián-Lara HM, Fantuzzi F, Oliveira RR, et al (2020) Dissociative single and double photoionization of biphenyl ($C_{12}H_{10}$) by soft X-rays in planetary nebulae. Mon Not R Astron Soc 499(4):6066–6083. https://doi.org/10.1093/mnras/staa3181

Rademacher J, Reedy ES, Campbell EK (2022) Electronic spectroscopy of monocyclic carbon ring cations for astrochemical consideration. J Phys Chem A 126(13):2127–2133. https://doi.org/10.1021/acs.jpca.2c00650

Rahul K, Shivakarthik E, Meka J, et al (2020) Residue from vacuum ultraviolet irradiation of benzene ices: insights into the physical structure of astrophysical dust. Spectrochim Acta, Part A, Mol Biomol Spectrosc 231:117797. https://doi.org/10.1016/j.saa.2019.117797

Ramanathan K, S A, Bouwman J, et al (2022) Photodissociation of quinoline cation: mapping the potential energy surface. J Chem Phys 157(6):064303. https://doi.org/10.1063/5.0092161

Rap DB, Schrauwen JGM, Marimuthu AN, et al (2022b) Low-temperature nitrogen-bearing polycyclic aromatic hydrocarbon formation routes validated by infrared spectroscopy. Nat Astron 6(9):1059–1067. https://doi.org/10.1038/s41550-022-01713-z

Rap DB, van Boxtel TJHH, Redlich B, et al (2022a) Spectroscopic detection of cyano-cyclopentadiene ions as dissociation products upon ionization of aniline. J Phys Chem A 126(19):2989–2997. https://doi.org/10.1021/acs.jpca.2c01429

Rap DB, Simon A, Steenbakkers K, et al (2023) Fingerprinting fragments of fragile interstellar molecules: Dissociation chemistry of pyridine and benzonitrile revealed by infrared spectroscopy and theory. Faraday Discuss. https://doi.org/10.1039/D3FD00015J

Rapacioli M, Spiegelman F, Joalland B, et al (2011) PAH-related very small grains in photodissociation regions: implications from molecular simulations. In: Joblin C, Tielens AGGM (eds) PAHs and the Universe. EAS Publications Series, pp 223–234. https://doi.org/10.1051/eas/1146024

Rapacioli M, Cazaux S, Foley N, et al (2018) Atomic hydrogen interactions with gas-phase coronene cations: hydrogenation versus fragmentation. Phys Chem Chem Phys 20(35):22427–22438. https://doi.org/10.1039/C8CP03024C

Rasmussen AP, Wenzel G, Hornekær L, et al (2023) Gas-phase electronic action absorption spectra of protonated oxygen-functionalized polycyclic aromatic hydrocarbons (OPAHs). Astron Astrophys 674:A103. https://doi.org/10.1051/0004-6361/202346003

Reitsma G, Zettergren H, Boschman L, et al (2013) Ion–polycyclic aromatic hydrocarbon collisions: kinetic energy releases for specific fragmentation channels. J Phys B, At Mol Opt Phys 46(24):245201. https://doi.org/10.1088/0953-4075/46/24/245201

Reitsma G, Boschman L, Deuzeman MJ, et al (2014) Deexcitation dynamics of superhydrogenated polycyclic aromatic hydrocarbon cations after soft-X-ray absorption. Phys Rev Lett 113(5):053002. https://doi.org/10.1103/PhysRevLett.113.053002

Reizer E, Fiser B (2022) Potential reaction initiation points of polycyclic aromatic hydrocarbons. Arab J Chem 15(6):103839. https://doi.org/10.1016/j.arabjc.2022.103839

Reizer E, Csizmadia IG, Nehéz K, et al (2021) Theoretical investigation of benzo(a)pyrene formation. Chem Phys Lett 772:138564. https://doi.org/10.1016/j.cplett.2021.138564

Reizer E, Viskolcz B, Fiser B (2022) Formation and growth mechanisms of polycyclic aromatic hydrocarbons: a mini-review. Chemosphere 291:132793. https://doi.org/10.1016/j.chemosphere.2021.132793

Rérat M, Rayez JC, Fábián B, et al (2022) A CRYSTAL-based parameterization of carbon atom dynamic polarizabilities to compute optical properties of curved carbonaceous nanostructures. Theor Chem Acc 141(11):65. https://doi.org/10.1007/s00214-022-02926-1

Reusch E, Holzmeier F, Constantinidis P, et al (2017) Isomer-selective generation and spectroscopic characterization of picolyl radicals. Angew Chem, Int Ed 56(27):8000–8003. https://doi.org/10.1002/anie.201703433. https://onlinelibrary.wiley.com/doi/10.1002/anie.201703433

Ricca A, Bauschlicher CW, Boersma C, et al (2012) The infrared spectroscopy of compact polycyclic aromatic hydrocarbons containing up to 384 carbons. Astrophys J 754(1):75. https://doi.org/10.1088/0004-637X/754/1/75

Ricca A, Bauschlicher CW, Allamandola LJ (2013) The infrared spectroscopy of neutral polycyclic aromatic hydrocarbon clusters. Astrophys J 776(1):31. https://doi.org/10.1088/0004-637X/776/1/31

Ricca A, Bauschlicher CW, Roser JE, et al (2018) Polycyclic aromatic hydrocarbons with straight edges and the 7.6/6.2 and 8.6/6.2 intensity ratios in reflection nebulae. Astrophys J 854(2):115. https://doi.org/10.3847/1538-4357/aaa757

Ricca A, Roser JE, Peeters E, et al (2019) Polycyclic aromatic hydrocarbons with armchair edges: potential emitters in class B sources. Astrophys J 882(1):56. https://doi.org/10.3847/1538-4357/ab3124
Ricca A, Boersma C, Peeters E (2021) The 6.2 μm PAH feature and the role of nitrogen: revisited. Astrophys J 923(2):202. https://doi.org/10.3847/1538-4357/ac28fc
Riffel RA, Zakamska NL, Riffel R (2020) Active galactic nuclei winds as the origin of the H_2 emission excess in nearby galaxies. Mon Not R Astron Soc 491(1):1518–1529. https://doi.org/10.1093/mnras/stz3137
Rigopoulou D, Barale M, Clary DC, et al (2021) The properties of polycyclic aromatic hydrocarbons in galaxies: constraints on PAH sizes, charge and radiation fields. Mon Not R Astron Soc 504(4):5287–5300. https://doi.org/10.1093/mnras/stab959
Rodriguez Castillo S, Simon A, Joblin C (2018) Investigating the importance of edge-structure in the loss of H_2 of PAH cations: the case of dibenzopyrene isomers. Int J Mass Spectrom 429:189–197. https://doi.org/10.1016/j.ijms.2017.09.013
Rodríguez-Cantano R, Pérez de Tudela R, Bartolomei M, et al (2015) Coronene molecules in helium clusters: quantum and classical studies of energies and configurations. J Chem Phys 143(22):224306. https://doi.org/10.1063/1.4936414
Rosenberg MJF, Berné O, Boersma C (2014) Random mixtures of polycyclic aromatic hydrocarbon spectra match interstellar infrared emission. Astron Astrophys 566:L4. https://doi.org/10.1051/0004-6361/201423953
Roser JE, Ricca A (2015) Polycyclic aromatic hydrocarbon clusters as sourceso of interstellar infrared emission. Astrophys J 801(2):108. https://doi.org/10.1088/0004-637X/801/2/108
Roser JE, Ricca A, Allamandola LJ (2014) Anthracene clusters and the interstellar infrared emission features. Astrophys J 783(2):97. https://doi.org/10.1088/0004-637X/783/2/97
Rouillé G, Krasnokutski SA, Fulvio D, et al (2015) Dissociative photoionization of polycyclic aromatic hydrocarbon molecules carrying an ethynyl group. Astrophys J 810(2):114. https://doi.org/10.1088/0004-637X/810/2/114
Rouillé G, Steglich M, Hemberger P, et al (2019) Threshold dissociation of the 1-ethynylpyrene cation at internal energies relevant to H I regions. Astrophys J 885(1):21. https://doi.org/10.3847/1538-4357/ab4418
Rouillé G, Krasnokutski SA, Carpentier Y (2021) The C_{60}:C_{60}^+ ratio in diffuse and translucent interstellar clouds. Astron Astrophys 656:A100. https://doi.org/10.1051/0004-6361/202142078. https://www.aanda.org/10.1051/0004-6361/202142078. Online. Accessed 2023-02-04
Ruschel-Dutra D, Pastoriza M, Riffel R, et al (2014) A mid-IR comparative analysis of the Seyfert galaxies NGC 7213 and NGC 1386. Mon Not R Astron Soc 438(4):3434–3442. https://doi.org/10.1093/mnras/stt2448
Sabbah H, Bonnamy A, Papanastasiou D, et al (2017) Identification of PAH isomeric structure in cosmic dust analogs: the AROMA setup. Astrophys J 843(1):34. https://doi.org/10.3847/1538-4357/aa73dd
Sabbah H, Commodo M, Picca F, et al (2021) Molecular content of nascent soot: family characterization using two-step laser desorption laser ionization mass spectrometry. Proc Combust Inst 38(1):1241–1248. https://doi.org/10.1016/j.proci.2020.09.022
Sabbah H, Carlos M, Jenniskens P, et al (2022) Detection of cosmic fullerenes in the Almahata Sitta meteorite: are they an interstellar heritage? Astrophys J 931(2):91. https://doi.org/10.3847/1538-4357/ac69dd
Sabirov DS, Tukhbatullina AA, Shepelevich IS (2022) Polarizability in astrochemical studies of complex carbon-based compounds. ACS Earth Space Chem 6(1):1–17. https://doi.org/10.1021/acsearthspacechem.1c00341
Sadjadi S, Zhang Y, Kwok S (2015a) On the origin of the 11.3 micron unidentified infrared emission feature. Astrophys J 807(1):95. https://doi.org/10.1088/0004-637X/807/1/95. arXiv:1505.03971
Sadjadi S, Zhang Y, Kwok S (2015b) A theoretical study on the vibrational spectra of polycyclic aromatic hydrocarbon molecules with aliphatic sidegroups. Astrophys J 801(1):34. https://doi.org/10.1088/0004-637X/801/1/34
Saha K, Chandrasekaran V, Heber O, et al (2018) Ultraslow isomerization in photoexcited gas-phase carbon cluster C_{10}^-. Nat Commun 9(1):912. https://doi.org/10.1038/s41467-018-03197-w
Sales DA, Robinson A, Axon DJ, et al (2015) An embedded active nucleus in the OH megamaser galaxy IRAS16399–0937. Astrophys J 799(1):25. https://doi.org/10.1088/0004-637X/799/1/25
Salomon E, Minissale M, Lairado FR, et al (2021) Pyrene adsorption on a Ag(111) surface. J Phys Chem C 125(20):11166–11174. https://doi.org/10.1021/acs.jpcc.1c01350
Sánchez M, Ruette F (2015) Hydrogen atom chemisorption and diffusion on neutral and charged polycyclic aromatic hydrocarbon (PAH) flakes in the interstellar media. Chem Phys Lett 640:11–15. https://doi.org/10.1016/j.cplett.2015.10.004
Sandstrom KM, Chastenet J, Sutter J, et al (2023) PHANGS-JWST first results: mapping the 3.3 μm polycyclic aromatic hydrocarbon vibrational band in nearby galaxies with NIRCam medium bands. Astrophys J 944:L7. https://doi.org/10.3847/2041-8213/acb0cf

Santaloci TJ, Fortenberry RC (2021) Electronically excited states of closed-shell, cyano-functionalized polycyclic aromatic hydrocarbon anions. Chemistry 3(1):296–313. https://doi.org/10.3390/chemistry3010022
Santoro G, Martinez L, Lauwaet K, et al (2020) The chemistry of cosmic dust analogs from C, C_2, and C_2H_2 in C-rich circumstellar envelopes. Astrophys J 895(2):97. https://doi.org/10.3847/1538-4357/ab9086
Santos JC, Fantuzzi F, Quitián-Lara HM, et al (2022) Multiply charged naphthalene and its $C_{10}H_8$ isomers: bonding, spectroscopy, and implications in AGN environments. Mon Not R Astron Soc 512(4):4669–4682. https://doi.org/10.1093/mnras/stac679
Sarangi A, Matsuura M, Micelotta ER (2018) Dust in supernovae and supernova remnants I: formation scenarios. Space Sci Rev 214(3):63. https://doi.org/10.1007/s11214-018-0492-7
Sarre PJ (2019) Graphene oxide nanoparticles in the interstellar medium. Mon Not R Astron Soc Lett 490(1):L17–L20. https://doi.org/10.1093/mnrasl/slz131
Schleier D, Hemberger P, Bodi A, et al (2022) Threshold photoelectron spectroscopy of quinoxaline, quinazoline, and cinnoline. J Phys Chem A 126(14):2211–2221. https://doi.org/10.1021/acs.jpca.2c01073. https://doi.org/10.1021/acs.jpca.2c01073
Schneiker A, Csonka IP, Tarczay G (2020) Hydrogenation and dehydrogenation reactions of the phenalenyl radical/1H-phenalene system at low temperatures. Chem Phys Lett 743:137183. https://doi.org/10.1016/j.cplett.2020.137183
Sciamma-O'Brien E, Salama F (2020) Characterization of cosmic grain analogs formed at low temperature from small hydrocarbon precursors in the NASA Ames COSmIC Facility. Astrophys J 905(1):45. https://doi.org/10.3847/1538-4357/abc00d
Sciamma-O'Brien E, Ricketts CL, Salama F (2014) The Titan Haze Simulation experiment on COSmIC: probing Titan's atmospheric chemistry at low temperature. Icarus 243:325–336. https://doi.org/10.1016/j.icarus.2014.08.004
Sciamma-O'Brien E, Upton KT, Salama F (2017) The Titan Haze Simulation (THS) experiment on COSmIC. Part II. Ex-situ analysis of aerosols produced at low temperature. Icarus 289:214–226. https://doi.org/10.1016/j.icarus.2017.02.004
Sebree JA, Trainer MG, Loeffler MJ, et al (2014) Titan aerosol analog absorption features produced from aromatics in the far infrared. Icarus 236:146–152. https://doi.org/10.1016/j.icarus.2014.03.039
Sebree JA, Roach MC, Shipley ER, et al (2018a) Detection of prebiotic molecules in plasma and photochemical aerosol analogs using GC/MS/MS techniques. Astrophys J 865(2):133. https://doi.org/10.3847/1538-4357/aadba1
Sebree JA, Wayson JM, Lopez JR (2018b) Variation in photon flux during extended photochemical aerosol experiments: implications for atmospheric laboratory simulations. J Photochem Photobiol A, Chem 360:1–5. https://doi.org/10.1016/j.jphotochem.2018.04.023
Sehring CM, Palmer CZ, Westbrook BR, et al (2022) The spectral features and detectability of small, cyclic silicon carbide clusters. Front Astron Space Sci 9. https://doi.org/10.3389/fspas.2022.1074879
Seitz F, Zettergren H, Rousseau P, et al (2013) Ions colliding with clusters of fullerenes—decay pathways and covalent bond formations. J Chem Phys 139(3):034309. https://doi.org/10.1063/1.4812790
Seok JY, Li A (2015) Dust and polycyclic aromatic hydrocarbon in the HD 34700 debris disk. Astrophys J 809(1):22. https://doi.org/10.1088/0004-637X/809/1/22
Seok JY, Li A (2016) Dust and polycyclic aromatic hydrocarbon in the pre-translational disk around HD 169142. Astrophys J 818(1):2. https://doi.org/10.3847/0004-637X/818/1/2
Seok JY, Li A (2017) Polycyclic aromatic hydrocarbons in protoplanetary disks around Herbig Ae/Be and T Tauri stars. Astrophys J 835(2):291. https://doi.org/10.3847/1538-4357/835/2/291
Seok JY, Hirashita H, Asano RS (2014) Formation history of polycyclic aromatic hydrocarbons in galaxies. Mon Not R Astron Soc 439(2):2186–2196. https://doi.org/10.1093/mnras/stu120
Shannon MJ, Boersma C (2019) Examining the class B to A shift of the 7.7 μm PAH band with the NASA Ames PAH IR spectroscopic database. Astrophys J 871(1):124. https://doi.org/10.3847/1538-4357/aaf562
Shannon MJ, Stock DJ, Peeters E (2015) Probing the ionization states of polycyclic aromatic hydrcarbons via the 15–20 μm emission bands. Astrophys J 811(2):153. https://doi.org/10.1088/0004-637X/811/2/153
Shannon MJ, Stock DJ, Peeters E (2016) Interpreting the subtle spectral variations of the 11.2 and 12.7 μm polycyclic aromatic hydrocarbon bands. Astrophys J 824(2):111. https://doi.org/10.3847/0004-637X/824/2/111
Shannon MJ, Peeters E, Cami J, et al (2018) Polycyclic aromatic hydrocarbon emission toward the galactic bulge. Astrophys J 855(1):32. https://doi.org/10.3847/1538-4357/aaae06
Shao Z, Jiang BW, Li A (2017) On the optical-to-silicate extinction ratio as a probe of the dust size in active galactic nuclei. Astrophys J 840(1):27. https://doi.org/10.3847/1538-4357/aa6ba4
Shao Z, Jiang BW, Li A, et al (2018) Probing the 9.7 μm interstellar silicate extinction profile through the Spitzer/IRS spectroscopy of OB stars. Mon Not R Astron Soc 478(3):3467–3477. https://doi.org/10.1093/mnras/sty1267

Shaw G, Ferland GJ (2021) Role of polycyclic aromatic hydrocarbons on the cosmic-ray ionization rate in the galaxy. Astrophys J 908(2):138. https://doi.org/10.3847/1538-4357/abdab2

Shaw G, Ranjan A (2022) Detecting PAHs in high- z galaxies in proxy: modelling physical conditions in an extremely strong damped Lyman α absorber towards QSO SDSS J1143+1420 at z = 2.323. Mon Not R Astron Soc 514(1):1335–1341. https://doi.org/10.1093/mnras/stac1290

Shiels OJ, Prendergast MB, Savee JD, et al (2021) Five vs. six membered-ring PAH products from reaction of o-methylphenyl radical and two C_3H_4 isomers. Phys Chem Chem Phys 23(27):14913–14924. https://doi.org/10.1039/d1cp01764k

Shingledecker CN, Lee KLK, Wandishin JT, et al (2021) Detection of interstellar H_2CCCHC_3N a possible link between chains and rings in cold cores. Astron Astrophys 652:L12. https://doi.org/10.1051/0004-6361/202140698

Shiryaev AA, Fisenko AV, Semjonova LF, et al (2015) Photoluminescence of silicon-vacancy defects in nanodiamonds of different chondrites. Meteorit Planet Sci 50(6):1005–1012. https://doi.org/10.1111/maps.12450

Shiryaev AA, Hinks JA, Marks NA, et al (2018a) Ion implantation in nanodiamonds: size effect and energy dependence. Sci Rep 8(1):5099. https://doi.org/10.1038/s41598-018-23434-y

Shiryaev AA, Sabin L, Valyavin G, et al (2018b) On possibility of detection of emission from nanodiamonds in vicinity of stellar objects: laboratory spectroscopy and observationsl data. In: Modern star astronomy, pp 321–324. https://doi.org/10.31361/eaas.2018-1.072. arXiv:1901.10360

Shiryaev AA, Trigub AL, Voronina EN, et al (2021) Behavior of implanted Xe, Kr and Ar in nanodiamonds and thin graphene stacks: experiment and modeling. Phys Chem Chem Phys 23(38):21729–21737. https://doi.org/10.1039/D1CP02600C

Shukla N, Vats A, Pathak A, et al (2022) Time-dependent density functional study of nitrogen-substituted polycyclic aromatic hydrocarbons and diffuse interstellar bands. ACS Earth Space Chem 6(12):2867–2876. https://doi.org/10.1021/acsearthspacechem.2c00176

Sidhu A, Peeters E, Cami J, et al (2021) A principal component analysis of polycyclic aromatic hydrocarbon emission in NGC 2023. Mon Not R Astron Soc 500(1):177–190. https://doi.org/10.1093/mnras/staa3175. arXiv:2010.04813 [astro-ph.GA]

Sidhu A, Bazely J, Peeters E, et al (2022a) A principal component analysis of polycyclic aromatic hydrocarbon emission in NGC 7023. Mon Not R Astron Soc 511(2):2186–2200. https://doi.org/10.1093/mnras/stac157. arXiv:2201.07172 [astro-ph.GA]

Sidhu A, Tielens AGGM, Peeters E, et al (2022b) Polycyclic aromatic hydrocarbon emission model in photodissociation regions – I. Application to the 3.3, 6.2, and 11.2 μm bands. Mon Not R Astron Soc 514(1):342–369. https://doi.org/10.1093/mnras/stac1255

Sidhu A, Tielens AGGM, Peeters E, et al (2023) Polycyclic aromatic hydrocarbon emission model in photodissociation regions - II. Application to the polycyclic aromatic hydrocarbon and fullerene emission in NGC 7023. Mon Not R Astron Soc 522(3):3227–3235. https://doi.org/10.1093/mnras/stad1180

Silva-Ribeiro A, Krabbe AC, Canelo CM, et al (2021) Polycyclic aromatic hydrocarbons and the ionized gas in galaxies with active nuclei. Mon Not R Astron Soc 509(1):327–344. https://doi.org/10.1093/mnras/stab3005

Simbizi R, Nduwimana D, Niyoncuti J, et al (2022) On the formation of 2- and 3-cyanofurans and their protonated forms in interstellar medium conditions: quantum chemical evidence. RSC Adv 12(39):25332–25341. https://doi.org/10.1039/D2RA04351C

Simon A, Noble JA, Rouaut G, et al (2017a) Formation of coronene: water complexes: FTIR study in argon matrices and theoretical characterisation. Phys Chem Chem Phys 19(12):8516–8529. https://doi.org/10.1039/C6CP08559H

Simon A, Rapacioli M, Rouaut G, et al (2017b) Dissociation of polycyclic aromatic hydrocarbons: molecular dynamics studies. Philos Trans R Soc A, Math Phys Eng Sci 375(2092):20160195. https://doi.org/10.1098/rsta.2016.0195

Simon A, Champeaux JP, Rapacioli M, et al (2018) Dissociation of polycyclic aromatic hydrocarbons at high energy: MD/DFTB simulations versus collision experiments: fragmentation paths, energy distribution and internal conversion: test on the pyrene cation. Theor Chem Acc 137(7):106. https://doi.org/10.1007/s00214-018-2287-z

Sita ML, Changala PB, Xue C, et al (2022) Discovery of interstellar 2-cyanoindene ($2\text{-}C_9H_7CN$) in GOTHAM observations of TMC-1. Astrophys J Lett 938(2):L12. https://doi.org/10.3847/2041-8213/ac92f4

Sittler EC, Cooper JF, Sturner SJ, et al (2020) Titan's ionospheric chemistry, fullerenes, oxygen, galactic cosmic rays and the formation of exobiological molecules on and within its surfaces and lakes. Icarus 344:113246. https://doi.org/10.1016/j.icarus.2019.03.023

Sivaraman B, Mukherjee R, Subramanian KP, et al (2014) Benzene formation on interstellar icy mantles containing propargyl alcohol. Astrophys J 798(2):72. https://doi.org/10.1088/0004-637X/798/2/72

Sivaraman B, Rahul KK, Ambresh M, et al (2023) N-graphene synthesized in astrochemical ices. Eur Phys J D 77(2):24. https://doi.org/10.1140/epjd/s10053-023-00590-z

Skov AL, Thrower JD, Hornekær L (2014) Polycyclic aromatic hydrocarbons – catalysts for molecular hydrogen formation. Faraday Discuss 168:223–234. https://doi.org/10.1039/C3FD00151B

Sloan GC, Lagadec E, Zijlstra AA, et al (2014) Carbon-rich dust past the asymptotic giant branch: Aliphatics, aromatics, and fullerenes in the Magellanic Clouds. Astrophys J 791(1):28. https://doi.org/10.1088/0004-637X/791/1/28

Smoker JV, Müller A, Ibero AM, et al (2023) A high resolution study of near-IR diffuse interstellar bands, search for small scale structure, time variability and stellar features. Astron Astrophys 672:A181. https://doi.org/10.1051/0004-6361/202142267

Spilker JS, Phadke KA, Aravena M, et al (2023) Spatial variations in aromatic hydrocarbon emission in a dust-rich galaxy. Nature 618(7966):708–711. https://doi.org/10.1038/s41586-023-05998-6

Srivastav S, Sil M, Gorai P, et al (2022) Astrochemical model to study the abundances of branched carbon-chain molecules in a hot molecular core with realistic binding energies. Mon Not R Astron Soc 515(3):3524–3538. https://doi.org/10.1093/mnras/stac1904

Stanley LH, Anstöter CS, Verlet JRR (2017) Resonances of the anthracenyl anion probed by frequency-resolved photoelectron imaging of collision-induced dissociated anthracene carboxylic acid. Chem Sci 8(4):3054–3061. https://doi.org/10.1039/C6SC05405F

Steber AL, Pérez C, Temelso B, et al (2017) Capturing the elusive water trimer from the stepwise growth of water on the surface of the polycyclic aromatic hydrocarbon acenaphthene. J Phys Chem Lett 8(23):5744–5750. https://doi.org/10.1021/acs.jpclett.7b02695

Steglich M, Maity S, Maier JP (2016) Visible absorptions of potential diffuse ism hydrocarbons: C_9H_9 and C_9H_5 radicals. Astrophys J 830(2):145. https://doi.org/10.3847/0004-637X/830/2/145

Stein T, Bera PP, Lee TJ, et al (2020) Molecular growth upon ionization of van der Waals clusters containing HCCH and HCN is a pathway to prebiotic molecules. Phys Chem Chem Phys 22(36):20337–20348. https://doi.org/10.1039/D0CP03350B

Stephens IW, Evans JM, Xue R, et al (2014) Spitzer observations of dust emission from HII regions in the Large Magellanic Cloud. Astrophys J 784(2):147. https://doi.org/10.1088/0004-637X/784/2/147

Stock DJ, Peeters E (2017) Polycyclic aromatic hydrocarbon emission in Spitzer /IRS maps. II. A direct link between band profiles and the radiation field strength. Astrophys J 837(2):129. https://doi.org/10.3847/1538-4357/aa5f54

Stock DJ, Peeters E, Tielens AGGM, et al (2013) Extinction and polycyclic aromatic hydrocarbon intensity variations across the H II region IRAS 12063–6259. Astrophys J 771(1):72. https://doi.org/10.1088/0004-637X/771/1/72

Stock DJ, Peeters E, Choi WDY, et al (2014) The mid-infrared appearance of the galactic mini-starburst W49A. Astrophys J 791(2):99. https://doi.org/10.1088/0004-637X/791/2/99

Stock DJ, Choi WDY, Moya LGV, et al (2016) Polycyclic aromatic hydrocarbon emission in SPITZER /IRS maps. I. Catalog and simple diagnostics. Astrophys J 819(1):65. https://doi.org/10.3847/0004-637X/819/1/65

Stockett MH, Zettergren H, Adoui L, et al (2014) Nonstatistical fragmentation of large molecules. Phys Rev A 89(3):032701. https://doi.org/10.1103/PhysRevA.89.032701

Stockett MH, Gatchell M, Chen T, et al (2015a) Threshold energies for single-carbon knockout from polycyclic aromatic hydrocarbons. J Phys Chem Lett 6(22):4504–4509. https://doi.org/10.1021/acs.jpclett.5b02080

Stockett M, Gatchell M, de Ruette N, et al (2015b) Isomer effects in fragmentation of polycyclic aromatic hydrocarbons. Int J Mass Spectrom 392:58–62. https://doi.org/10.1016/j.ijms.2015.09.005

Stockett MH, Wolf M, Gatchell M, et al (2018) The threshold displacement energy of buckminsterfullerene C_{60} and formation of the endohedral defect fullerene $He@C_{59}$. Carbon 139:906–912. https://doi.org/10.1016/j.carbon.2018.07.073

Stockett MH, Björkhage M, Cederquist H, et al (2019a) Intrinsic absorption profile and radiative cooling rate of a PAH cation revealed by action spectroscopy in the cryogenic electrostatic storage ring DESIREE. Proc Int Astron Union 15(S350):127–131. https://doi.org/10.1017/S1743921319007130

Stockett MH, Björkhage M, Cederquist H, et al (2019b) Storage time dependent photodissociation action spectroscopy of polycyclic aromatic hydrocarbon cations in the cryogenic electrostatic storage ring DESIREE. Faraday Discuss 217:126–137. https://doi.org/10.1039/C8FD00161H

Stockett MH, Bull JN, Buntine JT, et al (2020) Unimolecular fragmentation and radiative cooling of isolated PAH ions: a quantitative study. J Chem Phys 153(15):154303. https://doi.org/10.1063/5.0027773

Stockett MH, Avaldi L, Bolognesi P, et al (2021) Competitive dehydrogenation and backbone fragmentation of superhydrogenated PAHs: a laboratory study. Astrophys J 913(1):46. https://doi.org/10.3847/1538-4357/abf354

Stockett MH, Bull JN, Cederquist H, et al (2023) Efficient stabilization of cyanonaphthalene by fast radiative cooling and implications for the resilience of small PAHs in interstellar clouds. Nat Commun 14(1):395. https://doi.org/10.1038/s41467-023-36092-0

Strelnikov D, Kern B, Kappes MM (2015) On observing C_{60}^{+} and C_{60}^{2+} in laboratory and space. Astron Astrophys 584:A55. https://doi.org/10.1051/0004-6361/201527234

Stubbing JW, Salter TL, Brown WA, et al (2018) A fibre-coupled UHV-compatible variable angle reflection-absorption UV/visible spectrometer. Rev Sci Instrum 89(5):054102. https://doi.org/10.1063/1.5025405

Sundararajan P, Tsuge M, Baba M, et al (2018) Infrared spectrum of protonated corannulene $H^{+}C_{20}H_{10}$ in solid para-hydrogen and its potential contribution to interstellar unidentified infrared bands. ACS Earth Space Chem 2(10):1001–1010. https://doi.org/10.1021/acsearthspacechem.8b00089

Sundararajan P, Tsuge M, Baba M, et al (2019) Infrared spectrum of hydrogenated corannulene rim - $HC_{20}H_{10}$ isolated in solid para-hydrogen. J Chem Phys 151(4):044304. https://doi.org/10.1063/1.5111169

Tabone B, Bettoni G, van Dishoeck EF, et al (2023) A rich hydrocarbon chemistry and high C to O ratio in the inner disk around a very low-mass star. Nat Astron 7(7):805–814. https://doi.org/10.1038/s41550-023-01965-3

Taha AS, Labadie L, Pantin E, et al (2018) The spatial extent of polycyclic aromatic hydrocarbons emission in the Herbig star HD 179218. Astron Astrophys 612:A15. https://doi.org/10.1051/0004-6361/201732008

Takeuchi H (2013) Structures, stability, and growth sequence patterns of small homoclusters of naphthalene, anthracene, phenanthrene, phenalene, naphthacene, and pyrene. Comput Theor Chem 1021:84–90. https://doi.org/10.1016/j.comptc.2013.06.029

Tang Z, Simonsen FDS, Jaganathan R, et al (2022) Top-down formation of ethylene from fragmentation of superhydrogenated polycyclic aromatic hydrocarbons. Astron Astrophys 663:A150. https://doi.org/10.1051/0004-6361/202243202

Tarakeshwar P, Buseck PR, Timmes FX (2019) On the structure, magnetic properties, and infrared spectra of iron pseudocarbynes in the interstellar medium. Astrophys J 879(1):2. https://doi.org/10.3847/1538-4357/ab22b7

ten Brinck S, Nieuwland C, van der Werf A, et al (2022) Polycyclic aromatic hydrocarbons (PAHs) in interstellar ices: a computational study into how the ice matrix influences the ionic state of PAH photoproducts. ACS Earth Space Chem 6(3):766–774. https://doi.org/10.1021/acsearthspacechem.1c00433

Tennyson J, Yurchenko SN (2017) Laboratory spectra of hot molecules: data needs for hot super-Earth exoplanets. Mol Astrophys 8:1–18. https://doi.org/10.1016/j.molap.2017.05.002

Theis ML, Candian A, Tielens AGGM, et al (2015a) Electronically excited states of anisotropically extended singly-deprotonated PAH anions. J Phys Chem A 119(52):13048–13054. https://doi.org/10.1021/acs.jpca.5b10421

Theis ML, Candian A, Tielens AGGM, et al (2015b) Electronically excited states of PANH anions. Phys Chem Chem Phys 17(22):14761–14772. https://doi.org/10.1039/C5CP01354B

Thrower JD, Friis EE, Skov AL, et al (2014) Hydrogenation of PAH molecules through interaction with hydrogenated carbonaceous grains. Phys Chem Chem Phys 16(8):3381–3387. https://doi.org/10.1039/C3CP54073A

Tielens AGGM (2008) Interstellar polycyclic aromatic hydrocarbon molecules. Annu Rev Astron Astrophys 46:289–337. https://doi.org/10.1146/annurev.astro.46.060407.145211

Tielens A (2021) Molecular Astrophysics. https://doi.org/10.1017/9781316718490

Tielens AGGM (2022) Dust formation in astrophysical environments: the importance of kinetics. Front Astron Space Sci 9. https://www.frontiersin.org/articles/10.3389/fspas.2022.908217

Tokunaga AT, Bernstein LS (2021) The 3.3 μm infrared emission feature: observational and laboratory constraints on its carrier. Astrophys J 916(1):52. https://doi.org/10.3847/1538-4357/ac004b

Tokunaga AT, Bernstein LS, Connelley M (2022) The 3.3 μm infrared emission feature profile in HD 44179. Astrophys J 939(2):86. https://doi.org/10.3847/1538-4357/ac9969

Topchieva A, Wiebe D, Kirsanova MS (2018) Global photometric analysis of galactic HII regions. Res Astron Astrophys 18(8):091. https://doi.org/10.1088/1674-4527/18/8/91

Topchieva A, Akimkin V, Smirnov-Pinchukov G (2019) Infrared photometric properties of inner and outer parts of hii regions. Res Astron Astrophys 19(10):148. https://doi.org/10.1088/1674-4527/19/10/148

Trainer MG, Sebree JA, Heidi Yoon Y, et al (2013) The influence of benzene as a trace reactant in Titan aerosol analogs. Astrophys J 766(1):L4. https://doi.org/10.1088/2041-8205/766/1/L4

Trinquier G, Simon A, Rapacioli M, et al (2017a) PAH chemistry at eV internal energies. 1. H-shifted isomers. Mol Astrophys 7:27–36. https://doi.org/10.1016/j.molap.2017.02.001

Trinquier G, Simon A, Rapacioli M, et al (2017b) PAH chemistry at eV internal energies. 2. Ring alteration and dissociation. Mol Astrophys 7:37–59. https://doi.org/10.1016/j.molap.2017.02.002

Tseng CY, Wu YJ, Lee YP (2022) Infrared spectra of 1-quinolinium ($C_9H_7NH^{+}$) cation and quinolinyl radicals (C_9H_7NH and 3-, 4-, 7-, and 8-hc C_9H_7NH) isolated in solid para- hydrogen. J Phys Chem A 126(15):2361–2372. https://doi.org/10.1021/acs.jpca.2c01330

Tsuge M, Bahou M, Wu YJ, et al (2016a) Infrared spectra of ovalene ($C_{32}H_{14}$) and hydrogenated ovalene ($C_{32}H_{15}$) in solid para-hydrogen. Phys Chem Chem Phys 18(41):28864–28871. https://doi.org/10.1039/C6CP05701B

Tsuge M, Bahou M, Wu YJ, et al (2016b) The infrared spectrum of protonated ovalene in solid para-hydrogen and its possible contribution to interstellar unidentified infrared emission. Astrophys J 825(2):96. https://doi.org/10.3847/0004-637X/825/2/96

Tsuge M, Tseng CY, Lee YP (2018) Spectroscopy of prospective interstellar ions and radicals isolated in para-hydrogen matrices. Phys Chem Chem Phys 20(8):5344–5358. https://doi.org/10.1039/C7CP05680J

Tsuge M, Hama T, Kimura Y, et al (2019) Interactions of atomic and molecular hydrogen with a diamond-like carbon surface: H_2 formation and desorption. Astrophys J 878(1):23. https://doi.org/10.3847/1538-4357/ab1e4e

Tsuge M, Kouchi A, Watanabe N (2022) Penetration of nonenergetic hydrogen atoms into amorphous solid water and their reaction with embedded benzene and naphthalene. Astrophys J 933(2):138. https://doi.org/10.3847/1538-4357/ac752e

Tuli LB, Goettl SJ, Turner AM, et al (2023) Gas phase synthesis of the C_{40} nano bowl $C_{40}H_{10}$. Nat Commun 14(1):1527. https://doi.org/10.1038/s41467-023-37058-y

Vala M, Oomens J, Berden G (2017) Structure and dissociation pathways of protonated tetralin (1,2,3,4-tetrahydronaphthalene). J Phys Chem A 121(24):4606–4612. https://doi.org/10.1021/acs.jpca.7b01858

van de Sande M, Walsh C, Millar TJ (2020) Chemical modelling of dust–gas chemistry within AGB outflows – III. Photoprocessing of the ice and return to the ISM. Mon Not R Astron Soc 501(1):491–506. https://doi.org/10.1093/mnras/staa3689

van der Burgt PJM, Gradziel ML (2022) Coincidence mass spectrometry study of double ionization of anthracene by 70 eV electron impact. Eur Phys J D 76(3):60. https://doi.org/10.1140/epjd/s10053-022-00385-8

van der Tak FFS, Madden SC, Roelfsema P, et al (2018) Probing the baryon cycle of galaxies with spica mid- and far-infrared observations. Publ Astron Soc Aust 35:e002. https://doi.org/10.1017/pasa.2017.67

van Genderen AM, Nieuwenhuijzen H, Lobel A (2015) An early detection of blue luminescence by neutral PAHs in the direction of the yellow hypergiant HR 5171A? Astron Astrophys 583:A98. https://doi.org/10.1051/0004-6361/201526392

Vats A, Pathak A (2022) Rotational spectra of interstellar N- and CN-PAHs: pyrene and coronene. Mon Not R Astron Soc 517(4):5780–5790. https://doi.org/10.1093/mnras/stac3157

Vats A, Pathak A (2023) Infrared spectra of protonated and deuteronated C_{60} in interstellar environments. J Astrophys Astron 44(1):32. https://doi.org/10.1007/s12036-023-09925-z

Vats A, Pathak A, Onaka T, et al (2023a) C–H stretch vibrational modes: tracers of interstellar PAH geometries? ACS Earth Space Chem 7(7):1350–1364. https://doi.org/10.1021/acsearthspacechem.3c00028

Vats A, Srivastav S, Pandey A, et al (2023b) Theoretical microwave spectra of interstellar nitrogen-containing PAHs. Phys Chem Chem Phys 25(28):19066–19072. https://doi.org/10.1039/D3CP02722H

Veilleux S, Meléndez M, Stone M, et al (2021) Exploring the dust content of galactic haloes with Herschel – IV. NGC 3079. Mon Not R Astron Soc 508(4):4902–4918. https://doi.org/10.1093/mnras/stab2881

Vermeeren P, Brinkhuis F, Hamlin TA, et al (2020) How alkali cations catalyze aromatic Diels-Alder reactions. Chem Asian J 15(7):1167–1174. https://doi.org/10.1002/asia.202000009

Vinatier S, Schmitt B, Bézard B, et al (2018) Study of Titan's fall southern stratospheric polar cloud composition with Cassini/CIRS: detection of benzene ice. Icarus 310:89–104. https://doi.org/10.1016/j.icarus.2017.12.040

Vinitha MV, Nair AM, Kadhane UR (2020a) Production of PAH cations with narrow internal energy distribution using single nanosecond pulsed laser. Eur Phys J D 74(11):217. https://doi.org/10.1140/epjd/e2020-10340-0

Vinitha MV, Nair AM, Kumar AS, et al (2020b) Isomerization and dehydrogenation of highly vibrationally excited azulene$^+$ produced via S_2 vibrational manifold. Chem Phys Lett 745:137250. https://doi.org/10.1016/j.cplett.2020.137250

Vinitha MV, Mundlapati VR, Marciniak A, et al (2022a) Isomer differentiation of trapped $C_{16}H_{10}^+$ using low-energy collisions and visible/VUV photons. J Phys Chem A 126(33):5632–5646. https://doi.org/10.1021/acs.jpca.2c03304

Vinitha MV, Nair AM, Ramanathan K, et al (2022b) Understanding dehydrogenation sequence in fluorene$^+$ by multiphoton ionisation-excitation processes. Int J Mass Spectrom 471:116704. https://doi.org/10.1016/j.ijms.2021.116704

Wakelam V, Bron E, Cazaux S, et al (2017) H_2 formation on interstellar dust grains: the viewpoints of theory, experiments, models and observations. Mol Astrophys 9:1–36. https://doi.org/10.1016/j.molap.2017.11.001

Watrous AG, Westbrook BR, Fortenberry RC (2021) F12-TZ-cCR: a methodology for faster and still highly accurate quartic force fields. J Phys Chem A 125(49):10532–10540. https://doi.org/10.1021/acs.jpca.1c08355

Watrous AG, Westbrook BR, Fortenberry RC (2022) Theoretical spectra and energetics for c-C_3HC_2H, l-C_5H_2, and bipyramidal D_{3h} C_5H_2. Front Astron Space Sci 9. https://doi.org/10.3389/fspas.2022.1051535

Webster IJ, Beckham JL, Johnson ND, et al (2022) Photochemical synthesis and spectroscopy of covalent PAH dimers. J Phys Chem A 126(7):1144–1157. https://doi.org/10.1021/acs.jpca.1c10606

Wendt M, Husser TO, Kamann S, et al (2017) Mapping diffuse interstellar bands in the local ISM on small scales via MUSE 3D spectroscopy: a pilot study based on globular cluster NGC 6397. Astron Astrophys 607:A133. https://doi.org/10.1051/0004-6361/201629816

Wenzel G, Joblin C, Giuliani A, et al (2020) Astrochemical relevance of VUV ionization of large PAH cations. Astron Astrophys 641:A98. https://doi.org/10.1051/0004-6361/202038139

Wenzel G, Simon A, Banhatti S, et al (2022) Infrared spectroscopy of the benzylium-like (and tropylium-like) isomers formed in the –H dissociative ionization of methylated PAHs. J Mol Spectrosc 385:111620. https://doi.org/10.1016/j.jms.2022.111620

West B, Joblin C, Blanchet V, et al (2014a) Dynamics of hydrogen and methyl radical loss from ionized dihydro-polycyclic aromatic hydrocarbons: a tandem mass spectrometry and imaging photoelectron–photoion coincidence (iPEPICO) study of dihydronaphthalene and dihydrophenanthrene. J Phys Chem A 118(10):1807–1816. https://doi.org/10.1021/jp500430g

West B, Useli-Bacchitta F, Sabbah H, et al (2014b) Photodissociation of pyrene cations: structure and energetics from $C_{16}H_{10}^+$ to C_{14}^+ and almost everything in between. J Phys Chem A 118(36):7824–7831. https://doi.org/10.1021/jp506420u

West B, Rodriguez Castillo S, Sit A, et al (2018) Unimolecular reaction energies for polycyclic aromatic hydrocarbon ions. Phys Chem Chem Phys 20(10):7195–7205. https://doi.org/10.1039/C7CP07369K

Westbrook BR, Rio WAD, Lee TJ, et al (2020) Overcoming the out-of-plane bending issue in an aromatic hydrocarbon: the anharmonic vibrational frequencies of c-$(CH)C_3H_2^+$. Phys Chem Chem Phys 22(23):12951–12958. https://doi.org/10.1039/D0CP01889A

Westbrook BR, Patel DJ, Dallas JD, et al (2021) Fundamental vibrational frequencies and spectroscopic constants of substituted cyclopropenylidene (c-C_3HX, X = F, Cl, CN). J Phys Chem A 125(40):8860–8868. https://doi.org/10.1021/acs.jpca.1c06576

Westbrook BR, Beasley GM, Fortenberry RC (2022a) Polycyclic aliphatic hydrocarbons: is tetrahedrane present in UIR spectra? Phys Chem Chem Phys 24(23):14348–14353. https://doi.org/10.1039/D2CP01103D

Westbrook BR, Layfield JP, Lee TJ, et al (2022b) Reparameterized semi-empirical methods for computing anharmonic vibrational frequencies of multiply-bonded hydrocarbons. Electron Struct 4(4):045003. https://doi.org/10.1088/2516-1075/aca458

Wiebe DS, Khramtsova MS, Egorov OV, et al (2014) Dust evolution in the dwarf galaxy Holmberg II. Astron Lett 40(5):278–290. https://doi.org/10.1134/S1063773714050065

Wiersma SD, Candian A, Bakker JM, et al (2020) Photolysis-induced scrambling of PAHs as a mechanism for deuterium storage. Astron Astrophys 635:A9. https://doi.org/10.1051/0004-6361/201936982

Wiersma SD, Candian A, Bakker JM, et al (2021a) Ir photofragmentation of the phenyl cation: spectroscopy and fragmentation pathways. Phys Chem Chem Phys 23(7):4334–4343. https://doi.org/10.1039/D0CP05554A

Wiersma SD, Candian A, Rapacioli M, et al (2021b) Irmpd spectroscopy of a PAH cation using felice: the infrared spectrum and photodissociation of dibenzo[a,l]pyrene. J Mol Spectrosc 382:111545. https://doi.org/10.1016/j.jms.2021.111545

Wiersma SD, Candian A, Bakker JM, et al (2022) Gas-phase spectroscopy of photostable PAH ions from the mid- to far-infrared. Mon Not R Astron Soc 516(4):5216–5226. https://doi.org/10.1093/mnras/stac2627

Witt AN, Lai TSY (2020) Extended red emission: observational constraints for models. Astrophys Space Sci 365(3):58. https://doi.org/10.1007/s10509-020-03766-w

Wolf M, Kiefer HV, Langeland J, et al (2016) Photo-stability of super-hydrogenated PAHs determined by action spectroscopy experiments. Astrophys J 832(1):24. https://doi.org/10.3847/0004-637X/832/1/24

Xiang FY, Li A, Zhong JX (2017) Diffuse interstellar bands and the ultraviolet extinction curves: the missing link revisited. Astrophys J 835(1):107. https://doi.org/10.3847/1538-4357/835/1/107

Xiao CY, Li Q, Li A, et al (2020) On the absorption properties of metallic needles. Mon Not R Astron Soc 498(3):3560–3564. https://doi.org/10.1093/mnras/staa2614

Xie Y, Ho LC (2022) The ionization and destruction of polycyclic aromatic hydrocarbons in powerful quasars. Astrophys J 925(2):218. https://doi.org/10.3847/1538-4357/ac32e2

Xie Y, Li A, Hao L, et al (2015) A tale of three galaxies: deciphering the infrared emission of the spectroscopically anomalous galaxies IRAS F10398+1455, IRAS F21013–0739, and SDSS J0808+3948. Astrophys J 808(2):145. https://doi.org/10.1088/0004-637X/808/2/145

Xie Y, Li A, Hao L (2017) Silicate dust in active galactic nuclei. Astrophys J Suppl Ser 228(1):6. https://doi.org/10.3847/1538-4365/228/1/6

Xie Y, Ho LC, Li A, et al (2018a) A new technique for measuring polycyclic aromatic hydrocarbon emission in different environments. Astrophys J 860(2):154. https://doi.org/10.3847/1538-4357/aac3dc
Xie Y, Ho LC, Li A, et al (2018b) The widespread presence of nanometer-size dust grains in the interstellar medium of galaxies. Astrophys J 867(2):91. https://doi.org/10.3847/1538-4357/aae2b0
Yang XJ, Glaser R, Li A, et al (2013) Thr carriers of the interstellar unidentified infrared emission features: constraints from the interstellar C–H stretching features at 3.2–3.5 μm. Astrophys J 776(2):110. https://doi.org/10.1088/0004-637X/776/2/110
Yang T, Parker DSN, Dangi BB, et al (2014) Crossed beam reactions of the phenyl (C_6H_5; X^2A_1) and phenyl-d_5 radical (C_6D_5; X^2A_1) with 1, 2-butadiene ($H_2CCCHCH_3$; X^1A'). J Phys Chem A 118(25):4372–4381. https://doi.org/10.1021/jp411642w
Yang XJ, Glaser R, Li A, et al (2016a) On the aliphatic versus aromatic content of the carriers of the 'unidentified' infrared emission features. Mon Not R Astron Soc 462(2):1551–1562. https://doi.org/10.1093/mnras/stw1740. arXiv:1608.06706
Yang XJ, Li A, Glaser R, et al (2016b) The C–H stretching features at 3.2–3.5 μm of polycyclic aromatic hydrocarbons with aliphatic sidegroups. Astrophys J 825(1):22. https://doi.org/10.3847/0004-637X/825/1/22
Yang X, Glaser R, Li A, et al (2017a) The carriers of the unidentified infrared emission features: clues from polycyclic aromatic hydrocarbons with aliphatic sidegroups. New Astron Rev 77:1–22. https://doi.org/10.1016/j.newar.2017.01.001
Yang XJ, Li A, Glaser R, et al (2017b) Polycyclic aromatic hydrocarbons with aliphatic sidegroups: intensity scaling for the C-H stretching modes and astrophysical implications. Astrophys J 837(2):171. https://doi.org/10.3847/1538-4357/aa5fa9
Yang XJ, Li A, Glaser R (2020a) Deuterated polycyclic aromatic hydrocarbons in the interstellar medium: the C–D band strengths of monodeuterated species. Astrophys J Suppl Ser 251(1):12. https://doi.org/10.3847/1538-4365/abba28. arXiv:2009.08402
Yang XJ, Li A, Glaser R (2020b) Superhydrogenated polycyclic aromatic hydrocarbon molecules: vibrational spectra in the infrared. Astrophys J Suppl Ser 247(1):1. https://doi.org/10.3847/1538-4365/ab67b6
Yang Y, Zhang C, Hu X, et al (2021) Gas-phase laboratory study on PAH/amino-acid cluster cations. Mon Not R Astron Soc 508(2):3009–3022. https://doi.org/10.1093/mnras/stab2723
Yang Y, Hu X, Zhang C, et al (2022) Theoretical study of the formation of large, astronomically relevant PAH-organic molecule clusters. Astron Astrophys 663:A52. https://doi.org/10.1051/0004-6361/202243386
Yang S, Xie P, Liang E, et al (2023) Catalytic role of H I in the interstellar synthesis of complex organic molecule. Res Astron Astrophys 23(5):055019. https://doi.org/10.1088/1674-4527/accb25
Yeghikyan A (2017) On dust irradiation in planetary nebulae in the context of survivability of ices. Mol Astrophys 8:40–47. https://doi.org/10.1016/j.molap.2017.06.002
Yoon YH, Hörst SM, Hicks RK, et al (2014) The role of benzene photolysis in Titan haze formation. Icarus 233:233–241. https://doi.org/10.1016/j.icarus.2014.02.006
Zamith S, Ji MC, L'Hermite JM, et al (2019) Thermal evaporation of pyrene clusters. J Chem Phys 151(19):194303. https://doi.org/10.1063/1.5100264
Zang RX, Maragkoudakis A, Peeters E (2022) The spatially resolved PAH characteristics in the whirlpool galaxy (m51a). Mon Not R Astron Soc 511(4):5142–5157. https://doi.org/10.1093/mnras/stac214
Zettergren H, Rousseau P, Wang Y, et al (2013) Formations of dumbbell C_{118} and C_{119} inside clusters of C_{60} molecules by collision with α particles. Phys Rev Lett 110(18):185501. https://doi.org/10.1103/PhysRevLett.110.185501
Zettergren H, Domaracka A, Schlathölter T, et al (2021) Roadmap on dynamics of molecules and clusters in the gas phase. Eur Phys J D 75(5):152. https://doi.org/10.1140/epjd/s10053-021-00155-y
Zhai HJ, Zhao YF, Li WL, et al (2014) Observation of an all-boron fullerene. Nat Chem 6(8):727–731. https://doi.org/10.1038/nchem.1999
Zhang L, Ho LC (2023a) The contribution of evolved stars to polycyclic aromatic hydrocarbon heating and implications for estimating star formation rates. Astrophys J 943(1):60. https://doi.org/10.3847/1538-4357/acab60
Zhang L, Ho LC (2023b) Estimating molecular gas content in galaxies from polycyclic aromatic hydrocarbon emission. Astrophys J 943(1):1. https://doi.org/10.3847/1538-4357/aca8f1
Zhang Y, Kwok S (2014) On the viability of the PAH model as an explanation f the unidentified infrared emission features. Astrophys J 798(1):37. https://doi.org/10.1088/0004-637X/798/1/37
Zhang S, Zhou J, Wang Q, et al (2015) Penta-graphene: A new carbon allotrope. Proc Natl Acad Sci 112(8):2372–2377. https://doi.org/10.1073/pnas.1416591112
Zhang Y, Kwok S, Sadjadi S (2016) Fullerenes and fulleranes in circumstellar envelopes. J Phys Conf Ser 728:052004. https://doi.org/10.1088/1742-6596/728/5/052004
Zhang Y, Sadjadi S, Hsia CH, et al (2017a) Search for hydrogenated C_{60} (fulleranes) in circumstellar envelopes. Astrophys J 845(1):76. https://doi.org/10.3847/1538-4357/aa71ac

Zhang H, Telesco CM, Hoang T, et al (2017b) Detection of polarized infrared emission by polycyclic aromatic hydrocarbons in the MWC 1080 nebula. Astrophys J 844(1):6. https://doi.org/10.3847/1538-4357/aa77ff

Zhang H, Telesco CM, Pantin E, et al (2017c) The mid-infrared polarization of the Herbig AE star WL 16: An interstellar origin? Mon Not R Astron Soc 465(3):2983–2990. https://doi.org/10.1093/mnras/stw2761

Zhang W, Si Y, Zhen J, et al (2019) Laboratory photochemistry of covalently bonded fluorene clusters: observation of an interesting PAH bowl-forming mechanism. Astrophys J 872(1):38. https://doi.org/10.3847/1538-4357/aafe10

Zhang L, Ho LC, Xie Y (2020) A method to extract spatially resolved polycyclic aromatic hydrocarbon emission from spitzer spectra: application to M51. Astron J 161(1):29. https://doi.org/10.3847/1538-3881/abc693

Zhang D, Yang Y, Hu X, et al (2021) Gas phase formation of carbon cluster (fullerenes and graphenes)/prebiotic sugar complexes. Phys Chem Chem Phys 23(2):1424–1436. https://doi.org/10.1039/D0CP04366D

Zhang L, Ho LC, Li A (2022a) Evidence that shocks destroy small PAH molecules in low-luminosity active galactic nuclei. Astrophys J 939(1):22. https://doi.org/10.3847/1538-4357/ac930f

Zhang C, Hu X, Yang Y, et al (2022b) Gas-phase reaction of fullerene monocations with 2, 3-benzofluorene indicates the importance of charge exchanges. Astron Astrophys 662:A21. https://doi.org/10.1051/0004-6361/202243087

Zhang C, Hu X, Ge Y, et al (2023a) Laboratory hydrogenation of the photo-fragments of PAH cations: co-evolution interstellar chemistry. Astron Astrophys 669:A41. https://doi.org/10.1051/0004-6361/202244951

Zhang C, Zhu C, Turner AM, et al (2023b) Processing of methane and acetylene ices by galactic cosmic rays and implications to the color diversity of Kuiper Belt objects. Sci Adv 9(22):eadg6936. https://doi.org/10.1126/sciadv.adg6936

Zhao D, Doney KD, Linnartz H (2014) Laboratory gas-phase detection of the cyclopropenyl cation (c-$C_3H_3^+$). Astrophys J Lett 791(2):L28. https://doi.org/10.1088/2041-8205/791/2/L28

Zhao TQ, Li Q, Liu BS, et al (2016) Laboratory astrochemistry: catalytic conversion of acetylene to polycyclic aromatic hydrocarbons over sic grains. Phys Chem Chem Phys 18(5):3489–3496. https://doi.org/10.1039/C5CP06425B

Zhao L, Kaiser RI, Xu B, et al (2018) Low-temperature formation of polycyclic aromatic hydrocarbons in Titan's atmosphere. Nat Astron 2(12):973–979. https://doi.org/10.1038/s41550-018-0585-y

Zhao L, Kaiser RI, Xu B, et al (2019) Gas phase synthesis of [4]-helicene. Nat Commun 10(1):1510. https://doi.org/10.1038/s41467-019-09224-8

Zhao L, Kaiser RI, Lu W, et al (2020a) A free-radical prompted barrierless gas-phase synthesis of pentacene. Angew Chem, Int Ed 59(28):11334–11338. https://doi.org/10.1002/anie.202003402

Zhao L, Kaiser RI, Lu W, et al (2020b) Gas phase formation of phenalene via 10π-aromatic, resonantly stabilized free radical intermediates. Phys Chem Chem Phys 22(27):15381–15388. https://doi.org/10.1039/D0CP02216K

Zhao L, Kaiser RI, Lu W, et al (2020c) Gas phase formation of cyclopentanaphthalene (benzindene) isomers via reactions of 5- and 6-indenyl radicals with vinylacetylene. Phys Chem Chem Phys 22(39):22493–22500. https://doi.org/10.1039/D0CP03846F

Zhao L, Kaiser RI, Xu B, et al (2020d) A unified mechanism on the formation of acenes, helicenes, and phenacenes in the gas phase. Angew Chem, Int Ed 59(10):4051–4058. https://doi.org/10.1002/anie.201913037

Zhao L, Doddipatla S, Kaiser RI, et al (2021a) Gas-phase synthesis of corannulene – a molecular building block of fullerenes. Phys Chem Chem Phys 23(10):5740–5749. https://doi.org/10.1039/D0CP06537D

Zhao L, Lu W, Ahmed M, et al (2021b) Gas-phase synthesis of benzene via the propargyl radical self-reaction. Sci Adv 7(21):eabf0360. https://doi.org/10.1126/sciadv.abf0360

Zhao L, Prendergast M, Kaiser RI, et al (2021c) A molecular beam and computational study on the barrierless gas phase formation of (iso)quinoline in low temperature extraterrestrial environments. Phys Chem Chem Phys 23(34):18495–18505. https://doi.org/10.1039/D1CP02169A

Zhao G, Chang Q, Zhang X, et al (2022) Effect of surface H_2 on molecular hydrogen formation on interstellar grains. Mon Not R Astron Soc 512(3):3137–3148. https://doi.org/10.1093/mnras/stac655

Zhen J (2019) Laboratory formation of large molecules in the gas phase. Astron Astrophys 623:A102. https://doi.org/10.1051/0004-6361/201834847

Zhen J, Castellanos P, Paardekooper DM, et al (2014a) Laboratory formation of fullerenes from PAHs: top-down interstellar chemistry. Astrophys J Lett 797(2):L30. https://doi.org/10.1088/2041-8205/797/2/L30

Zhen J, Paardekooper DM, Candian A, et al (2014b) Quadrupole ion trap/time-of-flight photo-fragmentation spectrometry of the hexa-peri-hexabenzocoronene (HBC) cation. Chem Phys Lett 592:211–216. https://doi.org/10.1016/j.cplett.2013.12.005

Zhen J, Castellanos P, Paardekooper DM, et al (2015) Laboratory photo-chemistry of PAHs: ionization versus fragmentation. Astrophys J Lett 804(1):L7. https://doi.org/10.1088/2041-8205/804/1/L7
Zhen J, Castillo SR, Joblin C, et al (2016a) VUV photo-processing of PAH cations: quantititative study on the ionization versus fragmentation processes. Astrophys J Suppl Ser 822(2):113. https://doi.org/10.3847/0004-637X/822/2/113
Zhen J, Mulas G, Bonnamy A, et al (2016b) An optical spectrum of a large isolated gas-phase PAH cation: $C_{78}H_{26}^{+}$. Mol Astrophys 2:12–17. https://doi.org/10.1016/j.molap.2015.11.001
Zhen J, Castellanos P, Bouwman J, et al (2017) Infrared spectra of hexa-peri-hexabenzocoronene cations: HBC^{+} and HBC^{2+}. Astrophys J 836(1):28. https://doi.org/10.3847/1538-4357/836/1/28
Zhen J, Candian A, Castellanos P, et al (2018a) Laboratory gas-phase infrared spectra of two astronomically relevant PAH cations: diindenoperylene, $C_{32}H_{16}^{+}$ and dicoronylene, $C_{48}H_{20}^{+}$. Astrophys J 854(1):27. https://doi.org/10.3847/1538-4357/aaa7f2
Zhen J, Chen T, Tielens AGGM (2018b) Laboratory photochemistry of pyrene clusters: an efficient way to form large PAHs. Astrophys J 863(2):128. https://doi.org/10.3847/1538-4357/aad240
Zhu B, Bull JN, Ji M, et al (2022) Radiative cooling rates of substituted PAH ions. J Chem Phys. https://doi.org/10.1063/5.0089687
Zonca A, Casu S, Mulas G, et al (2015) Modeling dust in the magellanic clouds. Astrophys J 810(1):70. https://doi.org/10.1088/0004-637X/810/1/70
Zuo W, Li A, Zhao G (2021a) Interstellar extinction and elemental abundances. Astrophys J Suppl Ser 252(2):22. https://doi.org/10.3847/1538-4365/abcc6d
Zuo W, Li A, Zhao G (2021b) Interstellar extinction and elemental abundances: individual sight lines. Astrophys J Suppl Ser 257(2):63. https://doi.org/10.3847/1538-4365/ac2cc3

Authors and Affiliations

Helgi Rafn Hrodmarsson[1] · Isabel Aleman[2] · Alessandra Candian[3] · Sandra Wiersma[4] · Julianna Palotás[5] · David Dubois[6] · Ameek Sidhu[7,8] · Donatella Loru[9] · Pavithraa Sundarajan[10] · Ella Sciamma-O'Brien[6] · Alexander G.G.M. Tielens[10]

✉ H.R. Hrodmarsson
hr.hrodmarsson@gmail.com

I. Aleman
bebel.aleman@gmail.com

A. Candian
a.candian2@uva.nl

P. Sundarajan
sundararajan@strw.leidenuniv.nl

1 Université Paris-Est Créteil and Université Paris Cité, CNRS, LISA UMR 7583, Institut Pierre et Simon Laplace, 61 Avenue du Général de Gaulle, Créteil, 94010, France

2 Laboratório Nacional de Astrofísica, Rua dos Estados Unidos, 154, Bairro das Nações, Itajubá, MG, 37504-365, Brazil

3 Anton Pannekoek Institute for Astronomy, University of Amsterdam, Science Park 904, 1098XH Amsterdam, The Netherlands

4 Institut de Recherche en Astrophysique et Planétologie, Université Toulouse III - Paul Sabatier, CNRS, CNES, 9 Av. du Colonel Roche, Toulouse Cedex 04, 31028, France

5 School of Chemistry, University of Edinburgh, Joseph Black Building, Kings Buildings, David Brewster Road, Edinburgh, EH9 3FJ, UK

[6] NASA Ames Research Center, Space Science and Astrobiology Division, MS 245-6, Moffett Field, 94035-1000, CA, USA

[7] Department of Physics & Astronomy, The University of Western Ontario, London, ON N6A 3K7, Ontario, Canada

[8] Institute for Earth and Space Exploration, The University of Western Ontario, London, ON N6A 3K7, Ontario, Canada

[9] Deutsches Elektronen-Synchrotron DESY, Notkestr. 85, 22607 Hamburg, Germany

[10] Leiden Observatory, Leiden University, PO Box 9513, Leiden, 2300 RA, The Netherlands